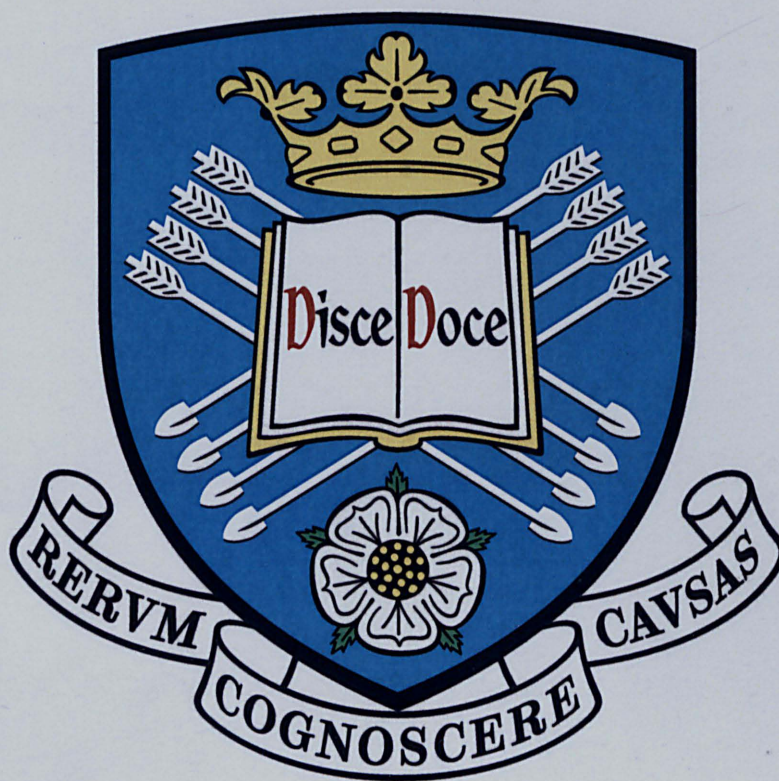# Photolithographic Patterning of Biological Light-Harvesting Complexes

A thesis submitted in fulfilment of the requirements for the degree of
Doctor of Philosophy

Department of Chemistry
University of Sheffield

Stefan J Janusz

May 2008

"And the boy herding the cows, and the surveyor driving in his chaise over the dam, and the gentleman out for a walk, all gaze at the sunset, and every one of them thinks it terribly beautiful, but no one knows or can say in what its beauty lies."

—Anton Chekhov, *"The Beauties"*

"Everything you know—your entire civilization:
It all begins right here in this little pond of goo."

—Q, *Star Trek: The Next Generation, "All good things..."*

Abstract

'Biokleptic' architectures, whereby biological material is literally stolen into an artificial fabrication, offer real-world solutions to nanotechnological engineering problems. The light harvesting 2 complex (LH2) from *Rhodobacter sphaeroides*, which increases the photosynthetic efficiency of the bacterium, has been successfully patterned on both micrometre and nanometre length scales using photolithographic techniques coupled with directive immobilisation chemistries. LH2 is present in some bacteria that use photosynthesis as a major energy source. Its function is to widen the spectral response of the organism and increase the photoresponsive chromophore cross-section. Retention of biological functionality—light harvesting and fluorescence—is demonstrated in patterned LH2 complexes on SAMs.

Patterning was achieved by the use of 'self-assembled' monolayers (SAMs) of alkylthiolates on gold. The 'tunable' nature of the surface chemistries of SAMs has been lauded as a means to impart a wide spectrum of properties, including wetting and tribological behaviours, and biocompatibility. Additionally, SAMs have attracted much interest in recent years as photoresists capable of facilitating nanometer-scale resolutions. Their proficiency as photoresists is due, in part, to the defined geometry of the molecular assembly and their molecular nature. An investigation into the mechanism of SAM photooxidation is presented for the case of alkylthiolates on gold and related systems of alkylthiolates on silver and palladium. The influence of structure on photooxidation kinetics is considered.

A simple, 'one-step' reversal of resistance to biological adhesion by exposure to UV light is presented for a protein resistant SAM. This has important implications for 'lab-on-a-chip' technologies. It is shown that biomolecules can be specifically immobilised with retention of biological functionality.

A simple coupling chemistry that suggests the possibility of transplanting thiol SAM systems onto silicon, including biologically resistant films with reversibility of response, is also presented.

Declaration of Originality

This thesis is submitted to the University of Sheffield in fulfillment of the requirements of the degree of Doctor of Philosophy. The work was carried out under the supervision of Professor Graham J. Leggett between October 2003 and May 2008. Unless otherwise stated, this work is that of the author and has not been submitted in whole, or part, at this or any other university.

....

Stefan Janusz

May 2008

Department of Chemistry, University of Sheffield.

Contents

Acknowledgements

the world has been worse off since his passing. Grannymother (Elizabeth) for being the most honest, hard-working, knowledgable and proud lady I know.

This work is also dedicated to the memories of Graham Stowe and Tim Rattray: two great friends who both died far too young, and also to the memory of Sam Hawxwell, formerly of the Department of Chemistry at The University of Sheffield, and later at New York University; without whom chemistry is worse off. As Newton said of the astronomer Roger Cotes, "If he had lived we might have known something", which is a fitting epitaph for all of these brilliant young men, although anyone who had the honour of being able to call just one of them a mate would agree that they already knew something about the world because of that friendship.

My beautiful, kind, intelligent and funny girlfriend, Kate, is the reason that I can finish this work happy. I love her very much.

Stefan Janusz, 30th October, 2007.

Glossary

IC	Integrated Circuit
LB	Langmuir-Blodgett (films)
SAMs	Self-Assembled Monolayers
fcc	face centred cubic
hcp	hexagonal close-packed
AES	Auger Electron Spectroscopy
AFM	Atomic Force Microscope/Microscopy
APD	Avalanche PhotoDiode
B.E.	Binding Energy
CCD	Charge-Coupled Device
CFM	Chemical Force Microscopy
CPD	Contact Potential Difference
EELS	Electron Energy-Loss Spectroscopy
FFM	Friction Force Microscopy
GIXD	Glancing Incidence X-ray Diffraction (spectroscopy)
IR	InfraRed (spectroscopy)
LEED	Low-Energy Electron Diffraction (spectroscopy)
MS	Mass Spectrometry
NEXAFS	Near Edge X-ray Adsorption Fine Structure (spectroscopy)
NIXSW	Near-Incidence X-ray Standing Wave (spectroscopy)
NSOM	Near-field Scanning Optical Microscope/Microscopy
RAIRS	Reflection Absorption Infra Red Spectroscopy
RCA-1	Radio Components America (cleaning protocol)

SPM	Scanning Probe Microscope/Microscopy
SPR	Surface Plasmon Resonance
SSIMS	Static Secondary Ion Mass Spectrometry
STM	Scanneling tunneling microscopy
TPD	Thermally-Programmed Desorption
UVS	UltraViolet Spectroscopy
XPS	X-ray Photoelectron Spectroscopy
XSW	X-ray Standing Wave
μCP	Microcontact printing
DPN	Dip-Pen Nanolithography
SNP	Scanning Near-field Photolithography
SPL	Scanning Probe Lithography
COHP	Crystal Orbital Hamilton Population
COOP	Crystal Orbital Overlap Population
EMR	Electromagnetic Radiation
MM	Molecular Modelling
MO	Molecular Orbital
IPA	Iso Propyl Alcohol (propan-2-ol)
OEO	Oligo(ethylene oxide)
PDMS	Poly(DiMethylSiloxane)
THF	Tetrahydrofuran
UV	UltraViolet (light)
ATP	Adenosine TriPhosphate
IgG	Immunoglobulin 'G'
LDAO	LaurylDimethylAmine Oxide
LH2	Light Harvesting Complex 2
PBS	Phosphate-Buffered Saline (solution)
RC	Reaction Centre
Tris	Tris(hydroxymethyl)aminomethane

Chapter 1

Introduction

»

"One of the reasons why this broad area of research is interesting is that if you think about *the world, there are certain major classes of things: in particular, there are gasses, liquids, and solids. There should be a fourth item on that list: surfaces. Surfaces are everything we see; they are where many properties of materials are determined, and they are what gives shape to everything. Surfaces are a particularly important arrangement of matter that should be ranked up there with those other three."*

- Professor George Whitesides, in an interview with ScienceWatch, July/August 2002

Introduction Contents

1.1   Phases and Interfaces

1.1.1   Matter, Phases and Interfaces

Matter in the universe is organised by the actions of fields and of flow into phases, bodies of energetically complimentary particulate species held together by interacting clouds of electrons. The manifest structural discontinuity of phase-separated matter is punctuated by the formation of interfaces; arrangements of component particulate species that assemble at the edges of phases, that serve to minimize the free energy of the system—maximising exothermic interactions at minimal structural cost[1-3].

In exposing particles from one phase to those of another, interfaces present a frontier of dynamic exchange and interaction; of chemical *reactions,* and physical forces.[4,5] Interfaces mark a boundary of compositional and structural difference—and so lend a given phase the property of being a discrete entity in the universe, with a finite size and certain shape.

While the size of a phase is derived largely from the quantity and thermal motion of the particles it contains, shape is influenced by external electrostatic and gravitational forces, and is constrained by contact with (and position relative to) other phases. Shape is governed also by the energetic transactions
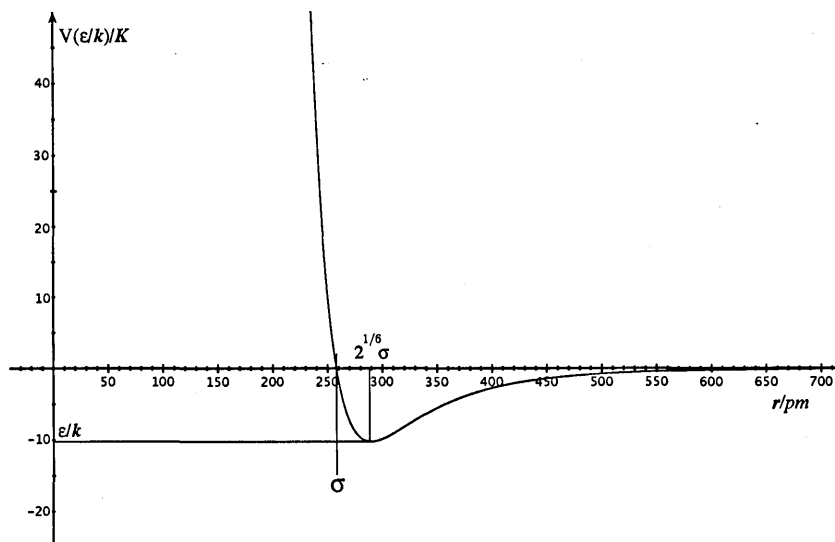
x-axis depicts separation/pm; y-axis effective temperature$\equiv (\varepsilon/k_B)/K$
data from Atkins' Physical Chemistry[1]

Figure 1.1.1   Lennard-Jones '6-12' Potential for Helium.

that take place at the interface: the degree of affinity of one phase for a neighbouring phase affects the size of their interfacial area, and consequently the shape of one or both phases must change to accommodate this. The beading of a droplet of water on a lotus leaf compares contrastingly with the flat puddle that spreads out on a clean silica glass surface[6]; paraffin oil will spread out on a pond until the advance of the film is limited by the number of molecules in the drop[7]; the amphiphilic molecules in soap form bubbles in the air to minimize their exposed surface area, while maximising lateral packing[8].

In the mundane realm of everyday human experience*, atoms and molecules have a finite size and will resist compression beyond a certain density, as precluded by the Pauli exclusion principle, which states that no two fermions with the same wavefunction descriptors may occupy the same physical space. The transient attractive forces that act as being proportional to $1/r^6$ are outweighed by a repulsive term that rises exponentially; as the wavefunctions approach a distance where they begin to overlap, the repulsive force rises to infinity. The interaction potential so described is shown in **figure 1.1.1**. With similar constraint at the opposite length scale, time puts a maximum limit on the size of a phase, such a bubble of gas expanding in space, because rates of diffusion are also finite ($\propto \sqrt{\frac{T}{M}}$)†.

---

*as apposed to exotic environments, such as as supercooled matter and the singularities that comprise black holes and the possible initial state of the universe

†*T*emperature; *M*ass

1.1.2   Compartmentalization of Phases in Biology

1.1.2.1   Limited phases and compartments

Within these broad limits, nature has selected for the compartmentalization of phases in organisms at a certain magnitude: large enough to contain all the infrastructure and materials needed to sustain life, while at the same time being small enough for metabolites and cellular machinery to be able to collide, interact and perform all the requisite functions of a living organism, *within a time-frame dictated by the rates of chemical reactions*. The physical act of compartmentalization also puts a limit on the selection of components that are contained within a cell. It ensures that chemistry that is useful for survival greatly outweighs that which is useless or detrimental to the organism[2].

(a)   (b)
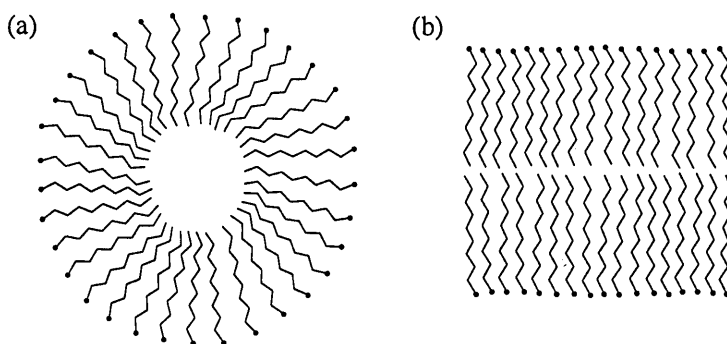
Figure 1.1.2   Self-assembly of amphiphiles in solution:
Cross-sections through (a) a micelle, and (b) a bilayer

The molecular structures that nature has selected for in providing such barriers to cells are assemblies of amphiphiles[*], organic molecules that contain both a polar, hydrophilic head group, and a hydrophobic hydrocarbon tail[9]. Amphiphiles self-assemble in suitable solvents to produce a variety of forms that aim to maximise intermolecular interactions (both within the assembly, and also between the assembly and its host media), again, at *minimal structural cost*: the minimal increase in entropy associated with least-surface-area forms. Above a critical concentration, when the amphiphile molecules have formed a single layer at the fluid-air[†] interface, they begin to spontaneously form **micelles**, approximately spherical aggregates with the more readily-solubilisable component (in water, the polar head group) forming a solvent-facing surface, shielding the inwardly-pointing insoluble tails. This is shown in part (a) of **figure 1.1.2**, above. At yet higher concentrations, the entropic cost to the solution of forming more

---

[*]augmented, of course, in some species by additional proteins and carbohydrate scaffolds
    [†]and fluid-container interface, if the containing vessel is of a composition differing to that of the fluid but similar to the insoluble component of the amphiphile

spherical micelles (because each micelle must be solvated by a surrounding 'cage' of solvent molecules) becomes an impetus for the formation of long tubes of the amphiphilic aggregates. From the close-packed 'honeycomb' arrangement that these tubular micelles must adopt as the concentration increases, it becomes thermodynamically favourable to form lamellar sheets: a bilayer[8,9] (shown in part (b) of figure 1.1.2 on the preceding page). The phospholipid membrane of a living cell is just such a lamellar bilayer sheet that is wrapped around on itself to form a vesicle, allowing the organism to maintain a chemical independence of the cell from the extracellular environment.

1.1.2.2   Regulation

In order for the organism to have have regulatory control over the biochemical composition of the cytoplasm, a number of pumps and channels are formed by the expression of proteins during the growth cycle of the cell. They traverse the membrane and selectively (by size, or electrostatic interactions, for example) allow the expulsion of waste materials to, and consumption of fresh metabolites from, the periplasmic outer-side[9]. In addition, they provide a means of assessing the nature of the external environment, and communicating with other cells. As well as numerous transmembrane transporter proteins (which comprise those that carry out the channel regulation described above), enzymes such as methane-metabolising methane monooxygenase, found in the bacterium *Methylococcus capsulatus*; and the light harvesting complexes found in the purple non-sulfur bacterium *Rhodobacter sphaeroides*, which increases its photosynthetic efficiency, are also expressed at the lipid bilayer. Therefore, the biological membrane provides not only a barrier against the external environment, but a foundational structure within and upon which functional cellular machinery may be built.

1.1.2.3   Integrated circuits

It is of note that the ubiquitous electronic technologies of the past 50+ years are themselves built around and directly upon surfaces. The printed circuit boards and transistor chips that make up the electronic devices used by contemporary society are vastly more reliable, inexpensive, compact and powerful than their valve-based predecessors. A layout plan of an integrated circuit (IC)—a computer microprocessor—is shown, in **figure 1.1.3** on the next page. The key to such remarkable improvement has been the development of fast, non-contact fabrication methods that rely on photochemical processes, developed principally at Bell Labs in the 1950s[10,11], and subsequently implemented at Fairchild semiconductor in the early 1960s[12].* The exposure of a photoresist to appropriate wavelength light through a

---

*Photochemical modification of surfaces will be discussed further in Subsection 1.4.3.2, and Chapter 3.
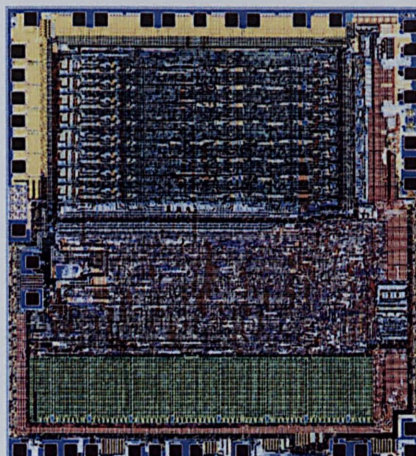
Figure 1.1.3   Core layout of a MOS Technology 6502 microprocessor:
An early, inexpensive chip that helped pave the way for the home computer revolution

negative mask, followed by an etchant wash, leaves exposed areas upon the substrate, which may then be coated by sputtering, evaporation, or ion beam deposition to create paths of electrically-conductive material. Once the previously unirradiated photoresist has been removed by a second washing procedure, the remaining conductive tracks traverse the surface of the substrate and connect the components of the device together. These are in many ways analogous to the transmembrane and intervacuole channels employed in biological cells, although they are solid and can only convey electrical charge (electrons in metals, or electrons plus 'holes' in semiconductor metalloids) as opposed to the ions, proteins and myriad chemical signallers that life employs in its processes.

1.1.2.4   Signalling in biological processes

It is particularly remarkable that it is *this* very complex, multiple signal approach to producing responses in systems on very small scales (nm– μm) that affords living matter such an advantage over human attempts to produce technology at a similar size. Despite the extremely fast switching speeds of transistors in present, desktop computers ($> 10^9$ s^{-1}), biological changes are brought about with a comparatively astounding rapidity, precisely because of this plurality. The binary nature of the state of a transistor requires that a much greater number of discrete instructions be issued to produce a significant change in an electronic system (*e.g.* multiplying two integers held in memory), as compared with a *transcriptase* enzyme that can process and duplicate complex polymeric, biomolecular structures with a single pass.

1.1.3   Nanobiotechnology: The Challenges

It has been suggested that, because of the new problems (such as Brownian motion, and quantum tunnelling) that present themselves as human technology enters the nanoscale regime (1–100 nm), engineers would benefit from adopting an approach that borrows from the successes of biology[13, 14]. At this scale, the water molecules that constitute the bulk medium of living processes perturb and interact chemically with biological structures, *e.g.* by deprotonating acid moieties. Natural, biological processes have adapted to make use of this fact, just as some enzymes apparently employ quantum tunnelling in their functionality, rather than working to circumvent it. There are fundamental physical differences between properties defined at the nanoscale, as compared with the same properties at the macroscale. Nanoscale structures have 'low dimensionality'; they are nearly *all surface*. Thermodynamics and mechanical properties of surfaces are different from those of the bulk, because atoms at surfaces have fewer neighbouring atoms to interact with. Atoms at surfaces have characteristics that lie somewhere between solid and liquid states, as can be seen from *e.g.* the depression of melting points in nanostructures made from metals[15].

It is clear that the fantastical view, à la K. Eric Drexler's *Engines of Creation*[16], where it is proposed that nanotechnological engineering solutions might take the form of shrunken, macroscale technology (*i.e.* the machinery will be familiar to us, but smaller), is not really a viable approach. The problem of creating functional devices on such small scales has been addressed—with some success—by the integration of biomimetic and biokleptic* structures into nanoscale devices, but totally successful integration, *i.e.* with a view to producing functional nanostructures, has often been problematic. This may stem from the presumption that biological structures, which may superficially resemble macroscale mechanical devices (*e.g.* the similarity of a Na^+/K^+ ATP*ase* rotor to a peristatic pump[14]), will be easy to immobilise and connect together like a LEGO® TECHNICS set; in actuality, immobilisation, integration and addressability of a biomolecule, especially with retention of proper functionality, cannot always be guaranteed. Nevertheless, some biological architectures display remarkable resilience to being manipulated into artificial systems, and provide excellent solutions to nanoscale engineering problems, as will be demonstrated.

---

*copying, and *stolen* from biology, respectively

1.1.4   Supramolecular Assemblies:

Learning New Manufacturing Methods from Nature

1.1.4.1   "Technology requires tools"

Throughout history, the development of tools with which human beings have endeavoured to gain control over their environment has been steered as much by the availability of suitable materials, as by human ingenuity[17]. Access to materials, when placed in the context of an adequately developed understanding of the physical properties of those materials, has driven technological progress; the tools and instruments made possible by newly available materials in turn provide a means to manipulate and probe the nature of those materials, and so improve our understanding of them. Over the past several hundred years, the gradual adoption of the scientific method has provided humanity with a firm foundation upon which to efficiently gauge the viability of potential technologies, and the rate of technological progress has accelerated accordingly.

Many of the most commonplace materials in human technologies have, however, remained little changed since being adopted by pre-scientific societies millenia ago. Raw materials (stone, flint, wood) are used in manufacturing because of their innate properties, while the processing of raw materials, *e.g.* metal ores—to yield metals and alloys; and natural zeolites and aluminosilcate clays, to make bricks and other architectural building materials; aims to improve upon natural properties, or change them in some desired way (*e.g.* silica sands yielding transparent glass). This may be compared with the (relatively—*ca.* 100 y) nascent field of the polymer industry, which from the outset has made a wide variety of new materials with a broad spectrum of properties, ensuring their rapid adoption in countless applications. Crucially, the ability to control—at the monomerical level—the composition of a polymer, has aided the development of polymer science, in such diverse areas of research as interfacial friction[18], biocompatibility[19], and molecular electronics. At the same time, absolute control of the chemical species at the surface of a polymer is difficult to achieve, as the orientation of monomers within a polymer is governed by self-organization processes that take place as the polymer superstructure is formed. If "surfaces... are where many properties of materials are determined", then precise control over the surface species is desirable in a new material, especially one designed for nanoscale applications. This particular property, among several others that are sought, has been offered by oriented organic thin films, which will form the larger part of the basis for this thesis, and will be introduced in section section 1.1.5 on page 10. Before these are fully introduced, some consideration might be given to the way nature employs self-assembly in living processes.

1.1.4.2   Organic molecules: weak interactions

In contrast with the materials used in human technology, which might consist of the heavier elements (metals, metalloids), are often crystalline, or have otherwise non-stoichiometric compositions (aluminosilicates), the chemical elements that form the infrastructures of living systems are largely made up of the covalently bonding elements that form the upper-right portion of the periodic table. Molecularity in organic molecules is favoured by the similar magnitude of the average bond enthalpies of C–C ($\sim$335 kJ mol^{-1}) and C–H ($\sim$410 kJ mol^{-1}), and the slightly larger latter quantity is reflected, to some extent, in the higher abundance of smaller hydrocarbons in abiotic environments. In the reductive conditions of prebiotic Earth[2], simple hydrocarbons such as these were subject, it is thought, to electrical storms and extreme conditions that catalysed the formation of branched, cyclized, aromatic and heteroatom-containing organic molecules that may have been adopted into the self-catalyzing, self-propogating processes of an early *proto*-life prior to the beginnings of biosynthesis in organisms at a considerably later time[2,20]. The huge variety of reactions that may take place under such conditions between various organic molecules and hetero-species, including molecules containing O, N, and S, halogens, and metallic elements, has been investigated to a great depth and breadth by the field of organic chemistry. Relatively recently, it has been shown that not only biologically relevant amphiphiles, but porphyrins, peptides and nucleobases, may all form in abiotic environments. Of those examples, amphiphiles have been highlighted as of particular interest as a means to compartmentalize self-propogating cyclic reactions in the 'prebiotic soup' (as it has been called), to increase the thermodynamic efficiency of systems that could have been the precursors to life. Although the speculative nature of such an assertion cannot be denied, it is clear that biological cellular membranes fulfil this function today: Amphilphilic bilayers demarcate cellular processes. As described previously in subsection 1.1.2.1 on page 4, amphiphiles are self-organizing molecules, a property which is ideally suited to forming assemblies on the nm–µm scale.

The discrete molecularity of organic molecules, with hydrogen as a passivating agent, has made them ideally suitable as the building materials for the fluid processes of life; cellular structures are not required to be rigid. Organic molecules may exist as many different isomers, and nature has evolved machinery to facilitate kinetic short-cuts—enzymes—to enable these structural changes to be made at ambient temperatures. Hydrocarbon chains are essentially apolar, and biological membranes rely on van der Waals or dispersion forces to hold these assemblies together. These so-called 'weak interactions' render the assemblies themselves more flexible, enabling structural changes to be made during the lifetime of the organism*.

---

*The exceptions here are the scaffolds of arthropods (shells) and vertebrates (bones), which are complex structures of calcium

1.1.4.3   Materials in human technologies

In comparison, human technology has traditionally required a vast input of energy during manufacture: for example, the use of melts or the elevated temperatures required for many industrial processes. Such extreme conditions become impractical at very small scales, with the ever-increasing intricacy of fabrication that is required. Self-organizing processes such as the self-assembly of bilayers often take place in mild conditions, and complexity can, to some extent, be built-in by careful choice of component molecules. Because of the thermodynamic impetus of a physical system to minimize its free energy— 'nature abhors a gradient'[3]—defects are repaired by rearrangement and replacement. This is as desirable a healing process in nanoscale technology as it is in living organisms.

Our understanding of self-assembly is, at present, not developed enough for us to hope to match the precise ergonomics of biological 'machines' with our own functioning nanostructures. In order to begin to understand the complexities of interactions at small scales, it is necessary to start with simple, predictable systems[21]. While many of the advances towards nanoscale fabrication have been brought about by 'top-down' methodologies employed by the semiconductor industry, a vast library of molecular structures with every desirable property has been made available by organic synthesis. Assemblies of oriented organic molecules can provide a means to exact control of surface properties, and are patternable by a number of methods, to produce two dimensional nanostructures.

1.1.5   Organic Thin Films

1.1.5.1   History

The capacity of thin films of organic molecules to drastically alter surface properties has long been of importance in a number of realms of enquiry, and has been exploited in humankind's technological and artistic endeavours. For example, numerous historical writings record observations of the calming effect of oil on water[22-24]. Investigations by Benjamin Franklin[7] regarding the spreading of small quantities of triolein over large areas of Clapham common pond would later be given a theoretical basis by Röntgen, Rayleigh and Pockels, among others[25]. The amenability of organic films to producing directed patterns also has an early precedent: The technique of Suminagashi was used by the Japanese 1200 years ago to colour paper[26]. It relies upon the formation upon a water surface of a film of a protein dye, which is facilitated by the carbon suspension that the water contains. This so-called 'Chinese ink' was then

---

carbonates and phosphates, with traces of magnesium and other elements. However, these only serve to support life above a certain size and are ultimately not essential for life to exist; some molluscs have no such support structures, for example.

transferred to paper using a horizontal lift. This method would be echoed in Irving Langmuir's creation of monolayer films on solid substrates in the early 20th century.*

Testament to her skills as a scientist, the work of Agnes Pockels was fundamental to the confirmation of the molecularity of matter; a fact made all the more impressive when it is considered that she had no formal scientific training and worked with household items. Pockels' apparatus, among other things, included a vessel for the containment of a fluid (usually water) and a tin strip dividing the fluid at its surface, allowing the area of the surface under study to be changed. A small button sat in the trough and was attached to a balance, allowing an accurate determination to be made of the surface tension in the region of fluid defined by the tin strip. This apparatus is a basic version of a Langmuir trough, named after industrial chemist Irving Langmuir, who would go on to give a molecular basis for Pockels' findings.

Pockels' careful studies of the pressure-area isotherms of surfactants would lead to direct evidence of the molecular structure of materials, and the monolayer nature of amphiphiles at interfaces. Her findings indicated structural *phase* transitions of surfactants as the surface area of the liquid substrate was reduced. From this it could be inferred that the fluid under study was compressible up to a limit, the *maximum packing density*; also, the sharp increase in film pressure per area was indicative of a molecular composition—it must consist of discrete entities with finite volumes. At the time, some scientists were still not convinced of the atomic nature of matter, and considered such notions merely to be useful mathematical models.

Pockels was astute enough to communicate her findings to Lord Rayleigh, who recommended their publication in Nature[27]. Inspired to conduct his own experiments, Rayleigh was led to conclude that such films were only one molecule thick, and was able to deduced a numerical value[25] for Avogadro's number: 6.08×10^{23} mol^{-1}.

The formation of thin films at the air/water interface is directed by the amphiphilic structure of the surfactant molecule. Free energy is greater at an interface due to reduced interactions as compared with the bulk. For this reason, impurities in materials eventually make their way to the surface (for example, 'slag' forms on a melt of iron during refining).

It has been shown that it is possible to form structured films on liquid surfaces, and at the interface between 2 immiscible liquids[28]. However, such films (either between air/liquid or liquid/liquid) are

---

*Crucially, Langmuir's method was an improvement because the substrate is drawn through the film, from liquid to air, perpendicular to its plane. The transfer ratio is close to 1 in this case—the packing density of molecules on the substrate will reflect that in the liquid phase. This may not be the case for a horizontal lift.

limited in their technological application because they are not rigid enough; they are difficult to work with because they are so delicate. The first step towards the engineering of surfaces therefore came with the transfer to a rigid, solid substrate.

1.1.5.2 Development

In a body of work spanning 1916–1917[4,29], Irving Langmuir explored the properties of organic thin films, and in 1918 demonstrated the possibility of transferring monolayer films to solid substrates[30]. By drawing a sheet of glass upwards through a thin film perpendicular to its plane, it is possible to achieve monolayer coverage. Such a surface-bound film will retain the structure of the 'liquid' monolayer, unless there is a specific interaction between the molecules in the film and the substrate that fosters an ordered morphology. The isotherm for adsorption of a species onto a solid substrate giving monolayer coverage now bears his name, as do the monolayer films themselves. The work carried out by his assistant, Katherine Blodgett, would lead to the fabrication of new materials based on successive deposition of multilayer. These are now called Langmuir-Blodgett (LB) films in their honour.

Interest in LB films as systems with potential technological applications was revived by Hans Kuhn in the late 1960s[31]. Kuhn and co-workers at the Max Planck institute in Göttingen demonstrated the application of LB films as information processing devices. It was realised that thin films could store information they could be patterned at a molecular scale and and that the short range co-operativity offered by high packing densities could be exploited to make rudimentary logic gates.

A programme of study that would be among the most important in the field of organic thin films had its beginnings in research carried out by Richard, Deutch and Whitesides in 1979[32], which explored the reactivity of an ω-alkene on oriented thin films of C_{18} fatty acids. Reactions where one reactant is held at a fixed position are of particular interest to the field of heterogeneous catalysis, and fixed orientation improves our understanding of the rôle of geometry in molecular dynamics. In order that the organic molecule be oriented correctly, it is desirable that the tethering functionality have a specificity of binding (preferably, chemisorption) for the substrate that far exceeds that experienced by other functionalities, especially if both groups are polar. This quality of differentiation has been called 'amphifunctionality'.[33] The particular class of materials that are formed by such interactions are termed Self-Assembled Monolayers (SAMs).
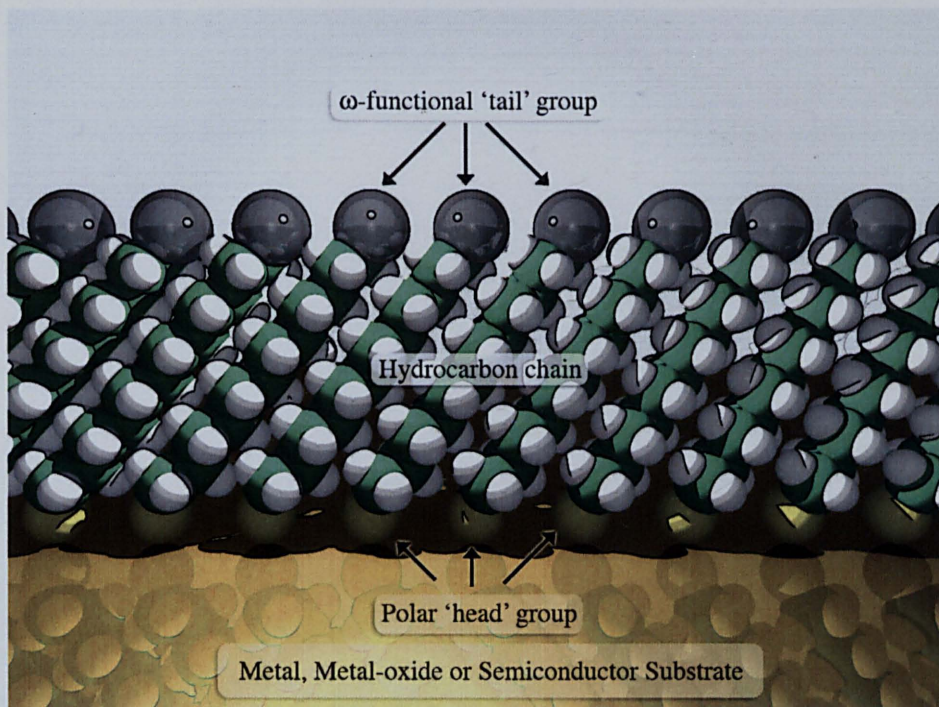
Figure 1.2.1   The General Structure of a SAM

1.2   Self-Assembled Monolayers

Self-Assembled Monolayers (SAMs) are oriented, organic, single-layer films of amphiphiles that are directed by specific interactions to adsorb on metallic or semiconductor substrates. They have the general structure depicted in **figure 1.2.1**. A polar 'head group' with high specificity for the substrate facilitates adsorption, while lateral dispersion interactions within the film provide a thermodynamic impetus for the molecule to stand up from the surface. Control (by synthesis of appropriate SAM molecules) of the ω-substituent 'tail group' allows for 'tunable' surface chemsitries.

SAMs based on many such interactions have been demonstrated, on substrates such as Si, Au, Ag, Cu, Pt, Pd, Ti, and Al, and various metal oxides, via alkoxysilane, carboxylic acid, phosphate and sulfur interactions, among others. The realisation that ordered organic films with a directed ('amphifunctional') attachment to a solid substrate could be used to modulate surface properties was principally explored by Sagiv[34], observing the formation of silane SAMs on silicon that demonstrated 'oleophobic' properties. Silicon SAMs are of immense importance, having a wide variety of potential applications in many nascent technologies—especially outside of the laboratory—and are discussed further in **Subsection 1.2.2.3** on page 27.

1.2.1 Organosulfur SAMs on Gold

1.2.1.1 The 'archetypal' SAM

Of the many SAM systems that have been demonstrated, organosulfur compounds on gold are easily the most widely studied[35–39]. Akanethiols on gold have been called the 'archetypal SAMs'[37]. These readily form large, ordered, crystalline monolayers with well-defined structures. The gold-thiolate bond is a highly specific interaction, worth in the order of $120\,kJ\,mol^{-1}$; sulfur groups that yield thiolates upon adsorption (thiols and disulfides) will readily displace other functionalities present on the substrate[40,41]. Sulfur and gold have very similar electronegativities (2.5 and 2.4 on the Pauling scale, respectively[42]). Indeed, gold is the most electronegative metal and is rightly classed as a 'soft' electrophile; gold does not readily form compounds with hard nucleophiles such as oxygen. Because it is chemically inert to atmospheric species, only weakly-bound physisorbed materials are present on well-prepared gold substrates. These are readily displaced by desired sulfur-containing adsorbates, and so gold is an ideal substrate for alkylthiolate SAM formation.

Mono– and polyfunctional sulfur-containing compounds were proposed as promoters for the drop-wise condensation of steam by Blackman and Dewer in 1957[43–45], as a means to increase efficiency in electricity generating plants. In a yet earlier work, Emmons proposed a similar industrial application, with the suggestion that the "metallophilic" sulfur causes the hydrocarbon chain to form a 'brush' on the surface[46], proposing that the hydrocarbon chains are oriented to the surface normal.

Interest in organic films based on the aurophilicity of sulfur was initially rekindled by Nuzzo and Allara[47]. Their 1983 paper outlined a technique that "employs solution adsorption of disulfides on zerovalent gold substrates" and realized the potential of SAMs with an investigation of different tail group functionalities. Nuzzo, Zegarski and Dubois carried out some of the first characterizations of these systems by multiple methods in 1987[48]. The stability of SAMs was probed using a thermally-programmed desorption (TPD) technique and determined via quadrupole mass analysis. The bond energy of chemisorbed thiolate (from organothiols and organodisulfides) was thus reported to be in the order of 30–$35\,kcal\,mol^{-1}$. The nature of the film-substrate binding was also probed by X-ray photoelectron spectroscopy (XPS), Auger electron spectroscopy (AES) and electron energy-loss spectroscopy (EELS). Many features of alkanethiolate SAMs on gold (which will from now be referred to as Au–SR SAMs) were thus made evident, of particular relevance being the XPS results proving chemisorption at the substrate through distinctive S_{2p} binding curves. These studies were augmented in the same year with further work by Nuzzo, Allara and Fusco[41], and Porter *et al.*[49], with studies of

'tethered'* ether-containing disulfides and alkyldisulfides, and *n*-alkanethiols adsorbed on gold films; by ellipsometry, Infrared (IR) spectroscopy, XPS and electrochemical measurements. XPS[41] of samples at raised temperatures suggested sulfur-gold bond energies corroborant with previous TPD studies[48], while electrochemical studies by Porter *et al.* indicated that the longer-chain thiols were resistant to ion penetration; their ellipsometric data suggested a "closest packed" molecular arrangement with a chain tilt of the aliphatic hydrocarbons of 20–30°. Such a structure was also proposed by Nuzzo *et al.*[41] for hexadecanedisulfide films, supported by transition dipole moments inferred from frequency shifts in IR spectra. Ulman, Eilers and Tilman[50] subsequently presented a model of Au–SR SAM structure based on a previous work by Rabe *et al.*[51] and their own Molecular Modelling (MM) calculations. Rabe *et al.*'s work on LB films on Si suggested that, because of the 'zig-zag' profile of a hydrocarbon chain (a consequence of carbon's tetrahedral geometry), only certain cant angles can be adopted that both maximise dispersive interactions between chains, while also avoiding steric clashes. These are given by:

$$tan\,\tau = \frac{nR}{D} \tag{1.2.1}$$

where R is the distance between next-nearest neighbour carbon atoms (2.52 Å), D is the minimum separation between chains (determined by Ulman, Eilers and Tilman[50] to be 4.24 Å from MM calculations). From this analysis, it could be reasoned that only certain, discrete angles would be observable: 0°, 30.7°, 49.9°...for n=1, 2, 3...resepectively; however, this neglects chain twists (α) that cause deviations from these angles. The precise geometry of molecular species within the adsorbate adlayer is therefore dependent not only on factors imposed by the available overlap of headgroup-substrate orbitals, which manifests itself through lattice spacing, but also the molecular orbitals within the hydrocarbon chain and, as will be shown, the nature of the ω surface substituent.

1.2.1.2   Model surfaces

Of the many self-assembling films investigated, organothiolates on gold have revealed themselves as ideal systems for probing diverse interfacial phenomena, with potential industrial applications that were first investigated some 50 years ago[43–46]. Wetting of mixed monolayers of dialkyl sulfides has since been investigated by Bain and Whitesides[52], in work which linked wettability† (a macroscopic phenomenon) to ellipsometric data and attenuation of photoelectrons ejected by X-rays (both microscopic phenonema). Scrupulous choice of different-length dialkyl sulfides in the binary mixtures indicated a thermodynamic preference to form monolayers containing a greater number of lateral interactions (*i.e.*

***i.e.* with additional bonding C–C in the carbon component

†The wetting phenomenon and its physical basis will be discussed in 1.3.1
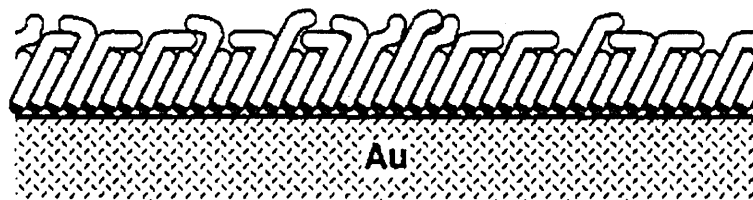
Figure 1.2.5 Eclipsing of shorter SAM components by longer ones, reproduced from *Ref.*[54]

the longer molecule is preferentially adsorbed over the shorter), reflected in a bias in the requisite composition ratio to produce a phase transition away from 1:1 to $\sim$10:1 (shorter : longer). This result is perhaps unsurprising, since SAM formation is in essence kinetically driven, with an estimate of $\Delta_{fusion}H=0.4\,\text{kcal mol}^{-1}$ per methylene group, drawn from studies of melting points of *n*-alkanes[53,54]. Also inferred from ellipsometric measurements was the fact that the longer chains in mixed monolayers must 'overhang' the shorter ones, effectively eclipsing their projected physical characteristics, while also exposing the methylene groups of the longer SAM. This is depicted in **figure 1.2.5**. The important consequence of this particular observation is that composite SAMs of two or more molecular components should be designed with a consideration of their respective lengths; unwarranted eclipsing of a shorter SAM molecule by a longer one negates any surface property sought by the inclusion of the former.

Further studies investigating the adsorption of dialkyl sulfides onto gold were carried out by Troughton *et al.*[55], and a number of interesting results were obtained:

- Wettability is a short-range phenomenon, operating at $<5\,\text{Å}$, which is at odds with earlier work carried out by Shafrin and Zisman[56] that suggested that ostensibly 'buried' dipolar groups within a film might impose long range effects on surface properties (since dipoles fall off as r^{-3}). However, this particular study was carried out on oriented organic films with less long-range order than organothiolate SAMs, or non-oriented films, and so the exact surface morphology may not have been that expected, *i.e.* the 'buried' groups could, in fact, have been partially exposed. Troughton *et al.* found that Langmuir's PRINCIPLE OF INDEPENDENT SURFACE ACTION[4], whereby macroscopic properties are determined as a sum of the free energy contributions, is obeyed.

- As dialkyl sulfides cannot dissociatively adsorb at a surface (because one of the products would have to be a primary carbocation), the bonding mode is necessarily different from organodisulfides (which may dissociatively adsorb by S–S scission) or thiolates. However, the bonding is specific and should not be thought of as a merely physisorbed state; the interaction is worth

$\sim$60 kJ mol^{-1}[157], which is more than most dispersion forces; moreover, it should be remembered that sulfur can adopt valencies of 4 and 6 as well as 2 (due to the availability of 3d orbitals) so it is possible that the sulfur in the case of dialkyl sulfide SAMs interacts with two gold atoms.

1.2.1.3   Kinetics of formation

Further studies by Bain *et al.*[58] on Au–SR SAMs formed from thiols in solution were reported in well-cited publication of 1989, in which a number of previous studies were drawn together, and elaborated upon. Work published in the same year by Bain, Biebuyck and Whitesides[40] demonstrated that SAMs formed from thiols and disulfides are indistinguishable from their S$_{2p}$ photoelectron spectra, indicating that the surface-bound species must be the same in each case; proposing, as suggested previously by Porter *et al.*[49], a thiolate. Bain, Biebuyck and Whitesides' work showed that thiolate adsorption is favoured over that of disulfides[40] from mixed solutions, seemingly contradicting earlier work by Nuzzo *et al.*[41], which placed disulfides over thiolates as better candidates for SAM formation.

Ellipsometric and contact angle data were used to follow the kinetics of SAM formation[58], revealing (at least) two distinct modes in the process. SAM formation is at first rapid, with ellipsometric data showing that 80–90 % of final thickness is achieved in only a few minutes. Thereafter follows a slower annealing process, lasting several hours, which was rationalised as a consolidation of the 2D crystal following an initial, disordered state. This is in agreement with several studies made since[37].

Eberhardt *et al.*[59] followed SAM formation with Glancing Incidence X-Ray diffraction (GIXD), and showed that initial monolayer growth could be described by first order Langmuir kinetics, followed by the appearance of a new Bragg peak at a critical coverage indicating the formation of a denser phase, which also follows normal Langmuir adsorption kinetics:

$$\Theta = \frac{k_a[RSH]}{k_a[RSH] + k_d} \tag{1.2.2}$$

(where Θ is the monolayer fraction, k_a is the rate of adsorption and k_d is the rate of desorption)—but with a time offset, *so:*

$$\eta = 1 - e^{R(t - t_c)} \tag{1.2.3}$$

for $t > t_c$, where k_a denotes rate of molecular adsortion, k_d of desorption; η denotes the degree of consolidation into the denser phase after monolayer coverage is achieved (when $\Theta = 1$).

SAM growth is often described[35,39] as consisting of four stages:

1. A 2D 'lattice-gas' structure, in which very little order is observed, with adsorbates seen to have a high degree of mobility by atomic force mircoscopy (AFM)[60].

2. Nucleation and growth of a low density, 'lying down' or 'striped' phase. in which the adsorbates are described as having a 'pinstripe' structure.

3. At critical coverage nucleation of the denser phase occurs. For this to happen, a reorientation to a 'standing up' mode must be made. This happens 3–4 times more slowly than 2. Specific orientation is dictated by packing, Van der Waals interactions, and the directionality imposed by the S–Au bond, as will be discussed further. There is evidence to show that this process is second order, which may indicate some cooperative processes.

4. 'Healing' of the SAM. This is rather ambiguous, but generally involves the rectification of point defects, and the consolidation into long-range order specific to crystallisation processes. However, evidence indicates that shorter chain alkanethiolate SAMs retain a high degree of mobility at room temperature that is characteristic of a liquid phase. No long-range order is seen in short-chain SAMs, which has been supported by evidence from friction force microscopy (FFM) experiments and oxidation studies.

The processes leading to SAM formation are fairly well-established, and are supported by a number of experimental studies, *e.g.* by time-resolved ellipsometric measurements, and SAMs in intermediate stages of development have been isolated. Poirier *et al.*[61] investigated liquid-like states of short chain SAMs, which do not posess the long hydrocarbon chains thought to be crucial to the later consolidation stages. Further evidence at low coverages, formed from solutions with a net deficit per adsorption site of thiol molecules, depicts island coverages consistent with a diffusion-limited process that was identified by Camillone[62]. Barrena *et al.*[63] and Munuera *et al.*[64] have identified routes to, and clear images of, SAMs at subsaturated coverages. Longer SAMs are comparitively more crystalline, due to the increased van der Waals interactions afforded by a greater number of methylene groups. It has been shown that thermal degradation may be employed to achieve a controllable subsaturation of adsorbates[65].

1.2.1.4   The nature of the adsorbate species

A number of important pieces of evidence indicate that the substrate-bound species is a thiolate, regardless of whether the adsorbate is formed from thiols or disulfides, or from solution or gaseous phase. Bryant and Pemberton demonstrated loss of S–H stretching in surface-Raman scattering experiments[66,67] on silver and gold, although there is evidence that methanethiol does not lose H upon

adsorption[68]. There is a kinetic barrier to loss of thiol hydrogen that may initially cause an initial

preference for disulfide adsorption, as described by Nuzzo *et al.*[41], whereas Bain *et al.*[40] found a

preference for thiol adsorption: thiols, once thiolates, are free to adopt the most thermodynamically

stable packing arrangement. Such complexity in adsorption characteristics arise from thermodynamic

and kinetic competition, which is discussed more thouroughly in the next subsection.

1.2.1.5   The influence of structure on growth mechanism: Thermodynamic *vs.* kinetic control

The relative rôles of thermodynamic and kinetic control in SAM formation were considered in-depth by

Folkers *et al.*[69,70] and Laibinis *et al.*[54]. It was shown that, despite the indication that SAM formation

is thermodynamically controlled, which was inferred from the observation that adsorption of molecules

capable of increased lateral interactions* is preferred from multicomponent solutions, the conditions

used for the formation of SAMs† are such that many films at least partly betray the initial imprint of

the kinetic product. Laibinis suggests that it is "only for the simplest adsorbates... or for very long

exposures that the true thermodynamic end points of the assembly are likely to be approached... the

significant steric repulsion expected for a chain trying to penetrate a high coverage [SAM] suggests

that the approach to equilibrium kinetics could be very slow." Furthermore, the initial, kinetic product

yielded by SAM formation from a solution of mixed adsorbates, which is "different from but parallel to

the composition... [of the solution]", over time yields a composition ever further from that of the initial,

'kinetic' SAM; the longer SAMs are thermodynamically preferred over the shorter and SAMs given

longer to form will more closely reflect this latter driving force[54].

Folkers considered the enthalpic drive for mixed monolayers to phase-separate[69] (phase-separated films

are characterised by a decrease in entropy, and must therefore be enthalpically favourable to occur),

and concluded that mixed SAMs demonstrate intermediate structures between being fully mixed and

fully phase-separated. Wetting experiments using two dissimilar media (water and hexadecane) on

hydroxy-terminated SAMs of different lengths indicated an increase in the water contact angle (*i.e.* a

hydrophobic effect) on the films when the solution composition reached a critical value, which was

not observed when the wetting medium was hexadecane. It was reasoned that this must indicate that

the binary SAMs are well mixed, because macroscopic islands would be both be hydrophilic and yield

similar contact angles, but well mixed SAMs (it was reasoned) would exhibit eclipsing of the shorter

hydroxy-terminated SAM component by the longer one, which would in turn expose the methylene

---

*(*i.e.* for *n*-alkanethiols, longer chains)

†influenced by results from ellipsometric studies reported by Nuzzo *et al.*[41], indicating that maxmium film thickness, corresponding to an endpoint in SAM formation following film healing, is reached after 18–20 h formation time; this makes up the standard SAM formation protocol in the majority of laboratories

groups of the longer, increasing the contact angle with water of the film of critical composition. The reason this dramatic change in wettability was not observed when hexadecane was the wetting medium, it was suggested, is that hexadecane molecules are of the same size as the gaps formed between longer adsorbates and can thus interleave them, reducing the enthalpic gain yielded by the eclipsing of the shorter adsorbates by the longer in the previous case of water, the molecules of which are much smaller, and also polar. Conversely, the close dependence of the film composition on the solution composition was interpreted as being a cooperative effect indicating a degree of phase separation. The concession was made that the 'islands' of separate phases may be smaller than can be probed by an effectively macroscopic technique such as contact angle measurements, with significant disorder and mixing at their fringes, but may nevertheless be present on the surface: a hypothesis which has since been supported by results yielded by Chemical Force Microscopy (CFM) measurements[71]. It was also suggested in this[69], and a later report by Folkers *et al.*[70], that characterisation of binary SAMs of mixed length and/or composition is best approached *via* analysis by XPS, which is of particular relevance to work presented in both Chapters 3 and 4 of this thesis.

1.2.1.6 Position of sulfur in Au–SR SAMs

Gold adopts a **face-centred cubic** (fcc) lattice arrangement that is characteristic of larger metals[42]. SPM studies indicate that evaporated and epitaxially-grown gold surfaces tend to present the lowest-energy (111) crystal plane at the surface, giving rise to a familiar hexagonal packing arrangement. Early SPM* work by Widrig *et al.*[72] indicated a substrate-commensurate adlayer morphology for the thiolate adsorbates, denoted $(\sqrt{3} \cdot \sqrt{3})R30°$. This is shown in **figure 1.2.6** on the next page.

$\sqrt{3}$ denotes the interatomic distance of sulfur headgroups, as related to the internuclear distance of the underlying gold atoms' threefold hollow sites ($\sqrt{3}a$, where a is the lattice constant). It has generally been thought that the sulfur position lies in these threefold hollows, although this has historically been a matter of some contention. Central to the discussion has been the observance of symmetry breakage in the SAM structure, initially indicated by early IR studies by Nuzzo *et al.*[73] and Nuzzo *et al.*[74], and subsequently observed in STM† images (*e.g.* Poirier *et al.*[60]). This is most often referred to as a $c(4 \times 2)$ superlattice, which has been noted (for instance, by Schreiber[37]) as being of an unconventional terminology; $p(3 \times 2\sqrt{3})$ is the more standard notation. However, early papers described the structure with the former terminology, and so subsequent studies have acquiesced to this decision. The structural consequence of this symmetry-breaking is that there are two non-equivalent structures of thiolate

---

*Scanning Probe Microscopy
†Scanning tunneling microscopy
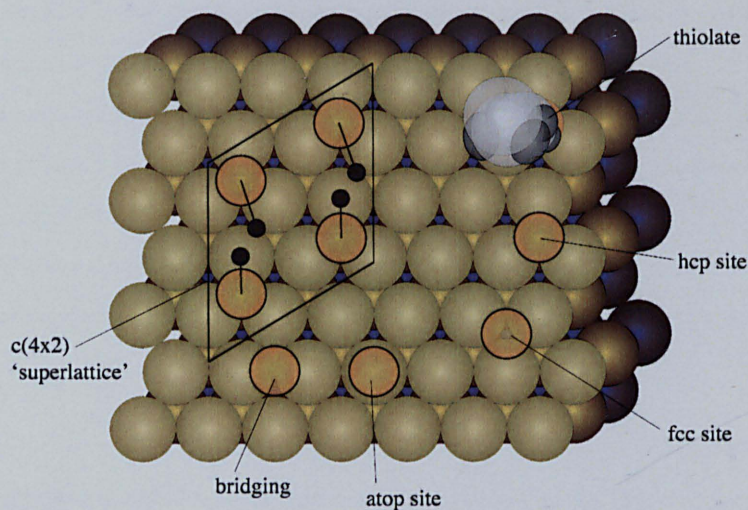
Figure 1.2.6   Position of sulfur headgroups in a Au–SR SAM

molecules per SAM unit cell. It has been suggested that this may arise either from thiolate molecules being set at a different height above the substrate (which would account for the variations in STM brightness observed by Poirier *et al.*[60]) or alternate rotations of thiolate molecules (which is supported by a doublet in methylene scissor bend in IR data[73,74]).

With regard to sulfur location, a number of alternate, contradictory structures have been proposed by different groups, including atop[75,76], bridge, and transitional sites. In this context, too, the origin of the c(4×2) symmetry breakage is debated. Fenter *et al.*[77] carried out near-incidence X-ray standing wave (XSW) measurements and interpreted the symmetry breakage as resulting from disulfide-like interaction at the interface, inferring from the absence of characteristic Bragg peaks that the position of sulfur is not the same for the two distinct molecules in the unit cell[77]. GIXD (Glancing Incidence X-ray Diffraction) results suggest that S–S distance between nonequivalent SAM molecules is 2.2 Å, close to a the bond length in the corresponding disulfide of $\sim$2 Å, as shown in **figure 1.2.6** (black circles map Fenter *et al.*'s proposed sulfur sites). This is very much at odds with the distance between hcp sites (4.98 Å), and in disagreement with STM studies that indicate an arrangement that would fit a packing model based on the availability of hcp sites. A bimolecular process is expected in thiol adsorption in order to evolve H_2 and yield thiolates, which would suggest the possibility of residual disulfide, as a by-product of this interaction, at the interface. However, Nuzzo *et al.*[41] report loss of S–S stretching in Raman spectra of adsorbed disulfides, indicating a dissociative adsorption mechanism; any transient bond formed by S–S interactions ultimately must undergo scission.

Furthermore, Biebuyck and Whitesides[78] reported replacement of one-half of an adsorbed disulfide

by solution-phase thiol, which indicates that both halves are separate entities on the surface, although it could be argued that the intrinsic asymmetry lends a thermodynamic impetus for displacement by a better-suited thiol. Roper and Jones[79] have observed a dynamic interchange between chemisorbed thiolate and a physisorbed disulfide adlayer, and have suggested that trapped disulfide species in mono-layers could contribute to spurious X-ray structure results. Work carried out by Noh *et al.*[80] suggests that structural changes occur during a SAM's useful lifetime, with a long-term rearrangement of the $c(4 \times 2)$ superlattice to a $6 \times \sqrt{3}$ structure, and it is possible that disulfides become trapped during this rearrangement.

It has also been suggested that the aberrant results yielded by NIXSW (Near-Incidence X-ray Standing Wave) and GIXD are, in fact, due to damage done to the samples by high-energy X-rays during analysis. The ejection of photoelectrons by exposing SAMs to X-ray radiation could (if this is indeed occurring) cause reordering of thiolate species to form disulfides. Early diffraction studies by Strong[81] and White-sides, and Chidsey *et al.*[82], did not demonstrate sulfur pairing, and so it could be that the choice of probe—in this case—interferes with the analyte structure. Indeed, recent work by O'Dwyer *et al.*[83] attributes the c(4× 2) splitting to alternate molecular twists alone (±50°), a consequence of packing; there is, perhaps, no need for the dimerisation model suggested by Fenter for some of the idiosyncratic features of SAMs (which are after all only indicated by certain types of measurement) to be explained.

1.2.1.7 Stability and Exchange in SAMs

Individual thiolate groups in organosulfur SAMs may, over time, be subject to oxidation, which renders them incompatible with the surrounding SAM structure. Misfittings are sometimes observed as vibrational modes in IR spectra that are indicative of gauche defects in individual molecules. There is a dynamic exchange of such 'corrupted' units of the molecular assembly with thiols[78] (or, possibly, disulfide adlayers[79]) in the solution phase. Schlenoff *et al.*[84] followed interchange of thiols by radiola-belling, and was able to elucidate many features of SAMs, including the result that dissolved molecular H_2 does not play a part in the exchange process. That desorption (characterized well by a pseudo-first order analysis) follows similar kinetics to self-exchange led them to postulate desorption of weak links in the SAM as disulfides. The observation that there always remains a fraction which is not subject to this form of dynamic interchange led to the suggestion that this results from stronger binding at defect sites, and a proposal was made that rough substrates would bind SAMs better. While it is true that SAMs at step edges on flat gold are more tightly bound (possibly due to stabilisation afford by a bridge-type ligation at the sulfur), long range order is not possible on very rough surfaces. Indeed, Baralia *et al.*[85]

suggested that interchange first occurs at gold grain boundaries with E_A equal to 66 ± 4 kJ mol^{-1} (from an Arrhenius temperature analysis).

Schoenfisch and Pemberton followed oxidation of Au–SR SAMs in air[86], and performed an ingenious experiment in which aerial oxidation was studied in a number of different environments in dark conditions (thus ruling out a photooxidative process). They observed that aerial oxidation proceeded rapidly in laboratory conditions at the university where they were based (Tucson, Arizona, USA), but that the rate was much slower at a private residence. By noting that the air in the university laboratory was being replaced with fresh air from outside by air conditioning, a feature which was not present in the room at the private residence, they were able to form the hypothesis that ozone could be the oxidative agent. Intense sunlight experienced by the southern United States facilitates the formation of atmospheric ozone at elevated quantities. Deliberate use of ozone has since been demonstrated as a means to oxidise SAMs[87, 88].

1.2.1.8   The Au–S bond

The enigmatic nature of the S–Au interaction has attracted much theoretical interest[68, 89], although a number of important studies by other methods have attempted to probe its precise structure, for example by XPS[90], near-edge X-ray adsorption fine structure (NEXAFS) and ultraviolet spectroscopy (UVS)[91].

Sellers *et al.*[33] performed *ab initio* calculations for gold and silver SAMs and concluded that the bonding mode was seen to flit between sp^3 and sp-type hybridization, postulating the involvement of this in SAM annealing.

Tachibana *et al.*[92] carried out a number of ab initio calculations that consider possible sulfur locations, and the likely molecular orbital ('MO') interactions associated with each. They concluded that S–Au bonding strength was greatest in threefold hollows, intermediate on bridge sites, and smallest on atop sites. Very little difference was predicted between hcp and fcc threefold hollow sites, suggesting that the layer of gold atoms beneath that directly at the surface has little influence. The greatest interaction, as a sum of crystal orbital overlap population (COOP) and crystal orbital Hamilton population (COHP) analyses, was seen to be from S_{3s}–$Au_{6p_z} \times 3$ in the fcc threefold hollow (COHP=-2.19); the next greatest was the same interaction on the hcp site (COHP=-2.18).

Whether the sulfur-metal bond of alkylthiolates to Au and other metals is sufficient to enable adsorbate-induced substrate reconstruction has been the subject of some debate. In 1991, Häussling *et al.*[93] reported pit-like vacancies in SAM-covered surfaces that were not observed on bare gold, and proposed

that these were defects in the SAM explicable by the presence of 'lying-down' or liquid-like phases. Poirier *et al.*[61] later observed that the depression depth corresponded to a single Au atom step height (2.4 Å), covering ≈6 % of the surface. Defect, or "vacancy island" growth was seen to occur by an 'Ostwald ripening' process, whereby the growth of larger defects at the expense of smaller ones proceeds by "diffusion of single atoms vacancies", rather than "coalescence...[of] whole pits". This was elaborated on by Poirier in a subsequent publication[94], in which it was suggested that the underlying 'herringbone' gold morphology, which harbours excess gold atoms in the ratio of 1 per 22 or 23 lattice constants, undergoes relaxation upon SAM desposition. STM and GIXD indicated that a 4.4 % lattice expansion occurs, which corresponds to the surfeit of gold atoms in the (111) surface, and single adatoms were observed on the gold surface. This and work by Zhang *et al.*[95] suggests that pits grow by the migration of gold atoms at the edges of defect sites into single vacancies.

The Au–S bond is, however, typically the weakest in a Au–SR SAM; 40 kcal mol^{-1} *cf.* 145, 81 and 171 kcal mol^{-1} for C–C, C–H and C–S, respectively. Selective removal or replacement of SAM molecules is therefore due to action targetted at the Au–S interface. This has been central to the exploration of SAMs as patternable assemblies, as will be discussed in Section 1.4.

1.2.1.9 'Odd-Even' effects

The inherant tetrahedral geometry introduced in a SAM film by the hydrocarbon component imparts alternating surface physical properties as the length of the chain is increased and the *n* of C$_n$ alternates between being odd and even. Many physical systems exhibit properties which alternate qualitatively and quantitatively depending on whether an odd or even number of a repeated subunit is present, such as $\Delta_{vap}H$ of *n*-alkanes. In SAMs, the fixed orientation of molecules in the film causes films where the terminal ω group features a directional dipole to exhibit alternating surface properties (*e.g.* wettability, tribology) depending on whether the film contains an odd or even number of carbon atoms[96]. This has important ramifications for organic films either of SAMs of molecules that contain structural changes somewhere along their length (*e.g.* amide links, or a transition from a hydrocarbon to an oligoether chain), or films formed by the attachment of new molecular or biomolecular species to reactive terminal ω functionalities: both cases should consider whether the transition or terminal group is odd or even, and whether the geometry imparted is optimal for the desired property.

1.2.1.10 Reactivity and Modification of SAMs

The organic structure of SAMs allows surfaces to be modified by a variety of means, although fixed orientation and constrained geometries that are not present in solution-phase chemistries restrict or alter reactivity accordingly. Nevertheless, a number of modification methods have been demonstrated. Yan *et al.*[97] showed that interchain carboxylic anhydride moieties may be formed on carboxylic acid-terminated SAMs by reacting them with acid anhydrides in anhydrous aprotic solvents. These may be further functionalised by adding amines, which may contain additional functional groups as desired, in aprotic, non-basic solvents. Hutt and Leggett[98] investigated acid anhydride functionalisation of hydroxy-terminated SAMs, and carbodiimide-driven esterification of carboxylic acid terminated SAMs, and observed that a yield of 60 % ester product was observed on a SAM compared to $\sim$100 % in bulk solution. This result was rationalised by considering constrained geometry at the SAM surface, which may have inhibited the access of the bulky di-*tert*-butlycarbodiimide. Chechik, Crooks and Stirling[99] investigated reactivity from a general viewpoint, including SAMs as templates for polymer growth, intrafilms reactions, and photo– and electrochemical reactions. Some of the most useful reactions are those that facilitate the inclusion of biological molecules, and these are often used in the context of protein patterning. This will be discussed in subsection 1.4.4 on page 59.

1.2.2 SAMs on Other Substrates

SAMs on other metallic systems, such as those on Ag and Pd presented here, can often be interpreted "by analogy"[100] with those on Au, and many of the structural and reactive attributes are very similar. Silane SAMs on Si have slightly different structures, largely due to the covalent nature of the bond at the adsorbate/substrate interface, but as many properties of SAMs are determined by the surface (ω) functionality, reactions and properties observed for M–SR systems are often also applicable to these systems.

1.2.2.1 SAMs on Silver

Ag–SR SAMs are more strongly-bound than are Au–SR, and despite similar lattice constants (4.08 Å on Au *cf.* 4.09 Å on Ag at 300 K), Ag–SR SAMs tend to adopt a much denser packing, being characterized as $(\sqrt{7} \times \sqrt{7})R10.9°$. Sulfur positioning for molecular S_2 was first characterized by low-energy electron diffraction (LEED) and Auger electron spectroscopy experiments, carried out by Schwaha, Spencer and

Lambert[101], and Rovida and Pratesi[102], who worked with SO_2. From their results, a nearest-neighbour S–S distance of 4.41 Å was calculated. Studies of SAMs have suggested a similar spacing, indicative of a dissociative adsorption mechanism. The closer packing causes Ag–SR SAMs to adopt a more moderate cant angle than Au–SR $(\sim 11\text{–}14°)[103]$. The maximum area per thiolate molecule on Ag is 19.1 Å^2, whereas on gold 21.7 Å^2 is available. As on gold, the majority of evidence points to the sulfur occupying the threefold hollow site, although recent work has suggested that some degree of adsorbate-induced surface reconstruction may occur. Yu *et al.*[104] reported such an observation from NIXSW analysis, which is supportive of the postulation made by Brewer *et al.*[105] that bulky ω-terminated adsorbates may adopt a looser packing on silver than do *n*-alkylthiolates. This is suggested to be a likely explanation for the inferred looser packing of carboxylic acid-terminated SAMs on Ag than methyl-terminated SAMs. Friction force* measurements made during the latter study indicated that Ag–SC$_n$CH$_3$ SAMs exhibited lower friction than their Au counterparts, as measured by interactions with an AFM cantilever in LFM mode; friction between an AFM tip and SAM is thought to be contributed to by gauche defects imposed by the force of the tip acting at the ω-position of the SAM, and such a rearrangement is impeded in Ag–SR SAMs by the greater packing density (more freedom of movement is available in Au–SR SAMs). However, in the case of Ag–SC$_n$COOH SAMs, increased friction is observed as compared with the same SAM on Au, which was interpreted as the SAM adopting a looser packing. Similarly, packing of SAMs formed from HSC$_{11}$(OCH$_2$CH$_2$)$_n$OH on Ag, as measured by the attenuation of photoelectrons†, was observed to be less than expected. A full discussion of this case is presented in subsection 1.2.3.4 on page 29.

1.2.2.2   SAMs on Palladium

Pd–SR SAMs are extolled for their simultaneous compatibility with CMOS technologies (gold is not, though silver is) and applicability to biological work (gold is biocompatible; silver is toxic). Indeed, Pd has been shown to exhibit increased biocompatibility *cf.* Au‡ when SAMs resistant to the adsorption of biological materials are considered. Pd–SR SAMs have been demonstrated as etch resists that better the resolution of analagous Au–SR SAMs. Love *et al.*[100] characterized methyl-terminated Pd–SR SAMs and deduced a structure that is somewhat more complex than analogous Au–SR films. It was suggested that, upon adsorption, a Pd–S interlayer forms, which implies at least some degree of S–C bond scission. Wetting experiments demonstrated a marked increase in contact angle hysteresis, which was attributed to either the increased film roughness over Au (evaporated Pd forms smaller crystals) or defects within the

---

*see subsection 1.3.4.3 on page 48
†See subsection 1.3.3.3 on page 44
‡see Subsection 1.2.3.7

SAM (although the concession was made that the experiments do not suggest widespread defects). From RAIRS spectra of a C_{18} film, characteristic vibrational modes were observed that indicate a chain cant intermediate between those of Au–SR and Ag–SR, with a consideration of the chain twist β suggesting a cant closer to that observed on Ag: within the range 14–18°. Many of the investigative probes of Pd–SR SAMs indicate that they have characteristics approximately halway between Ag and Au. Their promise of better integration between bionomics and CMOS technologies is discussed in subsection 1.2.3.7 on page 33.

1.2.2.3   SAMs on Silicon

While M–SR SAMs have been widely adopted in the laboratory, lauded as they are as an efficient route to oriented films that present tailorable surfaces, degradation and instability beyond the short-term preclude their adoption in mass-produced 'real world' devices. Attempts to rigorously investigate the nature of M–SR SAMs are often frustrated by structural changes that begin to take place over experimentally relevant timeframes, and under experimental conditions. Short chain Au–SR are known to desorb under UHV[106], which is a required condition for many surface analysis techniques, *e.g.* XPS, and SIMS, for instance; adventitious adsorbates from the laboratory atmosphere can quickly compromise a C_nCOOH SAM[105]. In contrast, silane SAMs exhibit increased stability, due to the more orthodox covalency of the bonding mode, and increased bond strength (Si–O=452 kJ mol^{-1}, Si–C=318 kJ mol^{-1}[142]; *cf.* 120 kJ mol^{-1}[148] for Au.

Silane SAMs have a long precedent, with some of the earliest SAM work being done on silicon[34]. Structurally, the component molecules in silane SAMs are thought to adopt a low-cant orientation very close to the surface normal[34,35,51].

Many nascent patterning techniques aim to exploit the enhanced stability of silane SAMs, and the possibility of introducing photoactive groups for spatially-selective reactions, for patterning and biomolecule integration. These will be discussed in subsection 1.4.4.3 on page 60.

1.2.3 Development of SAMs with a consideration of Biocompatibility and Biological Adhesion

1.2.3.1 The requirements for SAMs with biological applications

Surface properties have dramatic consequences for the compatibility of artificial structures with living matter[107]. The tailorable ω-functionalities of SAMs has allowed the development and investigation of SAMs that might facilitate biocompatibility in implants, or act as immobilisation templates for arrays in biochemical analysis. In the former case, it is desirable to resist adsorption to proteins present in an organism which, if denatured upon adsorption to a surface, may trigger an immune response. An additional requirement of biocompatibility is to promote intermeshing with local structures, such as bone or cartilage, and so SAMs that promote growth of cells related to bone deposition are of interest. When considering SAMs for spatial arrangement of biological samples (such as in a protein or genomic microarray, for instance), SAMs with structures or particular functionalites that are amenable to patterning are required. It is essential that immobilisation chemistries are sensitive to the delicate nature of biological structures, and biokleptic architectures require that the biomolecules are not damaged by the process. The patterning process itself will be covered in more detail in Section 1.4.

Additionally, SAMs are required to be stable in biological media. While SAMs have actually been demonstrated to exhibit enhanced stability in water as compared with ethanol, buffer salts may perturb the observed inhibition of desorption caused by the polar nature of water[108].

1.2.3.2 Surface free energy: Correlation with biological adhesion?

Cooper *et al.*[109] followed attachment of fibroblasts on patterned SAMs and observed greater cell density on acid-terminated regions (C_2COOH) than on methyl-terminated (C_7CH_3), correlating this effect with the comparitively higher surface free energy of a carboxylic acid group. Subsequent work[110,111] indicated increased human osteoblast cell growth on short chain acid– and hydroxy-terminated alkylthiol SAMs, slightly less on a long chain acid-terminated SAM ($C_{10}COOH$), and diminshed growth on methyl-terminated SAMs, with the least cell propogation observed on longer chains. A long chain hydroxy-terminated SAM ($C_{10}CH_2OH$) exhibited intermediate attachment. Fibroblast growth investigated as part of the same programme of study[111] indicated a greatly reduced affinity to hydroxy-terminated SAMs as compared with osteoblasts, with the least on the $C_{10}COOH$ SAM. In this sense, it was conluded that the trends are somewhat "phenomenological" and depend on the nature of the

28

outer tissue of the biological cell; however, increased order resulting from long chain length of methyl-terminated SAMs had the most pronounced resistance to biological cells, and it is clear that the integration of biological cells with SAMs is very sensitive to precise ordering at the surface. The adhesion of cells to SAMs following controlled adsorption of proteins was also investigated in an attempt to correlate the apparently phenomenological results with a proposed mechanism of attachment[112].

1.2.3.3 Poly(ethylene oxide): The gold-standard for protein resistance

Although attempts to correlate bioadhesion with wetting have been made, most plasma proteins in a complex organism will denature at a surface in order to lower the interaction energy, a process which is eventually rendered irreversible. Poly(ethylene oxide) ('PEO')* films and their derivatives have been shown to be almost singuarly effective at resisting biological adhesion, and are therefore of extreme importance in considering biocompatability, although the mechanism of resistance to biomolecules is not fully understood. While spin-coating of PEO onto surfaces or thiolating low M_W PEO[113] to facilitate adsorption onto noble metals is possible, surfaces prepared in this way do not exhibit the order or definite orientation observed in SAMs, that would allow fundamental studies of the structure and mechanism of resistance to be made.

1.2.3.4 Oligo(ethylene oxide) SAMs: a morphological basis for biomolecular resistance?

Pale-Grosdemange *et al.*[114] reported synthesis of oligo(ethylene oxide)†-terminated organothiolate SAMs by nucleophilic substitution of the Br of ω-bromoundecene, followed by radical addition of a thioacetic acid at the unsaturated position, to produce a readily hydrolysable thioester (which subsequently yields a thiol). C_{11} SAMs were chosen because a range of SAMs C_4–C_{10} have been demonstrated to contain gauche bonds at the ω-position, and it was suggested that this may affect the structure of attached OEO moieties at this position. Longer chains were not chosen because they are difficult to purify. An additional method by Chapman *et al.*[115] adapted chemistry reported by Yan *et al.*[97] to bind OEO-amine to acid anhydride SAMs. Both $HSC_{11}(OCH_2CH_2)_nOH$ and $HSC_{11}CO$-$NCH_2CH_2(OCH_2CH_2)_mOH$ SAMs have been demonstrated to resist biomolecular adsorption, as will be described later in this section.

Prime and Whitsesides[116] explored biomolecular resistance as a function of EO-terminated thiolate density in a binary SAM. Fractional compositions in multicomponent SAMs are often discussed in

---

*sometimes also called poly(ethylene glycol); 'PEG'

†'OEO'—again, in the same manner as its polymeric counterpart, often called oligo(ethylene glycol); OEG. For consistency, any further abbreviation in this thesis will be of the form 'OEO', or 'EO' (for ethylene oxide), as *per* the Glossary.

terms of mole fractions, given the symbol χ. $\chi_{SAM}(EO)$, the fraction of the SAM made up by molecules

terminated in the EO moiety, was deduced by XPS and wetting (as discussed previously, the absolute

composition of multicomponent SAMs is only influenced by the composition of the solution), and it

was determined that an intermediate density of EO-terminated molecules produced the most protein-

resistant films. Fitting the data to a power law model put forth by de Gennes[117], the initial onset of

protein resistance was seen to occur when $\chi_{SAM}(EO) = k_1 n^{-0.4}$ where n is the number of ethylene oxide

units, and the constant k_1 depends on the protein. Above a maximum threshhold, increased EO density

was actually seen to decrease protein resistance, although longer chains were better at resisting protein.

It is suggested that protein resistance is dependent on the oligo(ethylene oxide) moieties' freedom to

adopt a conformation maximising volume and interactions within the OEO chain—demonstrably, a

helix fulfils this criterion.

Harder *et al.*[118] presented a study of protein resistance on methoxy– and hydroxy-terminated, OEO-

containing thiols on gold and silver, which indicated that methoxy-terminated OEO-thiols on silver

were not effective at resisting protein. Hydroxy-terminated OEO-thiols on silver were protein-resistant,

however, although less so than on gold. IR data indicated that methoxy-terminated OEO-thiolate SAMs

on Ag were in an all-*trans* configuration (as indicated by the largest C-O stretch peak), whereas on

Au, amorphous and crystalline helical domains were observed, not dissimilar to those exhibited by

hydroxy-terminated OEO-thiolate SAMs on Au and Ag. In the bulk poymer, PEO chains adopt a

helical geometry, confirmed by XPS and computational methods[119], with a periodicity of 7/2. This

corresponds to a helix diameter of 21.3 Å, just small enough to fit into the 21.4 Å²/molecule available

on Au. On Ag, the 19.1 Å²/molecule constraint imposes a *trans* configuration for methoxy-OEO SAMs,

corresponding to a chain diameter of 17.1 Å. It was proposed that the observation of helical domains in

hydroxy-terminated OEO SAMs on Ag could arise from substrate defects (observed on Ag), or looser

packing densities being adopted. These ideas are lent credence by reports of substrate reconstruction and

mobile phases on Ag–SR SAMs by Yu *et al.*[104], and were supported by the observation that susbtrate

photoelectron attenuation (see 1.3.3.3 on page 44) was similar in hydroxy and methoxy-terminated films,

despite the difference in EO repeat unit length. The methoxy-terminated OEO films were 3 units long

(so-called 'EG-3'; EO_3 in the nomenclature used in this thesis), whereas the hydroxy-OEO was 6 units

long (EO_6).* Increased OEO length in EO_6 forming energetically-favourable helices may therefore

provide a thermodynamic impetus for film rearrangement in the alkyl or sulfur-substrate domains of the

SAM. A particularly insightful hypothesis was the suggestion that penetration of water into the OEO-

moieties promoted the helical geometry and (therefore) the protein resistance such films. This was

---

*Photoelectron attenuation increases for increased film thickness per area, so similar attenuation factors on longer films implies looser packing.

investigated by methods by Wang, Kreuzer and Grünze[120], and water molecules were seen to play an important rôle: H-bonding of water to helical domains was stronger, and the presence of an interfacial water layer was postulated to provide a physical barrier to protein adsorption.

Vanderah, Valincius and Meuse[121] reported deviations from the 7/2 helical domains on MeO-EO$_6$ SAMs, depending on the assembly solvent, from RAIRS results. Li *et al.*[122] carried out a systematic study of protein adsorption on hydroxy-OEO SAMs, varying the water content of the assembly solvent. Again, the suggestion that inter-helix water penetration is important in protein resistance was supported for EO$_6$ films, but not EO$_4$ films. EO$_4$ films were thought to pack closer from 95:5 ethanol:water mixtures than from pure ethanol, and may have adopted *trans*-OEO morphologies because of the lack of thermodynamic impetus to accomodate water by forming helices with such comparitively shorter chains. It is possible, however, that the water-barrier model of protein resistance is somewhat simplistic, as will be described.

A consideration of the remarkable resistance to bioadhesion of methoxy-terminated EO-3 SAMs on gold, despite the dimished density of EO units in the interfacial region, has led to the postulation that the density of H-bonding at the surface is a more important factor than water penetration. Such EO-containing films exhibit increased disorder, and so lack the extensive helical domains thought to promote protein resistance[123][124]. Finally, by combining consideration of surface free energy, disorder, and lateral packing density, a more complex model of protein resistance has been put forth by Herrworth *et al.*, where internal hydrophilicity and disorder are suggested to be key factors in providing resistance to bioadhesion[125]. This has been supported by subsequent theoretical studies[126].

1.2.3.5 Other SAM-supported systems that resist biomolecules

Ostuni *et al.*[127] surveyed structure-property relationships for bioadhesion. A wide range of organic molecules were attached via amide links to activated carboxylic acid-terminated SAMs: perfluoro, aromatic and aliphatic moieties; ethers, crown ethers, amines, amides and ammonium salts; sugars, amino acids and nitriles. It was observed that the functionalities exhibiting greater protein resistance share the following features:

1. They are hydrophilic

2. They include H-bond acceptors

3. They do not include H-bond donors

4. They have an overall neutral charge

Many of the functionalities demonstrated to be resistant to protein adsorption have molecular features selected for in the infrastructures of living things. For example, Hederos, Konradsson and Liedberg[128] have demonstrated galactose-terminated SAMs that resist proteins, while Chen *et al.*[129] have demonstrated the effectiveness of oligo(phosphorylcholine) SAMs as nonbiofouling surfaces. Integration of artificial implants might therefore adopt biomimetic molecular structures at their surfaces, as well as biocompatible synthetic polymers.

1.2.3.6   Conditions for immobilisation

In order to ensure retention of biological functionality during integration into a SAM, it is essential that the thermodynamic and kinetically-driven processes leading to biomolecule adsorption are tempered by careful control of the chemistry of the fluid environment. Covalent interactions that take place too vigourously may compromise the structure of the biomolecule. Outside of the organism, conditions even in 'pure' water are often too harsh; biomolecules exist in organisms under pH control, with maintained ionic concentrations, and small perturbations can cause large structural changes in, for instance, a folded protein. Denatured or even partially stressed biomolecules will have lost their precise shape, and this impinges on functionality. Therefore, manipulation of biomolecules is carried out in biological buffers that aim to mimic the environment *in vivo*, by controlling salt concentrations in the medium and so promoting solubilisation of the biomolecule. Biological buffers may contain separate buffer and detergent molecules, although surfactants have been developed that also have a salt-buffer polar group, *e.g.* LDAO, HEPES *etc.*; particularly delicate proteins or membrane complexes may be protected by synthetic amphiphilic surfactants (often based on saccharides, *e.g.* DDM, β-OG), which create a 'lipid-like' environment around the biomolecule.

It has been suggested that salt concentrations affect binding efficiency. Casetlino, Balaji and Majumdar[130] reported increased grafting density of DNA on short-chain hydroxy-terminated thiolate SAMs on Au with increasing NaCl concentration, but observed that the dependence of this effect drops off at higher concentrations, concluding that osmotic forces are replaced by hydration effects.

1.2.3.7 Palladium as an ideal substrate for SAMs that resist protein adsorption?

Jiang *et al.*[131] have reported enhanced protein resistance on EG-3, EG-6 and EG-7-terminated C_{11} and C_2 thiolate SAMs on palladium. Long-term resistance is seen to be twice that on gold, and it is postulated that increased bond strength of S–Pd (more similar in magnitude to that on Ag) delays desorption of the SAM in biological media. Due to the limited theoretical basis for the mechanism of protein resistance, a reason for the better performance of EG films on palladium was not put forth. Both increased bond strength and tighter packing could supress reductive desorption, and the tighter packing constraint imposed could increase the ratio of amorphous EO regions as compared with helical sites. It has been proposed that resistance to biomolecule adhesion could, in part, arise due to disorder[123][124]. Compared to silver, which is toxic, and has been shown to produce SAMs with poor protein resistance[118], palladium has an obvious enhanced capacity as a substrate for SAMs for biological integration. Compatibility with CMOS technologies makes OEO-SAMs on Pd ideal for integration of biomolecules in electronic devices *e.g.* bioMEMS.

1.2.3.8 Semiconductor-based biological arrays

The ultimate confluence of integrated circuit fabrication and bionomics technologies will most likely be on a semiconductor substrate. Despite the apparent advantages of Pd–SR SAMs over Au–SR SAMs in terms of long-term stability and biocompatibility, and indeed CMOS adapability, Pd–SR SAMs have been shown to require a more meticulous preparation, and exhibit an increased complexity of morphology over Au–SR SAMs. Silane-based systems can be prepared on atomically-flat CVD fabricated Si wafers, and are therefore not subject to the energetic peculiarities of SAM formation on polycrystalline or imperfect epitaxial metal films.

Of particular note are the recently-developed photoactive silane systems that allow photochemical modification of unmasked regions on silane-based SAMs. Some of these will be presented in subsection 1.4.4.3 on page 60. In principal, these offer simple steps to producing patterns that might facilitate biological compatibility.

Silane-based systems have not been as well-studied as systems for potential biological integration due to the difficulties in introducing some functional groups. When considering $\Delta_{Surface}G$ as a means to direct biomolecule immobilisation, it is somewhat more difficult to introduce carboxylic acid-terminated silanes than methyl-terminated silanes, although careful tuning of the reaction conditions has provided a route to acid-terminated silane SAMs.[132] Of some interest has been the introduction of protein-resistant

33

EO-based silanes[133, 134]. A novel route to the introduction of functional SAMs onto silicon will be presented in Chapter 3.

1.3   Probing Surface Chemistries

Many of the 'surface-sensitive' analysis techniques presented here are ideally suited to investigations of SAMs, because of the wide range of surface chemistries that can be introduced at the ω-position. The value of information yielded by contact methods such as wetting, scanning probe microscopies (SPM) and contact potential difference measurements* is bolstered by the degree of control and orientation of surface functionalities that SAMs afford, and the quantitation of photoeletron spectroscopies and surface-sensitive mass analyses (SSIMS, TPD-MS) is made sensible by both the definite orientation and single-layer morphology of SAMs. As will be demonstrated, a plural approach to analyses by multiple methods gives the most reliable information about surfaces, and in particular SAMs, because of the complimentary information each technique produces, as well as the varying degrees of damage each might potentially cause in the SAM structure.

1.3.1   Contact Angle Goniometry

1.3.1.1   The wetting experiment

Wetting of surfaces is a macroscale phenomenon with a molecular basis[4]. Because of this, wetting has been one of the most-used methods to investigate the character of a surface. In the context of SAMs, control over the surface functionality has allowed the specific characterization of a range of functional moieties, and has the potential to elucidate structual information pertaining to the energetic nature of the surface. Because of its simplicity and immediacy, contact angle goniometry has become a universal technique for initial assessment of SAM quality, with consistency over the duration of an experiment being indicative of a good SAM.

The most common method to measure the contact angle of a liquid on a material is the sessile drop method. A goniometer is an optical apparatus designed to facilitate accurate measurement of a drop profile, by means of an adjustable-angle crosshair. Older apparatus relies on the human eye only; modern apparatus is often fitted with a CCD camera replete with angle-measuring software on a desktop PC.

---

*which allows determination of the surface potentials imposed by SAMs—see on page 37

$$\theta_a > 90° \qquad\qquad \theta_a < 90° \qquad\qquad \theta_a < 10°$$
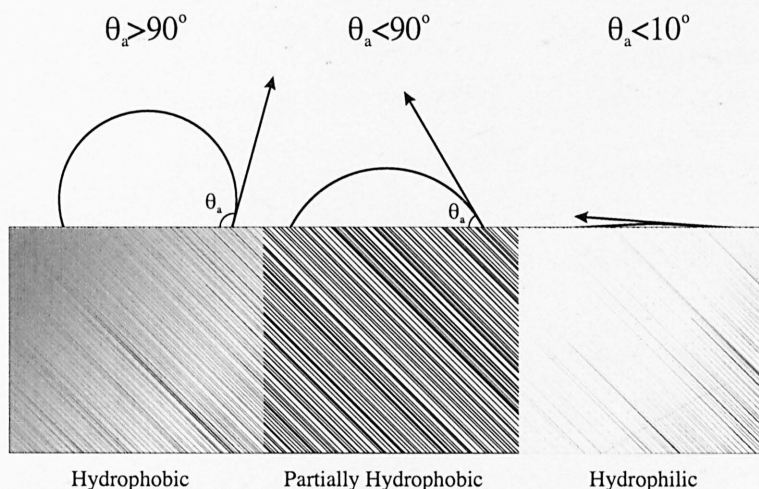
Figure 1.3.1   Wetting of a surface

Shown in **figure 1.3.1** are three characteristic types of behaviour observed when a drop of water rests on a surface. In the first instance, water beads up as it would on an aliphatic polymer, or the waxy coating of a leaf; this is characteristic of SAMs with hydrophobic tail groups, such as methyl, fluorinated, or aromatic species. The second instance shows a partially-hydrophobic surface, characteristic of a SAM presenting hydroxy or oligo(alkylether) moieties. The final case depicts full wetting by a hydrophilic functionality at the surface. This is typical behaviour for carboxylic acid groups in a monolayer, silicate glass, and metal oxides.

The physical basis for the wetting phenomenon is rationalised by considering the work of adhesion of a drop in contact with a surface:

$$W_{SLV} = \gamma_{SV} + \gamma_{LV} - \gamma_{LS} \tag{1.3.1}$$

where γ is the energy of the interface between surface/vapour, vapour/liquid and solid/liquid phases ($\mathrm{J\,m^{-2}} \equiv \mathrm{N\,m^{-1}}$). An expression for the total surface energy of the system may be formulated:

$$W_{Total} = \gamma_{LV}(A_{LS} + A_{LV}) - W_{SLV}A_{LS} \tag{1.3.2}$$

where A_{LS} and A_{LV} are areas of interface between the liquid and solid and the liquid and vapour (atmosphere), respectively. The situation is represented in **figure 1.3.2** on the next page. If the droplet is subjected to an infinitesimal displacement, then it may be shown that:

$$\gamma_{LV}(dA_{LS} + dA_{LV}) - W_{SLV}dA_{LS} = 0 \tag{1.3.3}$$

35
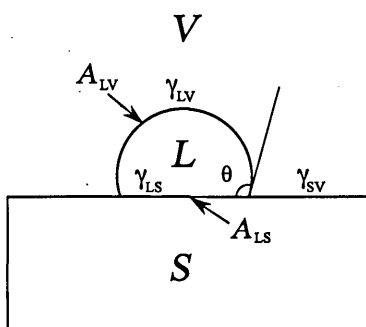
Figure 1.3.2 Interfacial energies that determine wetting behaviour

which, at constant volume of liquid L defines the relationship $\frac{dA_{LV}}{dA_{LS}} = cos\ \theta$, allowing 1.3.3 to be written as:

$$\gamma_{LV}(1+\cos\ \theta) = W_{SLV} \tag{1.3.4}$$

If V is an inert atmosphere, 1.3.4 and 1.3.1 may be combined to gives Young's equation:

$$\frac{\gamma_{SV} - \gamma_{LS}}{\gamma_{LV}} = \cos\ \theta \tag{1.3.5}$$

which demonstrates that contact angles correlate to interfacial energies.

1.3.1.2   Physical basis and models

Generally, interfacial forces are dominant when such small volumes* are used. Deviation of a droplet profile from that of a part circle is in many cases minimal, because surface energies in such a small mass of fluid are dominant over gravity. Indeed, algorithms empoyed in software-controlled θ_a measurement often treat the maximum interfacial cross-section length as a chord through a circle. θ_a is then given by:

$$\theta_a = \arcsin \frac{4s \cdot h}{s^2 + 4h^2} \tag{1.3.6}$$

In many cases, however, it is difficult to better the human eye, especially in situations where deviation from a part circle occurs, such as when hysteresis is observed (see 1.3.1.2 on the following page). Binary component SAM surfaces, in accordance with Langmuir's PRINCIPLE[4], have interfacial energies dependent upon fractional compositions, as formulated by Cassie:

$$\cos\ \theta_{AB} = f_B \cos\ \theta_B + f_A \cos\ \theta_A \tag{1.3.7}$$

---

*Typical drop is $\sim$20–100 µL

where A and B represent the component SAMs, and $f_B = 1 - f_A$. Cassie's law may be extended to multicomponent surfaces:

$$cos\ \bar{\theta} = \sum_n f_n \cos \theta_n \qquad (1.3.8)$$

where $\sum_n f_n = 1$.

In the sessile drop method, the angle formed between the drop and surface is termed the *advancing* contact angle, θ_a. When a negative hydraulic pressure is applied to the drop, by retracting some quantity of fluid from the drop with the Hamiltonian syringe, the angle is referred to as *receding*: θ_r. Contact angle hysteresis describes the condition when $\theta_a \neq \theta_r$. This may result from inhomogeneity of the surface, for example in a binary SAM that may be exhibiting phase separation. A more hydrophilic region can 'pin' the interface between the droplet, surface and air. This would manifest itself in the apparent increase of θ_a, and also the decrease of θ_r as the drop is being retracted into the syringe.

It has also been suggested that reordering of monolayers may occur during the wetting experiment[135], whereby SAM molecules may adust their bond geometries to minimize the interfacial free energy.

Surface roughness is also an important consideration, as rough surfaces tend to increase the hydrophobicity of $\theta > 90°$ surfaces, but make $\theta < 90°$ more hydrophilic. Wenzel[136, 137] described surface roughness thus:

$$roughness = \frac{\text{actual surface}}{\text{geometric surface}}$$

which alludes to the fractal-like nature of many surfaces at microscopic scales. Of particular relavance to this thesis is the size of 'grains' in evaporated polycrystalline films. It is generally considered desirable, when producing metal films for the preparation of SAMs, to maximise grain size by reducing the evaporation rate.

1.3.2   Contact Potential Difference

The work function, Φ, of a metal is defined as the energy required to move an electron at the Fermi level E_f to the vacuum level, just outside the material. Often, that energy is electromagnetic in nature, and the concept of work functions is instinctively related to the the action of radiation on conductors producing flow of electrical charge—*the photoelectric effect.*

1.3.2.1 The photoelectric effect

In 1839, Alexandre Edmond Becqerel recorded the flow of current in electrolythic cells exposed to sunlight[138], and noted that the current increased when the Sun's rays were more intense. That the voltage required to produce a spark between electrodes is reduced when ultraviolet light is incident on a metal was observed by Hertz[139] in spark gap experiments in 1887, although again he refrained from attemping to provide a theoretical basis for this result. It was not until Einstein applied the quantization-of-energies concept, introduced by Planck[140] to account for the energy profile emitted by a black body, that the following relationship was described[141]:

$$\frac{1}{2}m_e v^2 = h\nu - \Phi \qquad (1.3.9)$$

—so that, unless the photon energy $h\nu$ is greater than the work function, electrons will not be transported from the bulk, and no flow of charge will be observed. For this criterion to be met, it must be the case that the radiation is of a frequency ν equal to or above above a certain threshold. Only then does any increase in intensity have any effect in increasing the rate of flow of photoelectrons (from classical electrodynamics, one might expect the relationship to be directly proportional, with no dependence on $\nu_{minimum}$ being met). Greater photon energy, from higher frequencies, are passed on as increased kinetic energy.

1.3.2.2 The CPD method

The Contact Potential Difference (CPD) method of measuring the work function of a metal was first demonstrated by Lord Kelvin in a presentation to the Royal Society in 1898[142]; the instrument designed for this purpose is called a Kelvin probe. The principle is to form a capacitor out of two conductors, allow conduction, and detect the charge transfer. The CPD, ϕ, between two materials A & B investigated in this way relates their respective work functions, Φ_i, by:

$$\phi = (\Phi_B - \Phi_A)/e \qquad (1.3.10)$$

where e is the fundamental unit of charge, $\equiv 1.6 \times 10^{-19}$ C. The origins of the above relationship are more obvious when the quantities of ϕ (V) and e are simplified to SI units: $1\,\mathrm{V} \equiv 1\,\mathrm{J}\ \mathrm{A}^{-1}\ \mathrm{s}^{-1}$; $1\,\mathrm{C} \equiv 1\,\mathrm{A} \cdot \mathrm{s}$. To calculate an absolute value for ϕ, the work function of at least one of the conductors must be known, relating in the schematic to the tip, although relative measurements may be made that allow comparisons between different analytes, *e.g.* different SAMs. In order to form capacitance, the two
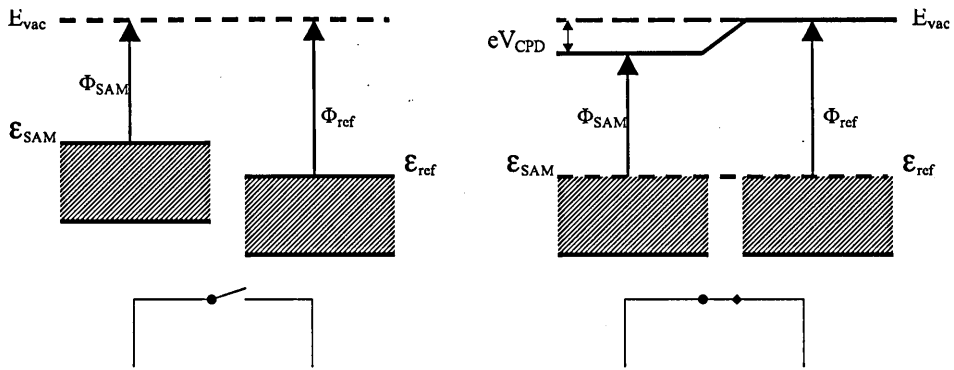
Figure 1.3.3 The CPD method

conductors' surfaces (tip and SAM, for instance) must be held in a parallel configuration. Gauss' law relates the electric field of a closed surface to the net charge, Q, within it:

$$\frac{Q}{\varepsilon_0} = \oint_S E \, dS \qquad (1.3.11)$$

$$= A \cdot E$$

where E is the electrical field vector. By definition, $E \cdot d = V$, where d dscribes the plate separations, so:

$$\frac{Q}{\varepsilon_0} = \frac{A \cdot V}{d}$$

$$\frac{Q}{V} = \frac{A \cdot \varepsilon_0}{d}$$

The left hand side is the definition of capacitance:

$$C = \frac{A \cdot \varepsilon_0}{d} \qquad (1.3.12)$$

which demonstrates that $C \propto \frac{1}{d}$. In the circuit depicted in the schematic, the modified AC Kelvin probe developed by Zisman[143] in 1932, the spatial separation the reference electrode and the sample is modulated by an oscillation, provided by a piezo. This causes AC current to flow around the circuit. A backing voltage V_b may be applied across the circuit, to null the flow of current so produced and indicate the CPD. This is summarised below:

$$d(t) = d_0 + a \sin \omega t \qquad (1.3.13)$$
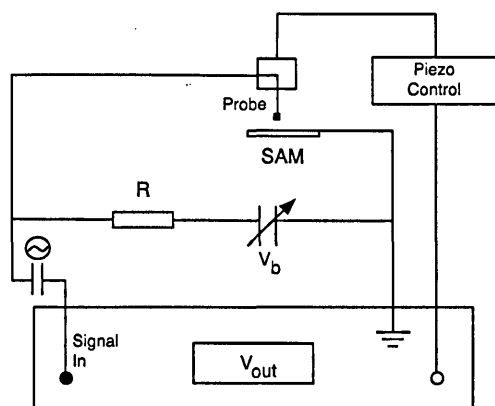
(Zisman design[143])

Figure 1.3.4   A/C Kelvin Probe

where d_0 is the plate separation when the reference electrode is at the midpoint of its oscillation, a is the amplitude of oscillation, and ω is the angular frequency in $\mathrm{rad\,s^{-1}}$ ($\equiv 2\pi f/\mathrm{s^{-1}}$). In the circuit described, this induces an AC current:

$$\frac{dC}{dt}\phi = \frac{dQ}{dt} = i \qquad (1.3.14)$$

in order to deduce ϕ from i, A, d and a, would each have known to a very high degree of accuracy, which could potentially introduce a lrage margin of uncertainty. In order to circumvent this, the introduction of the backing potential V_b allows ϕ to be found by nulling i, when

$$\frac{dC}{dt}(\phi + V_b) = i = 0 \qquad (1.3.15)$$

then

$$\phi = -V_b \qquad (1.3.16)$$

V_b can be accurately measured with a digital voltmeter.

1.3.2.3   Surface Potentials

When a conductor is covered by a thin layer of material that has a net dipole moment, such as a SAM, the adsorbate imparts a **surface potential**, ΔV. The dipole moment, orientation and distance from the substrate all affect the measured CPD[144, 145]. The surface potential is related to the measured contact potential differences of the bare metal ϕ, and metal with SAM adlayer ϕ^* thus:

$$\Delta V = \phi^* - \phi \qquad (1.3.17)$$

where ϕ is the work function of the bare substrate, *i.e.* ΔV is the change imposed on the work function by the adsorbate. Generally, a M–SR SAM consists of a more electronegative (*cf.* the metalic substrate) polar *i.e.* $\delta-$ve adsorbate (such as a thiolate), to which is attached a $\delta+$ve hydrocarbon chain. By virtue of the rules of nature, most ω substituents of organic SAMs, if heterogeneous functionalities are indeed present, are again $\delta-$ve. SAMs on adsorbates can then, therefore, be thought of as a series of stacked dipole sheets.

1.3.3 X-ray Photoelectron Spectroscopy

As has been described, eletromagnetic radiation with sufficient energy that is incident on a material will cause the emission of a photoelectron*. Practically speaking, this means that a threshhold frequency must be first be met before photoejection of an electron takes place; the magnitude of electron emission is proportional to the intensity of the EM radiation above this frequency, and the energy of EM radiation above this frequency is passed on to the photoelectron. The process of photoemission, from initial interaction, to excitation and emission, takes place in 10^{-15} s. This process may be summarised:

$$E_B = h\nu - E_K \tag{1.3.18}$$

where E_B is the binding energy of the electron, which is a function of the atom and its environment; $h\nu$ is the energy of the X-ray source, and E_K is the photoelectron kinetic energy, $\frac{1}{2}m_e v^2$.
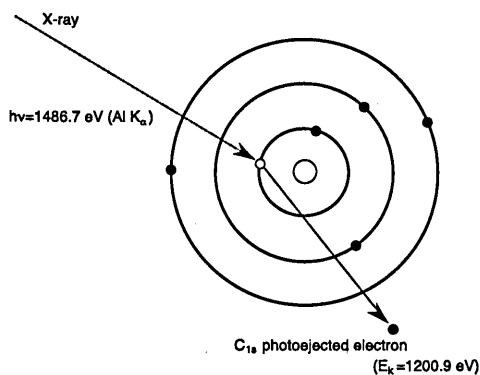
Figure 1.3.5 Principle of photoelectron emission as observed in ESCA

As we have seen previously in section 1.3.2 on page 37, for electromagnetic radiation to remove an

---

*Information in this section is largely taken from Refs.[1,146]

electron from an atom or material, it must have enough photon energy to overcome the work function, Φ_{spec}. (1.3.18) should be modified to:

$$E_B = h\nu - E_K - \Phi_{spec} \qquad (1.3.19)$$

although the work function is parameterized and accounted for in the normal running of modern instruments, so that (1.3.18) is given.

1.3.3.1 Koopman's theorem

Following photoemission, the electronic configuration relaxes to a new energy, and the difference in energy is equal to the binding energy. This may be written:

$$E_B = E_f(n-1) - E_i(n)$$

where $E_f(n-1)$ is the final state energy and $E_i(n)$ is the initial state energy. Assuming the process does not cause electronic rearrangement in the atom or material,

$$E_B \approx -\varepsilon_k \qquad (1.3.20)$$

where ε_k is the orbital energy, calculable via the Hartree-Fock method. Discrepancies do arise because rearrangement does occur, as depicted in *figure 1.3.6 on the following page* . A more complete description of E_B is therefore:

$$E_B = -\varepsilon_k - E_r(k) - \delta\varepsilon_{corr} - \delta\varepsilon_{rel} \qquad (1.3.21)$$

where $E_r(k)$ is the relaxation energy and $\delta\varepsilon_{corr}$ and $\delta\varepsilon_{rel}$ describe changes in the electron correlation and relativistic energies, respectively.

The initial energy E_i of an atom is altered by the chemical environment if the atom is bound in a molecule, such that there will be a change in binding energy, ΔE_B, referred to as the 'chemical shift', so-called because such modifications to E_B are analogous to chemical shifts in NMR spectroscopy. As photoelectron ejection occurs, the formal oxidation state of an element will increase, and subsequent E_{B_i} will increase. Final state parameters such as $E_r(k)$ are assumed to have similar magnitudes for different oxidation states, so that ΔE_B is dependent only on initial state effects:

$$\Delta E_B = -\Delta\varepsilon_k \qquad (1.3.22)$$
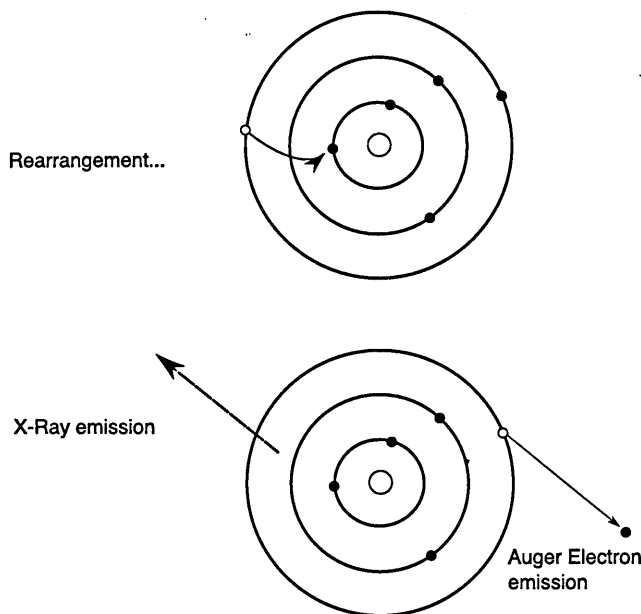
Figure 1.3.6   Secondary Processes in ESCA

where $\Delta\varepsilon_k$ is the corresponding change in orbital energy associated with accomodating an atomic orbital within a molecular environment. From this reasoning, we may arrive at Koopman's theorem: the **binding energy is equal to the orbital energy;** although, as has been shown, relaxation and other energetic considerations cause experimentally-determined values to deviate from this relationship.

1.3.3.2   The chemical shift effect

XPS spectra indicate shifts in elemental curves depending on the nature of an atom's chemical environment. These are, in many ways, analagous to chemical shifts in NMR spectroscopy, and may be interpreted as such, although the degree of the shift is dependent on both the initial and final electronic configuration of the atom. Software such as CASAXPS allows complex atom-orbital fingerprints to be modelled as a summation of component atom-orbital curves (usually Gauss-Lorentzian in profile, with some degree of tail-off towards higher energy), using iterative methods. Within a characteristic peak for an atom-orbital type within a molecule, therefore, are contributions from different environments, energy shifted, depending on the the respective energies of initial and final states. Typically, greater electron density shifts the curve to a higher energy, although the caution must be made that this is not always the

case. Chemical shifts are successfully explained by the charge potential model:

$$E_B = E_B^\circ + kq_i + \sum_{j \neq i}(q_j/r_{ij})$$
(1.3.23)

whereby E_B is referenced to a known E_B° (that for the neutral atomic species), and the investigated species i is charged and surrounded by charges q_j on atoms j at a distance r_{ij}. This means that shifts are exagerrated by having more of a particular chemical functional group in local enviornment of i, and that this falls off linearly with distance.

1.3.3.3 Attenuation of photoelectrons by films

Photoelectrons ejected from species in a material are attenuated to some extent by the layers of other species above them, and observed intensities in the spectra are seen to decrease[147] with increasing adlayer thickness. This may be described by a modified Beer-Lambert law:

$$I_A = I_0 e^{-d/\lambda_i sin\theta}$$
(1.3.24)

where d is the adlayer thickness, θ is the angle between the surface parallel and the detector ('the take-off angle'), I_0 is the unattenuated signal (*i.e.* bare substrate) and λ is the attenuation path length, given in most cases by:

$$\lambda_i = 9 + 0.022\, E_k(i)$$
(1.3.25)

as determined by Laibinis *et al.*[148], where E_k is the photoelectron kinetic energy, for a range of E_{k_i} between 1000 and 1500 eV.

Using the attenuation factor, it is possible to follow the interchange of thiol molecules if, for instance, a shorter thiol is being replaced by a longer one, then I_{Au} would be seen to decrease. However, variations in the X-ray beam intensity mean that this information needs to collected at the same time, or considered alongside supporting information (empirical inference from inspection of relative peak sizes in the spectra, for instance)*. It is possible to solve

$$I_A = I_0\{f \cdot e^{-d(m)/\lambda_i sin\theta} + (1-f)e^{-d(n)/\lambda_j sin\theta}\}$$

to find an estimate† for f, the fraction of SAM replaced, if the thicknesses $d(m)$ and $d(n)$ are of

---

*during a single run, it has been estimated that the X-ray intensity could vary by ∼5 %[69], although this figure will vary depending on the age of the machine and its components

†in monolayers of mixed film thickness, longer adsorbates may overhang shorter ones, as previously depicted in figure 1.2.5 on page 16, so the results may not be 100 % accurate

monolayers m and n are known.

The case in (1.3.24) applies either to the bulk or to a species at a fixed and single position within the SAM structure, *e.g.* the sulfur, or a single *ether* functionality. For peaks contributed to by photoelectrons from a particular environment at a number of positions along a SAM molecule, *e.g.* aliphatic C, the following model is applicable:

$$I_C = \sum_{j=1}^{n} I_{CL} e^{-(j-1)d_c/\lambda_C sin\theta} \tag{1.3.26}$$

where j is the position down the hydrocarbon chain (*i.e.* $\omega=1$, which would be unattenuated in this case).

1.3.4 Scanning Probe Microscopies (SPM)

1.3.4.1 The STM: The dawn of a new class of microscopy

The advent of scanning probe microscopies was heralded by the invention and development of the Scanning Tunneling Microscope (STM), by Röhrer and Binnig at IBM Zürich between 1981–1982[149, 150]. All variants of SPM share the feature that there is a probe, rastered—or 'scanned'—across the surface, that detects structural and/or compositional information, recording it on a desktop PC. In STM, a current is produced by electrons tunneling through a vacuum gap between a tip or probe (usually Pt/Ir but also Rh and W) and another conductive material. Whereas electron tunneling is classically forbidden, electron wavefunctions decay exponentially outside the electrodes (the tip and sample), and are permitted by quantum mechanics. This may be justified as follows:

The Schrödinger equation states that:

$$\mathscr{H} = -\frac{d^2}{dx^2}(\hbar^2/2m) \tag{1.3.27}$$

when $x < 0$, in the conductor, and:

$$\mathscr{H} = -\frac{d^2}{dx^2}(\hbar^2/2m) + V \tag{1.3.28}$$

where $x > 0$, in the vacuum gap. The solutions of (1.3.27) and (1.3.28) are:

$$\psi = Ae^{ikx} + Be^{-ikx}, \ k = \sqrt{2m \cdot E/\hbar^2} \tag{1.3.29}$$

$$\psi = Ce^{ik'x} + De^{-ik'x}, \; k' = \sqrt{2m(E-V)/\hbar^2} \tag{1.3.30}$$

The real component of (1.3.30) which results from the case when k' is imaginery (*i.e.* $V > E$) predicts a non-zero value for ψ in the vacuum gap. A one dimensional description of the tunneling current is given by:

$$I \propto e^{-2\kappa d} \tag{1.3.31}$$

where d is the separation between the probe and sample, and κ is related to the workfunction by:

$$\kappa = \sqrt{2m\phi/\hbar^2} \tag{1.3.32}$$

STM operation is carried out in either constant current or constant height mode. In the former, a feedback loop from the tunneling current modulates the 'z' (up/down) piezotransducer to keep the current constant, and the 'z' piezotransducer electric voltage is recorded (and from which, by calibration, topographical information may be gathered). In the latter mode of operation, the distance between the rastered probe and surface is kept constant and the tunnelling current is recorded.

STM has been extremely successful in elucidating nanoscopic surface structures on metals and semiconductors, having atomic-scale resolution. In an early experiment[151], Binnig *et al.* observed the 7×7 reconstruction of Si, a phenomenon which had not been well understood until then. STM has also been used to probe the structure of SAMs[60], in which case the tunnelling current is modulated by the surface potential imposed by the organic adlayer. However, STM is not able to image insulators, such as polymers or biological samples, and has the additional consequence of potentially disrupting the surface structure. This has been adressed by the subsequent development of surface force microscopies, which exploit the physical interactions that are, to some extent, an unwarranted feature of STM.

1.3.4.2 The atomic force microscope: History and principles

In 1985, Binnig developed the atomic force microscope[152] (AFM) with Gerber and Quate at Stanford. A schematic summarising the mode of operation is shown in figure 1.3.7 on the following page. In this set-up, a Si_3N_4 tip attached to the underside of a cantilever is rastered across a sample, and the tip is differentially deflected according to surface topography; a consequence of a combination of different intermolecular interactions. In other forms of SFM, magnetic or electrostatic forces are registered instead.

In order to maximise the sensitivity of the AFM technique to the intermolecular forces acting at the
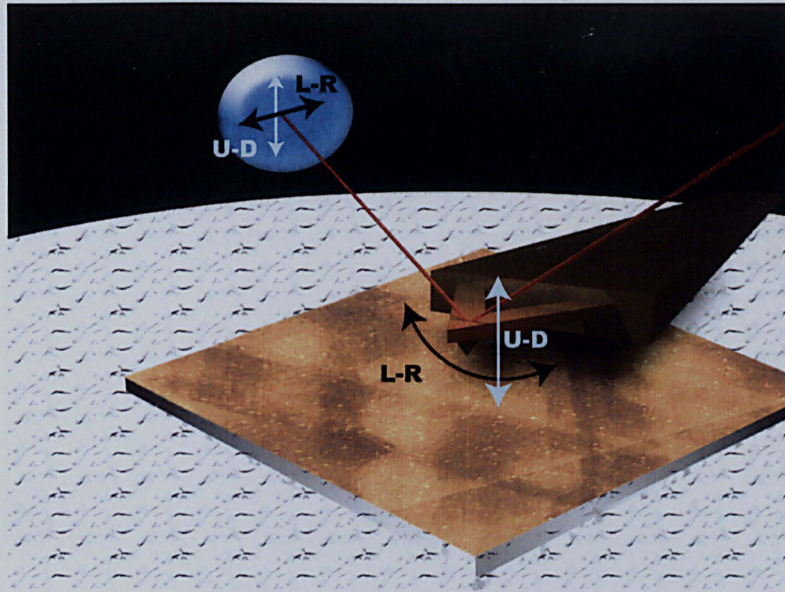
Figure 1.3.7   Schematic depicting AFM operation

atomic scale, which are minute, the deflection of the cantilever must be made maximized by choosing a material that is amenable to bending. At the same time, it is desirable to minimize the effect of external vibrational noise in the surrounding environment (at about 100 *Hz*), so a stiff cantilever with a high resonant frequency is most sensible. From:

$$f_0 = \frac{1}{2\pi}\sqrt{\frac{k}{m_o}} \qquad (1.3.33)$$

which can be rearranged to:

$$(2\pi f_0)^2 m_0 = k$$

where f_0 is the resonant frequency of the material (Hz), k is the spring constant ($N\,m^{-1}$) and m_0 is the mass of the material, it can be seen that low k values, indicative of an easily-deflected cantilever, are achievable by choosing small mass if f_0 is large, and subsequently commericial probes are made extremely small. Vertical deflection Δz can be described by Hooke's law:

$$F_{sum} = k\Delta z \qquad (1.3.34)$$

Deflection of the cantilever is detected in a modern instrument by means of a laser aligned to reflect off the top of the cantilever and onto a split photodiode, which may be achieved by a means of adjustable mirrors.

There are two principle modes of operation of an AFM system:

- Contact mode, whereupon the deflection of the cantilever is caused by the short-range repulsive forces dominant at $\leq r_0$. A dc bias is applied to a piezo to maintain contact of the probe with the surface (remaining sensible to the fragility of the sample).

- Non-contact mode; the tip is oscillated with large a above the sample, and detects longer range interactions. This does not damage soft samples as much as contact mode, but its resolving power is lower.

A variant of the latter mode of operation is intermittent contact mode, whereby the range of oscillation is brought closer to the sample, so that the probe is in contact with the sample for some part of the oscillation cycle. The hardness of tapping may be adjusted to account for the softness of the sample, which enables the high-resolution, non-destructive imaging of biological samples (see subsection 1.3.4.4).

1.3.4.3   Probing tip-sample interactions

While in contact mode, it is possible to measure lateral deflections experienced by the cantilever if the probe is scanned at right angles to the probe orientation (see figure). This has important consequences for SAMs that have been patterned by methods outlined in section 1.4 on page 51.[153] The magnitude of lateral deflection is increased when the analyte is polar in nature (due to attractive interactions with the polar tip), such as is the case with carboxylic acid-terminated SAMs, and decreased when the sample is apolar, *e.g.* with methyl-terminated SAMs. By exploiting this principle, is also possible to investigate a range of interactions and affinities by chemical modification of the tip. In this instance of the SFM experiment, termed chemical force microscopy (CFM), a SAM may be formed on the tip *e.g.* by the evaporation of gold onto a probe, followed by its immersion in an ethanolic solution of thiol. Thus, for example, apolar-apolar interactions may be investigated. It is also possible to investigate biomechanical interactions, e.g DNA strand affinities, or the affinity of streptavidin for biotin, by appropriate modification and immobilisation chemistries.

1.3.4.4   AFM of biological structures

While X-ray diffraction studies of biological structures have been invaluable to understanding life from a molecular viewpoint, AFM allows sub-cellular architectures to be observed in their native environment[154-156]. As well as providing structural information of static samples, AFM has been able to provide information pertaining to real-time cellular dynamics[157], biomechanics[158,159], and biomolecule-substrate interactions[160]. AFM has been lauded for its ability to probe biomolecular structures *in*
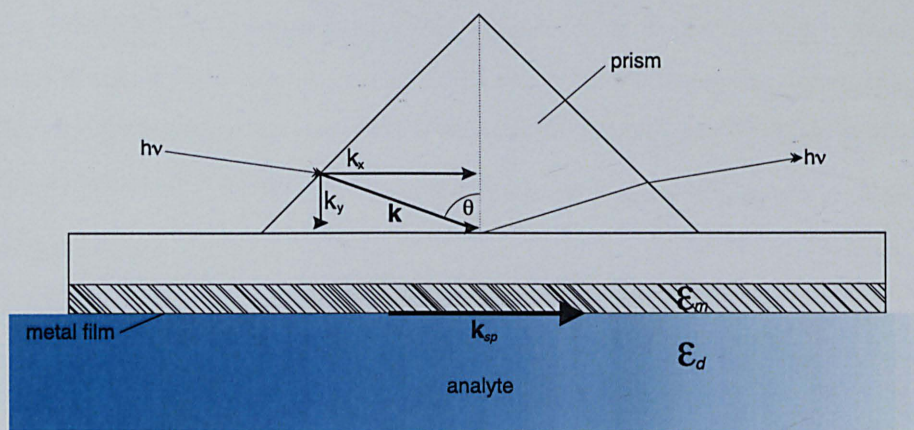
Figure 1.3.8   The Kretschmann configuration for surface plasmon resonance spectroscopy

situ. Despite all the ostensible advantages of using AFM, it is important to recognise that the size of biomolecules (or, indeed, any analyte that has nanoscale features) may be exagerrated by the comparitively large size of an AFM tip (~50 nm) compared to the minute structures being studied. Consequently, the sample biomolecule may begin to 'image' the tip, increasing the apparent size of the molecule (a so-called 'tip radius' effect). For example, the diameter of plasmid DNA has been reported to vary from 3.5–24 nm, which is 2–12 times wider than expected[161, 162].

It has been suggested that small and soft biological samples may be effectively imaged by means of force-mapping[163], whereby force information is collected for each pixel.

AFM has been used in many novel applications, including the study of fundamental self-assembly processes. The difference between chemisorption strength of polypodal and single head groups in SAMs has been investigated[164], as well as the surface stresses induced during self-assembly on a cantilever by vapour phase SAM formation[165, 166].

1.3.5   Surface Plasmon Resonance

Surface plasmon resonance (SPR) is a semi-quantitative means to assess physisorption of molecules, including biomolecules, on gold or SAM-modified gold. A surface plasmon is an EMR charge density wave packet propagated at an interface between a dielectric material and a conductive material, *e.g.* a metal. An excitation requires that incident EMR has the same wave vector K_{sp} as the surface plasmon. When excitation, or 'resonance' occurs, a sharp drop in the reflected light occurs.

A SPR system is shown in **figure 1.3.8**. This is the most common arrangement, called the Kretschmann configuration. The analyte cell has a gold-coated glass chip as one of its walls (the top of the cell in

this arrangement), the gold side proximal to the flow of the liquid. Typically, a laser is arranged so that it passes through a prism onto the glass side of the chip, where it is able to penetrate through to the 'underside' of the gold. It may then resonate with surface plasmons on the surface of the gold. The conditions for this are as follows:

In air, the wave vector of light is given by:

$$K_0 = \frac{\omega}{c}\sqrt{\varepsilon_0} \qquad (1.3.35)$$

where ω is the angular frequency (rad s^{-1}), c is the speed of EMR, and ε_0 is the dielectric constant in air. As the laser penetrates the dielectric medium, the component that must attain the criterion for excitation of a surface plasmon is given by:

$$K_{sp} = \frac{\omega}{c}\sqrt{\varepsilon_d} \cdot sin\theta_c = \frac{2\pi}{\lambda}\sqrt{\frac{\varepsilon_m \cdot \varepsilon_d}{\varepsilon_m + \varepsilon_d}} \qquad (1.3.36)$$

where K_{sp} is the wave vector of the surface plasmon, ω is the angular frequency of the EMR, θ_c is the critical SPR angle, λ is the wavelength of the EMR, ε_m is the dielectric constant of the metal, and ε_d is the dielectric constant of the analyte. For resonance to occur, it must be the case that $\varepsilon_m < -\varepsilon_d$, which is fulfilled for several metals including silver and gold, in the IR–visible region of the spectrum (HeNe lasers emmitting at 633 nm are therefore commonly used). Gold is the most obvious choice: It is not susceptible to oxidation, unlike silver, and the cytotoxicity of the latter precludes it from biological work.

The precise dependence of θ_c on the refractive index η_d of the analyte cell is exploited to assess the physisorption of *e.g.* biomolecules that are in the region immediately proximal to the gold or Au–SR surface. Changes in the refractive index due to interfacial interactions caues the surface plasmon resonance curve is seen to shift to higher angles, and so the observed quantity in the Kretschmann configuration is $\Delta\theta_c$. In many commercial machines, this is parameterized within a function that gives an effective adsorbate coverage in ng cm^{-2}, but this is absolutely dependent on the fabrication of the chips. Therefore, SPR is considered here a 'semi-quantitative' method; relative adhesion of biological molecules on a range of SAMs may be investigated, but in-depth analyses, or comparison across multiple samples, should be approached with some caution. SPR does allow an assessment of specific versus non-specific binding at a surface for individual samples, however. Introduction of small quantities of saline solution at an elevated concentration ($\sim$400 mM), or 0.1–1 % ionic surfactant, *e.g.* SDS—are usually sufficient to remove physisorbed adsorbates, while allowing the degree of material that is chemisorbed or otherwise more specifically immobilised to be determined.

1.4 Patterning SAMs

The molecular nature of SAMs makes them ideal systems for introducing patterns on a range of scales, from nm–μm. Pattern and structure are the cornerstones of any functional system, so a range of tools for pattern fabrication are required, that are appropriate to the materials being used. Because the problems raised by nanoscale engineering are quite different from those encountered in previous technological developments, it has transpired that patterning molecular assemblies has necessitated the introduction of new tools and methodologies. As has happened during the introduction of previous technologies, tools for manipulating new materials have presented themselves in the very instruments originally used to probe their nature. A number of comprehensive reviews of SAM patterning have been published, and new methods are still being developed.

1.4.1 Microcontact Printing

Microcontact printing (μCP) is recognized as an quick route to patterned SAMs, and consequently has been one of the most investigated techniques, being used to fabricate large structures with minimum feature sizes ranging from 50 nm–1000 μm)[38]. Kumar and Whitesides first demonstrated μCP using a PDMS stamp to deposit alkanethiol 'inks' on gold[167], using these as a resist against cyanide etching[168] to produce 3D microstructures.

μCP relies on the transferral of dilute solutions (0.1–10 mM) of amphifunctional SAM molecules (*e.g.* thiols) in appropriate solvent (*e.g.* ethanol), or biological molecules in a suitable buffer solution, from an 'ink pad' (cotton or lint-free paper) to a substrate to which the 'ink' has a specific affinity.

Compared with films formed from solution, μCP SAMs exhibit lower molecular density, suffering from the problems of a 'horizontal lift' (see $*$ on page 11). Although some c(4×2) domains are formed, $p \times \sqrt{3}$ regions and 'lying down' phases are also observed[38]. The polymeric stamps most often used are siloxanes, and siloxanes are well known to degrade and leach out constituent molecules, which could lead to contamination of artefacts fabricated by stamping. The reproducjblity and adressability (for example, for alignment for 'multicolour' printing, see) of μCP patterns has also been questioned. Because μCP is typically carried out on bare substrates (*i.e.* those devoid of adsorbates), mass transport of SAM molecules may occur away from the stamp position, either by diffusion across the surface, or in the vapour phase from the stamp to other regions on the substratum. The quality of features formed by

μCP may therefore be dimished by edges that exhibit poor contrast (producing features that are 'fuzzy' rather than sharp).*

One of the arguments for μCP has been the increasing difficulty (and cost) of using photolithographic processes at ever-shorter wavelengths in order to produce ever-smaller features. However, approaches that attempt to circumvent the diffraction limit have been presented both by the semiconductor industry, using such techniques as stretching the photoresist during exposure, and the nascent field of scanning near-field photolithography, which is still at this stage the preserve of the laboratory worker. This latter technique will be discussed in more detail in subsection 1.4.3.4 on page 56.

1.4.2 Dip-Pen Nanolithography

Using a pen-based system to transfer SAM molecules to a substrate was first demonstrated by Kumar *et al.*, although the (X,Y) plotter system they used was not able to write structures less than 1 μm fine. In order to compete with photolithographic methods, a considerable increase in resolution was required.

The introduction of SPM techniques necessitated the devlopment of spatially-precise, piezo-driven systems that experience minimal drift as the probe scans the sample. The deposition of SAMs by μCP had shown that contact methods were a route to patterned surfaces, and AFM suggested a convenient route to writing features smaller than 100 nm. Dip-pen nanolithography (DPN) relies on wetting an AFM probe with a liquid SAM molecule, and 'writing' a linear SAM directly onto a surface. The ultimate resolution of DPN is dictated by the radius of the AFM tip, although Piner *et al.*[170] reported that the smallest features are seemed to be of the same size as gold grains on a polycrystalline film (~30 nm), perhaps indicating molecular transport from the tip apex to the logical edge of a domain (the grain boundary).

Nanoscale features have been succesfully fabricated using DPN. Gold 'wires' formed by etching a gold substratum partially protected by writing lines of thiol[171]; protein 'nanolines'[172,173]; deposition of metal lines using a sol-gel inspired approach from fluid metal precursors[174]; direct writing of conducting polymers[175]. Silicon surfaces have also been successfully patterned using amines as inks[176].

Xu *et al.*[177] demonstrated 'nanografting' of alkylthiol SAMs via selective removal of a SAM by the use of excessive force applied to an AFM tip; the initial SAM molecules are replaced by contrasting thiols in the solution phase. Liu, Xu and Qian[178] presented a number of SPL techniques capable of

---

*Subsequently, this quirk of fabrication has been exploited by allowing spreading between two regions of photoresist to reduce the size of the gap between them[169].

producing patterns in SAMs, including 'nanoshaving', nanografting and STM-driven evaporation and electron-induced diffusion. Clearly, SPL-based fabrication methods enable manipulation of molecular assemblies to produced patterns with dimensions in the nanoscale regime.

Presently, however, the uptake of DPN and variant SPL techniques in industrial applications has been hindered by their status as 'serial' (as opposed to parallel) fabrication processes; structures are written as lines, and so the fabrication time depends on the length of lines and structures being formed. Compared to mask-based photolithography, which is used extensively by the semiconductor inductry, SPL has previously been a slow process. It has therefore been desirable to write structures at an increased rate by the coupling of several pen units that can operate independantly. Inspired by IBM's 'Millipede'[179] data storage device, DPN systems with "massively parallel" multiple plotters have been demonstrated[180, 181]. Such tools might augment, and even rival more traditional 'top-down' fabrication techniques in the near future.

1.4.3 Photolithography

1.4.3.1 History of photoresists

The advent in the 1950s of the IC is inextricably tied to the realisation that photolithography could be used to direct diffusion of dopants (donors and acceptors) within a silicon crystal: Frosch and Derick[10] determined that this could be achieved by the use of a metal oxide mask, and Bond and Andrus[11] demonstrated that the oxide could be patterned using a photoresist. Industrial photoresists used for IC fabrication are usually polymeric materials spin-coated $\sim$1 μm thick onto a crystalline semiconductor substrate, which undergo a photochemical change upon irradiation. The very oldest photoresists used in electronics microfabrication, such as the photocatalysed bisazide crosslinking of cyclized rubber*, leaves cross-linked those regions that are exposed to light in the near UV, 500–300 nm. Following washing with a solvent, these are the regions which remain as masks during the deposition of conductive metal. Because the resulting conductive tracks are the inverse of the template pattern in the original mask, this is termed a negative tone photoresist.

The mainstay of the electronics revolution has been the Novolaks system, in which a 'Novolak' resin made by the condensation of a methylphenol with formaldehyde is doped with a small concentration of diazonaphthaquinone, which renders the resin less soluble in aqueous base. Upon irradiation with UV, the diazonaphthaquinone dopant undergoes the photochemical Wolf rearrangement to yield a carboxylic

---

*acid treating poly(*cis*-isoprene) partially cyclizes it, a process which lowers its T_g

acid, which is readily soluble in aqueous base. The exact mechanism by which the rate of dissolution is increased is a matter of contention, as the dissolution is increased by orders of magnitude above that which might be expected.

1.4.3.2   SAMs as photoresists

The fact that organothiolate SAMs may be photo-oxidized to corresponding sulfonates was reported by Huang and Hemminger[182] and spatial photopatterning was first demonstrated by Tarlov, Burgess and Gillen[183]. Because the irradiated regions are those rendered more soluble (in organic solvent, and especially when in contact with other thiol molecules). Both groups observed a shift in the S_{2p} binding energy away from 162 to 167 eV, interpreted as being characteristic of a SO_3 group. Rieley *et al.*[91] studied the photo-oxidation of *n*-octanethiolate Au–SR SAMs by NEXAFS and were able to observe similarities between a photooxidised SAM spectrum and an adsorbed film of sodium -octane sulfonate, which indicated that the oxidised species was structurally similar to the reference adsorbate. Conversely, an adsorbed zinc sulfide film was dissimilar. The stoichiometry of the proposed oxidation product was confirmed by Hutt and Leggett[184] by emprirical analysis of photoelectron intensities, and the kinetics and mechanism of photo-oxidation have been investigated for a range of SAMs[184–186].

The SO_3 does not experience a strong interaction with the metallic substrate and photooxidized SAM molecules are readily displaced by contrasting solution-phase thiols. This is depicted in the cartoon, **figure 1.4.1** on the following page.

SAMs afford a potential molecular-scale resolution in photopatterning, where other systems are limited by macromolecular scales. This has important implications when the tools of photolithography allow circumvention of the optical diffraction limit, which will be discussed in subsection 1.4.3.4 on page 56.

1.4.3.3   Details of SAM photo-oxidation

Zhang *et al.*[88] suggested that the key agent involved in UV photooxidation of SAMs is ozone. However, Brewer *et al.*[187] demonstrated photooxidation at a longer wavelength (254 nm): insufficient to generate ozone in the local environment.

One problem presented by the fabrication of micropatterned SAMs with multiple desired functionalities (termed 'multicolor [sic] patterning') is accurate addressability and alignment between the serial photooxidation steps. Photooxidation of mixed binary SAMs with differential response to two wavelengths
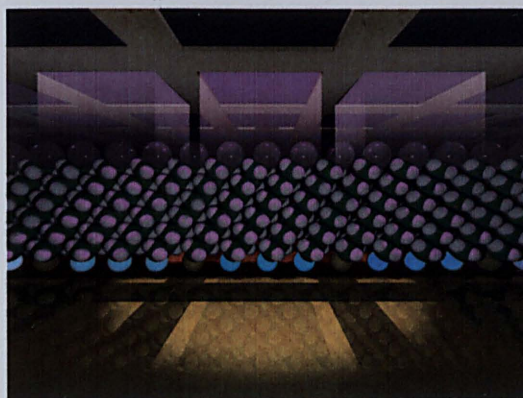
(a) A SAM is irradiated through a Cu mask—blue thiolate species indicate those that are converted to sulfonates due to the laser

(b) In the regions of the SAM irradiated by UV, thiolates are converted to sulfonates, which are less strongly bound than thiolates
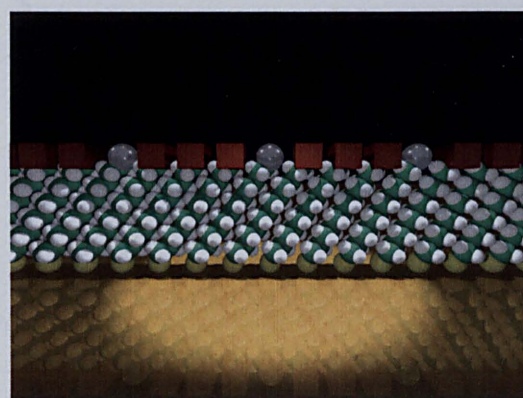
(c) 'Contrasting' SAMs (red cubes indicate a different ω functionality than that of the initial SAM) adsorb from solution onto the irradiated regions

Figure 1.4.1   Schematic showing patterning of a SAM through a Cu mask

(220 nm and 365 nm) has been carried out[188] by using a mask with with spatially separated 220 nm and 365 nm transparent regions, in order to negate the requirement to remove the mask before chemical modification or washing prior to a further photooxidation step. This methodology requires that the final chemical wash differentiates between the two monolayer types, and in this case the photocleavable linker responsive to 365nm was not affected by introduction of a contrasting thiol after photoxidation to the 220 nm-exposed regions yielded weakly-bound sulfonates.

1.4.3.4 Scanning near-field photolithography: Circumventing the diffraction limit

By coupling a 244 nm laser to a near-field scanning optical microscope (NSOM)* system, it has been shown that features smaller than the diffraction limit can be written. This technique has been termed 'Scanning Near-field Photolithography' (SNP).

In conventional photolithography, the smallest feature sizes that may be written are constrained by the Rayleigh-Abbe diffraction limit, otherwise called the Rayleigh criterion, given by:

$$d = \frac{0.61\lambda}{n\,sin\,\alpha} \qquad (1.4.1)$$

where d is the resolving power, λ is the wavelength of the light, and $n\,sin\,\alpha$ is the numerical aperture. The origin of the term $0.61 \equiv \frac{1}{2}1.22$ —the latter value is the relative distance of the first node surrounding an Airy disc, which Abbe arrived at by inspection. For all practical purposes, the refractive index of most lenses is $\sim$1.4, so achievable resolution is given by:

$$d \approx \frac{\lambda}{2} \qquad (1.4.2)$$

which has historically imposed a restraint on optical microscopy, due to the fact that the human eye cannot see wavelengths shorter than 400 nm (with an upper limit of 700 nm). The very best conventional optical microscopes cannot therefore resolve features <200 nm in size. This limit also has dire ramifications for the photolithographic processes used in semiconductor device fabrication, which rely on focussing down through a mask template: Although the wavelengths used for photochemistry now reach far into the invisible ultraviolet region of the electromagnetic spectrum, materials that are photoactive at increasingly shorter wavelengths are increasingly difficult to synthesize, and are subsequently increasingly expensive.

---

*alternately also called a 'SNOM'—a scanning near-field optical microscope
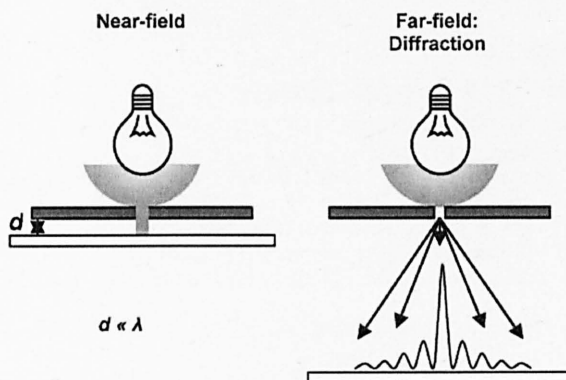
Figure 1.4.2 Cartoon showing the origin of the difference between near-field (left) and far field (right) methods from *Ref.*[191]

The idea of circumventing the diffraction limit in optical microscopy arrived with the work of Irishman E. H. Synge[189] in 1932, who realised that by using a probe held in the near-field ($<50\,\mathrm{nm}$) of the object under study, features smaller than the wavelength of the light could be resolved. The physical basis for the technique is given a full treatment and mathematical derivation elsewhere. For the purpose of this thesis, it may be stated that an angular spectrum representation of an electromagnetic field allows a separation of the terms describing the homogeneous plane waves, and inhomogenous evanescent waves[190]. The near-field is that region, very close to an object, where the evanescent waves that are coupled to it, and which decay exponentially into space, are significant and therefore cannot be ignored. Typically, evanescent waves are created whenever there is a case of total internal reflection, such as occurs in an optical fibre. Electrical and magnetic fields cannot be discontinuous at a boundary, and so an exponentially-decaying evanescent wave propogates into free space. The field has its greatest intensity up to one-third of the wavelength of the reflected light away from the dielctric boundary (*i.e.* the edge of the transducer from which it originates), and then falls off sharply. A cartoon showing the origin of the difference between near and far field microscopy is shown in **figure 1.4.2**.

Synge's original idea was a modification of dark-field microscopy: fix a particle to a quartz plate, irradiate it, and then collect the reflected rays by the use of a collecting apparatus such as a photographic plate. The experimental leap was to envisage the rastering of a biological section at close distance (the near-field) over the irradiated particle, and record the modulation of the collected light intensity, in order to build up a picture of the section at potentially higher resolution than allowed by the diffraction limit of the light used. This was the first description of a sub-wavelength scanning microscopy, and interestingly involves an 'antenna' (the particle) rather than an aperture as the source of the evanescent waves. Synge communicated his idea to Einstein, who suggested using a very small aperture in an opaque plate; in a

further communication, Synge would prophetically suggest the use of a cone or pyramid of quartz glass brought to a point of 10^{-6} cm[192].

Due to the crudity of the then-current technology and the difficulty in achieving such precise motion control, a practical demonstration of the technique could not be made for the submicroscopic samples that the technique would purport to illuminate. That the NSOM concept were to remain a largely esoteric theoretical invention for many years is attested to by an independent reinvention of the concept by the mathematician J. A. O'Keefe in 1956[193], and subsequent workers often proceeded largely ignorant of Synge's pioneering work.

The near-field probing technique was demonstrated in principle by Baez in 1956, who investigated the effect using an acoustic experiment. This was followed in in 1972 by microwave experiments, performed by Eric Ash and G. Nicholls at University College, London. The advent of STM in the early 1980s suggested that the precise control necessitated by the NSOM technique might be provided by the use of piezoelectric transducers, and the technique in its common form was encapsulated in a paper by Betzig and Trautman in 1992[194], who realised its potential as a non-invasive technique for probing biological structures.

A NSOM probe typically consists a a optical fibre down which optical signals may be transmitted by total internal reflection, which is brought to an apex at the 'probe' end by either mechanical pulling or etching in HF. This is then commonly coated in a reflective metal, *e.g.* aluminium, and an aperture is formed by gently colliding the probe with a surface. The most common methods of maintaining a NSOM probe in the near-field is by the use of a shear-force feedback system, whereby the probe is attached to a piezoelectric tuning fork. A cartoon depicting this arrangement is shown in **figure 1.4.3** on the next page. The circuit in this arrangement is able to detect perturbations to the resonant frequency of the tuning fork as it is brought into the region of the near-field, and then adjust accordingly the distance of the probe from the sample by means of a piezoactuator. An alternative method is to use the signal from a split photodiode in a modified AFM setup, in which the probe is either fixed to an AFM cantilever, or the light is passed through the AFM tip, as a means to maintain the probe in the near-field of the sample, very much like it stops the AFM tip impacting on the sample in normal AFM operation.[191]

It was quickly realised that the technique could also be used for lithography[195], and an elegant magneto-optical digital storage device was demonstrated. However, some of the earliest lithographic applications used conventional photoresists. Since then, SAMs have been demonstrated as excellent photoresists capable of potentially better resolution[38], and many of the best results from SNP have been on SAMs.
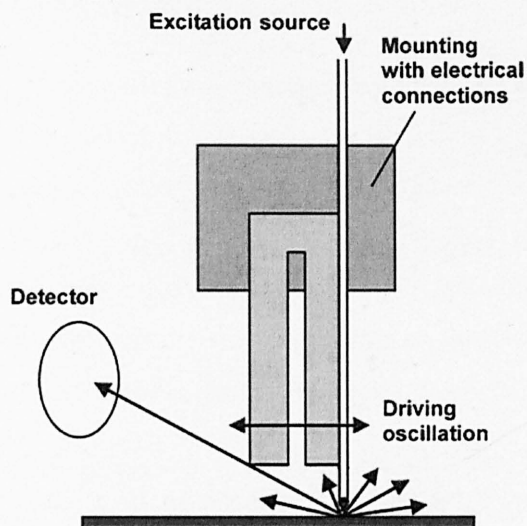
Figure 1.4.3   The method of shear-force feedback operation in NSOM, from *Ref.*[191]

Sun, Chong and Leggett demonstrated SNP on acid ($C_{10}COOH$) and hydroxy– ($C_{11}OH$) terminated SAMs on gold[196], achieving feature sizes of 39 nm (fwhm). Sun and Leggett[197] then showed that cyanide etching chemistry[168] could be used at the nanoscale to produce three-dimensional features. Since then, a body of work[198–200] on gold and silicon substrates has demonstrated that structures far smaller than the wavelength of the photolithographic radiation can be fabricated, reaching resolutions of $\lambda/22$.[191]

1.4.4   Patterning of Biological Molecules

1.4.4.1   Overview

Patterning biological structures on SAMs requires all the considerations that are made in terms of immobilising biomolecules on surfaces, plus the additional consideration that the patterning process will not risk compromising the biomolecular structure, which in many cases would cause of loss of biological functionality. Many of the processes already discussed have been used to successfully pattern biomolecules. Of particular relevance to this thesis in terms of producing patterns is the development of surfaces that require a minimal number of activation steps to bind proteins.

1.4.4.2   Biomolecule attachment protocols

Patel *et al.*[201] proposed a method of amine attachment more sensitive to the mild conditions necessitated by biolomolecular attachment, using chemistries developed for selective capturing of proteins on solid (polymer-bound) phase columns for biochemical separations. Again, carbodiimide activation was used, in order to introduce an *N*-succinimide-attached activated ester, which is readily displaced by primary sp^3 amine groups in biomolecules in aqueous biological buffer solution. This methodology has been used to bind both proteins[201] and DNA[202]. Some of these systems are photoreactive, undergoing photolysis or modification to the surface ω functionality that has wider implications than those restricted to biomolecule immobilisation *e.g.* in molecular electronics.

Another method which has been used previously is the activation of an amine-terminated SAM by the use of glutaraldehyde. This yields an aldehyde surface, which can bind free primary amines, as is described in the next subsection.

1.4.4.3   Photoactive groups in SAMs

A particularly useful class of SAMs for the patterning of biomolecules are those that have switchable responses to biological adhesion. One particular approach has been the development of photocleavable molecules that have halogenated leaving groups. Prior to irradiation, the low surface free energies of the halogenated groups are at the interface are able to resist the adhesion of some biological molecules for limited periods. Once irradiated, the photocleavable group might present a group that can be to further activated to direct the immobilisation of biomolecules.

Chloromethylphenylsiloxane SAMs on silicon initially present just such a low-energy surface. Upon irradiation with 244 nm light, the chlrorine is cleaved from the methylene group by a radical process, and the methylene in turn is converted into carbonyl species (at first aldehydes, then carboxylates) which can readily immobilise proteins with available lysine groups. Aldehydes require no further activation to attach primary amines (such as are offered by lysine residues in proteins), and the surface can also be activated by the use of carbodiimide chemistry, as mentioned above, in order to render amenable to protein attachment those groups which have become carboxylic acids.

1.4.4.4   SAM Molecular Gradients

It is possible to introduce surface functionality gradients along the suface of a SAM.[203] The most common method is to allow diffusion of similar-length but differently ω-substituted SAM through a

polysaccharide matrix. Gradiated SAMs have far-reaching applications in 'lab-on-a-chip'-type devices, and could be used to generate artificial routes similar to the very simplist metabolic pathways.

1.5   Functional Membrane Structures: Biological Light Harvesting Complexes

1.5.1   Harvesting Light

Photosynthesis—literally, 'making with light'—is ubiquitous and pervasive in nature, and is observed in plants and algae, as well as several phyla* of bacteria[20]. Photosynthetic organisms—those which harness light from the Sun as a primary or significant energy source—are extremely successful, and this is reflected in their abundance. It is by no means an exaggeration to make the assertion that photosynthesis is the basis of life on Earth: The vast majority of known organisms' metabolisms are dependent on chemical energy that can be traced back to the actions of incident photons on biological chromophores[†].

At this significant time in human history, the awesome transmogrifying power of photosynthesis, evident in the dwindling, yet once vast reserves of crude oil (—and, to a lesser extent, natural gas and coal), could not be more starkly obvious. Ancient photosynthesis, and the ecosystems that it supported, has driven modern human society. Petroleum as a fuel is unsupassed in the return in energy density that it yields; it can be burned relatively safely and cleanly, and produces only small amounts of toxic by-products during the release of large quantities of usable work. Hydrocarbons derived from crude oil also form the basic building blocks of the organic chemist's repertoire. By proxy, they are also the basis of the pharmaceutical and polymer industries, and now form the units from which new materials are being made. Indeed, the power of photosynthesis has inspired a (arguably misguided) lobby for a switch to biofuels by governments worried that their steady supplies come from increasingly politically turbulant areas of the globe. The ability of plants to produce chemical energy on a large scale is therefore widely recognized[‡].

The realisation that a significant proportion of the energy requirements of human society could be garnered from sunlight itself was made in the 19th Century, although early attempts focussed on the extraction of the thermal component of the Sun's rays. It was not until the 1950s that recognisable

---

*a taxonomic grouping above class and below kingdom in hierarchy
[†]chromophores are chemical groups that are able to absorb electromagnetic radiation
[‡]—however, the sense of devoting significant portions of arable land to biofuel production has been questioned

photovoltaic cells were developed at Bell labs for use in space. While the efficiency of photovoltaics has increased dramatically, many devices still have very narrow spectral responses, one of the reasons why photosynthesis, with its use of light-harvesting antennae (see next section), has the advantage. The spatially-directed integration of antennae complexes into artifical systems like SAMs is the first step towards a fully 'biokleptic' architecture.

1.5.2 Photosynthesis

1.5.2.1 Historical perspective

Despite important work by van Helmont (*c.*1640), who determined that, contrary to Aristotle, a willow tree did not get its mass from the soil, but (as we now know, *in part*) from the water supplied to it; and Priestley (*c.*1770), who realised the power of plants to reinstate "vital" air* following contamination by burning, the the rôle of (sun) light in photosynthesis was not recognised until the work of Ingenhousz in the late 18th Century. Concurrently, Senebier and de Saussure later established the requirement for carbon dioxide and water, formulating a basic scheme for plant-based photosynthesis[20]:

$$CARBON\ DIOXIDE + WATER \xrightarrow{SUNLIGHT} ORGANIC\ MATTER + OXYGEN$$
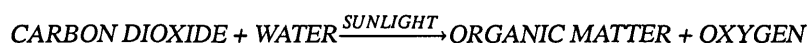
While the oxygenic apparatus of plants, algae and cyanobacteria is often seen as the pinnacle of the evolution of photosynthesis from a human perspective—changing Earth's atmosphere from being mildly reducing to strongly oxidising[2], and allowing the evolution of higher forms of life (*i.e.* animals)—it is of note that many photosynthetic species do not house an oxygen-evolving complex. Indeed, some photosynthetic organisms are actually anaerobes, as is the case for many of the more ancient photosynthetic organisms, which often grow better under anearobic conditions. Photosynthesis is therefore a more general process.

A chemical rationalisation for photosynthesis was advanced by Van Niel[204] in 1941, with the understanding that it is essentially a redox process. Van Niel stated:

$$CO_2 + 2H_2A \rightarrow (CH_2O) + A_2 + H_2O \tag{1.5.1}$$

---
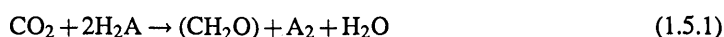
*which Lavoisier, thanks to information from Priestley and Carl Willhelm Scheele, realised was oxygen: an element. Priestley interpreted his "vital" air to be air that had been purified of phlogiston, the fire-giving substance that was released from a flammable material was burned

—this may be expressed as two separate events:

$$2H_2A \rightarrow 2A + 4e^- + 4H^+ \qquad (1.5.2)$$

$$CO_2 + 4e^- + 4H^+ \rightarrow (CH_2O) + H_2O \qquad (1.5.3)$$
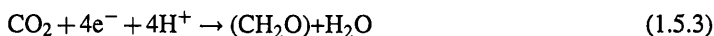
Equation (1.5.1) on the preceding page is a summation of equation (1.5.2) and equation (1.5.3), which had been determined by researchers working in the years immediately preceeding van Niels's paper, but the separation of the two events were also supportive of a spatiotemporal separation of the photosynthetic process into a series of subtasks within the organism.

In an ingenious experiment by Hill[205] reported in 1939, the reduction of Fe(III) to Fe(II) was observed in aqueous solutions of chloroplasts when they were irradiated with visible light. This suggested that the molecular mechanism of photosynthesis was electrochemical in nature, and would require some species capable of carrying a charge. This is achieved in nature by using simple hydrocarbons that contain heteroatoms capable of holding interchangeable oxidation states, as will be explained in the next section. Previously discussed in the introductory section of this chapter, was the use of myriad organic signallers by nature to 'communicate' between the cellular machinery of the cell (and between cells), as compared with the ubiquitous electron in the human technology of this era. In this instance, an organic molecule 'communicates' an electrochemical potential in a form that is specific (unlike an electron), allowing spatial separation of components in the photosynthetic unit.

Photosynthesis is a physical *process* and is therefore characterised by a series of steps with a defined chronology. The temporal separation of events was elegantly demonstrated by Emerson and Arnold[206,207] in 1932, by investigations using a pulsed light source. The rate of photosynthesis carried out by the oxygenic alga *Chlorella pyrrenoidosa* was determined by measuring the rate at which the organism evolved O_2. The flash-pulse spacing and system temperature was varied and the rate of O_2 evolution was monitored. It was found that, when the time between pulses was long, evolution of O_2 was not dependent on temperature. However, shortening the pulse intermission caused the O_2 evolution rate to vary with temperature, following an Arrhenius-like relationship that was suggestive of at least one other secondary process that must occur in photosynthesis, quite apart from the initial absorbance of incident photons by chromophores. In fact, it is now known that the metabolism of all photosynthetic organisms is supported by a large number of reactions which do not need light to drive them, and many photosynthetic organisms are able to support themselves independent of the requirement for light.

1.5.2.2   Chromophores relevant to photosynthesis

Organisms that use sunlight as significant or primary energy source can be roughly divided into those that use light-catalysed rhodopsin isomerisation to pump either H^+ or Cl^- though a cell membrane, and thus produce an electrochemical gradient which can be used to drive metabolism; and a much larger group that use chlorophyll to perform charge separation. It is the ability of the latter group to bring about chemical change (by the movement of electrons between molecular species) that has shaped the world around us. Rhodopsin photosynthesis will not be considered any further in this thesis. The central of the variants of chlorophyll found in bacteria and plants is the chlorin subunit; a tetrapyrrole derivative. Tetrapyrroles such as the porphyrin molecule will self-assemble from acetaldehyde and pyrrole in strongly oxidising conditions, both of which will have almost certainly have been present in the prebiotic soup. The chlorophyll molecules in photosynthetic organisms alive today, however, are manufactured by a series of enzyme-catalysed reactions, using glutamic acid as a starting point[208]. Chlorophyll has a reduced symmetry as compared with porphyrins, and again, this has important implications, especially for its spectroscopic characteristics. The planarity of the chlorin subunit, which allows the electronic transitions necessary for photosynthesis, is promoted by its chelation of Mg^{2+}, which is a very soluble ion that is present in the world's oceans in great abundance. In some extremophilic bacteria, Zn^{2+} replaces magnesium to produce a more thermodynamically stable chlorophyll; however, the ion is only sparingly soluble in water compared to Mg^{2+}, which precludes its inclusion in the majority of photosynthetic organisms.

Shown in **figure 1.5.1** on the next page are the structures of (a) chlorophyll *a* (found in all plants); (b) bacteriochlorophyll *a*; and (c) porphyrin. Also shown in part (a) is the IUPAC labelling system for chlorins. The additional structures introduced by biosynthesis, as compared with the simple porphyrin in (a), are evident. As well as the extracyclic ring '*E*' which extends the conjugation along one axis, thus reducing the molecular symmetry for the purpose of electronic transitions, chlorophylls feature a phytol or isoprenoid tail, connected to position 17 of ring *D*, whose purpose is to anchor the molecule within the larger, protein based structures where it is found in nature. (c) has particular relevance to this thesis: it is the primary chromophore in the light harvesting complexes of its title.

The inherant spectroscopic characteristics of chlorophyll are instrumental in its power as a system capable of processing electromagnetic radiation; its ability to retune light and produce chemical change. Shown in **figure 1.5.2** on page 66, **part (a)**, are the absorption and emission spectra of bacteriochlorophyl *a* in diethyl ether. Also shown, in **figure 1.5.2** on page 66 **part (b) and (c)** respectively, are a simplified molecular orbital (MO) transition diagram, and schematic representing the electron density
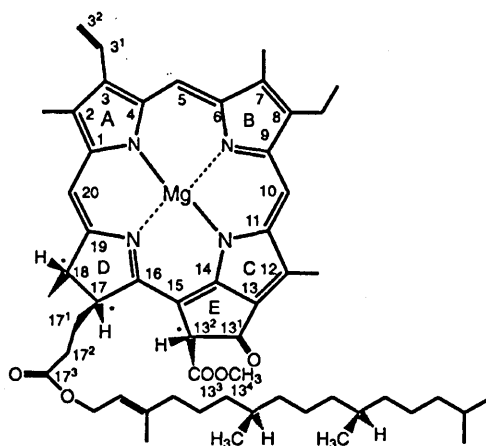
(a) Chlorophyll *a* with IUPAC labelling system for chlorins
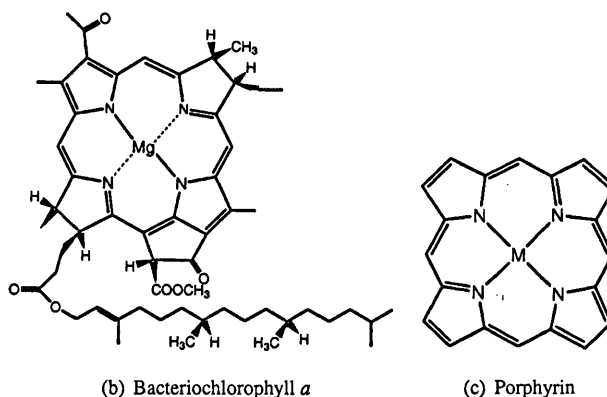
(b) Bacteriochlorophyll *a*　　　　　　(c) Porphyrin

Figure 1.5.1　Chlorin structures

change associated with the $\pi \rightarrow \pi^*$ transitions that give rise to the spectra. Because the shapes of the ground and excited states of bacteriochlorophyll are very similar, the molecular vibrations excited during absorption are also excited during emission, giving rise to a signal with a degree of reflective symmetry along the y-axis of its spectrum. However, the emission resuls from a transition between the ground vibrational state of the electronically excited state as it relaxes to an excited vibrational state of the ground elctronic state, which gives rise to what is termed a *Stokes shift:* the fluorescence maximum occurs at a longer wavelength than the absorbance maximum[20]. The strongest intensity and longest wavelength transition, which influences the spectral profile of the fluorescnce, is polarised along the Q_y axis, and is dependent upon incident EMR having its electric vector parallel to the y-axis of the chlorin to occur. It can be seen in figure 1.5.1 (c), that the biosynthesis of bacteriochlorophyll a extends the conjugation of the chromophore along this axis by the addition of the extracylic ring to chlorin subunit *E*, and by the carbonyl at the 3 position of ring *A*; the conjugation is reduced along the x-axis by the saturation of the bond between positions 7 and 8 of ring *B*. The exagerration
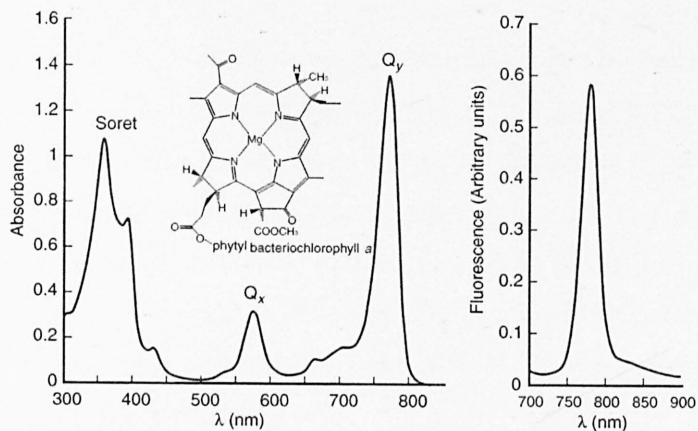
(a) Absorbance (left) and emission (right) spectra of bacteriochlorophyll a in diethyl ether
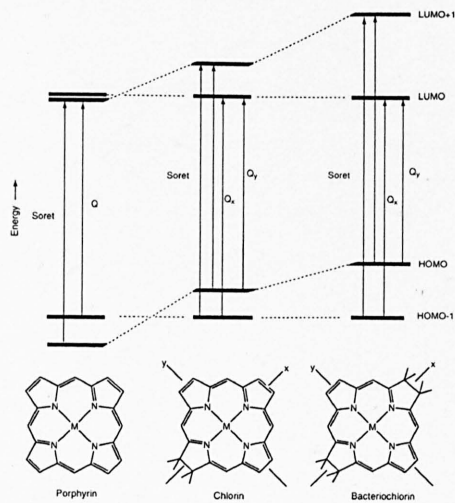
(b) Simplified MO transition diagram showing routes to excited states in (left to right) porphyrin, chlorin and bacteriochlorin
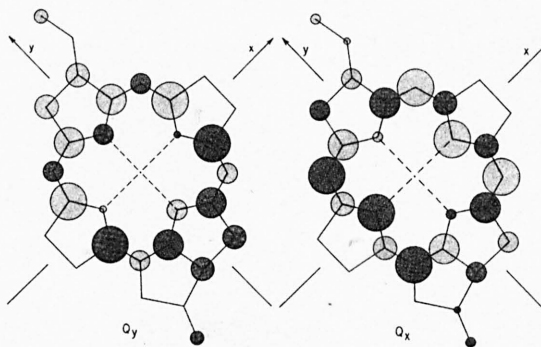
(c) 'Q$_y$' (left) and 'Q$_x$' (right) of electron density diagrams for excited states in bacteriochlorophyll a; originally from Ref.[209]

Figure 1.5.2   The spectral properties of bacteriochlorophyll a; images reproduced from *Ref.*[20]

of the conjugation along the y axis of the chlorin increases the strength of the HOMO→LUMO*

transition of Q_y in bacteriochlorophyll *a*, at the expense (by dimishing the conjugation along the x

axis) of the weakening of the HOMO-1→LUMO transition of Q_x (seefigure 1.5.2 on the previous page

(b)) and therefore the biosynthesis pathway is ideally suited in its promotion of chromophores which

fluoresce strongly at longer wavelengths. As will be shown, this is entirely fit-for-purpose in terms of

photosynthetic efficiency. Apart from chlorins, there are two ther major classes of chromophores that

used by photosynthetic organisms: carotenoids, which are conjugated or partially conjugated derivatives

of isoprene; and bilins, which are found in some types of antennae (see next subsection), and also

in phytochromes, which regulate gene expression (such as those involved in antennae biosyntheis)

dependent upon the ambient light intensity.

The primary rôles of carotenoids in photosynthesis are:

1. Absorbance of light in the visible region of the spectrum (400–500 nm), followed by fluorescence

   at longer (lower energy) wavelengths

2. Photoprotection by the quenching of chlorophyll triplet states, and excited singlet states of oxygen

   if there are any proximal to the photosynthetic apparatus

They are also involved in the regulation of energy transfer in antennae *via* the xanthophyll cyle[20], the

full details of which are beyond the scope of this thesis

1.5.2.3   Photosynthetic Antennae

All photosynthetic organisms contain light harvesting antennae[210]. The structure of the light harvesting

2 complex of the purple bacterium *Rhodobacter spaheroides* is introduced in detail in subsection 1.5.3

on page 70. Antennae have two primary functions:

1. To increase the total cross section of chromophores able to absorb incoming photons and inititate

   photosynthesis

2. To increase the spectral range of photons that may be used for photosynthesis

It can be shown[20] that, in full sunlight, only ∼10 photons s^{-1} are incident on a chlorophyll molecule.

0.1 s is a near-eternity on a biological time-scale, and thus the incoming flux of photons would be a

---

*Highest Occupied Molecular Orbital; Lowest Unoccupied Molecular Orbital

limiting factor, were the number of chlorophylls only of the same magnitude as the number of photo-synthetic reaction centres (RC); the centres where charge separation is carried out. Nature circumvents this limiting factor by the expression and growth of light harvesting antennae to capture photons for the RC. Antennae are three dimensional arrays of chlorophylls and carotenoids, and there are in fact typically thousands of photosynthetically useful chromophores serving a single RC.

In order to channel photon energy to the RC, chromophores (chlorophylls, but also carotenoids) within antennae; and between one antenna and neighbouring antennae, have to transfer energy between each other. There are two models of energy transfer that are applicable in the case of light harvesting: Förster energy transfer, and exciton coupling. The former is a long range effect that is slightly weaker than the latter, and arises due to transient dipole-dipole interactions, which allow an excited state chromophore to induce an excited state in a neighbour. Exciton coupling typically occurs at distances of less than $10\,\text{Å}$, when the molecular orbitals of chromophores in the array begin to overlap, and the induction is more direct than in Förster energy transfer. It has been remarked that these two models essentially describe the same process, but that the effect is enhanced over short distances.

As has been discussed previously, fluorescence in individual chlorophylls and also in carotenoids occurs at a longer wavelength than absorbance, due to a Stokes shift. The effects of Förster energy transfer and exciton coupling that take place when the chromophores are held in light harvesting complexes are such that each increases the shift to longer wavelength; exciton coupling produces a greater shift than Förster energy transfer. Antennae therefore absorb EMR over a large spectral range and, though a complex system of excitation and fluorescence, re-tune it to produce narrow wavelength band low energy photons suitable for use by the RC to produce charge separation. Antennae have been considered analagous to satellite dishes, in their collection and focussing of incoming pulses of EMR toward a single point, but another useful analogy is that of the funnel concept, shown in **figure 1.5.3** on the next page.

1.5.2.4 Charge separation and carbon metabolism

While the charge separation at the heart of chlorophyll-based organisms is subsequent to the action of harvesting light, it is the ultimate purpose of photosynthesis and therefore merits brief discussion. As an example, the RC and subsequent elctron transfer pathways of purple nonsulfur bacteria will be discussed; they have the best characterised of the RCs that are known, and are relevant to this thesis because the organism from which the light harvesting complexes of its title are extracted from a purple nonsulfur bacterium, *Rhodobacter sphaeroides.*
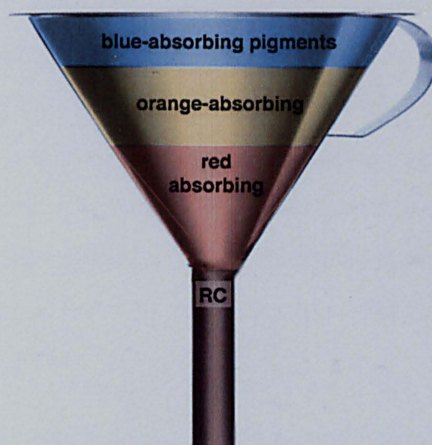
Figure 1.5.3   The transmission of photon energy from chromophores that absorb at shorter wavelengths, and fluoresce at longer wavelengths, is illustrated well by the funnel concept

The RC consists of three or four protein subunits, which are either transmembrane, or are partially anchored within the membrane. The proteins give the RC a defined geometry, necessary for the excitation and electron transfer reactions to take place. The 'noncovalently associated cofactors' which carry out the process of charge transfer are typically four molecules of bacteriochlorophyll, two molecules of bacteriopheophytin (bacteriochlorophylls that do not have a chelated metal ion in the chlorin subunit), one Fe^{2+} ion, and one molecule of carotenoid. Two of the bacteriochlorophyll molecules are termed the 'special pair' due to their strong interaction. The wavelength of their maximum (Q_y) absorbance band is 870 nm; as will be described, the arrangement of chromophores in the antennae complexes is such that exciton coupling re-tunes all of the incident EMR to this wavelength before it reaches the RC. The 'special pair' is the central engine of photosynthesis, losing an electron to form a primary ion-pair state, which approximately shares the resulting unpaired electron. The electron donated by the excited state special pair is transferred to a bacteriopheophytin, and then on to first one quinone, and then another. Quinones are two-electron gates; molecular charge carriers that, in being reduced to quinols, can move electrochemical potential across the membrane, from the cytoplasmic side to the periplasm. Once a quinone has been fully reduced to a quinol, which requires two charge separation cycles, it is released to the periplasmic side, creating a net flow of protons (in the hydroxy groups of the quinol). A coupling factor enzyme then uses the free energy derived from this proton electrochemical gradient to form phosphate bonds in ATP (Adenosine TriPhosphate), the universal currency of biology, which can drive some (but not all) cellular metabolic processes. One of the main features of chlorophyll-based photosynthesis is the reduction of CO_2 to form sugars (the 'Calvin cycle'), which is also dependent on NADH, a cellular coenzyme. This is beyond the scope of this thesis, but is well documented elsewhere.

In order to reduce the oxidised ion-state pair, which must take place after every cycle of electron transfer, an electron is donated from the charge carrier cytochrome c_2. Cytochromes contain a heme group, which is a porphyrin group chelating Fe. The multiple redox states that iron is able to adopt make cytochromes ideal cellular charge carriers, and in contrast to chlorophyll, there is no change to the redox state of the tetrapyrrole unit. The cytochrome that rereduces the special pair may be freely mobile or tethered to the periplasmic side of the membrane in the form of a tetraheme cytochrome complex. The reoxidation of the expelled quinol is also carried out by the cytochrome bc_1 complex, which forms a quinone that can replace quinol expelled from the RC.

In total, the processes in the RC take two electrons from the periplasm, via the cytochrome, special pair and bacteriopheophytin to the first, then second quinone, and in expelling the resullting quinol, move two protons from the cytoplasm to the periplasm. This may be summarised:

$$2\text{cyt}\, c_{2_\text{red}} + \textbf{UQ} + \textbf{2H}^+ + 2h\nu \rightarrow 2\text{cyt}\, c_{2_\text{ox}} + \textbf{UQH}_2 \qquad (1.5.4)$$
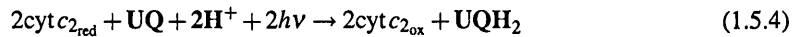
As stated above, the cycle of electron and proton transfer is completed by the cytochrome bc_1 complex, in a reaction which may be summarised as:

$$2\textbf{UQH}_2 + 2\text{cyt}\, c_{2_\text{ox}} + \textbf{UQ} + \textbf{2H}^+ \rightarrow 2\textbf{UQ} + \textbf{4H}^+ 2\text{cyt}\, c_{2_\text{red}} + \textbf{UQH}_2 \qquad (1.5.5)$$
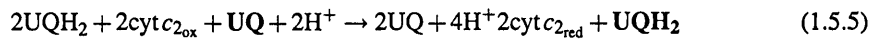
In the above equations, cyt c_2 is cytochrome c_2, which rereduces the special pair ready for excitation by another photon, while **UQ** is ubiquinone, the electron transporting molecule in purple bacteria RC. Of the processes described in the initial stages of charge transfer, the only step which is thermally activated is the transfer of the electron from the first quinone, Q_A, to the second, Q_B. The rates of the other charge transfer steps are actually increased at cryogenic temperatures. The reduction of the special pair by the cytochrome is temperature independent, and again proceeds at extreme cryogenic temperatures. This was the first evidence for quantum tunneling in a biological process.

1.5.3   The LH2 Complex of *Rhodobacter sphaeroides*

1.5.3.1   *Rhodobacter sphaeroides*

Rhodobacter sphaeroides is a purple nonsulfur bacterium of the phylum proteobacteria. It is widely distributed, and abundant in anaerobic environments such as sewage treatments ponds. Under these conditions, when no oxygen is present, the photosynthetic architectures are expressed, and the cell

membrane invaginates to form intracytoplasmic tubules that house the photosynthetic complexes. Purple

bacteria are among the most widely studied of organisms that use photosyntheis, and have perhaps the

most comprehensively understood photosystem. *Rhodobacter sphaeroides* has been extensively studied

by the Hunter group at the University of Sheffield, and is the source of the light harvesting complexes

whose directed immobilisation form the basis for a large part of this thesis.

1.5.3.2   Light Harvesting Complex 2

Rhodobacter sphaeroides LH2 is a nonameric, ring-shaped complex where each repeated unit is com-

posed of two polypeptides, denoted α and β, two carotenoids, and three bacteriochlorophylls. It is

thought that the second bacteriochlorophyll has a purely photoprotective rôle, which it fulfils via cis-

trans isomerisation. One of the bacteriochlorophylls is positioned approximately a third of the way

from the cytoplasmic face of the complex in an approximately horizontal orientation, and is referred

to as B 800 after the position of its maximum absorbance band (800 nm). The other two bacteri-

ochlorophylls are vertically arranged so that the two chromophores are proximal to each other, and also

the bacteriochlorophylls in neighbouring subunits, having their maximum absorbance band at 850 nm;

they are thus denoted B 850. The difference in the maximum absorbance band of the two distinctly

arranged bacteriochlorophylls is due to the manner in which they are coupled. The B 800 units can

be characterised as being coupled by Förster energy transfer, while the B 850 units exhibit exciton

coupling, which as previously described shifts the position of the maximum absorbance band to a longer

wavelength, and subsequently the maximum fluorescence band is also shifted to longer wavelength.

Shown in **figure 1.5.4** on the following page are cartoons depicting the LH2 complex of the purple

bacterium *Rhodopseudomonas acidophila*. The top of the figure in (a) is the periplasmic side. The

bacteriochlorophylls are highlighted in purple and the carotenoids in orange; the polypeptide domains

have been rendered as translucent.

Light of wavelength 400–500 nm is absorbed by the carotenoid molecules, which fluoresce at a longer

wavelength, exciting the B 800 bacteriochlorophylls. These in turn fluoresce at a longer wavelength,

exciting the B 850 bacteriochlorophylls. Once these fluoresce, the resultant EMR is passed onto the LH1

antenna complex, which surrounds the RC. LH1 has a maximum absorbance band of 870 nm, and is a

ring composed of repeated polypeptide heterodimers (in *Rhodobacter sphaeroides*, of 16 units) which

each contain two bacteriochlorophylls, all arranged in much the same way as the B 850 of LH2. Once

the excited LH1 chromophores fluoresce, they pass on the EMR to the RC, where charge separation

takes place.

(a) LH2 from the side   (b) LH2 from the top
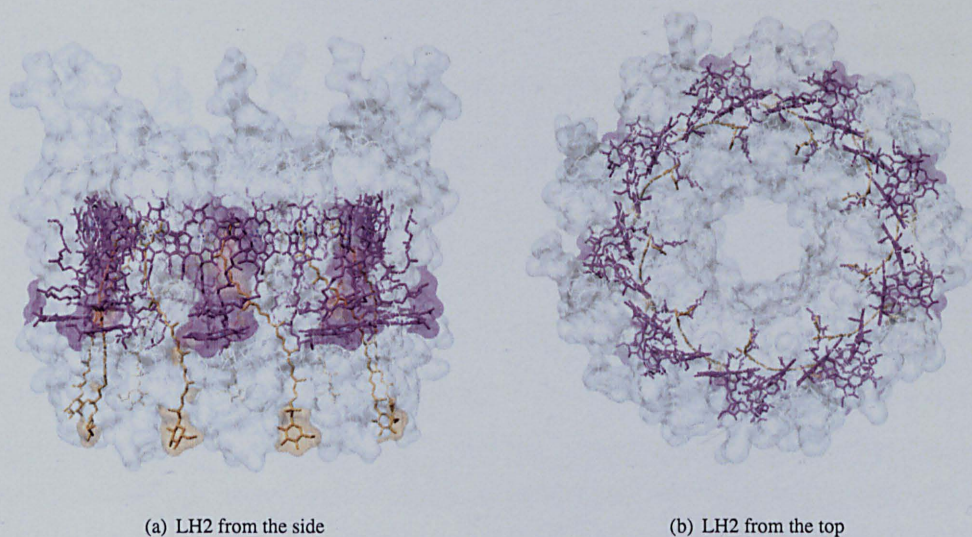
Figure 1.5.4   Light harvesting 2 complex from *Rhodopseudomonas acidophila*

1.5.4   Integration of Photosynthetic Apparatus into Photovoltaic Devices

The possibility of integrating biological structures related to photosynthesis into photovoltaic cells has only in very recent years begun to be properly explored. Previously, the technology for manipulating biomolecules, and for creating artificial structures suited to the integration of biomolecules, was not sufficiently developed. Additionally, biomolecular probes have only in recent years fully elucidated the structures of the biomolecules under study; once the structures have been solved, it has been possible to design surfaces to specifically tether the appropriate biomolecular building blocks to artificial structures and devices.

The stucture of purple bacterial LH2 was originally solved by X-ray diffraction[211]. Some important early work (see *Refs.*[154, 158, 212]) towards elucidating the structure of LH2 by AFM used image averaging techniques to obtain high resolution images from a large number of AFM micrographs. While the images yielded by these studies were very impressive, one of the advantages of AFM over the long-standing probe of choice for biological structures, XRD, is that AFM can probe the structure of a single molecule. XRD relies on the formation of a crystal of the structure (often facilitated by the inclusion of other structures which help the crystal to form), and when the XRD pattern is solved an 'average' structure is deduced. Work by Scheuring *et al.*[154, 212] approached AFM in much the same way, averaging over many scans, and while much information about 2D crystals of LH2 was yielded, it did not give information about how LH2 sits in the context of a native photosynthetic bacterial membrane. This important information was later provided by Bahatyrova *et al.*[213], who used a combined AFM-confocal

system. It was shown that there could be significant deviation from completely circular in the case LH2, but more especially in LH1.

Recent spectroscopic experiments have elucidated some of the energy transer processes that take place in light harvesting antennae. Lin *et al.*, for instance, used femtosecond transient absorbance spectroscopy to follow the transfer of energy from carotenoids to bacteriochlorophyll in the RC of *Rhodobacter sphaeroides*[214]. Information such as this has later informed the design of artificial light harvesting systems[215,216].

The integration of bacteriochlorophyll into SAMs[217], and chlorophyll derivatives into mesostructured silica films on indium tin oxide electrodes[218] have both been investigated, and the integration of LH2 into folded-sheet silica mesoporous material has also been explored[219]. A considerable body of previous work has centred on the integration of photosystem I into SAMs[220,221], but the integration of *Rhodobacter sphaeroides* RC[222] and LH1-RC complexes from *Rhodospirillum rubrum*[223] into SAMs have also yielded promising results. In addition to integration into SAMs, the study of biological photosynthesis and the specialisation of its components as light harvesting or charge separation devices has informed artifical designs that aim to improve on conventional photovoltaics, *e.g.*[224,225]. It is noteworthy that some of the most impressive recent developments in photovoltaics that improve their efficiency adopt similar concepts from photosynthesis—for instance, multiple chromophores were used for the cell that hold the photovoltaics efficiency 'world record' (42.7 %), developed by a team at the University of Delaware[226].

The integration and patterning of biological light harvesting complexes into artificial systems such as SAMs is of great interest, with wide-ranging implications. Advances in patterning (such as SNP) allow the precision modification of surfaces, while a growing array of SAM ω-group chemistries allow the specific immobilisation of biological (and, indeed, artificial) macromolecules. There are several aspects regarding the integration of LH2 into SAMs that are novel. Much previous work has centred on the patterning of plasma proteins or biological macromolecules that have relevance to bionomics arrays in medical research. The patterning of membrane proteins, including those involved in photosynthesis, has some precedent, but the confluence of (nano)photolithography, biological light harvesting, and integration into SAMs is relatively new, and is of relevance to light hravseting and photovoltaics research. Because there is an obvious optical aspect to the biological functionality of LH2, spectrographic investigations offer an immediate method of probing and assessing that integration.

1.6 Synopsis

In this chapter, a large number of concepts and analytical techniques were presented in order to provide the reader with a firm and comprehensive understanding of all of the pertinent aspects relating to the integration of functional biological light harvesting structures into self-assembling molecular systems. The extensive review of research related to SAMs presented in this chapter is intended to be broad-ranging, yet provide enough detail for the reader to understand all the facets pertaining to the integration of biological structures into SAMs. First of all, a comparison between SAMs and biological membranes was drawn. SAMs are a good model for the self-assembly interactions that nature employs in its cellular structures, but more importantly for this work, they present a means to introduce structure by chromophore-specific photochemical interactions, and tailorable surfaces that are largely independent of the hydrocarbon components that aid stability in the SAM. The consequence of molecular morphology, particular to SAM component molecules, on micro– and macroscopic surface properties was introduced to explain how small changes can affect overall structural attributes. A review of oligo(ethylene oxide)-terminated SAM chemistry, and the physicochemical basis from which it might derive its remarkable protein resistance, explored this concept in greater depth.

The probes used to elucidate structural information about surfaces, and self-assembling systems such as SAMs vary in the information that they can yield, and also the damage they do to the sample. Ever since Robert Hooke introduced systematic structural investigations using a microscopic as a means by which the workings of nature might be explored, some 300 years ago, samples have required modification and dissection. SPM techniques can be nearly non-destructive, but other analytical methods could interfere with structures, especially at a dynamic interface, and the contention and contradictory results yielded by GIXD, NIXSW and XPS regarding the nature of the M–S interface may stem from damage done to the sample by X-rays. The method of probing and preparing samples therefore requires careful consideration.

Patterning is central to the fabrication of structure on surfaces, and photolithography has been the mainstay of IC fabrication since its development over fifty years ago. Scanning near-field photolithography offers a way to circumvent the diffraction limit and therefore avoids the necessitation of extreme UV chromophores. SAMs are demonstrably good positive-tone photoresists, but they also offer the ability to introduce chromophores that undergo photochemical change, at wavelengths independent of that used to photooxidise the sulfur at the M–S interface. Additionally, they offer a means to introduce patterns with a specific interaction (either attractive, or repulsive) with biological structures.

The control of surface chemistries, and precision of patterning of SAMs seem ideally suited to the patterning of LH2, and this will form a central part of this thesis.

1.7 Aims

1. To investigate and provide a physical rationalisation for the photolithographic process as it occurs on a variety of SAMs on Au, and similar SAMs on Ag.

2. To explore the structure and properties of Pd–SR SAMs, and compare the photooxidation process, central to the photolithography of Pd–SR SAMs, with findings for Au–SR and Ag–SR SAMs.

3. To investigate photochemical change in ω functionalities.

4. To investigate the nature of interaction of LH2 with a variety of SAMs.

5. To demonstrate a patterning protocol for LH2, with retention of biological functionality (spectral characteristics).

List of Figures in Chapter 1

Notes and References for Chapter 1

[1] P. Atkins and J. De Paula, *Atkins' Physical Chemistry*. Oxford University Press, March 2006.

[2] R. J. P. Williams and F. J. J. R. da Silva, *The Natural Selection of the Chemical Elements: The Environment and Life's Chemistry*. Oxford University Press, May 1996.

[3] E. D. Schneider and D. Sagan, *Into the Cool: Energy Flow, Thermodynamics, and Life*. University Of Chicago Press, December 2006.

[4] I. Langmuir, "The constitution and fundamental properties of solids and liquids. part i. solids.," *Journal of the American Chemical Society*, vol. 38, no. 11, pp. 2221–2295, 1916.

[5] J. N. Murrell, S. F. A. Kettle, and J. M. Tedder, *The Chemical Bond*. John Wiley and Sons Ltd, October 1985.

[6] A. Otten and S. Herminghaus, "How plants keep dry: A physicist's point of view," *Langmuir*, vol. 20, pp. 2405–2408, March 2004.

[7] B. Franklin, W. Brownrigg, and Rev.-Farish, "Of the stilling of waves by means of oil," *Philosophical Transactions of the Royal Society*, vol. 64, pp. 445–460, 1774.

[8] P. Ball, *The Self-Made Tapestry : Pattern Formation in Nature*. Oxford University Press, USA, October 2001.

[9] L. Stryer, *Biochemistry*. W.H. Freeman & Company.

[10] C. J. Frosch and L. Derick, "Surface protection and selective masking during diffusion in silicon," *Journal of the Electrochemical Society*, vol. 104, pp. 547–552, 1957.

[11] W. L. Bond and J. Andrus, "Photographs of the stress field around edge dislocations," *Physical Review*, vol. 101, pp. 1211+, February 1956.

[12] J. A. Hoerni, "Planar silicon diodes and transistors," *IRE Transactions: Electronic Devices*, March 1961.

[13] G. M. Whitesides, "The 'right' size in nanobiotechnology," *Nat Biotech*, vol. 21, pp. 1161–1165, October 2003.

[14] P. Ball, "Natural strategies for the molecular engineer," *Nanotechnology*, vol. 13, no. 5, pp. R15–R28, 2002.

[15] F. Delogu, "Thermodynamics on the nanoscale," *Journal of Physical Chemistry B*, vol. 109, pp. 21938–21941, November 2005.

[16] E. K. Drexler, *Engines of Creation*. Bantam Doubleday Dell, 1986.

[17] A. P. Usher, *A History of Mechanical Inventions: Revised Edition*. Harvard University Press, January 1954.

[18] C. R. Hurley and G. J. Leggett, "Influence of the solvent environment on the contact mechanics of tip-sample interactions in friction force microscopy of poly(ethylene terephthalate) films," *Langmuir*, vol. 22, pp. 4179–4183, April 2006.

[19] D. Luo, K. Haverstick, N. Belcheva, E. Han, and W. M. Saltzman, "Poly(ethylene glycol)-conjugated pamam dendrimer for biocompatible, high-efficiency dna delivery," *Macromolecules*, vol. 35, pp. 3456–3462, April 2002.

[20] R. E. Blankenship, *Molecular Mechanisms of Photosynthesis*. Blackwell Publishing Limited, December 2001.

[21] G. M. Whitesides and C. J. Love, "The art of building small," *Scientific American*, September 2001.

[22] Plutarch, *Natural Questions*, ch. IX. 46-127. Why does pouring oil on the sea make it clear and calm? Is it for that the winds, slipping the smooth oil, have no force, nor cause any waves?

[23] P. the Elder, *Natural History*, pp. 234+. No. II. Everything is soothed by oil, and this is the reason why divers send out small quantities of it from their mouths, because it smooths every part which is rough.

[24] Bede, *The Eclesiastical History of the English People*. 731. The venerable Bede relates that Bishop Adain (A. D. 651) gave to a company about to take a journey by sea "some holy oil, saying, 'I know that when you go abroad you will meet with a storm and contrary wind; but do you remember to cast this oil I give you into the sea, and the wind shall cease immediately.'".

[25] P. Becker, "History and progress in the accurate determination of the avogadro constant," *Reports on Progress in Physics*, vol. 64, no. 12, pp. 1945–2008, 2001.

[26] T. Terada, R. Yamamoto, and T. Watanabe, "untitled," *Scientific papers of the Institute of Physical and Chemical Research*, vol. 23, pp. 173+, 1934.

[27] A. Pockels, "Surface tension," *Nature*, vol. 46, pp. 437+, 1891.

[28] R. A. Walker, J. A. Gruetzmacher, and G. L. Richmond, "Phosphatidylcholine monolayer structure at a liquid-liquid interface," *Journal of the American Chemical Society*, vol. 120, pp. 6991–7003, July 1998.

[29] I. Langmuir, "The constitution and fundamental properties of solids and liquids. ii. liquids.," *Journal of the American Chemical Society*, vol. 39, no. 9, pp. 1848–1906, 1917.

[30] I. Langmuir, "The adsorption of gases on plane surfaces of glass, mica and platinum.," *Journal of the American Chemical Society*, vol. 40, no. 9, pp. 1361–1403, 1918.

[31] H. Kuhn, "Energieübertragung in monomolekularen schichten," *Naturwissenschaften*, vol. 54, no. 15, pp. 429–435, 1967.

[32] M. A. Richard, J. Deutch, and G. M. Whitesides, "Hydrogenation of oriented monolayers of ω-unsaturated fatty acids supported on platinum," *Journal of the American Chemical Society*, vol. 100, no. 21, pp. 6613–6625, 1978.

[33] H. Sellers, A. Ulman, Y. Shnidman, and J. E. Eilers, "Structure and binding of alkanethiolates on gold and silver surfaces: implications for self-assembled monolayers," *Journal of the American Chemical Society*, vol. 115, no. 21, pp. 9389–9401, 1993.

[34] J. Sagiv, "Organized monolayers by adsorption. 1. formation and structure of oleophobic mixed monolayers on solid surfaces," *Journal of the American Chemical Society*, vol. 102, no. 1, pp. 92–98, 1980.

[35] A. Ulman, "Formation and structure of self-assembled monolayers," *Chemical Reviews*, vol. 96, no. 4, pp. 1533–1554, 1996.

[36] E. Delamarche, B. Michel, H. A. Biebuyck, and C. Gerber, "Golden interfaces: The surface of self-assembled monolayers," *Advanced Materials*, vol. 8, no. 9, pp. 719–729, 1996.

[37] F. Schreiber, "Structure and growth of self-assembling monolayers," *Progress in Surface Science*, vol. 65, no. 5-8, pp. 151–257, 2000.

[38] J. C. Love, L. A. Estroff, J. K. Kriebel, R. G. Nuzzo, and G. M. Whitesides, "Self-assembled monolayers of thiolates on metals as a form of nanotechnology," *Chemical Reviews*, vol. 105, no. 4, pp. 1103–1170, 2005.

[39] C. Vericat, M. E. Vela, G. A. Benitez, J. A. M. Gago, X. Torrelles, and R. C. Salvarezzo, "Surface characterization of sulfur and alkanethiol self-assembled monolayers on au(111)," *Journal of Physics: Condensed Matter*, vol. 18, pp. R867–R900, 2006.

[40] C. D. Bain, H. A. Biebuyck, and G. M. Whitesides, "Comparison of self-assembled monolayers on gold: coadsorption of thiols and disulfides," *Langmuir*, vol. 5, no. 3, pp. 723–727, 1989.

[41] R. G. Nuzzo, F. A. Fusco, and D. L. Allara, "Spontaneously organized molecular assemblies. 3. preparation and properties of solution adsorbed monolayers of organic disulfides on gold surfaces," *Journal of the American Chemical Society*, vol. 109, no. 8, pp. 2358–2368, 1987.

[42] A. Earnshaw and N. Greenwood, *Chemistry of the Elements, Second Edition*. Butterworth-Heinemann, November 1997.

[43] L. C. F. Blackman and M. J. S. Dewar, "Promoters for the dropwise condensation of steam. part i. preparation of compounds containing monofunctional sulfur groups," *Journal of the Chemical Society*, pp. 162–165, 1957.

[44] L. C. F. Blackman and M. J. S. Dewar, "Promoters for the dropwise condensation of steam. ii. preparation of compounds containing polyfunctional sulfur groups," *Journal of the Chemical Society*, pp. 165–169, 1957.

[45] L. C. F. Blackman and M. J. S. Dewar, "Promoters for the dropwise condensation of steam. iv. discussion of dropwise condensation and testing of compounds," *Journal of the Chemical Society*, pp. 171–176, 1957.

[46] H. Emmons, "untitled," *Transactions of the American Institute of Chemical Engineers*, vol. 35, pp. 109+, 1939.

[47] R. G. Nuzzo and D. L. Allara, "Adsorption of bifunctional organic disulfides on gold surfaces," *Journal of the American Chemical Society*, vol. 105, no. 13, pp. 4481–4483, 1983.

[48] R. G. Nuzzo, B. R. Zegarski, and L. H. Dubois, "Fundamental studies of the chemisorption of organosulfur compounds on gold(111). implications for molecular self-assembly on gold surfaces," *Journal of the American Chemical Society*, vol. 109, no. 3, pp. 733–740, 1987.

[49] M. D. Porter, T. B. Bright, D. L. Allara, and C. E. D. Chidsey, "Spontaneously organized molecular assemblies. 4. structural characterization of n-alkyl thiol monolayers on gold by optical ellipsometry, infrared spectroscopy, and electrochemistry," *Journal of the American Chemical Society*, vol. 109, no. 12, pp. 3559–3568, 1987.

[50] A. Ulman, J. E. Eilers, and N. Tillman, "Packing and molecular orientation of alkanethiol monolayers on gold surfaces," *Langmuir*, vol. 5, no. 5, pp. 1147–1152, 1989.

[51] J. P. Rabe, J. D. Swalen, D. A. Outka, and J. Stohr, "Near-edge x-ray absorption fine structure studies of oriented molecular chains in polyethylene and langmuir-blodgett monolayers on si(111)," *Thin Solid Films*, vol. 159, pp. 275–283, May 1988.

[52] C. D. Bain and G. M. Whitesides, "Correlations between wettability and structure in monolayers of alkanethiols adsorbed on gold," *Journal of the American Chemical Society*, vol. 110, no. 11, pp. 3665–3666, 1988.

[53] M. G. Broadhurst, "Melting points of n-alkanes," *Journal of Research of the National Bureau of Standards*, vol. 66, no. 241–249, 1962.

[54] P. E. Laibinis, R. G. Nuzzo, and G. M. Whitesides, "Structure of monolayers formed by coadsorption of two n-alkanethiols of different chain lengths on gold and its relation to wetting," *Journal of Physical Chemistry*, vol. 96, no. 12, pp. 5097–5105, 1992.

[55] E. B. Troughton, C. D. Bain, G. M. Whitesides, R. G. Nuzzo, D. L. Allara, and M. D. Porter, "Monolayer films prepared by the spontaneous self-assembly of symmetrical and unsymmetrical dialkyl sulfides from solution onto gold substrates: structure, properties, and reactivity of constituent functional groups," *Langmuir*, vol. 4, no. 2, pp. 365–385, 1988.

[56] E. G. Shafrin and W. A. Zisman, "Effect of progressive fluorination of a fatty acid on the wettability of its adsorbed monolayer," *Journal of Physical Chemistry*, vol. 66, no. 4, pp. 740–748, 1962.

[57] D. J. Lavrich, S. M. Wetterer, S. L. Bernasek, and G. Scoles, "Physisorption and chemisorption of alkanethiols and alkyl sulfides on au(111)," *Journal of Physical Chemistry B*, vol. 102, pp. 3456–3465, April 1998.

[58] C. D. Bain, B. E. Troughton, Y. T. Tao, J. Evall, G. M. Whitesides, and R. G. Nuzzo, "Formation of monolayer films by the spontaneous assembly of organic thiols from solution onto gold," *Journal of the American Chemical Society*, vol. 111, no. 1, pp. 321–335, 1989.

[59] A. Eberhardt, P. Fenter, and P. Eisenberger, "Growth kinetics in self-assembling monolayers: a unique adsorption mechanism," *Surface Science*, vol. 397, pp. L285–L290, February 1998.

[60] G. E. Poirier and M. J. Tarlov, "The c(4x2) superlattice of n-alkanethiol monolayers self-assembled on au(111)," *Langmuir*, vol. 10, no. 9, pp. 2853–2856, 1994.

[61] G. E. Poirier, M. J. Tarlov, and H. E. Rushmeier, "Two-dimensional liquid phase and the px.sqroot.3 phase of alkanethiol self-assembled monolayers on au(111)," *Langmuir*, vol. 10, no. 10, pp. 3383–3386, 1994.

[62] N. Camillone, "Diffusion-limited thiol adsorption on the gold(111) surface," *Langmuir*, vol. 20, pp. 1199–1206, February 2004.

[63] E. Barrena, E. Palacios-Lidon, C. Munuera, X. Torrelles, S. Ferrer, U. Jonas, M. Salmeron, and C. Ocal, "The role of intermolecular and molecule-substrate interactions in the stability of alkanethiol nonsaturated phases on au(111)," *Journal of the American Chemical Society*, vol. 126, pp. 385–395, January 2004.

[64] C. Munuera, E. Barrena, and C. Ocal, "Chain-length dependence of metastable striped structures of alkanethiols on au(111)," *Langmuir*, vol. 21, pp. 8270–8277, August 2005.

[65] L. B. Picraux, C. D. Zangmeister, and J. D. Batteas, "Preparation and structure of a low-density, flat-lying decanethiol monolayer from the densely packed, upright monolayer on gold," *Langmuir*, vol. 22, pp. 174–180, January 2006.

[66] M. A. Bryant and J. E. Pemberton, "Surface raman scattering of self-assembled monolayers formed from 1-alkanethiols at silver [electrodes]," *Journal of the American Chemical Society*, vol. 113, no. 10, pp. 3629–3637, 1991.

[67] M. A. Bryant and J. E. Pemberton, "Surface raman scattering of self-assembled monolayers formed from 1-alkanethiols: behavior of films at gold and comparison to films at silver," *Journal of the American Chemical Society*, vol. 113, no. 22, pp. 8284–8293, 1991.

[68] O. Alexiadis, V. A. Harmandaris, V. G. Mavrantzas, and L. D. Site, "Atomistic simulation of alkanethiol self-assembled monolayers on different metal surfaces via a quantum, first-principles parametrization of the sulfur-metal interaction," *Journal of Physical Chemistry C*, vol. 111, pp. 6380–6391, May 2007.

[69] J. P. Folkers, P. E. Laibinis, and G. M. Whitesides, "Self-assembled monolayers of alkanethiols on gold: comparisons of monolayers containing mixtures of short- and long-chain constituents with methyl and hydroxymethyl terminal groups," *Langmuir*, vol. 8, no. 5, pp. 1330–1341, 1992.

[70] J. P. Folkers, P. E. Laibinis, G. M. Whitesides, and J. Deutch, "Phase behavior of two-component self-assembled monolayers of alkanethiolates on gold," *Journal of Physical Chemistry*, vol. 98, no. 2, pp. 563–571, 1994.

[71] N. J. Brewer and G. J. Leggett, "Chemical force microscopy of mixed self-assembled monolayers of alkanethiols on gold: Evidence for phase separation," *Langmuir*, vol. 20, pp. 4109–4115, May 2004.

[72] C. A. Widrig, C. A. Alves, and M. D. Porter, "Scanning tunneling microscopy of ethanethiolate and n-octadecanethiolate monolayers spontaneously absorbed at gold surfaces," *Journal of the American Chemical Society*, vol. 113, no. 8, pp. 2805–2810, 1991.

[73] R. G. Nuzzo, L. H. Dubois, and D. L. Allara, "Fundamental studies of microscopic wetting on organic surfaces. 1. formation and structural characterization of a self-consistent series of polyfunctional organic monolayers," *Journal of the American Chemical Society*, vol. 112, no. 2, pp. 558–569, 1990.

[74] R. G. Nuzzo, E. M. Korenic, and L. H. Dubois, "Studies of the temperature-dependent phase behavior of long chain n-alkyl thiol monolayers on gold," *The Journal of Chemical Physics*, vol. 93, no. 1, pp. 767–773, 1990.

[75] M. G. Roper, M. P. Skegg, C. J. Fisher, J. J. Lee, V. R. Dhanak, D. P. Woodruff, and R. G. Jones, "Atop adsorption site of sulphur head groups in gold-thiolate self-assembled monolayers," *Chemical Physics Letters*, vol. 389, pp. 87–91, May 2004.

[76] P. Maksymovych, D. Sorescu, D. Dougherty, and J. Yates, "Surface bonding and dynamical behavior of the ch$_3$sh molecule on au(111)," *Journal of Physical Chemistry B*, vol. 109, no. 47, pp. 22463–22468, 2005.

[77] P. Fenter, F. Schreiber, L. Berman, G. Scoles, P. Eisenberger, and M. J. Bedzyk, "On the structure and evolution of the buried s/au interface in self-assembled monolayers: X-ray standing wave results," *Surface Science*, vol. 412-413, pp. 213–235, September 1998.

[78] H. A. Biebuyck and G. M. Whitesides, "Interchange between monolayers on gold formed from unsymmetrical disulfides and solutions of thiols: evidence for sulfur-sulfur bond cleavage by gold metal," *Langmuir*, vol. 9, no. 7, pp. 1766–1770, 1993.

[79] M. G. Roper and R. G. Jones, "Direct observation of thiolate displacement reactions on au(111): the role of physisorbed disulfides," *Langmuir*, vol. 21, pp. 11684–11689, December 2005.

[80] J. Noh, H. S. Kato, M. Kawai, and M. Hara, "Surface structure and interface dynamics of alkanethiol self-assembled monolayers on au(111)," *Journal of Physical Chemistry B*, vol. 110, pp. 2793–2797, February 2006.

[81] L. Strong and G. M. Whitesides, "Structures of self-assembled monolayer films of organosulfur compounds adsorbed on gold single crystals: electron diffraction studies," *Langmuir*, vol. 4, no. 3, pp. 546–558, 1988.

[82] C. E. D. Chidsey, G. Y. Liu, P. Rowntree, and G. Scoles, "Molecular order at the surface of an organic monolayer studied by low energy helium diffraction," *The Journal of Chemical Physics*, vol. 91, no. 7, pp. 4421–4423, 1989.

[83] C. O'Dwyer, G. Gay, B. Viarisdelesegno, and J. Weiner, "The nature of alkanethiol self-assembled monolayer adsorption on sputtered gold substrates," *Langmuir*, vol. 20, pp. 8172–8182, September 2004.

[84] J. B. Schlenoff, M. Li, and H. Ly, "Stability and self-exchange in alkanethiol monolayers," *Journal of the American Chemical Society*, vol. 117, no. 50, pp. 12528–12536, 1995.

[85] G. G. Baralia, A. S. Duwez, B. Nysten, and A. M. Jonas, "Kinetics of exchange of alkanethiol monolayers self-assembled on polycrystalline gold," *Langmuir*, vol. 21, pp. 6825–6829, July 2005.

[86] M. H. Schoenfisch and J. E. Pemberton, "Air stability of alkanethiol self-assembled monolayers on silver and gold surfaces," *J. Am. Chem. Soc.*, vol. 120, pp. 4502–4513, May 1998.

[87] Y. Zhang, R. H. Terrill, T. A. Tanzer, and P. W. Bohn, "Ozonolysis is the primary cause of uv photooxidation of alkanethiolate monolayers at low irradiance," *Journal of the American Chemical Society*, vol. 120, no. 11, pp. 2654–2655, 1998.

[88] Y. Zhang, R. H. Terrill, and P. W. Bohn, "Ultraviolet photochemistry and ex situ ozonolysis of alkanethiol self-assembled monolayers on gold," *Chem. Mater.*, vol. 11, pp. 2191–2198, August 1999.

[89] J. A. Rodriguez, J. Dvorak, T. Jirsak, G. Liu, J. Hrbek, Y. Aray, and C. Gonzalez, "Coverage effects and the nature of the metal-sulfur bond in s/au(111): High-resolution photoemission and density-functional studies," *Journal of the American Chemical Society*, vol. 125, pp. 276–285, January 2003.

[90] Y. W. Yang and L. J. Fan, "High-resolution xps study of decanethiol on au(111): Single sulfur-gold bonding interaction," *Langmuir*, vol. 18, pp. 1157–1164, February 2002.

[91] H. Rieley, N. J. Price, R. G. White, R. I. R. Blyth, and A. W. Robinson, "A nexafs and ups study of thiol monolayers self-assembled on gold," *Surface Science*, vol. 331-333, pp. 189–195, July 1995.

[92] M. Tachibana, K. Yoshizawa, A. Ogawa, H. Fujimoto, and R. Hoffmann, "Sulfur-gold orbital interactions which determine the structure of alkanethiolate/au(111) self-assembled monolayer systems," *Journal of Physical Chemistry B*, vol. 106, pp. 12727–12736, December 2002.

[93] L. Häussling, B. Michel, H. Ringsdorf, and H. Rohrer, "Direct observation of streptavidin specifically adsorbed on biotin-functionalized self-assembled monolayers with the scanning tunneling microscope," *Angewandte Chemie International Edition in English*, vol. 30, no. 5, pp. 569–572, 1991.

[94] G. E. Poirier, "Mechanism of formation of au vacancy islands in alkanethiol monolayers on au(111)," *Langmuir*, vol. 13, pp. 2019–2026, April 1997.

[95] J. Zhang, A. Bilic, J. R. Reimers, N. S. Hush, and J. Ulstrup, "Coexistence of multiple conformations in cysteamine monolayers on au(111)," *J. Phys. Chem. B*, vol. 109, pp. 15355–15367, August 2005.

[96] F. Tao and S. Bernasek, "Understanding odd-even effects in organic self-assembled monolayers," *Chemical Reviews*, vol. 107, no. 5, pp. 1408–1453, 2007.

[97] L. Yan, C. Marzolin, A. Terfort, and G. M. Whitesides, "Formation and reaction of interchain carboxylic anhydride groups on self-assembled monolayers on gold," *Langmuir*, vol. 13, pp. 6704–6712, December 1997.

[98] D. A. Hutt and G. J. Leggett, "Functionalization of hydroxyl and carboxylic acid terminated self-assembled monolayers," *Langmuir*, vol. 13, pp. 2740–2748, May 1997.

[99] V. Chechik, R. M. Crooks, and C. J. M. Stirling, "Reactions and reactivity in self-assembled monolayers," *Advanced Materials*, vol. 12, no. 16, pp. 1161–1171, 2000.

[100] J. C. Love, D. B. Wolfe, R. Haasch, M. L. Chabinyc, K. E. Paul, G. M. Whitesides, and R. G. Nuzzo, "Formation and structure of self-assembled monolayers of alkanethiolates on palladium," *Journal of the American Chemical Society*, vol. 125, pp. 2597–2609, March 2003.

[101] K. Schwaha, N. D. Spencer, and R. M. Lambert, "A single crystal study of the initial stages of silver sulphidation: The chemisorption and reactivity of molecular sulphur (s2) on ag(111)," *Surface Science*, vol. 81, pp. 273–284, February 1979.

[102] G. Rovida and F. Pratesi, "Sulfur overlayers on the low-index faces of silver," *Surface Science*, vol. 104, pp. 609–624, March 1981.

[103] P. E. Laibinis, G. M. Whitesides, D. L. Allara, Y. T. Tao, A. N. Parikh, and R. G. Nuzzo, "Comparison of the structures and wetting properties of self-assembled monolayers of n-alkanethiols on the coinage metal surfaces, copper, silver, and gold," *Journal of the American Chemical Society*, vol. 113, no. 19, pp. 7152–7167, 1991.

[104] M. Yu, D. P. Woodruff, N. Bovet, C. J. Satterley, K. Lovelock, R. G. Jones, and V. Dhanak, "Structure investigation of ag(111) by x-ray standing waves: A case of thiol-induced substrate reconstruction," *Journal of Physical Chemistry B*, vol. 110, pp. 2164–2170, February 2006.

[105] N. J. Brewer, T. T. Foster, G. J. Leggett, M. R. Alexander, and E. Mcalpine, "Comparative investigations of the packing and ambient stability of self-assembled monolayers of alkanethiols on gold and silver by friction force microscopy," *J. Phys. Chem. B*, vol. 108, pp. 4723–4728, April 2004.

[106] N. J. Brewer, R. E. Rawsterne, S. Kothari, and G. J. Leggett, "Oxidation of self-assembled monolayers by uv light with a wavelength of 254 nm," *Journal of the American Chemical Society*, vol. 123, no. 17, pp. 4089–4090, 2001.

[107] K. M. Evans-Nguyen and M. H. Schoenfisch, "Fibrin proliferation at model surfaces: Influence of surface properties," *Langmuir*, vol. 21, pp. 1691–1694, March 2005.

[108] N. T. Flynn, T. N. T. Tran, M. J. Cima, and R. Langer, "Long-term stability of self-assembled monolayers in biological media," *Langmuir*, vol. 19, pp. 10909–10915, December 2003.

[109] E. Cooper, R. Wiggs, D. A. Hutt, L. Parker, G. J. Leggett, and T. L. Parker, "Rates of attachment of fibroblasts to self-assembled monolayers formed by the adsorption of alkylthiols onto gold surfaces," *Journal of Materials Chemistry*, vol. 7, no. 3, pp. 435–441.

[110] C. A. Scotchford, E. Cooper, G. J. Leggett, and S. Downes, "Growth of human osteoblast-like cells on alkanethiol on gold self-assembled monolayers: The effect of surface chemistry," *Journal of Biomedical Materials Research*, vol. 41, no. 3, pp. 431–442, 1998.

[111] E. Cooper, L. Parker, C. A. Scotchford, S. Downes, G. J. Leggett, and T. L. Parker, "The effect of alkyl chain length and terminal group chemistry on the attachment and growth of murine 3t3 fibroblasts and primary human osteoblasts on self-assembled monolayers of alkanethiols on gold," *The Journal of Materials Chemistry*, vol. 10, no. 1, pp. 133–139, 2000.

[112] C. A. Scotchford, C. P. Gilmore, E. Cooper, G. J. Leggett, and S. Downes, "Protein adsorption and human osteoblast-like cell attachment and growth on alkylthiol on gold self-assembled monolayers," *Journal of Biomedical Materials Research*, vol. 59, no. 1, pp. 84–99, 2002.

[113] J. Rundqvist, J. H. Hoh, and D. B. Haviland, "Poly(ethylene glycol) self-assembled monolayer island growth," *Langmuir*, vol. 21, pp. 2981–2987, March 2005.

[114] C. Pale-Grosdemange, E. S. Simon, K. L. Prime, and G. M. Whitesides, "Formation of self-assembled monolayers by chemisorption of derivatives of oligo(ethylene glycol) of structure hs(ch2)11(och2ch2)moh on gold," *Journal of the American Chemical Society*, vol. 113, no. 1, pp. 12–20, 1991.

[115] R. G. Chapman, E. Ostuni, L. Yan, and G. M. Whitesides, "Preparation of mixed self-assembled monolayers (sams) that resist adsorption of proteins using the reaction of amines with a sam that presents interchain carboxylic anhydride groups," *Langmuir*, vol. 16, pp. 6927–6936, August 2000.

[116] K. L. Prime and G. M. Whitesides, "Adsorption of proteins onto surfaces containing end-attached oligo(ethylene oxide): a model system using self-assembled monolayers," *Journal of the American Chemical Society*, vol. 115, no. 23, pp. 10714–10721, 1993.

[117] P.-G. De Gennes, *Scaling Concepts in Polymer Physics*. Cornell University Press, January 1980.

[118] P. Harder, M. Grunze, R. Dahint, G. M. Whitesides, and P. E. Laibinis, "Molecular conformation in oligo(ethylene glycol)-terminated self-assembled monolayers on gold and silver surfaces determines their ability to resist protein adsorption," *Journal of Physical Chemistry B*, vol. 102, pp. 426–436, January 1998.

[119] G. Beamson, B. T. Pickup, W. Li, and S. M. Mai, "Xps studies of chain conformation in peg, ptrmo, and ptmg linear polyethers," *Journal of Physical Chemistry B*, vol. 104, pp. 2656–2672, March 2000.

[120] R. L. C. Wang, H. J. Kreuzer, and M. Grunze, "Molecular conformation and solvation of oligo(ethylene glycol)-terminated self-assembled monolayers and their resistance to protein adsorption," *Journal of Physical Chemistry B*, vol. 101, pp. 9767–9773, November 1997.

[121] D. J. Vanderah, G. Valincius, and C. W. Meuse, "Self-assembled monolayers of methyl 1-thiahexa(ethylene oxide) for the inhibition of protein adsorption," *Langmuir*, vol. 18, pp. 4674–4680, June 2002.

[122] L. Li, S. Chen, J. Zheng, B. D. Ratner, and S. Jiang, "Protein adsorption on oligo(ethylene glycol)-terminated alkanethiolate self-assembled monolayers: The molecular basis for nonfouling behavior," *Journal of Physical Chemistry B*, vol. 109, pp. 2934–2941, February 2005.

[123] M. Zolk, F. Eisert, J. Pipper, S. Herrwerth, W. Eck, M. Buck, and M. Grunze, "Solvation of oligo(ethylene glycol)-terminated self-assembled monolayers studied by vibrational sum frequency spectroscopy," *Langmuir*, vol. 16, pp. 5849–5852, July 2000.

[124] A. J. Pertsin and M. Grunze, "Computer simulation of water near the surface of oligo(ethylene glycol)-terminated alkanethiol self-assembled monolayers," *Langmuir*, vol. 16, pp. 8829–8841, November 2000.

[125] S. Herrwerth, W. Eck, S. Reinhardt, and M. Grunze, "Factors that determine the protein resistance of oligoether self-assembled monolayers - internal hydrophilicity, terminal hydrophilicity, and lateral packing density," *J. Am. Chem. Soc.*, vol. 125, pp. 9359–9366, August 2003.

[126] J. Zheng, L. Li, S. Chen, and S. Jiang, "Molecular simulation study of water interactions with oligo (ethylene glycol)-terminated alkanethiol self-assembled monolayers," *Langmuir*, vol. 20, pp. 8931–8938, September 2004.

[127] E. Ostuni, R. G. Chapman, R. E. Holmlin, S. Takayama, and G. M. Whitesides, "A survey of structure-property relationships of surfaces that resist the adsorption of protein," *Langmuir*, vol. 17, pp. 5605–5620, September 2001.

[128] M. Hederos, P. Konradsson, and B. Liedberg, "Synthesis and self-assembly of galactose-terminated alkanethiols and their ability to resist proteins," *Langmuir*, vol. 21, pp. 2971–2980, March 2005.

[129] S. Chen, L. Liu, and S. Jiang, "Strong resistance of oligo(phosphorylcholine) self-assembled monolayers to protein adsorption," *Langmuir*, vol. 22, pp. 2418–2421, March 2006.

[130] K. Castelino, B. Kannan, and A. Majumdar, "Characterization of grafting density and binding efficiency of dna and proteins on gold surfaces," *Langmuir*, vol. 21, pp. 1956–1961, March 2005.

[131] X. Jiang, D. A. Bruzewicz, M. M. Thant, and G. M. Whitesides, "Palladium as a substrate for self-assembled monolayers used in biotechnology," *Anal. Chem.*, vol. 76, pp. 6116–6121, October 2004.

81

[132] M. Perring, S. Dutta, S. Arafat, M. Mitchell, P. J. A. Kenis, and N. B. Bowden, "Simple methods for the direct assembly, functionalization, and patterning of acid-terminated monolayers on si(111)," *Langmuir*, vol. 21, pp. 10537–10544, November 2005.

[133] T. Bocking, K. A. Kilian, T. Hanley, S. Ilyas, K. Gaus, M. Gal, and J. J. Gooding, "Formation of tetra(ethylene oxide) terminated si-c linked monolayers and their derivatization with glycine: An example of a generic strategy for the immobilization of biomolecules on silicon," *Langmuir*, vol. 21, pp. 10522–10529, November 2005.

[134] T. L. Clare, B. H. Clare, B. M. Nichols, N. L. Abbott, and R. J. Hamers, "Functional monolayers for improved resistance to protein adsorption: Oligo(ethylene glycol)-modified silicon and diamond surfaces," *Langmuir*, vol. 21, pp. 6344–6355, July 2005.

[135] S. D. Evans, R. Sharma, and A. Ulman, "Contact angle stability: Reorganization of monolayer surfaces?," *Langmuir*, vol. 7, no. 1, pp. 156–161, 1991.

[136] R. N. Wenzel, "Resistance of solid surfaces to wetting by water," *Industrial & Engineering Chemistry*, vol. 28, no. 8, pp. 988–994, 1936.

[137] R. N. Wenzel, "Surface roughness and contact angle.," *Journal of Physical Chemistry*, vol. 53, no. 9, pp. 1466–1467, 1949.

[138] A. E. Becquerel, "Mémoire sur les effets électriques produits sous l'influence des rayons solaires," *Comptes Rendus des Séances Hebdomadaires*, vol. 9, pp. 561–567, 1839.

[139] H. Hertz, "Ueber einen einflußdes ultravioletten lichtes auf die electrische entladung," *Annalen der Physik und Chemie*, vol. 267, no. 8, pp. 983–1000, 1887.

[140] M. Planck, "Über das gesetz der energieverteilung im normalspectrum," *Annalen der Physik und Chemie*, vol. 4, pp. 553–563, 1901.

[141] A. Einstein, "Über einen die erzeugung und verwandlung des lichtes betreffenden heuristischen gesichtspunkt," *Annalen der Physik*, vol. 17, pp. 132–144, 1905.

[142] Kelvin, "Contact electricity of metals," *Philosophical Magazine and Journal of Science*, vol. 46, pp. 82–120, 1898.

[143] W. A. Zisman, "A new method of measuring contact potential differences in metals," *Review of Scientific Instruments*, vol. 3, no. 7, pp. 367–370, 1932.

[144] S. D. Evans and A. Ulman, "Surface potential studies of alkyl-thiol monolayers adsorbed on gold," *Chemical Physics Letters*, vol. 170, pp. 462–466, July 1990.

[145] D. M. Alloway, M. Hofmann, D. L. Smith, N. E. Gruhn, A. L. Graham, R. Colorado, V. H. Wysocki, T. R. Lee, P. A. Lee, and N. R. Armstrong, "Interface dipoles arising from self-assembled monolayers on gold: Uv-photoemission studies of alkanethiols and partially fluorinated alkanethiols," *J. Phys. Chem. B*, vol. 107, pp. 11690–11699, October 2003.

[146] D. Briggs, *Surface Analysis of Polymers by XPS and Static SIMS (Cambridge Solid State Science Series)*. Cambridge University Press, May 1998.

[147] C. D. Bain and G. M. Whitesides, "Attenuation lengths of photoelectrons in hydrocarbon films," *Journal of Physical Chemistry*, vol. 93, no. 4, pp. 1670–1673, 1989.

[148] P. E. Laibinis, C. D. Bain, and G. M. Whitesides, "Attenuation of photoelectrons in monolayers of n-alkanethiols adsorbed on copper, silver, and gold," *Journal of Physical Chemistry*, vol. 95, no. 18, pp. 7017–7021, 1991.

[149] G. Binnig, H. Rohrer, C. Gerber, and E. Weibel, "Tunneling through a controllable vacuum gap," *Applied Physics Letters*, vol. 40, no. 2, pp. 178–180, 1982.

[150] G. Binnig, H. Rohrer, C. Gerber, and E. Weibel, "Surface studies by scanning tunneling microscopy," *Physical Review Letters*, vol. 49, pp. 57–60, July 1982.

[151] G. Binnig, H. Rohrer, C. Gerber, and E. Weibel, "7x7 reconstruction on si(111) resolved in real space," *Physical Review Letters*, vol. 50, pp. 120+, January 1983.

[152] G. Binnig, C. F. Quate, and C. Gerber, "Atomic force microscope," *Physical Review Letters*, vol. 56, pp. 930+, March 1986.

[153] J. L. Wilbur, H. A. Biebuyck, J. C. Macdonald, and G. M. Whitesides, "Scanning force microscopies can image patterned self-assembled monolayers," *Langmuir*, vol. 11, no. 3, pp. 825–831, 1995.

[154] S. Scheuring, "Single proteins observed by atomic force microscopy," *Single Molecules*, vol. 2, no. 2, pp. 59–67, 2001.

[155] J. K. H. Hörber and M. J. Miles, "Scanning probe evolution in biology," *Science*, vol. 302, pp. 1002–1005, November 2003.

[156] M. Knez, M. P. Sumser, A. M. Bittner, C. Wege, H. Jeske, D. M. P. Hoffmann, K. Kuhnke, and K. Kern, "Binding the tobacco mosaic virus to inorganic surfaces," *Langmuir*, vol. 20, pp. 441–447, January 2004.

[157] A. V. Bolshakova, O. I. Kiselyova, and I. V. Yaminsky, "Microbial surfaces investigated using atomic force microscopy," *Biotechnol. Prog.*, vol. 20, pp. 1615–1622, December 2004.

[158] D. J. Müller, D. Fotiadis, S. Scheuring, C. Möller, and A. Engel, "Conformational changes, flexibilities and intramolecular forces observed on individual proteins using afm," *Single Molecules*, vol. 1, no. 2, pp. 115–118, 2000.

[159] N. C. Santos and M. A. Castanho, "An overview of the biophysical applications of atomic force microscopy," *Biophysical Chemistry*, vol. 107, pp. 133–149, February 2004.

[160] M. S. Wang, L. B. Palmer, J. D. Schwartz, and A. Razatos, "Evaluating protein attraction and adhesion to biomaterials with the atomic force microscope," *Langmuir*, vol. 20, pp. 7753–7759, August 2004.

[161] T. Thundat, D. P. Allison, R. J. Warmack, G. M. Brown, K. B. Jacobson, J. J. Schrick, and T. L. Ferrell, "Atomic force microscopy of dna on mica and chemically modified mica.," *Scanning Microscopy*, vol. 6, pp. 911–918, December 1992.

[162] C. Bustamante, J. Vesenka, C. L. Tang, W. Rees, M. Guthold, and R. Keller, "Circular dna molecules imaged in air by scanning force microscopy," *Biochemistry*, vol. 31, no. 1, pp. 22–26, 1992.

[163] Y. Jiao and T. E. Schaffer, "Accurate height and volume measurements on soft samples with the atomic force microscope," *Langmuir*, vol. 20, pp. 10038–10045, November 2004.

[164] K. C. Langry, T. V. Ratto, R. E. Rudd, and M. W. Mcelfresh, "The afm measured force required to rupture the dithiolate linkage of thioctic acid to gold is less than the rupture force of a simple gold-alkyl thiolate bond," *Langmuir*, vol. 21, no. 26, pp. 12064–12067, 2005.

[165] R. Berger, E. Delamarche, H. P. Lang, C. Gerber, J. K. Gimzewski, E. Meyer, and H.-J. Guntherodt, "Surface stress in the self-assembly of alkanethiols on gold," *Science*, vol. 276, pp. 2021–2024, June 1997.

[166] M. Godin, P. J. Williams, T. V. Cossa, O. Laroche, L. Y. Beaulieu, R. B. Lennox, and P. Grutter, "Surface stress, kinetics, and structure of alkanethiol self-assembled monolayers," *Langmuir*, vol. 20, no. 17, pp. 7090–7096, 2004.

[167] A. Kumar and G. M. Whitesides, "Features of gold having micrometer to centimeter dimensions can be formed through a combination of stamping with an elastomeric stamp and an alkanethiol "ink" followed by chemical etching," *Applied Physics Letters*, vol. 63, no. 14, pp. 2002–2004, 1993.

[168] A. Kumar, H. A. Biebuyck, N. L. Abbott, and G. M. Whitesides, "The use of self-assembled monolayers and a selective etch to generate patterned gold features," *Journal of the American Chemical Society*, vol. 114, no. 23, pp. 9188–9189, 1992.

[169] M. Geissler, J. M. Mclellan, and Y. Xia, "Edge-spreading lithography: Use of patterned photoresist structures to direct the spreading of alkanethiols on gold," *Nano Lett.*, vol. 5, pp. 31–36, January 2005.

[170] R. D. Piner, J. Zhu, F. Xu, S. Hong, and C. A. Mirkin, ""dip-pen" nanolithography," *Science*, vol. 283, pp. 661–663, January 1999.

[171] H. Zhang, S. W. Chung, and C. A. Mirkin, "Fabrication of sub-50-nm solid-state nanostructures on the basis of dip-pen nanolithography," *Nano Lett.*, vol. 3, pp. 43–45, January 2003.

[172] K. Wadu-Mesthrige, S. Xu, N. A. Amro, and Liu, "Fabrication and imaging of nanometer-sized protein patterns," *Langmuir*, vol. 15, pp. 8580–8583, December 1999.

[173] K. Wadu-Mesthrige, N. A. Amro, J. C. Garno, S. Xu, and G.-Y. Liu, "Fabrication of nanometer-sized protein patterns using atomic force microscopy and selective immobilization," *Biophys. J.*, vol. 80, pp. 1891–1899, April 2001.

[174] M. Su, X. Liu, S. Y. Li, V. P. Dravid, and C. A. Mirkin, "Moving beyond molecules: Patterning solid-state features via dip-pen nanolithography with sol-based inks," *Journal of the American Chemical Society*, vol. 124, pp. 1560–1561, February 2002.

[175] B. W. Maynor, S. F. Filocamo, M. W. Grinstaff, and J. Liu, "Direct-writing of polymer nanostructures: Poly(thiophene) nanowires on semiconducting and insulating surfaces," *Journal of the American Chemical Society*, vol. 124, pp. 522–523, January 2002.

[176] W. B. Lee, Y. Oh, E. R. Kim, and H. Lee, "Nanopatterning of self-assembled monolayers on si-surfaces with afm lithography," *Synthetic Metals*, vol. 117, pp. 305–306, February 2001.

[177] S. Xu, S. Miller, P. E. Laibinis, and Liu, "Fabrication of nanometer scale patterns within self-assembled monolayers by nanografting," *Langmuir*, vol. 15, pp. 7244–7251, October 1999.

[178] G. Y. Liu, S. Xu, and Y. Qian, "Nanofabrication of self-assembled monolayers using scanning probe lithography," *Acc. Chem. Res.*, vol. 33, pp. 457–466, July 2000.

[179] U. Dürig, G. Cross, M. Despont, U. Drechsler, W. Häberle, M. I. Lutwyche, H. Rothuizen, R. Stutz, R. Widmer, P. Vettiger, G. K. Binnig, W. P. King, and K. E. Goodson, ""millipede" – an afm data storage system at the frontier of nanotribology," *Tribology Letters*, vol. 9, pp. 25–32, December 2000.

[180] S. Hong, J. Zhu, and C. A. Mirkin, "Multiple ink nanolithography: Toward a multiple-pen nano-plotter," *Science*, vol. 286, pp. 523–525, October 1999.

[181] K. Salaita, Y. Wang, J. Fragala, R. A. Vega, C. Liu, and C. A. Mirkin, "Massively parallel dip-pen nanolithography with 55 000-pen two-dimensional arrays," *Angewandte Chemie International Edition*, vol. 45, no. 43, pp. 7220–7223, 2006.

[182] J. Huang and J. C. Hemminger, "Photooxidation of thiols in self-assembled monolayers on gold," *Journal of the American Chemical Society*, vol. 115, no. 8, pp. 3342–3343, 1993.

[183] M. J. Tarlov, D. R. F. Burgess, and G. Gillen, "Uv photopatterning of alkanethiolate monolayers self-assembled on gold and silver," *Journal of the American Chemical Society*, vol. 115, no. 12, pp. 5305–5306, 1993.

[184] D. A. Hutt and G. J. Leggett, "Influence of adsorbate ordering on rates of uv photooxidation of self-assembled monolayers," *J. Phys. Chem.*, vol. 100, pp. 6657–6662, April 1996.

[185] D. A. Hutt, E. Cooper, and G. J. Leggett, "Structure and mechanism of photooxidation of self-assembled monolayers of alkylthiols on silver studied by xps and static sims," *Journal of Physical Chemistry B*, vol. 102, pp. 174–184, January 1998.

[186] K. S. L. Chong, S. Sun, and G. J. Leggett, "Measurement of the kinetics of photo-oxidation of self-assembled monolayers using friction force microscopy," *Langmuir*, vol. 21, pp. 3903–3909, April 2005.

[187] N. J. Brewer, R. E. Rawsterne, S. Kothari, and G. J. Leggett, "Oxidation of self-assembled monolayers by uv light with a wavelength of 254 nm," *Journal of the American Chemical Society*, vol. 123, no. 17, pp. 4089–4090, 2001.

83

[188] D. Ryan, B. A. Parviz, V. Linder, V. Semetey, S. K. Sia, J. Su, M. Mrksich, and G. M. Whitesides, "Patterning multiple aligned self-assembled monolayers using light.," *Langmuir*, vol. 20, pp. 9080–9088, October 2004.

[189] E. H. Synge, "An application of piezoelectricity to microscopy," *Philosophical Magazine and Journal of Science*, vol. 13, p. 297, 1932.

[190] L. Novotny, *Progress in Optics*, ch. 5: The History of Near-field Optics, pp. 137–184. No. 50, Amsterdam, The Netherlands: Elsevier, 2007.

[191] G. J. Leggett, "Scanning near-field photolithography—surface photochemistry with nanoscale spatial resolution," *Chemical Society Reviews*, vol. 35, pp. 1150–1161, 2006.

[192] D. McMullen, "The prehistory of scanned image microscopy. part i: Scanned optical microscopes," *Royal Microscopical Society Proceedings*, vol. 25, no. 2, pp. 127–131, 1990.

[193] J. A. O'Keefe, "Resolving power of visible light," *Journal of the Optical Society of America*, vol. 46, no. 359, 1956.

[194] E. Betzig and J. K. Trautman, "Near-field optics: Microscopy, spectroscopy, and surface modification beyond the diffraction limit," *Science*, vol. 257, pp. 189–195, July 1992.

[195] E. Betzig, J. K. Trautman, R. Wolfe, E. M. Gyorgy, P. L. Finn, M. H. Kryder, and C. H. Chang, "Near-field magneto-optics and high density data storage," *Applied Physics Letters*, vol. 61, no. 2, pp. 142–144, 1992.

[196] S. Sun, K. S. L. Chong, and G. J. Leggett, "Nanoscale molecular patterns fabricated by using scanning near-field optical lithography," *Journal of the American Chemical Society*, vol. 124, pp. 2414–2415, March 2002.

[197] S. Sun and G. J. Leggett, "Generation of nanostructures by scanning near-field photolithography of self-assembled monolayers and wet chemical etching," *Nano Lett.*, vol. 2, pp. 1223–1227, November 2002.

[198] R. E. Ducker and G. J. Leggett, "A mild etch for the fabrication of three-dimensional nanostructures in gold," *J. Am. Chem. Soc.*, vol. 128, pp. 392–393, January 2006.

[199] M. Montague, R. E. Ducker, K. S. L. Chong, R. J. Manning, F. J. M. Rutten, M. C. Davies, and G. J. Leggett, "Fabrication of biomolecular nanostructures by scanning near-field photolithography of oligo(ethylene glycol)-terminated self-assembled monolayers," *Langmuir*, vol. 23, pp. 7328–7337, June 2007.

[200] S. Sun, M. Montague, K. Critchley, M. S. Chen, W. J. Dressick, S. D. Evans, and G. J. Leggett, "Fabrication of biological nanostructures by scanning near-field photolithography of chloromethylphenylsiloxane monolayers," *Nano Lett.*, vol. 6, pp. 29–33, January 2006.

[201] N. Patel, M. C. Davies, M. Hartshorne, R. J. Heaton, C. J. Roberts, S. J. B. Tendler, and P. M. Williams, "Immobilization of protein molecules onto homogeneous and mixed carboxylate-terminated self-assembled monolayers," *Langmuir*, vol. 13, pp. 6485–6490, November 1997.

[202] E. Huang, F. Zhou, and L. Deng, "Studies of surface coverage and orientation of dna molecules immobilized onto preformed alkanethiol self-assembled monolayers," *Langmuir*, vol. 16, pp. 3272–3280, April 2000.

[203] M. Riepl, M. Östblom, I. Lundstrom, S. C. T. Svensson, A. W. Deniervandergon, M. Schäferling, and B. Liedberg, "Molecular gradients: An efficient approach for optimizing the surface properties of biomaterials and biochips," *Langmuir*, vol. 21, pp. 1042–1050, February 2005.

[204] C. B. van Niel, "The bacterial photosyntheses and their importance for the general problem of photosynthesis," *Advanced Enzymology*, vol. 1, pp. 263–328, 1941.

[205] R. Hill, "Oxygen produced by isolated chloroplasts," *Proceedings of the Royal Society of London Series B*, vol. 127, pp. 192–210, 1939.

[206] R. Emerson and W. Arnold, "A separation of the reactions in photosynthesis by means of intermittent light," *Journal of General Physiology*, vol. 15, pp. 391–420, 1932.

[207] R. Emerson and W. Arnold, "The photochemical reactions in photosynthesis," *Journal of General Physiology*, vol. 16, no. 191–205, 1932.

[208] S. I. Beale, "Enzymes of chlorophyll biosynthesis," *Photosynthesis Research*, vol. 60, pp. 43–73, 1999.

[209] K. Sauer, *Bioenergetics of Photosynthesis*, ch. Primary Events and the Trapping of Energy, pp. 116–181. New York: Academic Press, 1975.

[210] B. R. Green and W. W. Parson, eds., *Light Harvesting Antennas*. Dordrecht: Kluwer Academic Press, 2001.

[211] G. Mcdermott, S. M. Prince, A. A. Freer, A. M. Hawthornthwaite-Lawless, M. Z. Papiz, R. J. Cogdell, and N. W. Isaacs, "Crystal structure of an integral membrane light-harvesting complex from photosynthetic bacteria," *Nature*, vol. 374, pp. 517–521, April 1995.

[212] "High-resolution afm topographs of rubrivivax gelatinosus light-harvesting complex lh2," *The European Molecular Biology Organization Journal*, vol. 20, no. 12, pp. 3029–3035, 2001.

[213] S. Bahatyrova, R. N. Frese, A. C. Siebert, J. D. Olsen, K. O. van der Werf, R. van Grondelle, R. A. Niederman, P. A. Bullough, C. Otto, and N. C. Hunter, "The native architecture of a photosynthetic membrane," *Nature*, vol. 430, no. 7003, pp. 1058–1062, 2004.

[214] S. Lin, E. Katilius, A. K. W. Taguchi, and N. W. Woodbury, "Excitation energy transfer from carotenoid to bacteriochlorophyll in the photosynthetic purple bacterial reaction center of rhodobacter sphaeroides," *J. Phys. Chem. B*, vol. 107, pp. 14103–14108, December 2003.

[215] I. W. Hwang, D. M. Ko, T. K. Ahn, Z. S. Yoon, D. Kim, X. Peng, N. Aratani, and A. Osuka, "Excitation energy migration in a dodecameric porphyrin wheel," *J. Phys. Chem. B*, vol. 109, pp. 8643–8651, May 2005.

[216] G. Kodis, C. Herrero, R. Palacios, E. Marino-Ochoa, S. Gould, L. Delagarza, R. Vangrondelle, D. Gust, T. A. Moore, A. L. Moore, and J. T. M. Kennis, "Light harvesting and photoprotective functions of carotenoids in compact artificial photosynthetic antenna designs," *J. Phys. Chem. B*, vol. 108, pp. 414–425, January 2004.

[217] N. Filip-Granit, R. Yerushalmi, A. Brandis, M. E. Vanderboom, and A. Scherz, "Uniform approach to bacteriochlorophyll-based monolayers on conducting, semiconducting, and insulating substrates," *J. Phys. Chem. B*, vol. 109, pp. 6933–6935, April 2005.

[218] H. Furukawa, N. Inoue, T. Watanabe, and K. Kuroda, "Energy transfer between chlorophyll derivatives in silica mesostructured films and photocurrent generation," *Langmuir*, vol. 21, pp. 3992–3997, April 2005.

[219] I. Oda, K. Hirata, S. Watanabe, Y. Shibata, T. Kajino, Y. Fukushima, S. Iwai, and S. Itoh, "Function of membrane protein in silica nanopores: Incorporation of photosynthetic light-harvesting protein lh2 into fsm," *J. Phys. Chem. B*, vol. 110, pp. 1114–1120, January 2006.

[220] I. Carmeli, L. Frolov, C. Carmeli, and S. Richter, "Photovoltaic activity of photosystem i-based self-assembled monolayer," *J. Am. Chem. Soc.*, September 2007.

[221] M. Ciobanu, H. A. Kincaid, G. K. Jennings, and D. E. Cliffel, "Photosystem i patterning imaged by scanning electrochemical microscopy," *Langmuir*, vol. 21, pp. 692–698, January 2005.

[222] R. Das, P. J. Kiley, M. Segal, J. Norville, A. A. Yu, L. Wang, A. S. Trammell, L. E. Reddick, R. Kumar, F. Stellacci, N. Lebedev, J. Schnur, B. D. Bruce, S. Zhang, and M. Baldo, "Integration of photosynthetic protein molecular complexes in solid-state electronic devices," *Nano Lett.*, vol. 4, pp. 1079–1083, June 2004.

[223] M. Ogawa, K. Shinohara, Y. Nakamura, Y. Suemori, M. Nagata, K. Iida, A. T. Gardiner, R. J. Cogdell, and M. Nango, "Self-assembled monolayers of light-harvesting 1 and reaction center (lh1-rc) complexes isolated from rhodospirillum rubrum and amino-terminated ito electrode," *Chemistry Letters*, vol. 33, no. 6, pp. 772–773, 2004.

[224] G. M. Hasselman, D. F. Watson, J. R. Stromberg, D. F. Bocian, D. Holten, J. S. Lindsey, and G. J. Meyer, "Theoretical solar-to-electrical energy-conversion efficiencies of perylene-porphyrin light-harvesting arrays," *J. Phys. Chem. B*, vol. 110, pp. 25430–25440, December 2006.

[225] B. Rybtchinski, L. E. Sinks, and M. R. Wasielewski, "Combining light-harvesting and charge separation in a self-assembled artificial photosynthetic system based on perylenediimide chromophores," *J. Am. Chem. Soc.*, vol. 126, pp. 12268–12269, October 2004.

[226] C. B. Honsberg, A. M. Barnett, and D. Kirkpatrick, "Nanostructured solar cells for high efficiency photovoltaics," in *Photovoltaic Energy Conversion, Conference Record of the 2006 IEEE 4th World Conference on*, vol. 2, pp. 2565–2568, 2006.

Chapter 2

Experimental Procedures

"These I mention, that I may excite the World to enquire a little farther into the improvement of Sciences, and not think that either they or their predecessors have attained the utmost perfection on any one part of knowledge, and to throw off that lazy and pernicious principle, of being contented to know as much as their Fathers, Grandfathers, or great Grandfathers ever did, and to think they know enough, because they know somewhat more than the generality of the World besides...Let us see what the improvement of instruments can produce."

- Robert Hooke, Animadversions on the First Part of the Machina Colestis of Johannes Hevelius, 1674

Experimental Procedures Contents

2.1   General Notes

The need for absolute cleanliness at all times during the preparation, storage and handling of SAMs is paramount. Contaminants—especially organic contaminants and biological molecules—have an extremely strong preference for interfaces, and so adventitious adsorbates on glass substrates that are not handled with sufficient care may compromise the integrity of the SAMs being formed. Silicones and phthalates (as plasticizers) are ubiquitous in many laboratory containers, and chemicals of the former group are particularly liable to leach out and coat surfaces. Therefore, plastic wash bottles for solvents were avoided in favour of 'piranha'-cleaned (see *below*) glass containers.

All samples were handled with tweezers cleaned with isopropyl alcohol (IPA) and wiped with clean paper tissue, and surfaces used for cutting samples were similarly cleaned with IPA. Nitrile or latex disposable gloves were worn to remove the risk of contamination from oils or salts from skin. Following washing of samples (HPLC grade ethanol was used, unless indicated otherwise), samples were dried under streams of CP grade nitrogen from gas bottles or dry compressed piped nitrogen. Exposure to the laboratory atmosphere and associated dust *etc.* was minimised as much as possible.

2.2   Cleaning of Glassware

All glassware used in the preparation, storage, and modification of SAMs, and as vessels for the directed assembly of protein patterns, was cleaned using 'piranha' solution. This is a 30 : 70 mix of 100 wt. (vol.) hydrogen peroxide : concentrated sulfuric acid. The combination is highly exothermic (rapidly reaching

$\geq 80\,^{\circ}C$) and is potentially explosive when in contact with organic materials. *Great care should be taken when handling piranha solution.*

After ~ 1 h, when the reaction had subsided and cooled, the remaining fluid was poured into a large water dilution tank in order to raise the pH to a reasonable level for disposal into normal drainage ($\sim pH\,4–5$). The glassware was then rinsed several (≥ 6) times in order to remove any traces of residue, and then dried in an $80\,^{\circ}C$ oven overnight.

2.2.1 Preparation of Silicon for Silane Monolayers

Additional cleaning and preparation by use of the RCA-1 procedure was required for silicon substrates. This is as follows: to 5 parts deionised ($18.2\,M\Omega$) water were added 1 part 30 % hydrogen peroxide and 1 part ammonium hydroxide. Sample tubes containing the substrate and RCA solution were heated until boiling for 1 h. After cooling, these were the rinsed with copious amounts of water (≥ 5 times) and dried in a clean oven ($120\,^{\circ}C$).

2.3 Materials and Chemicals

2.3.1 Formation of SAMs

Borosilicate glass microscope coverslips ('#2' thickness, $64\,mm \times 22\,mm$) were obtained from Chance Propper Ltd., Netherlands. Gold wire (0.5 mm diameter, >99.99 % purity) and silver wire (0.5 mm diameter, >99.96 % purity were purchased from Goodfellows Ltd., UK. Palladium wire (0.5 mm diameter, 99.99 % purity) and titanium wire (0.05 mm diameter, 99.9 % purity) were obtained from Sigma-Aldrich Ltd., UK. Chromium chips (99 %) were purchased from Agar scientific.

1-butanethiol (99 %) and 3-mercapto-1-propanoic acid (99 %) were purchased from Acros Organics. 3-mercapto-1-propanol (95 %), 3-mercaptopropanoic acid (96 %, 1-dodecanethiol (96 %), 11-mercapto-undecanol (97 %), 11-mecaptoundecanoic acid and 1H,1H,2H,2H-perfluorooctanethiol were purchased from Sigma Chemical company, UK.
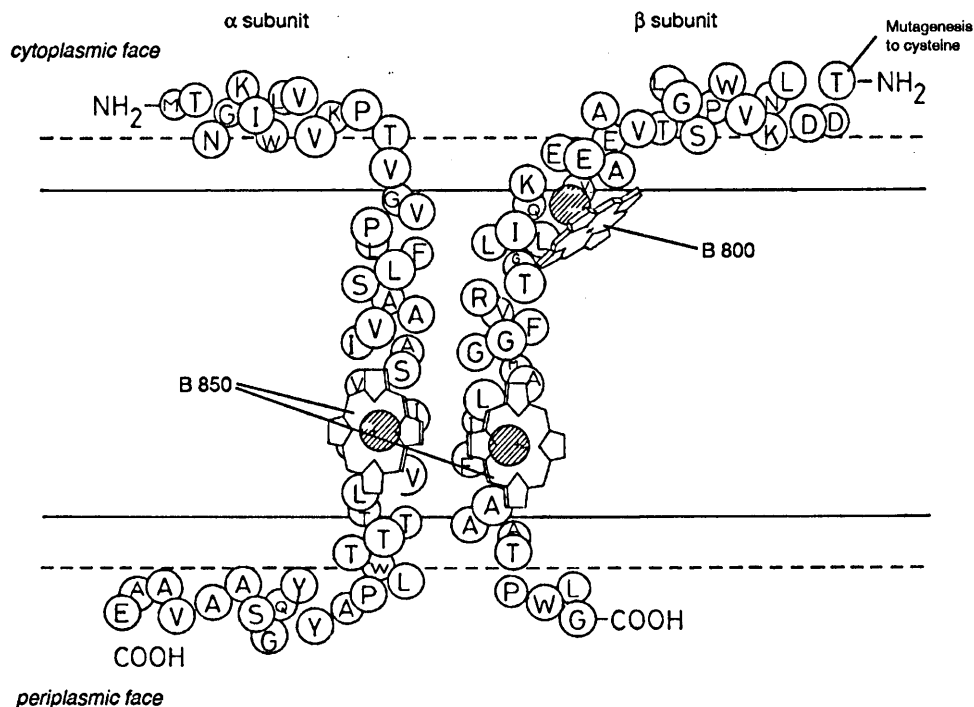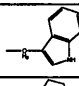
2.3.2 Epitaxial Gold Films
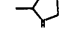
Epitaxial gold films supported on mica were purchased from Georg Albert at the Physical Chemistry Institute of the University of Heidelberg, Germany. Although supplied as atomically flat, it was found that the films contained large defects, including fissures on scales used for micron-scale patterning, but invisible to the eye. Therefore, flame annealing was used to consolidate the film and promote the formation of atomic terraces. This will be described in subsection 2.4.2 on page 91.

2.3.3 Biological Molecules

2.3.3.1 LH2

LH2 'wildtype' complex from wildtype *Rhodobacter sphaeroides* 2.4.1. was a gift from Drs. John Olsen and John Timney of the Hunter research group, Department of Molecular Biology and Biotechnology, *this university*. LH2 cysteine mutant complex was also used (cysteine replacing threonine at the N terminus of the β polypeptide, this is shown in **figure 2.3.23** on the following page), and was extracted from a *Rba. sphaeroides* mutant (mutagenesis carried out by Drs. John Timney and John Olsen). The bacterium was grown photosynthetically at low light (5 W m^{-2}) before disruption through a French press at a pressure of 18,000 psi. The resulting fluid was centrifuged for 30 min at 100,000 g to remove unbroken cells and other debris. This was further centrifuged at 200,000 g for 2 h to form a pellet of material consisting primarily of the intracytoplasmic mebrane. This was resuspended in a working buffer of 20 mM *tris*(hydroxymethyl)-aminomethane ('Tris')at pH 8. The membrane material was solubilised with 4 % LDAO for 45 min. Insoluble material was removed by further centriguation at 200,000g for 1 h. The solubilized LH2 was then applied to a DEAE (Sigma) ion exchange column and eluted using a 0–250 mM NaCl gradient, in working buffer plus 0.1 % LDAO. The LH2 was then applied to a Resource Q column (GE healthcare) with a NaCl gradient 0f 0–500 mM. The fraction yielded at a salt concentration of ~300 mM was collected, and then this was filtered through a Superdex 200 gel filtration column (GE healthcare). The quality of eluted fractions was monitored by spectrographic methods and those fractions with a ratio of absorbance peaks 850 nm : 220 nm >3.4 were used.

Figure 2.3.23　Mutagenesis of LH2 complex, adapted from a cartoon originally drawn by Dr. John Olsen

Label	Amino Acid	R
Non-polar residues		
G	Glycine	–H
A	Alanine	–CH_3
V	Valine	–$CH(CH_2)_2$
L	Leucine	–$CH_2CH(CH_2)_2$
I	Isoleucine	–$CH(CH_3)(CH_2CH_3)$
M	Methionine	–$(CH_2)_2SCH_3$
F	Phenylalanine	–CH_2Ph
W	Tryptophan	(structure)
P	Proline	(structure)

Label	Amino Acid	R
Polar residues		
S	Serine	–CH_2OH
T	Threonine	–$CH(CH_3)OH$
N	Asparagine	–CH_2CONH_2
Q	Glutamine	–$(CH_2)_2CONH_2$
Charged, +ve		
K	Lysine	–$(CH_2)_4NH_2$
R	Arginine	–$(CH_2)_5NHNH_2$
Charged, –ve		
D	Aspartic acid	–CH_2COOH
E	Glutamic acid	–$(CH_2)_2COOH$
Cysteine mutagenesis		
C	Cysteine	–CH_2SH

2.3.3.2　Other biological molecules

Streptavidin, bovine serum albumin (BSA) and biotinylated anti-rabbit immunoglobulin G (IgG) were purchased from Sigma-Aldrich. Acyl carrier protein and Phosphopantethienyl Transferase from *Bacillus circulans* were a gift from Dr. Lu Shin Wong, University of Manchester Interdiscipliniary Science Centre.

2.3.4 Biological Buffer and Immobilisation Chemistries

Phosphate buffered saline ('PBS') tablets, glutaraldehyde ('GA') (50 % aqueous), trifluoroacetic anhydride ('TFAA'), *N*-(3-Dimethylaminopropyl)-*N*-ethylcarbodiimide ('EDC') and *N*-hydroxysuccinimide ('NHS') were all obtained from Sigma-Aldrich.

2.4 Metal film preparation

2.4.1 Evaporation of Metals

Metal films were deposited onto piranha-cleaned coverlips by evaporation under vacuum (carried out using a BOC Edwards Auto 306 Evaporator, operating at 10^{-7}–10^{-6} mbar). Typically, a primer layer ($\sim$2 nm) was first deposited prior to the desired substrate, in order to promote adhesion: Chromium for gold and silver, and titanium for palladium films. Following deposition of the primer layer, the vacuum was allowed to settle and return to a pressure similar to that before initial evaporation. Tungsten baskets were used for the Cr chips, molybdenum boats were used for the evaporation of Au and Ag wire, and tungsten boats were used for titanium and palladium, which require higher temperatures. Rate of film deposition and cumulative thickness were measured by the change in the resonant frequency of a quartz crystal; density of materials were parameterised, and thicknesses of films determined by topographical AFM were regularly used to calibrate the sensor. Evaporation rates were typically 0.01–0.05 nm s^{-1} for Au and Ag, and 0.2 nm s^{-1} for Pd; the latter material required 'flashing' onto the surface to prevent the boat from being subjected to prolonged periods of excessive temperatures, which could cause it to break. After the film reached the desired thickness, the films so-formed were allowed to cool in the evaporator ($\sim$3 h for Pd, $\sim$2 h for Ag, 1–2 h for Au).

2.4.2 Flame Annealing Epitaxial Films

Epitaxial gold as received was washed with IPA and HPLC grade ethanol before being carefully dried under a stream of hydrogen. A butane flame was passed over the surface of the gold with an oscillatory motion at as steady a rate as possible, with the flame approximately 2 cm from the surface. This was done is a darkened room so that, once the film reached the very dullest red colour, the heating of the film could be maintained at that temperature for at least 30 s. Once carried out, these films were considered 'flame-annealed' and were used, primarily for the deposition of biological molecules from solution.

2.5   Organothiolate SAM formation

Following venting to nitrogen, the films were removed within 1–2 min and immediately immersed in ethanolic solutions of the appropriate thiol. Again, extra care was taken in the case of Pd, as it was thought the the increased susceptibility of Pd to aerial oxidation could give rise to unstable films. In the case of some gold films used for SPR experiments, samples were cut using a diamond scribe to appropriate dimensions (12 mm × 9 mm) before immersion in ethanolic solutions of appropriate thiol. Au metal films were typically immersed in 1 mM solutions of thiol for a minimum of 18 h before usage, and were used within 1–2 weeks. Pd films were given longer to form (typically at least 24 h), were kept in a nitrogen atmosphere and were used within 1 week.

2.6   Preparation of Silane SAMs

Piranha-cleaned, *n*-type (boron-doped) Si(111) wafers were cut to size using a diamond scribe and cleaned using the standard RCA-1 protocol (desribed in subsection 2.2.1 on page 88), which passivates the silicon with hydroxy groups. Substrates so-prepared were placed in Schlenk tubes and attached to a Schlenk line, and the vessels were evacuated and then refilled with nitrogen 3 times. After a final evacuation, the tap to each tube was closed, and a volume of Grubbs' catalyst-dried toluene was introduced via injection by a syringe penetrating the rubber seal. To this was added 10 % by volume of 50 mM stock solution of silane, to produce 5 mM silane solutions. A positive pressure of nitrogen was re-introduced and the solutions containing the substrates were sonicated for 5 min to promote the formation of ordered monolayers. SAMs were left to form for 90–120 minutes. After this, each SAM so-formed was rinsed with ethanol, dried under a stream of nitrogen, then rinsed with toluene, before a further sonication in toluene for 15 minutes. These were then dried in a stream of nitrogen, and baked in a vacuum of oven (>1020 mbar negative pressure) for 1 h at 120), and left to cool under vacuum. Following removal, these were kept in sealed tubes in the dark before use (~1 week).

2.7 Patterning

2.7.1 Photolithography

2.7.1.1 Micron-scale photolithography

Copper electron microscope grids, used as photolithography masks (600–2000 mesh, 3.05 mm diameter) were obtained from Agar scientific. These were used to produce micron-scale patterns by the photooxidation of SAMs, as depicted in figure 1.4.1 on page 55. They were also used for the spatial photodegradation of OEO SAMs presented in Chapter 3. Photolithography was primarily carried out using a Coherent FreD 300C argon ion laser (Coherent UK Ltd., Ely, UK). The fundamental wavelength was halved (*i.e.* 'frequency-doubled') by the use of a Brewster-cut beta barium borate crystal; this is a second harmonic generation (SHG) mode, hence the laser profile is not gaussian, but features fringes to either side of a central spot. In order to ensure a homogeneous exposure through the mask (thus optimising contrast between the exposed and masked regions), the beam was expanded on the patterning stage so that the central spot was the same size as the mask. Nominal power used for micron-scale photolithography was 100 mW, but this was often reduced for photochemical kinetics experiments.

2.7.1.2 Scanning Near-field Photolithography (SNP)

A combination of commercially sourced probes and 'home-made' probes were used for nanoscale lithography. Commercially-sourced probes were purchased from Veeco Ltd. (Cambridge, UK) or Jasco UK Ltd. (Great Dunmow, UK), and were specified as being transparent to 244 nm UV light. For the home-made probes, a UV-transparent fused silica optical fibre was etched to a cone at one end by immersion in HF, before coating in Al by rapid rotation in the vacuum evaporator. To produce an aperture, the probes was gently impacted onto a surface. It was found that it was possible to create apertures of approximately the same diameter as commerically-sourced probes (50–80 nm). These were then attached to silicon chips to which had been pre-mounted (commercially-sourced; Veeco, UK Ltd.) 92 kHz tuning forks, which allows the distance between the stylus and surface to be maintained in the near-field, by the use of a shear-force feedback system. The chips were compatible with the Aurora II and III NSOM systems used to control the lithography probes, and were of the same type as the commercially-sourced probes. Lithography was controlled using Veeco Nanolithography v. 1.2.1 and SPM tools v. 6.0.3 software.

For the source, the Coherent FreD 300C laser, as described in 2.7.1.1 on the previous page was used. Nominal power for nanolithography was 1–4 mW, with a writing speed of 0.1–0.5 $\mu m\,s^{-1}$. The output (set for setting up the arrangement to 1 mW) was coupled to the fibre by passing the beam, in an opaque enclosure, through a 15 cm focal-length divergent lens, onto the cleaved fibre. This was done in very dim lighting, so that the optimal position of the fibre (judged when the end of the fibre was seen to pick up a glow) could be achieved, which was done by carefully adjusting an XYZ stage. The SPM tools software was used to calibrate the feedback of the tuning fork to a setpoint of −30−−32 nA. After bringing the probe into contact with the surface at a setpoint of −64 nA, it was moved into the 'near-field' by adding 0.8 to the average signal. The lithography software was then used to write the desired features.

2.7.2   Biomolecule Immobilisation

2.7.2.1   Streptavidin/Biotin

For streptavidin (Chapter 3), films of OEO-terminated thiol were immersed in nanopure water for approximately $\frac{1}{2}$ h to allow penetration of water molecules into the oligoether moieties. As detailed in 1.2.3.4 on page 29, this is thought to improve resistance to biological molecules. Following photopatterning, samples were immediately immersed into solutions of streptavidin (5 $\mu g\,mL^{-1}$, in aqueous 0.1 mM phosphate-buffered saline ('PBS') solution) for 20 min. These were then, if necessary, transferred into a 5 $\mu g\,mL^{-1}$ solution of biotinylated IgG in 0.1 mM PBS. Prior to imaging, these were washed with PBS buffer, followed by 0.25 mM aqueous ammonium acetate solution, then nanopure water, and were then dried under a stream of nitrogen.

For LH2 (Chapter 4), immobilisation was carried out using carbodiimide chemistry, which allows the formation of an 'activated ester'. This is shown in **figure 2.7.1** on the next page. The N is α to two carbonyl groups and thus aims to be sp^2-hybridised (it has a lone pair available for conjugated π-bonding), but is prevented from adopting this geometry due to steric constraints. Biomolecules with exposed lysine residues (or indeed any molecule that contains an sp^3-hybridised nitrogen with an available lone pair) may be attached using this method, as there is a thermodynamic impetus to remove the sterically constrained leaving group in favour of another species that allows greater p-orbital overlap within the peptide link. For the purpose of the work presented in this thesis, the carbodiimide and N-hydroxysuccinimide were dissolved in HPLC grade ethanol at a concentration of 20 mM. It is thought that aqueous media would hydrolyse the activated ester fairly rapidly after its formation. For topgraphical AFM imaging, samples activated in this way were immersed into 6.5 $\mu g\,mL^{-1}$ of LH2 in

20 mM Tris, 0.1 % (wt.) LDAO buffer for 5 min, before removal and careful washing with Tris/LDAO buffer, 1 % (wt.) aqueous ammonium acetate solution, and nanopure water, before being dried under a stream of nitrogen.

For spectrographic measurements, samples were quickly transferred from LH2-LDAO buffer solution to 'clean' LDAO to remove excess complexes. Samples were then dried under a stream of helium (to 'push' excess buffer to the side of the sample) before being glued to a copper mount in a high-vacuum cryostat. It was found that washing with water compromised the optical functionality of the complexes (presumably because it washes away the magnesium in the bacteriochlorophylls).
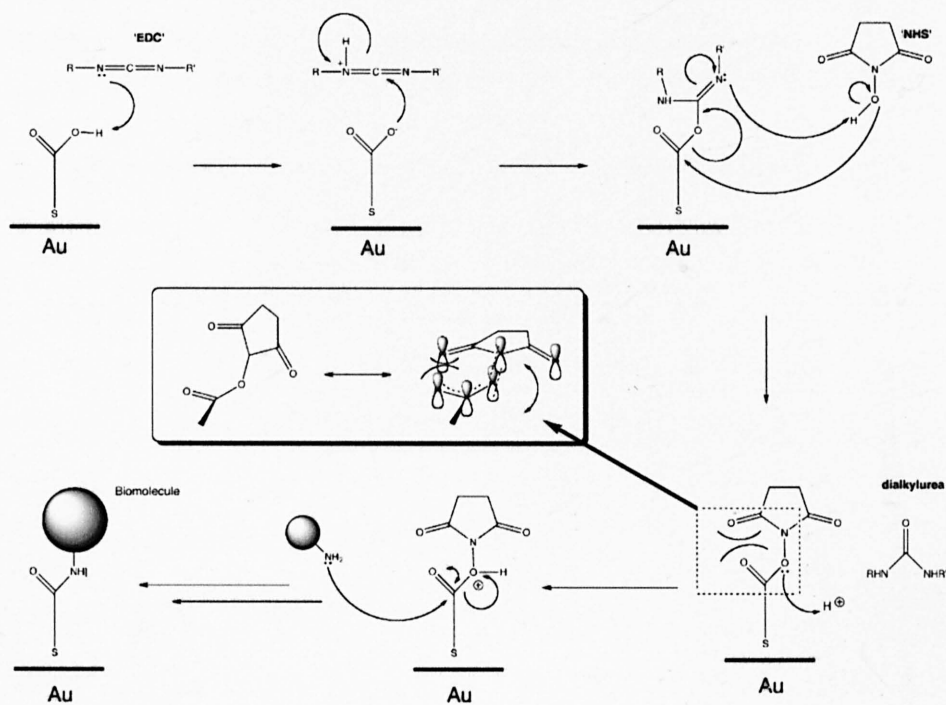

Figure 2.7.1 'EDC-NHS' Reaction

2.8 Instrumentation and Methods for Analysis

2.8.1 Surface Potential Measurements

Surface potentials were measured using a home-built Kelvin probe, loaned to the author by Dr. Kevin Critchley. The circuit was constructed to the specifications of the Zisman arrangement (see Chapter 1, on page 40). A Keighley system electrometer was used to measure V_b, and an EG&G lock-in amplifier was used to produce a workable signal. The modulation of the tip vibration was carried out by the use of a Jena piezo controller. The platinum tip (area 2.7 mm ^{2}) was vibrated at a frequency of 800 Hz, using a piezoactuator (P200-16, Linos Photonics) to create the required alternating current.

2.8.2 Contact Angle Measurements

Contact angle measurements were made using a Rame-Hart contact angle goniometer (Rame-Hart, New Jersey, USA). Droplets (20–50 μL) of 'nanopure' water (18.2 MΩ, Elgar purification system) were touched onto SAMs by the careful lowering of a Hamilton syringe, allowing precise volumes to be deposited. The goniometry technique is explained in subsection 1.3.1 on page 34.

2.8.3 X-Ray Photoelectron Spectroscopy

The instrument used for the acquisition of XPS spectra was a Kratos Axis Ultra X-Ray Photoelectron Spectrometer with Delay Line Detector (DLD) fitted, a photograph of which is shown in **figure 2.8.1** on the following page. X-rays are formed by the targetting of an Al source (the anode) by the heating of a filament (the cathode); a current of 6.0 mA is used. HT voltage is set to 15 kV with an X-Ray power of 90 W. The X-Rays are monochromated Al K_α ($h\nu$=1486.6 eV). The sample chamber used in the analysis is a UHV system obtaining a base pressure of 10^{-10} mbar. Survey scan ('wide') spectra were collected at 160 eV, while high resolution spectra for curve fitting (*e.g.* for the kinetics data presented herein) were collected at 20 eV. XPS runs were set up by Nick Reynolds and Tracie Whittle.

2.8.4 Atomic Force Microscopy

Lateral force images and intermittent contact ('Tapping') mode images were acquired using a Digital Instruments Nanoscope Multimode IIIa AFM. Images presented in this thesis were acquired in air. For
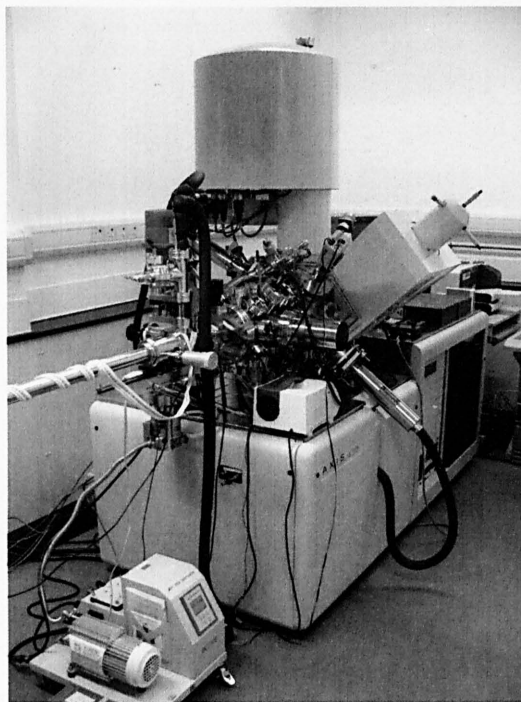
Figure 2.8.1　Kratos Axis DLD Ultra 400

lateral force images, a Si_3N_4 probe was used (nominal force constant $0.06\,N\,m^{-1}$), while for tapping mode images, a silicon probe (nominal force constant $30\,N\,m^{-1}$, f_0=232–264 kHz) was used.

2.8.5　Surface Plasmon Resonance

For SPR measurements, a commercial Biacore 3000 SPR spectrometer was used (Biacore AB, Upsalla, Sweden). Typical biomolecule conentrations in appropriate buffer (as detailed in each case) were $5\,\mu g\,mL^{-1}$ and the flow rate (in a buffer-matched carrier stream) was either $10\,\mu L\,min^{-1}$ or $20\,\mu L\,min^{-1}$, depending on the availability of the protein. It was found that the faster flow rate produced smoother traces, although the slower rate did not preclude an assessment of the affinity of the biomolecule for the surface.

2.8.6　Spectrographic Measurements

Optical measurements were made using an optical setup designed by Dr. Luke Wilson*. The excitation source consisted of a 800 nm laser photodiode, the output of which was reflected by a mirror onto a vertically-ratcheted stack which could be moved up and down to focus the excitation spot on the

*Department of Physics and Astronomy, University of Sheffield

97

sample. Power to the photodiode was modulated using a Keithley model 2400 general source-meter. Typical nominal output was 80–100 mW. For the spectral measurements, light from the sample was passed through a long pass (>825 nm) filter, down an optical fibre to a Pixis (Princeton, NJ, USA) charge coupled device (CCD) unit. For measurements of photoluminescence (fluorescence) intensity, the CCD unit was switched for an avalanche photodiode (APD). The signal was amplified using an EG&G lock-in amplifier. For spatially resolved measurements, a the vertical optical stack could be moved in the XY plane (that of the sample) by a computer controlled piezotransducer. The software used to do this was created in the LabView development system by Dr. Luke Wilson and Pu Xian*.

List of Figures in Chapter 2

---

*now in the Department of Microbiology and Biotechnology, University of Sheffield; previously in the Department of Physics and Astronomy, University of Sheffield

Chapter 3

Photochemical Modification of

Self-Assembled Monolayers

Photochemical Modification of SAMs Contents

3.1 Introduction

3.1.1 Photooxidation of SAMs

It has been said that, in microelectronics, everything scales exponentially[1]. This applies as much to fabrication costs as it does to the well-known exponential increase in transistor density on a computer chip*. A significant obstacle to producing ever smaller features is the development of photoresists that have chromophores opaque to ever-shorter wavelength UV light. As described in subsection 1.4.3.4 on page 56, the devlopment of novel photolithographic tools provide a means to circumvent the diffraction limit that augments methods being presently explored by the semiconductor industry†. In turn, these have required and driven the development of photoresists that are capable of achieving nanoscale resolution.

SAMs of organosulfur compounds on a variety of substrates—in particular gold, silver and palladium—are effective photoresists. They can be used to form patterns and, therefore, structured systems. Crucially, their ability to provide effective photoresists for nanoscale lithography has been demonstrated. Kinetic studies reveal that the rate of photooxidation of SAMs depends both upon the length of the alkyl chain and the nature of the ω functionality. The first area of investigation with which this chapter is concerned is the mechanism of photooxidation of organosulfur SAMs on gold, silver and palladium substrates.

Previous work[3] has indicated that the rates of photooxidation of M–SR SAMs are dependent on the alkyl chain length of the adsorbate, the nature of the terminal group, and the nature of the substrate. Longer SAMs are more crystalline, and it was proposed that this might impede the diffusion of the oxidative species down to the sulfur. Conversely, it was proposed that the liquid-like state of shorter SAMs allows relatively unimpeded diffusion of the oxidative species. However, the nature of the ω functionality too had an observable consequence: carboxylic acid-terminated SAMs had been shown to oxidise faster than methyl-terminated SAMs.

The mechanism of photooxidation of M–SR SAMs has historically been the subject of some debate. Early XPS and SIMS work by Tarvlov, Burgess and Gillen indicated that photooxidation was marked

---

*In 1965, Gordon Moore predicted the doubling of transistor density every 12 months[2]—later amended to every 18 months—a relationship which has more or less held true since then.

†*although not exclusively*—electron beam (e-beam) lithography has produced some of the highest resolution lithographic features to date

by a shift in S_{2p} binding energy from 162–167 eV[4], and contemporaneous results published by Huang and Hemminger were supportive of this hypothesis as being the chemical change that occurs[5]. The latter group theorized that incident radiation on the substrate caused the transmission of "hot electrons from the metal to either the RS species or to coadsorbed O_2". 'Hot' or sub-vacuum electrons may be produced instead of or alongside photoelectrons in a wide distribution of energies by incident electromagnetic radiation (EMR) of sufficient photon energy[6,7]. Rieley *et al.* proposed that hot electrons might cause the formation of O_2^- at or near the surface, and that this was the oxidative species[7]. In this model, it is of note, the rate-limiting step is the formation of an activated oxygen species. That hot electrons might act on the R–S bond was not considered.

A study of aerial SAM oxidation (in the dark) by Schoenfisch and Pemberton[8] suggested that ozone was the likely oxidative agent in the absence of UV light. Later studies of SAMs exposed to ozone by Bohn and co-workers (Zhang *et al.*[9,10]) led the group to make the assertion that ozone, which would require a source of <200 nm light to be formed from ambient oxygen, was necessary for photooxidation to occur, on *all* SAMs. Again, it is the formation of a high-energy oxygen species that is considered to be the rate-limiting step. Their study earlier study centred on $C_{15}CH_3$ SAMs, and methyl-terminated SAMs had been shown to photooxidise slower than acid-terminated SAMs[3].

Zhang *et al.*'s assertion was refuted by work carried out by Brewer *et al.*[11], in which the same lamp used for the studies presented in this thesis, supplied as ozone-free* and emitting principally at 254 nm, was demonstrated to rapidly photoxidise a $C_{10}COOH$ SAM, showing that ozone was not necessary for photooxidation to occur. However, in-keeping with Zhang *et al.*'s findings, the extent of photooxidation of a $C_{11}CH_3$ SAM over a comparable period was much lower, indicating that ozone may be required for the rapid photooxidation of methyl-terminated SAMs. Moreover, the results suggest that more than one process may be occurring when, as in earlier studies, a wide-spectrum source is used (*e.g.* a mercury arc lamp).

The two principal UV sources used to photo-oxidise M–SR SAMs are a 254 nm UV lamp and a 244 nm laser. A simple calculation:

$$E = \frac{hc}{\lambda} \qquad (3.1.1)$$

—where h is Planck's constant (6.626×10^{-34} J s), c is the speed of light in a vacuum (2.998×10^8 m s^{-1}), and λ is the wavelength of the light (m)—indicates that the former emits light with a photon energy E of 7.82×10^{-19} J $\equiv$ 4.88 eV, while the latter emits light with a photon energy of 8.14×10^{-19} J $\equiv$ 5.08 eV;

---

*confirmed by N.B. by use of a Draeger tube: O_3 was undectable at the lower limit of sensitivity (0.005 ppm).

determinations of Φ_{Au} are often given as substantially higher, *e.g.* 5.31 eV[12], although complimentary techniques for Φ determination are often not as accurate as the CPD method. According to the photo-electric criterion, equation (1.3.9) on page 38, no electrons within the Au lattice should be made mobile by incident radiation of insufficient energy. However, it has been shown that adsorbed thin films on metals impose a so-called 'surface potential' at the interface, which may alter the work function of the substrate[13,14]. The origins of surface potentials, denoted ΔV, are directional dipoles imposed by the many SAM molecules in a thin film acting *en masse*; like contact angles, they are the macroscopic consequence of cumulative microscopic properties. The cause of the directional polarity, the difference in electronegativity between the polar headgroup and carbon chain, is often (but not always) augmented by the presence of a heterogeneous ω group with its own polarity; polar groups might also be present at other positions along the chain. Due to the uniformity of the SAM film, the polar components can be treated as stacked dipole sheets.

In order to ascertain to what extent the ω functionality affects the rate of photooxidation, it was therefore neccessary to undertake a systematic study of the surface potentials imposed by a range of SAMs. Particular consideration was given to those SAMs (*e.g.* Au–SR) that have been previously used to create patterns at the micro– and nanometre length scales; these studies were put in context by an extension of the investigation to include Ag–SR and Pd–SR SAMs. Pd–SR SAMs have been lauded for their simultaneous biological and CMOS compatibilities, and viability as high resolution etch resists, as previously discussed. However, work reported by Love *et al.*[15] has indicated that Pd–SR SAMs have structures that are more complex than analagous films on gold. Fundamental studies of the photooxidation of Pd–SR SAMs are therefore crucial in developing fabrication methods, and this was explored.

3.1.2   Photodegradation of OEO-SAMs

3.1.2.1   Investigation into Surface Composition as a Function of Exposure to 244 nm Light

Oligo(ethylene oxide)-terminated SAMs ('OEO-SAMs') have been widely adopted as protein-resistant films, and have been demonstrated as suitable SAMs for the fabrication of biomolecular patterns. However, previous work, such as that reported by Monatague *et al.*[16] has indicated that photooxidation of OEO-SAMs might be accompanied by a competing process of photodegradation occurring within the oligoether moiety. XPS results presented in the aforementioned publication indicate that the functional groups formed by photodegradation are carboxylic acids and aldehydes. Such functionalities have

previously been shown to be useful in immobilising biological structures. It was therefore decided that this merited further exploration.

3.1.2.2   Biological Attachment to Photodegraded OEO-SAMs

As has been previously stated, the integration of biological units—proteins, nucleic acids, protein complexes—into artificial structures is only really successful if their functionality is retained. For many such units, functionality is very much dependent on the architecture and relative geometry of certain domains within the biomolecule, and so immobilisation chemistries need to be sensitive enough not to disrupt inter-domain interactions, yet efficient enough to covalently attach and secure the biological unit.

The suitability of SAMs to the study of molecular recognition has inspired much work in the growing field of biointerfaces. One of the most widely-studied cases of molecular recognition is the highly specific affinity of streptavidin for biotin[17]. Because the recognition that takes place is dependent on the existence of domains in streptavidin that form a 'hollow' that can envelop biotin (thus stabilising both structures), perturbation of the geometry of the site leads to loss of this biological functionality. To assess whether immobilisation of streptavidin is successful according to tthe criterion of retained functionality, therefore, the attachment of a biotinylated protein was explored by AFM.

3.1.3   Glutaraldehyde Coupling of Thiols to Mercaptosiloxane SAMs

A third area with which this chapter is concerned presented itself during investigations into OEO-SAM photodegradation. A serendipitous discovery (presented in this chapter) indicated that thiols would, in fact, covalently bind to aldehydes. The availability of thiol-terminated silanes presented an opportunity to investigate this attachment chemistry as a possible means to attach thiols, by using a readily-available linker molecule. The broad range of readily available thiols could, it is proposed, be translated onto silicon, and would allow a greater degree of tunability than is presently easily afforded by silane systems. The potential of this has also been explored.

3.2 Experimental Details

3.2.1 Photooxidation of SAMs

3.2.1.1 Measurements of Surface Potentials of SAMs

Au–SR SAMs were formed according the procedure detailed in section 2.4 on page 91. SAMs of Ag–SR were also made; determination of their surface potentials provided a comparison with Au–SR SAMs, and rates of photooxidation of Ag–SR SAMs had also been prevoiusly determined. Measurements were made using a Kelvin probe apparatus built and loaned to the author by Dr. Kevin Critchley*. A schematic is shown in figure 1.3.4 on page 40. For each sample, a total of six measurements were made at different locations on the SAM surface, and three samples, made on different days, were measured to determine the SAM surface potential (ΔV). For Au–SR SAMs, results were normalized to $\Delta V_{C_{11}CH_3}=+527\,mV$ against a large number of measurements made previously; the average discrepancy (15.4 mV) was within 1σ for all SAMs. Fluctuations and deviations occur because the parallel plate method is sensitive to the morphology of the polycrystalline film. In addition, external radiation in the laboratory—even cosmic rays—can cause substantial fluctuations. In the case of Ag–SR SAMs, additional care was taken in preparation, as detailed in Chapter 2. In order to measure the work function of a virgin Ag film, Φ_{Ag}, it was assumed that an adventitious oxide adlayer would form under ambient conditions, and so the 6 samples analysed in its determination were immersed in 0.25 M ferric nitrate solution for approximately 20 s prior to washing with deionised (18.2 MΩ) water and HPLC grade ethanol, before drying under a stream of helium immediately before measurement.

For the surface modification to produce a perfluorinated surface, a solution of trifluoroacetic anhydride (TFAA) (50 mM) and triethylamine (TEA) (50 mM) in anhydrous tetrahydrofuran (THF) was prepared and a $C_{11}OH$ SAM was immersed in it for 1 h. Samples were rinsed with anhydrous THF before measurement of ΔV.

For the measurement of the work function of bare Pd, the sample was immersed in 0.5 M ferric (III) chloride solution, followed by quick washing with water and ethanol, and drying under a stream of helium.

Φ_{Eff} were determined by considering the manner in which the surface potential imposed by the adsorbate affects the work function of the underlying metal. Evans and Ulman[13] considered the SAM to be a

---

*then at the University of Leeds, School of Physics and Astronomy

planar, dipole sheet, "with a sheet of negative charges residing close to the metal/monolayer interface and a sheet of positive charges closer to the monolayer/air interface". Their work showed that surface potential ΔV increases linearly with alkyl chain length for *n*-alkanethiolate SAMs. The directionality of the dipole so-formed acts like an electrostatic gradient, so that the methyl-terminated SAMs, which are effectively $\delta+$ at the ω position, expedite transmission of photoelectrons from the Fermi level to the vacuum level, whereas $\delta-$ve groups (like carboxylic acids) impede their ejection into the vacuum. Equation (1.3.10) on page 38 states that

$$\phi = (\Phi_B - \Phi_A)/e$$

where Φ is the workfunction in eV, e is the electron charge (1.602×10^{-19} C) and ϕ is the contact potential difference; B represents the reference electrode (Pt tip) and A is the sample. When the above equation is considered alongside equation (1.3.17) on page 40

$$\Delta V = \phi^* - \phi$$

it can be seen that *a measured increase in contact potential difference ϕ of a bare metal, once it has been modified by the presence of a SAM (represented here as ϕ^*), implies that the SAM imposes a positive surface potential ΔV, which means that the adsorbate must have decreased the work function Φ;* conversely, *a value ϕ^* lower than ϕ indicates a negative ΔV, which effectively increases the work function.* In the experimental setup used to determine the surface potential, a 'backing potential' V_b is used to null ϕ, as per equations 1.3.14 to 1.3.16 on page 40, and the two values are related thus:

$$\phi = -V_b$$

Due to the relationship between ϕ and Φ given in equation (1.3.10) on page 38 and repeated on the current page, the following relationship can be drawn:

$$-V_b \cdot e + \Phi = \Phi_{\text{Eff}} \tag{3.2.1}$$

which means in practical terms that **the modulus of the backing voltage, measured by a voltmeter (in Volts), can be deducted from the work function modulus (in electronvolts) to give an effective workfunction, Φ_{Eff}.**

3.2.1.2   Determination of photooxidation kinetics of Pd–SR SAMs

Samples of Pd–SR SAMs, cut into approximately 22×10 mm rectangles*, were exposed to a 254 nm lamp for a series of different durations. For the measurement of contact angles, a Rame-Hart contact angle goniometer was used. The technique of contact angle goniometry is described in subsection 1.3.1 on page 34. For each sample, three contact angle measurements were made following exposure and subsequent immersion in 1 mM of a contrasting thiol for 2 h, and these were repeated in triplicate with SAMs made on different days. 'Contrasting' thiols were chosen to maximise the contact angle difference: Methyl SAMs were immersed in ethanolic solutions of carboxylic-acid terminated thiols of approximately equal hydrocarbon chain length, and acid– and hydroxy-terminated SAMs were immersed in methyl-terminated thiols of the same length[†]. Higher concentrations of contrasting thiols were not used because of the suggestion that this may invoke elevated exchange with unirradiated SAM molecules, as previously reported by Biebuyck and Whitesides[18], and thus may add an unnecessary complexity to the results. SAMs were made as detailed in Chapter 2, and were used within 1–2 weeks. During the experiment, the integrated power of the lamp was measured to be $100 \pm 10 \mu$W over the range 249–259 nm using a Coherent Fieldmaster power meter.

In order to solve f values for Cassie's equation (equation (1.3.7) on page 36) to determine the extent of SAM replacement, the solve function in MATHEMATICA[19] was used. The method is shown in the notes at the end of this chapter[20]. This allows the determination of f values to be carried out quickly and accurately.

For analysis of surface composition by XPS, samples were removed from 1 mM ethanolic solutions of thiol immitaely prior to being placed under the lamp. Commencement of exposure was staggered, so that all samples would be ready at this same time, *i.e.* a 5 min exposure would be placed under the lamp 5 min before the end of the experiment, when all SAMs were then placed in 1 mM ethanolic solutions of 'contrasting' thiol for 2 h prior to being removed and taken for XPS analysis (a $\sim$10 min journey). The purpose of this was to displace the weakly-physisorbed sulfonates, and reinstate the structural integrity of the film; it has been demonstrated[21] that short SAMs especially may desorb under vacuum conditions. Further to this, the alkyl chains of Au–SR SAMs at sub-monolayer coverage have been shown to lie down, which could frustate XPS measurements by altering the relative attenuation of ejected photoelectrons as compared with molecules in their normal 'standing up' orientation.

---

*22 mm is the width of a coverslip; cutting samples into elongated rectangles allows facile measurement of the contact angle at three positions, while minimizing sample handling, which could compromise the integrity of the SAM

[†]SAMs of approximately equal length were chosen because disparities in hydrocarbon chain length can cause a longer SAM to eclipse a shorter one, as detailed in Chapter 1, on page 16.

Spectra were collected at a pass energy of 20 eV for the 'narrow' high-resolution single element scans (principally C_{1s}, plus Pd_{3d} to provide a signal against which the carbon areas could be normalised). Additionally, the quality of films were monitored by the acquisition of survey scans carried out at 160 eV.

For each SAM, XPS spectra of the same time points measured in the contact angle experiment were collected. In each case, a characteristic curve in the C_{1s} spectrum that is representative of the SAM being studied (denoted as SAM_A) was chosen, and the change in the relative proportion of area that this curve contributes to the total C_{1s} area is considered. This allows a determination of the mole fraction χ_A, analagous to $1 - f$ from the contact angle data (where f is the fraction equivalent to χ_B). Thus, if P is the relative area of a component of the C_{1s} core level of SAM_A in the photooxidation-replacement reaction:

$$SAM_A \xrightarrow{time \times h\nu} \xrightarrow{HSR_B} SAM_{nA+mB}$$
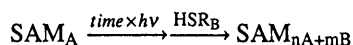
and the date is normalised so that $P_{t=0}=1$, then for $[P]_{t>0}$

$$\chi_A = \frac{[P]_t}{[P]_{t=0}} \tag{3.2.2}$$

Again, values for χ_A given are mean values from three seperate determinations. For the methyl-terminated C_3CH_3 and $C_{11}CH_3$ SAMs, it was acknowledged that the aliphatic C-$\underline{C}$-C environment is also represented in the SAMs that replace the initial monolayers following photooxidation and immersion in a contrasting thiol, and so were not *uniquely* characteristic of these particular films. In both cases, the contrasting thiol chosen featured carboxylic acid ω functionality, and so the relative fraction of the O-$\underline{C}$=O curve in the the binary SAM's C_{1s} spectrum was considered against the fraction that the O-$\underline{C}$=O curve contributes to the area of the virgin carboxylic acid-containing SAM's C_{1s} spectrum. Ratios were then taken of the fraction in the binary SAM to the fraction in the virgin SAM, to determine the extent of replacement. This may be summarised:

$$\chi(C_nCH_3) = 1 - \frac{[O\text{-}\underline{C}\text{=}O]/C_{1S}}{[O\text{-}\underline{C}\text{=}O]^*_{t=0}/C_{1S}} \tag{3.2.3}$$

where $[C\text{-}\underline{C}\text{=}O]/C_{1s}$ is the fractional contribution of the carboxylic acid group of the replacing, acid-terminated thiol to the total C_{1s} core levelspectrum and $[O\text{-}\underline{C}\text{=}O]^*_{t=0}/C_{1s}$ is the size of that fractional contribution in a virgin C_nCOOH SAM.

3.2.2   Photodegradation of OEO-SAMs

3.2.2.1   Investigation into Surface Composition as a Function of Exposure to 244 nm Light

$HSC_{11}(EO)_3OH$ had been previously synthesized according to a method reported by Pale-Grosdemange *et al.*[22]. SAMs were formed of the EO-thiolate by incubation in de-gassed ethanol for ≥ 18 h. As the suggestion that competing processes may occur was first indicated by patterning processes made using the laser[16], attempts to quantify the effect were also initially made using the laser. That the SHG mode for the frequency-doubled argon-ion laser produces a beam profile that deviates from the Gaussian TEM_{00}*, as previously detailed in Chapter 2, should be noted. The large central spot in the beam profile was expanded by removal of the objective lens in the patterning stage, producing an irradiated region of ~ 1 cm^2 in area. Nominal power was adjusted in order to allow easy calculation of the dosage, but was kept constant for any one experiment (10 mW, 50 mW and 100 mW were used). The power used for each batch is indicated in the plotted results. XPS spectra of the C_{1s} and Au_{4f} regions were collected at 20 eV for the unirradiated OEO-SAM and for OEO-SAMs exposed to a range of durations of exposure to 244 nm UV laser light.

Additionally, the potential for functionalisation of the new surface chemistry was investigated. Indications that aldehydes were formed during the photodegradation process were investigated by the introduction of a trifluoroethylamine. Previous work[†] has shown that primary amines can be attached by aldehydes. Photodegraded OEO-SAMs (dosage=1.2 J cm^{-2}) were immersed in 1 mM ethanolic (HPLC grade) solutions of trifluoethylamine to which was added HCl[‡] to a concentration 10^{-5} mol dm^{-3} (thus achieving pH 5) for 20 min, and were then removed, washed with HPLC grade ethanol and analysed by XPS. C_{1s} and F_{1s} spectra were collected at pass energies of 20 eV, alongside Au_{4f} spectra also at 20 eV in order to provide a signal against which they were normalised. They were then analysed using CASAXPS software to determine their surface compositions.

3.2.2.2   Biological Attachment to Photodegraded OEO-SAMs

An investigation of photodegraded OEO-SAMs as potential biomolecule immobilisation templates was carried out. Immobilisation of strepavidin was assessed by measured topgraphical 'height' differences by atomic force microscopy. SAMs of OEO-terminated thiol on gold were irradiated by a 244 nm laser

---

*Transverse Electrical and Magnetic mode — '00' is the fundamental transverse mode of the laser resonator, and has the same form as a gaussian beam

†See the *discussion*: A mechanism for the attachment of 1° amines is shown in figure 3.4.2 on page 139

‡imine formation is optimal between pH 4–5

set at a nominal power output of 10 mW through a copper mask for 2 min with a laser spot of area

0.25 cm^2, corresponding to a nominal dosage of 4.8 J cm^{-2}; however, later measurements of the beam

strength, made with a Coherent Fieldmaster power meter, indicated that attenuation by the air and optics

of the patterning stage caused it fall to 83 % of the nominal value at the position of patterning. This

corresponds to a real dosage of 3.98 J cm^{-2}. Following photodegradation, samples were rinsed with PBS

buffer and immersed into a 5 µg mL^{-1} solution of streptavidin diluted in PBS buffer for 20 min. These

were then removed and washed with PBS buffer, and either (**a**) washed again with 1 % ammonium

acetate solution and nanopure water for imaging under a Nanoscope IIIa AFM in tapping mode; or

(**b**) immersed in a second solution of biotinylated IgG (5 µg mL^{-1}) for 20 min, then washed with 1

ammonium acetate solution and nanopure water and imaged under the AFM. This was to show the

difference in height that would be achieved if biotinylated IgG was successfully captured by surface-

bound streptavidin, (**b**−**a**), which is dependent on the retention of the absolute geometry of biotin-

capturing site of streptavidin following immobolisation.

3.2.3   Glutaraldehyde Coupling of Thiols to Mercaptosiloxane SAMs

SAMs of 3-mercaptopropyltrimethoxysilane were formed according to procedures outlined in sec-

tion 2.6 on page 92. Contact angles of the monolayers so-formed were in the region 69° (observed

on glass) to 75° (observed on silicon). This is commensurate with studies of wetting behaviour on

SAMs of dithiothreitol (HS(CHOH)$_2$SH) on gold. The SAMs were then immersed in 50 % (vol.)

aqueous glutaraldehyde solution for 2 h. Samples were removed and washed with water and then

HPLC grade ethanol, after which the contact angle fell to 47°. Subsequent attachment of 1H,1H,2H,2H-

perfluorooctanethiol (immersion in 2.5 mM solution of the thiol in HPLC grade ethanol for 2 h) caused

this to rise again to 84°, which is suggestive of (at least partially) successful attachment.

Samples of glutaraldehyde ('GA')-attached HSC$_{11}$(EO)$_3$OH films on the silane SAM (made in the same

way as the GA-attached perfluorooctanethiol described above, 2.5 mM in HPLC grade ethanol) were

exposed to a dosage of 4.8 J cm^{-2} of 244 nm laser light, before being immersed in a 10 mM ethanolic

solution of trifluoroethylamine (pH 5; with HCl added to make a concentration of 10^{-5} mol dm^{-3}) for

2 h. XPS spectra of the C$_{1s}$, F$_{1s}$ and Si$_{3d}$ regions were collected at a pass energy of 20 eV and were

interpreted using CASAXPS software. Because the sulfur-terminated silane is a short chain, it was

supposed that the contributions to the C$_{1s}$ spectra from the C-C̲-Si and and C-C̲-S components would

both be significant. Therefore, position and area constraints were put in place for these environments.

Typical shifts for these environments were taken from Briggs[23]. Previous work[24,25] had indicated that

SAMs of silanes on silicon stand very nearly parallel to the surface normal, and so the application of equation (1.3.25) on page 44 and equation (1.3.24) on page 44, plus some rudimentary trigonometry in estimating the increase in film thickness per additional atom in the tetrahedral arrangement, allowed the relative sizes of the curves expected from each environment to be arrived at. It can be estimated that the signal from C-$\underline{C}$-S (at B.E.=285.12 eV) should be 1.048× the size of the C-$\underline{C}$-C (aliphatic) environment in 3-mercaptopropyltrimethoxysilane, if the assumption is made that the the mercaptiosilane is oriented with the silane attached to the silicon; conversely, C-$\underline{C}$-Si (B.E.=284.39 eV; Si shifts the B.E. to lower energy, whereas most other substituents shift the B.E. to higher energy) is more attenuated than C-$\underline{C}$-C and is therefore estimated by this method to be 0.897× the size of the aliphatic environment (to which the spectra are universally calibrated, B.E.=285 eV). It was found that imposing these constraints gave a close fit to the spectral signature, as well as being chemically sensible.

For the subsequent curve fitting, the C-$\underline{C}$-Si environment was used to calculate the reduced attenuation of each adlayer environment (*i.e.* each would exhibit an increase in peak area as compared with C-$\underline{C}$-Si). From the increase in [C-C-C], and [C=O], the extent of glutaraldehyde attachment was deduced. Subsequently, in order to probe attachment of the OEO-thiol and its photoegradation, constraints were removed, but the attenuation of silicon was used to monitor and compare suggested attachment levels.
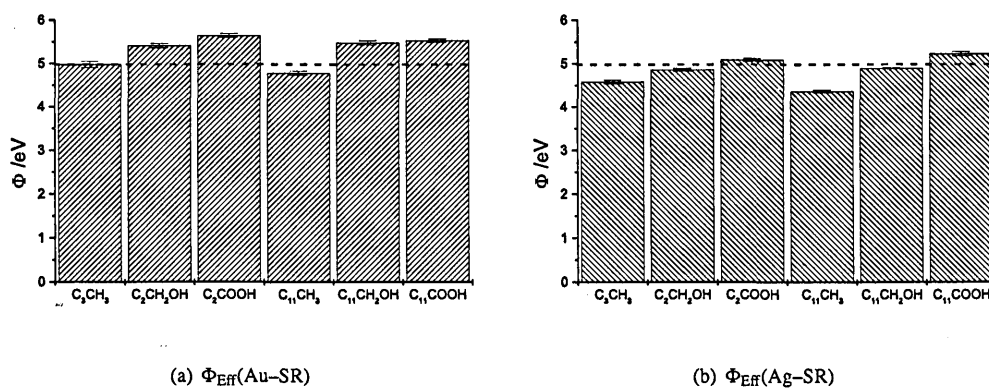
3.3 Results

3.3.1 Photooxidation of SAMs

3.3.1.1 Measurement of Surface Potentials of SAMs

(a) Au–SR   (b) Ag–SR
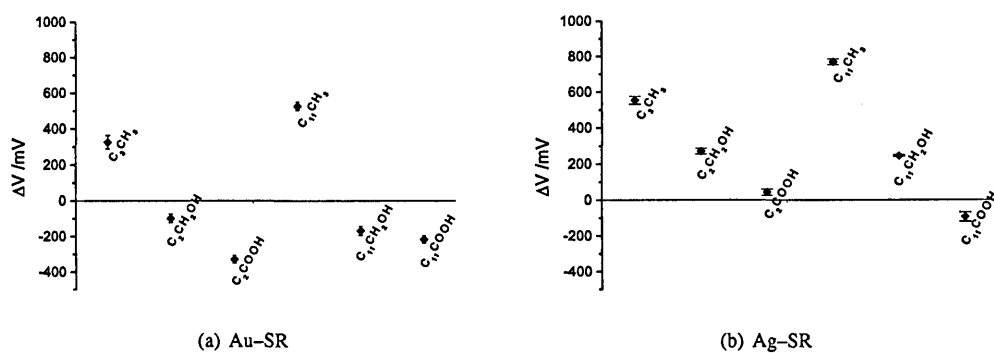
Figure 3.3.1   Surface potentials for a range of SAMs on gold and silver. Error bars indicate standard errors (n=18)

(a) Φ_{Eff}(Au–SR)   (b) Φ_{Eff}(Ag–SR)

Figure 3.3.2   Plot showing relative work functions of a range of SAMs on gold and silver
Error bars indicate standard errors (n=18). The dashed line indicates the mean photon energy from the 254 lamp used.

Shown in **figure 3.3.1** are the measured surface potentials of SAMs on Au and Ag. Error bars indicate standard errors (n=18). These values were used to calculate effective work functions Φ_{Eff} on Au and Ag, which are shown in **figure 3.3.2**. The dashed line depicts the photon energy of the 254 nm lamp ($h\nu$=4.98 eV), previously used in the investigation of rates of photooxidation of Au–SR and Ag–SR

SAMs. Values of Φ_{Eff} are summarised in table 3.1. Also shown are previously determined[3] rate constants for Au–SR and Ag–SR SAM photooxidation.

Adsorbate	$\Phi_{Eff}(Au)$/eV	k_{Au}/min^{-1}	$\Phi_{Eff}(Ag)$/eV	k_{Ag}/min^{-1}
C_3CH_3	(4.98)	0.0371	4.58	0.0198
C_2CH_2OH	5.41	Untested	(4.86)	Untested
C_2COOH	5.64	0.1339	5.09	0.1339
$C_{11}CH_3$	4.78	0.0200	4.36	0.0015
$C_{10}CH_2OH$	5.48	Untested	(4.89)	Untested
$C_{10}COOH$	5.53	0.0325	5.22	0.0405

Table 3.1 Table showing effective work functions Φ_{Eff} in electronvolts (eV) for a range of SAMs on gold and silver, and also the associated first order rate constants of photooxidation as determined from SIMS experiments carried out by Brewer[3,26]. Underlined values of Φ_{Eff} are below the photon energy of the 254 nm lamp used in the photooxidation experiment; values where the photon energy lies $2\times$ the standard error (whether the average value is either below or above the photon energy) are given in brackets.

Underlined in table 3.1 are Φ_{Eff} for which the SAM adsorbate has lowered the Φ relative to the bare metal (by imposing a positive ΔV) to a value below the photoelectron energy of the lamp. Values in brackets are Φ_{Eff} for which the photon energy lies with 2σ(due to variations in the experimentally-determined values) and could therefore indicate that Φ_{Eff} may be greater *or* less than the photon energy.

The SAMs that were studied can be characterised as being either 'short' or 'long'. 'Short' SAMs are all of $\sim C_4$ in length*, while 'long' SAMs are all $\sim C_{12}$ in length. Of the short SAMs on gold, it can be seen that C_3CH_3 has effectively lowered the Φ of the bare metal to give a Φ_{Eff} of 4.98 eV (which are below the photon energy, accounting for experimental uncertainty), while both C_2CH_2OH and C_2COOH have both effectively increased the Φ of the bare metal to give Φ_{Eff} of 5.41 eV and 5.64 eV respectively. When viewed alongside previously-determined rate constants, it can be seen that the photooxidation of C_2COOH (which has increased Φ_{Eff} far in excess of the photon energy) proceeds much more rapidly ($\sim 3.6\times$) than in the case of C_3CH_3. Of the long SAMs on gold, $C_{11}CH_3$ has lowered Φ to give a Φ_{Eff} of 4.78 eV, while the adsorption of $C_{10}CH_2OH$ and $C_{10}COOH$ SAMs have increased Φ to give Φ_{Eff} of 5.48 eV and 5.53 eV respectively. Thus, the adsorption of $C_{11}CH_3$ has lowered Φ_{Eff} to below that of the photon energy. Again, the tabulated rate constant results show that $C_{11}CH_3$ photooxidises more slowly than $C_{10}COOH$, although the difference is less than for short SAMs ($\sim 1.6\times$). A reason for this is suggested in the *discussion*.

Ag–SR SAMs give rise to Φ_{Eff} that follow a similar pattern to those on gold. However, $\Phi(Ag)$ is lower than $\Phi(Au)$, and so the value of $\Phi_{Eff}(Ag$–$SR)$ for each SAM tends to be lower than its analogue on gold.

---

*the abbreviated notation employed here, and in table 3.1 and elsewhere, indicates the hydrocarbon length and the nature of the ω moiety only; as all the SAMs are organothiolates, the sulfur is implied though not explicitly stated

Of the short SAMs on silver, C_3CH_3 gives the lowest Φ_{Eff} at 4.58 eV; again it is much slower ($\sim 6.8\times$)
to photooxidise than C_2COOH, which has a Φ_{Eff} of 5.09 eV. Φ_{Eff} for C_2CH_2OH is again intermediate,
at 4.86 eV. Of the long SAMs on silver, $C_{11}CH_3$ has the lowest Φ_{Eff} at 4.36 eV, far below the lamp
photon energy, and undergoes photooxidation at a far slower rate than $C_{10}COOH$ (27$\times$), which has a
Φ_{Eff} of 5.22 eV. Again, Φ_{Eff} for $C_{10}CH_2OH$ is intermediate, at 4.89 eV.

Oligo(ethylene oxide)-terminated SAMs, and SAMs containing fluorine were investigated. Oligo(ethylene
oxide)-terminated (OEO)-SAMs had been used extensively to control protein adsorption, and had been
explored at photoresists in forming protein patterns. SAMs of $C_{11}(EO)_3OH$ on gold were determined
to have Φ_{Eff}=5.23±0.046 eV, which is somewhat lower than might be expected from the cumulative
effect of four oxygen atoms. However, it should be considered that the microscopic origin of surface
potentials is a directional dipole, and the oligoether moieties in OEO-SAMs can adopt amorphous or
helical geometries[27]*, which give rise to a more isotropic dipole field that would reduce ΔV. Previous
work has indicated that the photooxidation of $C_{11}(EO)_3OH$ SAMs may be frustrated by competing
processes. This will be explored in subsection 3.3.2 on page 122.

The Φ_{Eff} of a $C_{11}OH$ film that was modified using TFAA to produce a perfluorinated ester was deter-
mined to be 6.97±0.106 eV. Previous work by Hutt and Leggett[28] demonstrated a route to perfluoro-
terminated films by the surface modification of hydroxy-terminated SAMs. Perfluorinated SAMs have
also been explored as surfaces that resist biological adhesion, as will be demonstarted in the next chapter.

---

*although, it should be noted, the hydration thought to give rise to helical conformations would not have been acheived, as
the films' ΔV were measured immediately after removal from ethanolic solution, without a water immersion step

3.3.1.2 Determination of photooxidation kinetics of Pd–SR SAMs
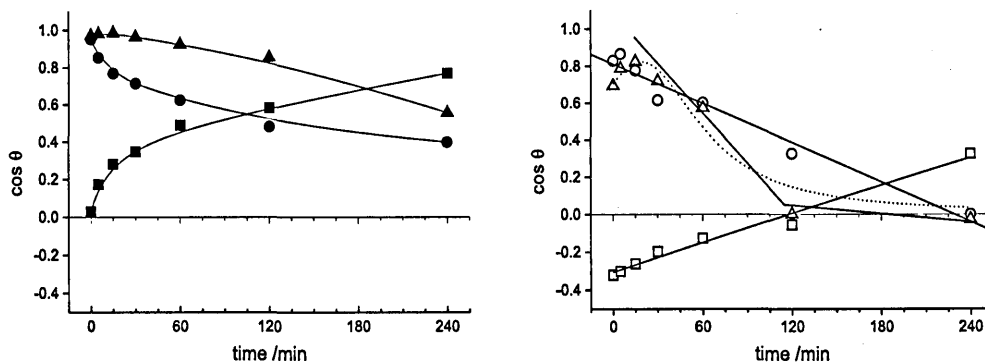
(a) Change in cos θ for 'short' SAMs   (b) Change in cos θ for 'long' SAMs

SAM(1)	SAM(2)		$\theta_a(t=0)$	$\theta_a(t=240\,\text{min})$	SAM(1)	SAM(2)		$\theta_a(t=0)$	$\theta_a(t=240\,\text{min})$
C_3CH_3	C_2COOH	■	88.3°	39.7°	$C_{11}CH_3$	$C_{10}COOH$	□	108.7°	71.0°
C_3OH	C_3CH_3	●	17.7°	66.5°	$C_{11}OH$	$C_{11}CH_3$	O	30.0°	90.0°
C_2COOH	C_3CH_3	▲	13.3°	56.2°	$C_{10}COOH$	$C_{11}CH_3$	△	34.5°	91.5°

Figure 3.3.3   Plots illustrating changing cos θ values, where θ is the contact angle made between a droplet of water and a SAM of initial thiol adsorbate SAM(1), following irradiation by a 254 nm lamp for a range of times (shown on the x axis), and then immersion into contrasting displacing thiols SAM(2) for 2 h to form a mixed SAM nSAM(1), mSAM(2). Displacing thiols have functionalities that have the opposite wetting characteristic of the SAM under study (see table). Lines are guides for the eye.

Shown in **figure 3.3.3** are the changes in cos θ, as determined by contact angle goniometry, for Pd–SR SAMs exposed to a 254 nm UV lamp for different lengths of time*. These were used to determine f values for Cassie's equation (equation (1.3.7) on page 36)[†]. 'Short' chain SAMs ($\sim$C$_4$ approximate length) are depicted by filled symbols, and relevant data are shown in the left-hand plot (a), while data for 'long' chain SAMs ($\sim$C$_{12}$ approximate length) are depicted by open symbols in the right-hand plot (b). C_3CH_3 SAMs (filled squares, **a**), following exposure to the UV lamp and subsequent immersion in 1 mM solutions of C_2COOH thiol for 2 h, initially exhibit a rapid increase in cos θ for a duration of $\sim$40 min, after which the change is slower. This change corresponds to a decrease in θ, as the hydrophobic C_3CH_3 SAM component is replaced by the hydrophilic C_2COOH component. C_3OH SAMs (filled circles) exposed to the lamp and then immersed in 1 mM solutions of C_3CH_3 for 2 h exhibit a similar pattern of replacement as for the C_3CH_3 SAM, in that the rate of change is initially fast (again, for 30–40 min); subsequently the rate then slows for the remainder of the duration of the experiment. In the latter case,

---

*cos θ is used because it relates directly to interfacial free energy, as *per* equation (1.3.5) on page 36—'Young's equation'—and can be used to determine proportional composition of the binary SAM due to each thiol adorbate's individual contribution to the surface free energy

[†]determined by using `Solve` in MATHEMATICA[19]

however, the value of $\cos\theta$ decreases, corresponding to an increase in θ as the hydrophilic hydroxy-terminated C_3OH is replaced by the hydrophobic C_3CH_3. A slightly different pattern of change of $\cos\theta$, as compared with the two previous SAMs, is observed in the case of C_2COOH (filled triangles) as it is replaced by C_3CH_3: $\cos\theta$ at first appears to increase very slightly, but then decreases, corresponding to an increase in θ as the hydrophilic C_2COOH is replaced by the hydrophobic C_3CH_3. The rate of change appears to be increasing for the limited duration of the experiment, which, alongside the aberrative initial change (increase in $\cos\theta$, caused by an initial decrease in θ) *may* be indicative of a multiple stage process. This will be considered in depth in the *discussion*.

For the 'long' SAMs, the $\cos\theta$ values of photooxidised samples of which are shown in figure 3.3.3 on the preceding page part (b), the behaviour is markedly different. $C_{11}CH_3$ (depicted by open square symbols) initially starts with a $-$ve $\cos\theta$ value, indicative of $\theta > 90°$, which is characteristic of very hydrophobic surfaces. As the duration of photooxidation increases and the photooxidised SAM is replaced by the hydrophilic $C_{10}COOH$ thiol, the contact angle θ falls. This is represented graphically by an increase in $\cos\theta$, although the total change in terms of the range of $\cos\theta$ during the photooxidation experiment is much smaller than for the C_3CH_3 SAM, commensurate with previous studies[29] which show that photooxidation of longer SAMs proceeds at a slower rate. $C_{11}OH$ SAMs (open circles) initially exhibit a decrease in $\cos\theta$ as the contact angle increases, resulting from replacement of the photooxidised $C_{11}OH$ component with hydrophobic $C_{11}CH_3$. As for the 'short' SAMs, the change of $\cos\theta$ for the hydroxy- and methyl-terminated SAMs is similar in magnitude and line shape, but with opposite gradient; again, the acid-terminated 'long' SAM shows a different pattern of photooxidative behaviour from the methyl- and hydroxy-terminated 'long' SAMs. $C_{10}COOH$ (open triangles) appears to undergo change rapidly as indicated by $\cos\theta$ values, with little change after 120 min. However, the initial contact angle (at $t=0$ min), is anomalously high for a SAM with a terminal ω functionality that should be hydrophilic: 34.5°. A possible explanation for this aberration will be proposed in the discussion.

Assuming a similar pattern of photooxidation kinetics as for Au–SR and Ag–SR SAMs, which have been previously modelled as a first order change, $\ln(1 - f)$ values were plotted against time in order to fit straight lines (shown in **figure 3.3.4** on the next page) , the negative of the gradients of which are pseudo first order rate constants for the replacement of the SAM under study. These provide a means of comparing the rates of photooxidation of Pd–SR SAMs, with analogous SAMs on Au and Ag.
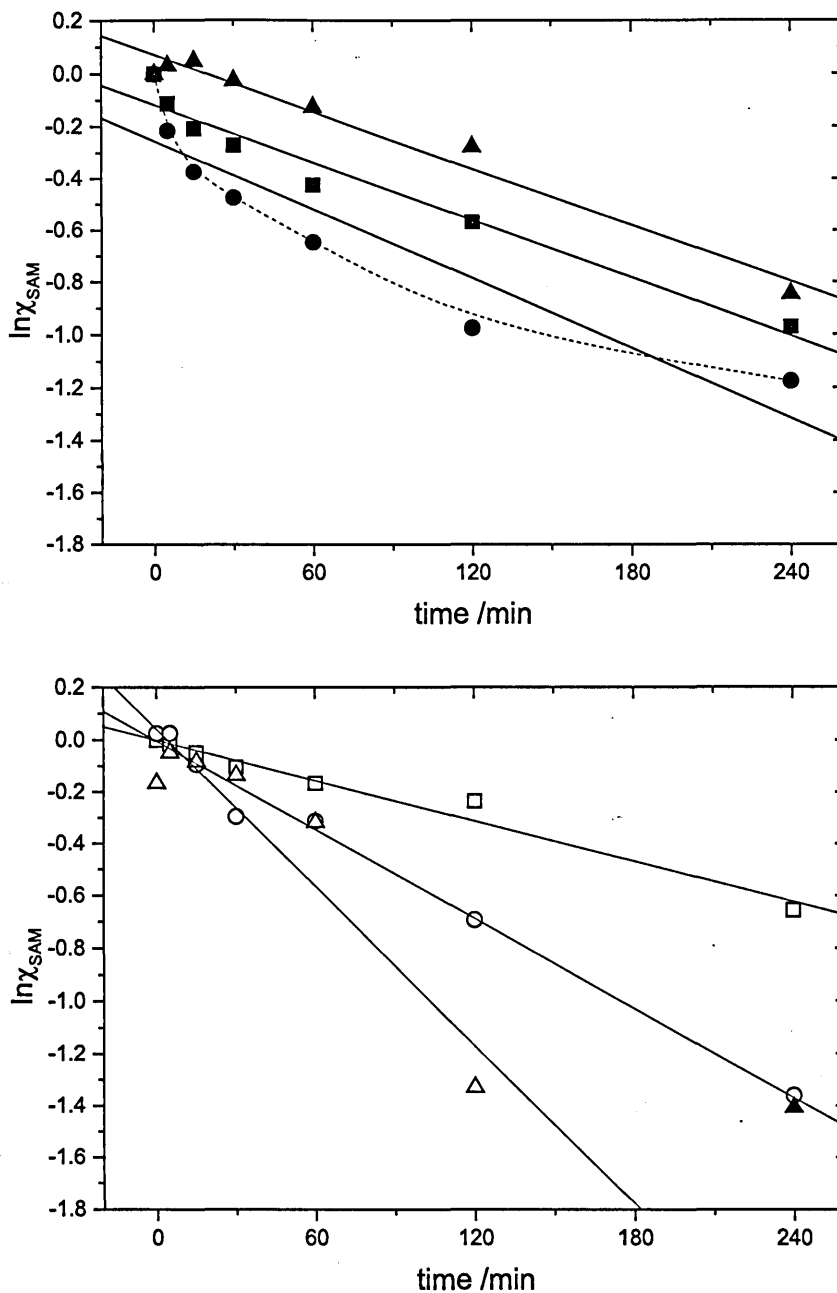
SAM(1)	SAM(2)	Symbol	k_{Pd} /min^{-1}	SAM(1)	SAM(2)	Symbol	k_{Pd} /min^{-1}
C_3CH_3	C_2COOH	■	0.00369 ± 0.00034	$C_{11}CH_3$	$C_{10}COOH$	□	0.00259 ± 0.00019
C_2CH_2OH	C_3CH_3	●	0.00442 ± 0.00082	$C_{10}CH_2OH$	$C_{11}CH_3$	○	0.00569 ± 0.00030
C_2COOH	C_3CH_3	▲	0.00362 ± 0.00027	$C_{10}COOH$	$C_{11}CH_3$	△	0.0101 ± 0.00189

Figure 3.3.4 Plots showing changes in $\ln \chi_{SAM}$ against time in order to determine first order rate constants k. The dashed line in the top figure illustrates the deviation from linearity of the change of $\ln \chi$ for the C_3CH_2OH SAM. This may be due to complexity in the mechanism of photooxidation. The fitting of a line for the $C_{10}COOH$ SAM has been done discounting the value of $\ln \chi$ at 240 min, because the reaction is approaching completion, as indicated by the figure 3.3.3 on page 114. The discounted datapoint is indicated by a filled, rather than open, triangle. $\pm$ values indicate the error in each gradient.
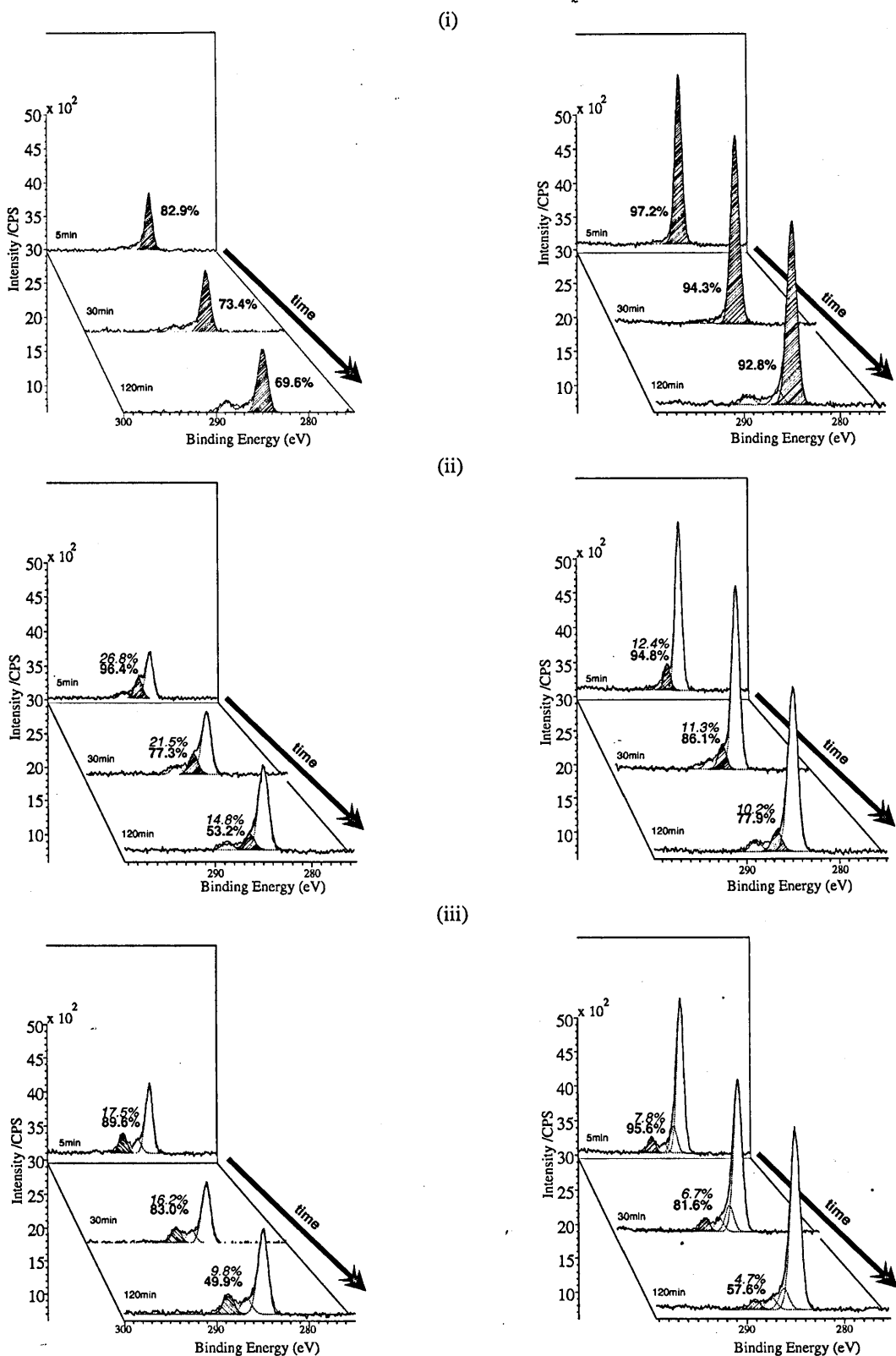
In part (a) of figure 3.3.4 on the preceding page, which shows rates of change of $\ln(1-f)$ values for 'short' SAMs, it can be seen that the steepest gradient, corresponding to the quickest rate of change and therefore fastest rate of photooxidation, is for the C_3OH SAM, with the general ordering of k values being $C_3OH > C_3CH_3 > C_2COOH$. As will be discussed, this is at odds with findings for analagous systems on Au and Ag, which prompted a complimentary study by XPS analysis. Another major difference is the lack of distinction between the rates of photooxidation of the three short SAMs on Pd, as compared with the clear distinction between photooxidation rates of the same SAMs on Au and Ag. Of additional note is the deviation from linearity of the $\ln(1-f)$ values for the C_3OH SAM, highlighted by a dashed line—a guide for the eye; no attempt to model this as a higher order change has been made. This may be indicative of a complexity in the mechanism of photooxidation, which is likely to derive from a structural nuance of this particular SAM. The implications for the change in order of rates for the short SAMs will also be considered alongside findings from the XPS analyses (see discussion, subsection 3.4.1.2 on page 133).

In part (b) of figure 3.3.4 on the preceding page, which shows $\ln(1-f)$ values for 'long' SAMs against time, there is a much clearer distinction between the three different ω-functionality bearing SAMs. In-keeping with reported findings for photooxidation kinetics on Au and Ag, rates of change follow the pattern $C_{10}COOH > C_{11}OH > C_{11}CH_3$. Indeed, the change progresses rapidly for the $C_{10}COOH$ SAM, which has largely reached its endpoint by 120 min. as determined by the levelling off of $\cos\theta$ in figure 3.3.3 on page 114. Hence, the point at 240 min is discounted in producing the linear fit.

XPS spectra were also collected for samples treated in the same way as for the contact angle measurements. Isometric plots show typical C_{1s} curves for samples of each of the six SAMs exposed to the 254 nm lamp for the duration 5, 30 and 120 min in **figure 3.3.5** on the following page. Not all time points are shown, but the omissions have been made in order to enhance the clarity of the spectra shown, and demonstrate the principles used to setermine the extent of photooxidation. Peak areas of interest were considered as in equation (3.2.2) on page 107; as it is the *fraction* of the total C_{1s} curve that is used, variations in the X-ray intensity from day-to-day do not affect the investigation. For each of curves in the isometric plots, the fractional percentage that each curve makes up of the total C_{1s} area is given in italics, while the values in bold type, $\chi_\%$, indicate the percentage of the initial monolayer remaining after photooxidation (*i.e.* taking the peak at t=0 to be 100 %). Note that the introduced perspective between the timepoints in figure 3.3.5 on the following page does not imply an increase in the C_{1s} peak area and is for clarity of illustration only—The key consideration is the proportional contribution of the characteristic peak to the total C_{1s} area. The fraction of the monolayer remaining following photooxidation, $\chi \equiv \frac{\chi_\%}{100}$. where represents the mean fractional contribution of the carboxylic acid peak to the C_{1s} area from three acid terminated films.

In order to allow comparison of these data with those attained by contact angle measurements, the change was modelled as being first order, which was found to be the a good fit for the photooxidation kinetics of Au–SR and Ag–SR SAMs. Shown in **figure 3.3.6** on page 120 are natural logarithm plots against time of the remaining mole fraction of the initial monolayers in each (binary) SAM.

(i)

(ii)

(iii)

(a) (i) C$_3$CH$_3$; (ii) C$_3$OH; (iii) C$_2$COOH at 5, 30 and 120 mins exposure

(b) (i) C$_{11}$CH$_3$; (ii) C$_{11}$OH; (iii) C$_{10}$COOH at 5, 30 and 120 mins exposure

Figure 3.3.5 XPS spectra of a range of SAMs exposed to a 254 nm UV lamp for 5, 30 and 120 min. Percentage values in *italics* indicate the contribution of the characteristic component to the core level area, whilst the values in **bold** show how this relates proportionally to the initial value for the un-photooxidised monolayer.   119
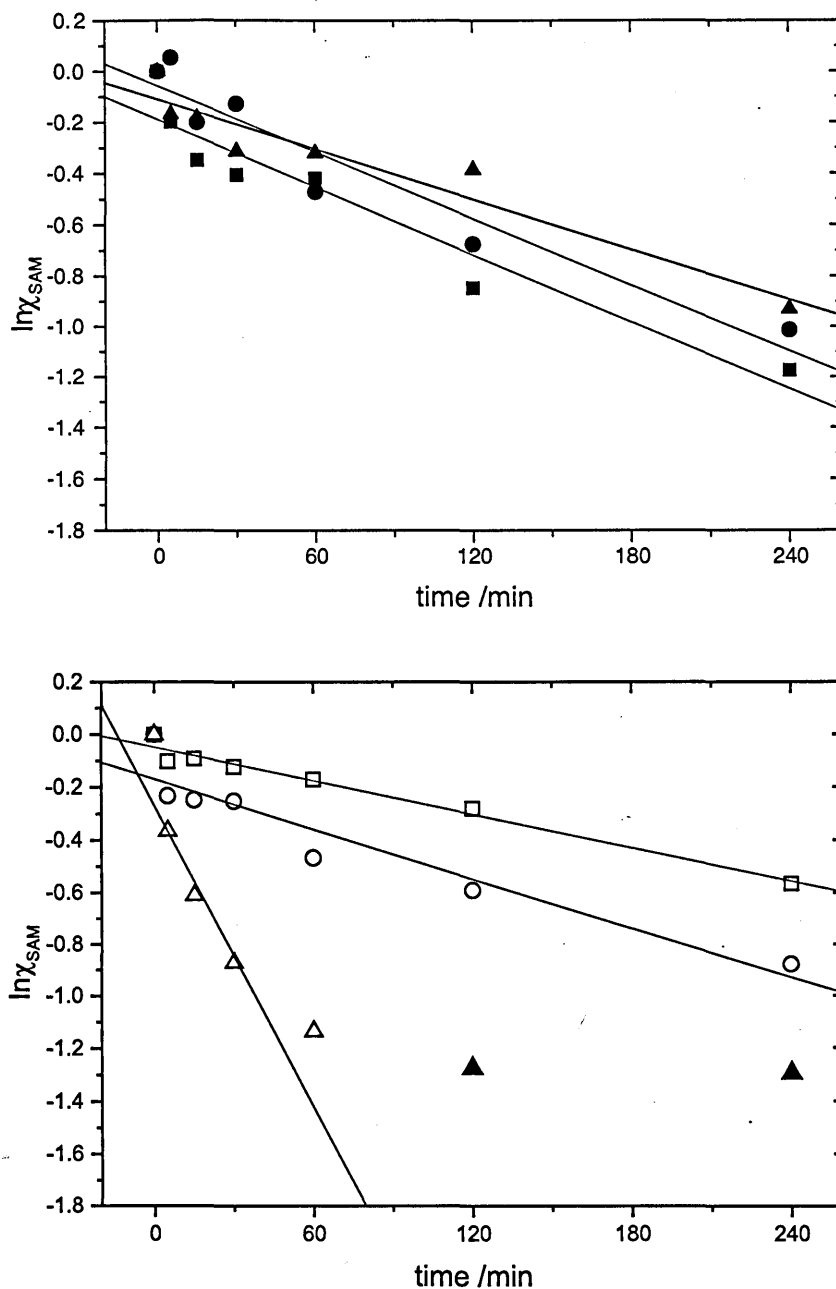
SAM(1)	SAM(2)	Symbol	k_{Pd} /min^{-1}	SAM(1)	SAM(2)	Symbol	k_{Pd} /min^{-1}
C_3CH_3	C_2COOH	■	0.00383 ± 0.00048	$C_{11}CH_3$	$C_{10}COOH$	□	0.00212 ± 0.00015
C_2CH_2OH	C_3CH_3	●	0.00433 ± 0.00093	$C_{10}CH_2OH$	$C_{11}CH_3$	O˙	0.00316 ± 0.00046
C_2COOH	C_3CH_3	▲	0.00326 ± 0.00042	$C_{10}COOH$	$C_{11}CH_3$	△	0.0267 ± 0.00592

Figure 3.3.6   Plots of $\ln\chi_A$ against time in order to determine first order rate constants for the photooxidation of Pd–SR SAMs, where χ is the fraction of the initial monolayer that is being photooxidised. χ_A were calculated from the XPS C_{1s} spectra shown in figure 3.3.5 on the previous page. Filled triangles for $\ln\chi$ values for the $C_{10}COOH$ SAM, at 120 and 240 min were discounted in determining a value for the first order rate constant. $\pm$ values indicate the error in each gradient.

	Adsorbate	$k_{Pd}(\theta)$ /min^{-1}	k_{Pd}(XPS) /min^{-1}	$\bar{k}_{Pd}$/min^{-1}	Φ_{Eff}
'Short'	C_3CH_3	0.00369	0.00383	0.00376	<u>4.83</u>
	C_3OH	0.00442	0.00433	0.00518	5.30
	C_2COOH	0.00362	0.00326	0.00344	5.43
'Long'	$C_{11}CH_3$	0.00259	0.00212	0.00236	<u>4.74</u>
	$C_{11}OH$	0.00569	0.00316	0.00443	(4.86)
	$C_{10}COOH$	0.0101	0.0267	0.0184	5.00

Table 3.2 1st order rate constants for Pd–SR photooxidation, as determined by contact angle goniometry ($k_{Pd}(\theta)$) and change in characteristic components in the C_{1s} core-level XPS signal (k_{Pd}(XPS)), plus effective work functions Φ_{Eff}. Underlined values of Φ_{Eff} are below the photon energy of the 254 nm lamp used in the photooxidation experiment; values where the photon energy lies 2× the standard error (whether the average value is either below or above the photon energy) are given in brackets.

In order to if and how the ω functionalities of Pd–SR SAMs affect the rate of photooxidation, measurements of ΔV were made. These are presented in table 3.2. Rate constants (k) as determined by contact angle measurements and XPS analysis are both considered, and mean values of these two methods of determination are also given, in the third column of rate constants, labelled $\bar{k}_{Pd}$. Similar to the previous Φ_{Eff} values given for Au and Ag, values below the photon energy of the lamp (4.88 eV) are underlined, and those values falling within 2× the standard error of the photon energy are shown in brackets.

It can be seen that, in keeping with findings for 'long' SAMs on Au and Ag, there is a correlation between Φ_{Eff} and the ω functionality of long SAMs on Pd. Compare table 3.2 with table 3.1 on page 112. Like its counterparts on Au and Ag, the $C_{11}CH_3$ SAM on Pd is the slowest to photooxidise, and is characterised by the lowest Φ_{Eff} value of the SAMs investigated: a value considerably lower than the photon energy of the lamp. The $C_{11}OH$ SAM has an intermediate rate constant for photooxidation, and is also characterised by an intermediate Φ_{Eff}, roughly equivalent to average photon energy of the lamp. The value of Φ_{Eff} for the $C_{10}COOH$ SAM is the highest for the 'long' SAMs, and its rate constant is also the greatest, at over 4 times the value for the $C_{11}OH$ SAM and almost 8 times the value for the $C_{11}CH_3$ SAM.

The 'short' Pd–SR SAMs exhibit more complex photooxidation behaviour that does not seem to be parallel to equivalent SAMs on Au or Ag. Despite Φ_{Eff} following a similar pattern to 'short' SAMs on Au or Ag (*i.e.* COOH>OH>CH₃), the rate constants follow the pattern OH>CH₃>COOH. While this is at odds with what might be expected, it is remarkable that both methods of determination of the extent of photooxidation yield results that are in close agreement with each other. The implications for this result will be considered in the *discussion*.
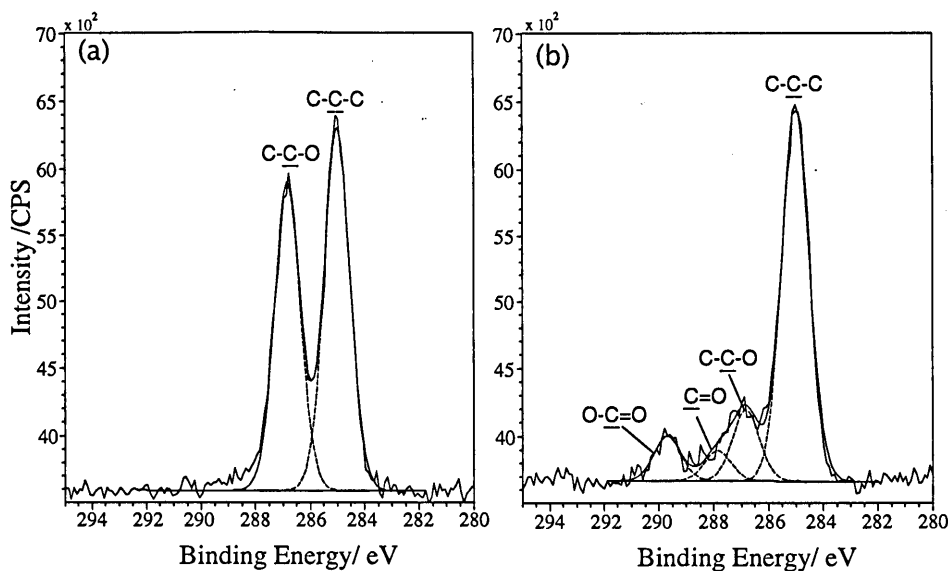
Figure 3.3.7   XPS spectra of a $C_{11}(EO)_3OH$ SAM (a) before; and (b) after, irradiation under a 254 nm
UV lamp for 1 h

3.3.2   Photodegradation of OEO-SAMs

3.3.2.1   Investigation into Surface Composition as a Function of Exposure to 244 nm Light

OEO-SAMs were exposed to UV laser light (dosage: 1.04 J *approx.*); C_{1s} spectra were recorded both for 'virgin' (*i.e.* unexposed) and UV-exposed films. **Figure 3.3.7** shows the change in the C_{1s} spectrum, before (part **a**) and after exposure (**b**). There are marked differences between the two spectra. In (**a**), there are two prominent peaks, one characteristic of aliphatic carbon environments (C-C-C; B.E.=285 eV) and another characteristic of carbon environments neighbouring oxygen substituents, consistent with the ether and alcohol carbons from the OEO ω moiety (C-C-O; B.E.=287.25 eV). In spectrum (**b**), the C-C-O peak is greatly reduced, and new peaks are present at higher binding energies that are characteristic of carbonyl environments. the peak at 279.9 eV has been assigned to an aldehyde environment, while the peak at 289.5 eV has been assigned to a carboxylic acid environment.

In order to quantify the rate of loss of the EO moiety from the SAM, and the formation of carbonyl groups, a wider study of the photodegradation process was made. In order to optimise the ratio of aldehydes to carboxylic acid groups for immobilisation, the surface composition was determined for a range of durations of exposure to the UV laser. Representative spectra are shown in figure 3.3.9 on page 124. The proportional contribution of characteristic peaks of chemical environments to the C_{1s} spectrum were calculated and plotted against the dosage at the surface. This is shown in **figure 3.3.8** on the next page. It can be seen that aldehydes (filled circles) are formed rapidly, reaching $\sim$50 %

of the maximum proportional contribution (an effective 'surface concentration') at a dosage of 1–2 J cm^{-2}, whereas the surface concentration of carboxylic acids grows more gradually. Following the disappearance of the C-$\underline{C}$-O moiety at a dosage of 10–15 J cm^{-2}, whereupon the loss of structures that impart protein resistance is completed, aldehyde surface concentration rises parallel to that of carboxylic acid, but the thiolate is, at this point, also undergoing photooxidation. It was decided that the optimum timepoint to test for amenability to protein attachment will be 4.8 J, immediately after loss of C-$\underline{C}$-O where the ratio of aldehyde : acid is high, but loss of integrity in the SAM due to photooxidation at the sulfur has not progressed to a point where its stability in biological media might be compromised (*i.e.* by desorption of SAM molecules as weakly-bound sulfonates).
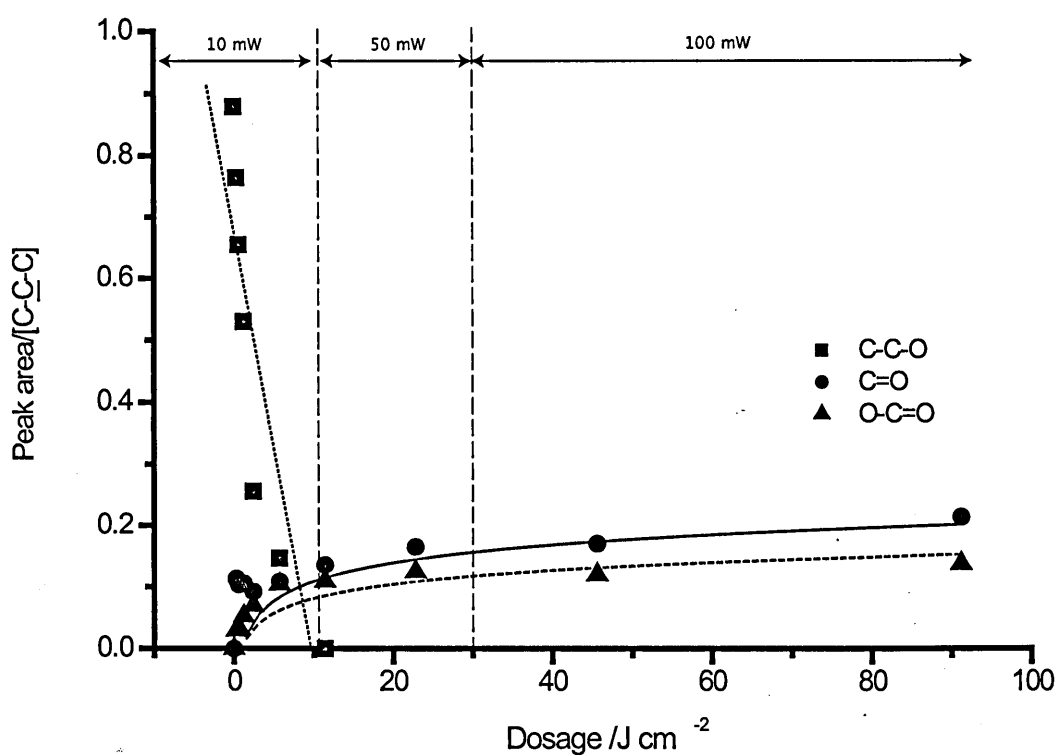
**Figure 3.3.8**   Plot showing change in composition of OEO SAMs as the dosage of 244 nm laser incident on the films is varied. The beam was expanded to 1 cm^2 to allow easy calculation. Irradiation was carried out at three power levels; the time in seconds was multiplied by the power level to calculate the dosage. Typical spectra used in the calculation of these points are shown in figure 3.3.9 on the next page.
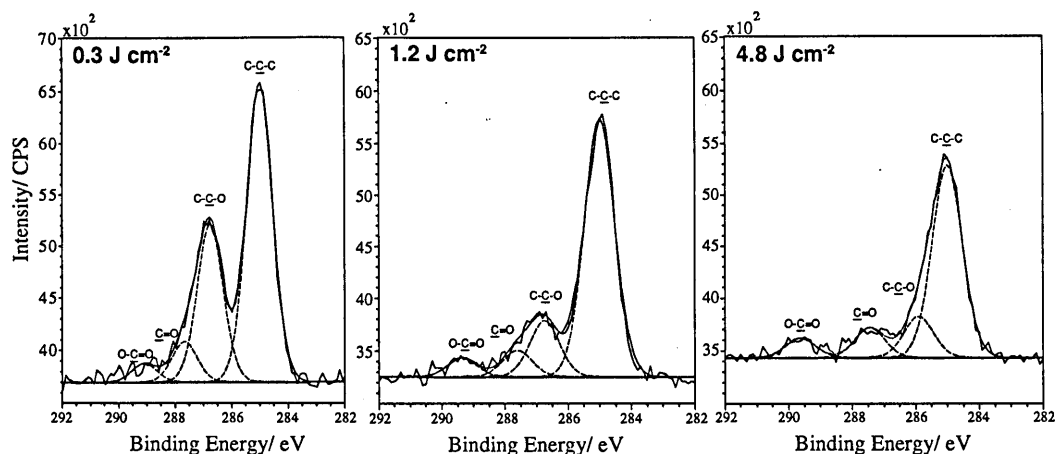
Figure 3.3.9   XPS spectra showing the change in the C_{1s} spectrum of an OEO SAM on gold following varying dosages of 244 nm laser. The beam was expanded to 1 cm^2, and the time in seconds was multiplied by the power level to calculate the dosage.

Shown in **figure 3.3.10** are two XPS spectra: one acquired from a 'virgin' OEO-SAM, and another following a 4.8 J dosage of UV light. Both SAMs were immersed in a 10 mM ethanolic solution of trifluoroethylamine at pH 5 (with conc. HCl added to yield a final concentration of $10^{-5} \text{ mol dm}^{-3}$) for 20 min; slightly acidic solutions catalyse the forward direction of the formation of imine equilibrium[30]. A fluorinated amine was used as fluorinated carbon has a large chemical shift in the C_{1s} binding energy, and F also produces its own characteristic binding energy peak at $\sim$688 eV. Clearly, the 'virgin' OEO film does not bind the fluorinated amine, as indicated by the lack of a peak in the F_{1s} region of the spectrum, and the associated C_{1s} chemical shift that might also be expected. Following photodegradation, however, a new peak is clearly visible, in both the F_{1s} and C_{1s} regions of the spectrum. This is supportive of the hypothesis that aldehydes are formed, which can bind amines by the formation of imine linkages.
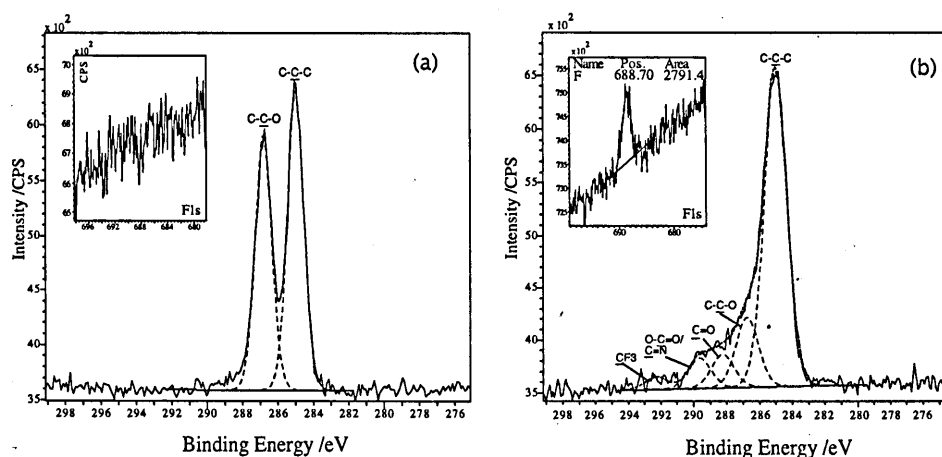

Figure 3.3.10   XPS Spectra of OEO SAMs on gold immersed in a 1 mM ethanolic solution of $CF_3CH_2NH_2$ for 20 min (a) before and (b) after irradiation by 244 laser (dosage=1.2); note that there is a F signal in (b) but not (a).

3.3.2.2 Biological Attachment to Photodegraded OEO-SAMs

Shown in **figure 3.3.11** are AFM tapping mode images indicating attachment of streptavidin to an OEO-SAM that has been exposed to a dosage of $4.8 \, \mathrm{J \, cm^{-2}}$ 244 nm UV laser, through a 1500 gauze copper electron microscope grid. Due to the small size of the protein ($\sim$1–2 nm average diamater) in comparison to the underlying gold grain size, it is difficult to register the pattern in print, so a dashed line follows the edge of a square as a guide for the eye for the topographical image in part figure 3.3.11 (a). Also shown, in part (b), is a phase image of the same sample, which shows slightly increased contrast. It should made clear that phase contrast does not necessarily pertain to topographical features, although in this case the contrast almost certianly results from a difference in the deformability of the biological regions as compared with the surrounding SAM. An average height difference analysis, shown in figure 3.3.11 (c), demonstrates that the regions where the streptavidin is thought to be, are higher than the the the surrounding areas by $\sim$1 nm. Although this is at the lower end of the diameter range for streptavidin, this is likely to be due to compression from the AFM tip rather than markedly diminished coverage, which would result in no pattern registering at all.
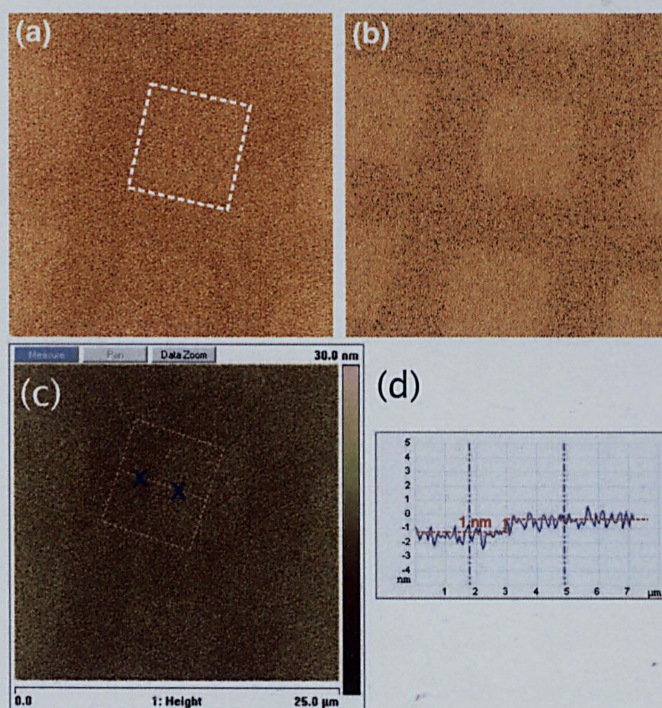
Figure 3.3.11   25 µm square AFM images of an OEO SAM exposed to 244 nm UV laser through a 1500 gauze copper grid. The dosage (accounting for attenuation of the beam due to air and mirrors on the patterning stage) was $3.98 \, \mathrm{J \, cm^{-2}}$. (a) is a tapping mode height image; (b) is a phase image collected at the same time as (a). (c) Shows the points in the image that were used to determine the average height difference between the patterned streptavidin-covered sections (squares) and the unpatterned regions; (d) is the section of the region indicated in (c).

Shown in **figure 3.3.12** is an AFM topograph of a patterned photodegraded OEO-SAM which has been first immersed in a solution of streptavidin like the sample shown in figure 3.3.11 on the previous page, washed, and then immersed in a solution of biotinylated IgG. As can be seen from the line section, there is a marked increase in height difference as compared to that in figure 3.3.11 on the preceding page (c), which is interpreted as being indicative of capture of the biotin function by the active pocket of stretavidin, as expected. This demonstrates that the geometry of the binding site in the streptavidin secondary structure is intact, and biological functionality has been retained, and also confirms that the pattern in figure 3.3.11 on the previous page is due to streptavidin.
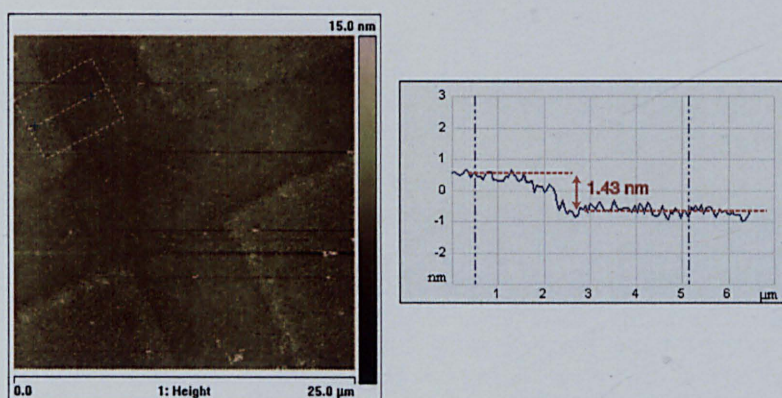

Figure 3.3.12   AFM intermittent contact mode image indicating attachment of biotinylated IgG to streptavidin immobilised on an OEO-SAM that has been photodegraded by $3.98\,\mathrm{J\,cm^{-2}}$ $244\,\mathrm{nm}$ UV laser through a 600 gauze Cu grid. Following washing with buffer and water, only specifically bound biological material remains. The excess height of the material as compared with the streptavidin-only pattern shown in figure 3.3.11 on the previous page indicates that the biotin functionality of the IgG has been captured by the binding pocket in streptavidin. This demonstrates that the binding of streptavidin by the UV-formed aldehydes has not compromised the geometry of the binding pocket, and the structure of streptavidin bound in this way is likely to be largely intact.

3.3.3   Glutaraldehyde Coupling of Thiols to Mercaptosiloxane SAMs

A perfluorinated thiol, $HSC_2(CF_2)_5CF_3$, was mistakenly used in place of trifluoroethylamine during investigations of attachment to a photodegraded OEO-SAM on gold. The spectrum in **figure 3.3.13** on the following page was acquired, the positive F_{1s} signal and eccentuated chemical shifts in the C_{1s} spectrum clearly indicating that a perfluorinated amine was present on the surface, despite the lack of an amine functionality. Samples had been washed according to standard procedures with ethanol, so these signals could not be due to aggregation of non-specifically-bound thiol on the surface. Instead, it is suggested that the thiol attacks the aldehyde carbonyl to form a hemithioacteal ('full' thioacetals, which would introduce two organic chains per aldehyde, are thought to be too sterically hindered to form). A scheme for this reaction is shown in **figure 3.3.14** on the next page.
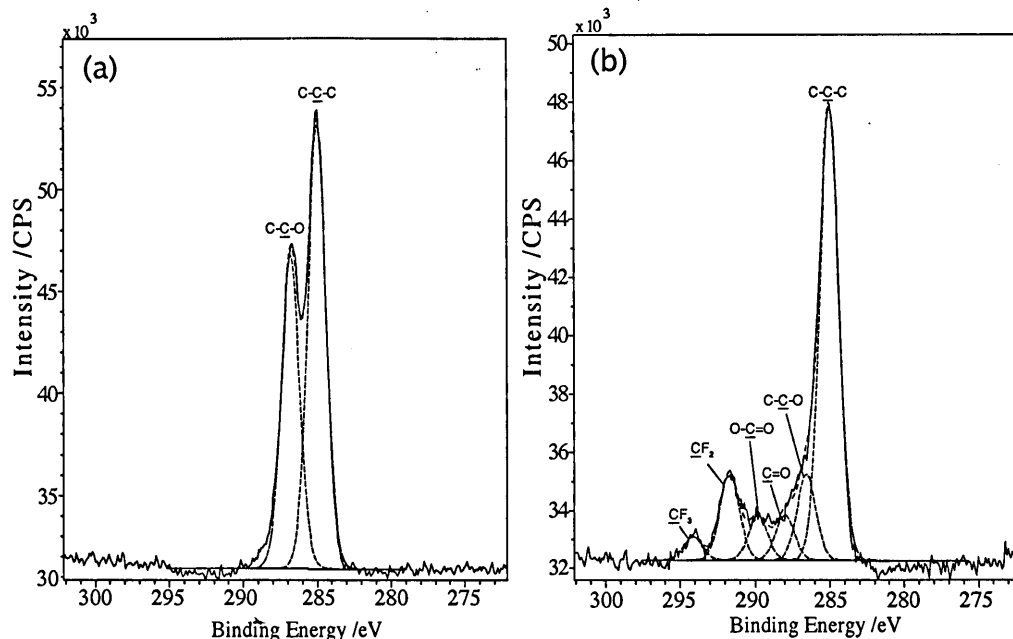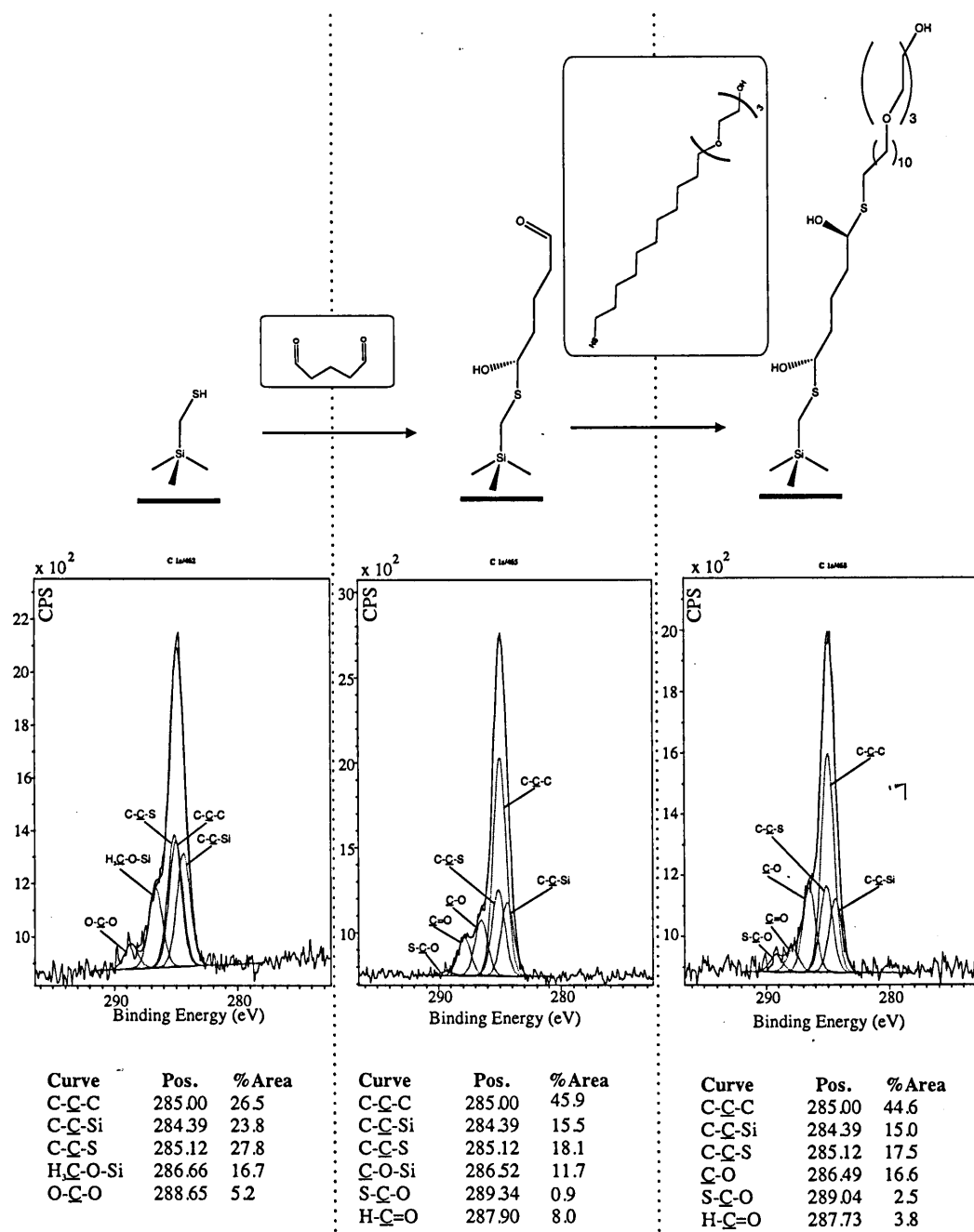
Figure 3.3.13   XPS Spectra of OEO SAMs following immersion in 1 mM $HSC_2(CF_2)_5CF_3$ in ethanol for 20 min (a) before, and (b) after exposure to 244 nm laser (dosage=1.2 J cm^{-2}).
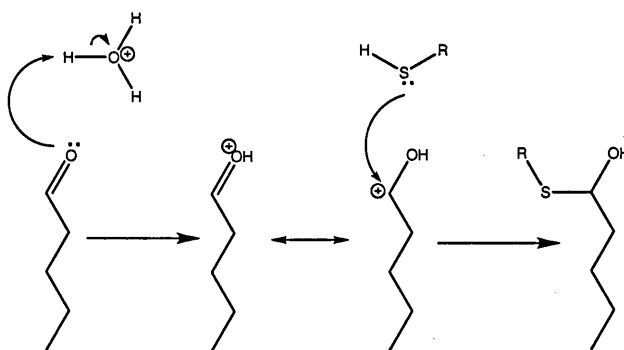
Figure 3.3.14   Mechanism of hemithioacetal coupling

The apparent attachment of a thiol to aldehydes formed by the photodegradation of an OEO-SAM film on gold merited further study. As will be shown in the *discussion* (figure 3.4.2 on page 139), the glutaraldehyde method can be used to immobilise biomolecules containing primary amines on amine surfaces, but the formation of imine links. The potential of hemithioacetal coupling suggested that thiols could be linked by glutaraldehyde in the same way. Shown in **figure 3.3.15** on the next page are spectra indicating the attachment of an OEO-terminated thiol to a mercaptosiloxane SAM formed on silicon by the use of a glutaraldehyde linker.

Curve	Pos.	% Area
C-C-C	285.00	26.5
C-C-Si	284.39	23.8
C-C-S	285.12	27.8
H,C-O-Si	286.66	16.7
O-C-O	288.65	5.2

Curve	Pos.	% Area
C-C-C	285.00	45.9
C-C-Si	284.39	15.5
C-C-S	285.12	18.1
C-O-Si	286.52	11.7
S-C-O	289.34	0.9
H-C=O	287.90	8.0

Curve	Pos.	% Area
C-C-C	285.00	44.6
C-C-Si	284.39	15.0
C-C-S	285.12	17.5
C-O	286.49	16.6
S-C-O	289.04	2.5
H-C=O	287.73	3.8

Figure 3.3.15 Attachment of $HSC_{11}(EO)_3OH$ to a mercaptosilane SAM on silicon by using a glutaraldehyde linker. (a) shows the XPS C_{1s} spectrum and tabulated film composition of a 3-mercaptopropylsilane SAM on Si, formed according to section 2.6 on page 92. (b) shows a similar film to (a) following immersion in 50 % (vol.) aqueous glutaraldehyde solution for 2 h. (c) is a film of (b) that has been immersed in 2.5 mM $HSC_{11}(EO)_3OH$ for 2 h. Relative intensity of certain characteristic components was constrained according to their relative depths within the film.

Due to the desirability of an easily-obtainable protein resistant film on silicon substrates, it was decided that attachment of $HSC_{11}(OCH_2CH_2)OH$ should be investigated. In figure 3.3.15 on the preceding page, characteristic peaks are evident in the progression of spectra that are indicative of attachment. Assessment of the degree of attachment should be made with some caution, as not all species have the same detection cross-section, and accurate determination requires careful calibration of the instrument. However, the ratio of carbonyl peak in the second spectrum (for glutaraldehyde attached to mercaptosilane) to the thiol carbon peak in the first spectrum (the 'virgin' mercaptosilane SAM), gives a value of 29 %. While this value is lower than the typical 50–60 % commonly observed for a variety of surface-bound reactions, it might be suggested that, running contrary to the initial hypothesis of hemithioacetal formation, 'full' thioacetals *may* be forming instead. A surface yield of $\sim$60 % (*i.e.* double 29 %) is in-keeping with that observed for other reactions. Regardless of whether or not this is the case, however, the density of carbonyl species able to facilitate (hemi)thioacetal attachment is given by the lower value*. Subsequently, $HSC_{11}(EO)_3OH$ attachment is also reduced. The $\underline{C}$-O peak comprises $\sim$15 % of the C_{1s} area, whereas in a typical $Au–C_{11}(EO)_3OH$ SAM, 45 % is observed. Assuming the $\underline{C}$-O peak in this experiment is largely representative of the ether functionalities, rather than alcohols (formed in the hemithioacetal) or residual alkoxy species from the silane headgroup, $\frac{15}{45}$=33 %, which is very close to the estimate for glutaraldehyde attachment yields. This is below the OEO density χ=0.4–0.6 reported by Prime and Whitesides to be optimal for protein resistance, but would still be in the region of being protein resistant to a degree[31].

Photodegradation of the attached films by UV light was also explored. The results are shown in **figure 3.3.16** on the next page are four spectra. Representative XPS Spectra of the C_{1s} and F_{1s} regions (figure 3.3.16 on the following page, part (c)) indicate that the amine attachment is successful following photodegradation (A_{F1s}/CPSeV=429.7). Also shown are data for a control experiment: (d) shows C_{1s} and F_{1s} spectra for a GA-attached $HSC_{11}(EO)_3OH$ film that has subsequently been immersed in a solution of trifluoroamine for the same period (2 h). There is a suggestion of very limited attachment (A_{F1s}/CPSeV=46.9), which must be occurring either through residual carbonyls from the GA surface (*i.e.* that initially failed to form thioacetal linkages) or by interchange with thioacetals to form imines on the GA-layer. However, any such attachment is negligible in comparison with that observed for the photodegraded OEO film, at just over $\frac{1}{9}$th of the latter, and barely over the noise level.

---

*—of course, each of these could attach two thiols, but further quantitative work needs to be carried out to ascertain whether this is this case.
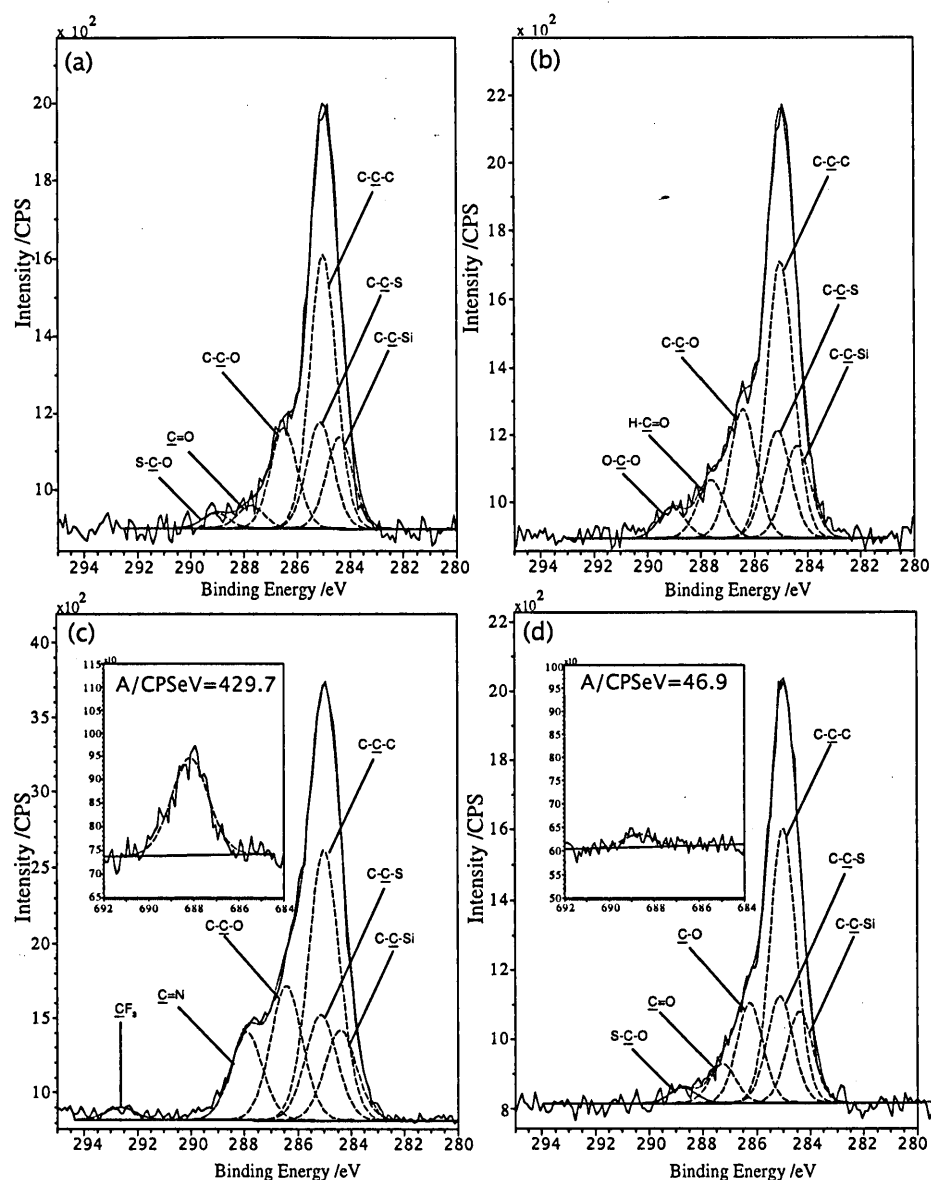
C_{1s}	Film Composition							
	a		b		c		d	
Peak	Posn. /eV	% Area	Posn. /eV	% Area	Posn. /eV	% Area	Posn. /eV	% Area
C-C-C	285.00	44.6	285.00	39.6	285.00	38.3	285.00	43.4
C-C-Si	284.39	15.0	284.39	13.3	284.39	12.9	284.39	14.6
C-S	285.12	17.5	285.12	15.6	285.12	15.1	285.12	17.1
C-O	286.49	16.6	286.42	18.7	286.42	19.3	286.25	16.0
C=O	289.04	2.5	××	××	××	××	××	××
H-C=O	××	××	287.61	8.4	××	××	287.26	6.3
S-C=O	287.73	3.8	××	××	××	××	××	××
O-C=O	××	××	289.06	4.5	××	××	288.74	2.6
C=N	××	××	××	××	287.91	12.6	××	××
CF₃	××	××	××	××	292.65	1.8	××	××

Figure 3.3.16   XPS C_{1s} spectra indicating composition of organic films yielded by OEO-thiol coupling experiment (*via* glutaraldehyde to a mercaptosiloxane SAM); (a) is a mercaptosiloxane SAM to which an OEO-thiol has been attached using glutaraldehyde. (b) shows a photodegraded film of (a). (c) is photodegraded and immersed in a solution of trifluoroethylamine, while (d) is a film of (a) (*i.e.* unphotodegraded) also immersed in a similar trifluoroethylamine solution as was (c).

3.4 Discussion

3.4.1 Photooxidation of SAMs

3.4.1.1 Measurement of Surface Potentials of SAMs

Previous work by Hutt and Leggett[29] has demonstrated the importance of SAM packing on observed rates of photooxidation. Longer SAMs, which exhibit closer packing, photooxidise more slowly. It was suggested that the closer packing impedes the migration of the oxidative species down to the sulfur, which is not the case for the liquid-like state of shorter SAMs, which photooxidise quickly. Following the general trend, methyl-terminated Ag–SR SAMs undergo photooxidation more slowly than the same SAMs on Au, which is commensurate with the former system adopting closer packing*. However, these data suggest that packing cannot be the only paramater determining photooxidation rates.

For those SAMs for which kinetics of photooxidation has been previously investigated, it has been shown that *SAMs with lower Φ_{Eff} undergo photooxidation at a slower rate*. For example, $C_{11}CH_3$ and $C_{10}COOH$ are adsorbates of approximately equal length, and the former, which lowers Φ_{Eff} to below $h\nu_{lamp}$ on both Au and Ag, is associated with a slower photooxidation rate on both substrates. Conversely, those *SAMs which increase Φ_{Eff} exhibit comparitively rapid photooxidation kinetics*—acid-terminated SAMs photo-oxidise faster on both substrates.

In order to rationalise these findings, the data can be considered in the context of the surface potentials imposed by each SAM. When EMR of a photon energy greater than Φ_{SAM} is incident on a SAM, photoelectrons are emitted to the vacuum level, whereas when EMR of photon energy close to, but below Φ_{SAM} is incident, hot electrons are formed in their stead. Acid-terminated SAMs increase Φ by imposing a negative surface potential on the substrate, and so the electrons' kinetic energies are reduced by the downward-pointing dipole. This modulates the electrons' kinetic energies to a level where, it is proposed, they are able to tunnel into the Au–S* antibonding orbital and initiate photooxidation. Conversely, methyl-terminated SAMs lower Φ and it is therefore likely that the vast majority of electrons are ejected up through the SAM to the vacuum level, where they are not able to initiate photoxidation. This is illustrated in **figure 3.4.1** on the next page.

That anomalously high rate constants for photooxidation of Ag–SC$_n$COOH SAMs are not mirrored by anomalously high work functions suggests that imposed surface potentials are not the primary

---

*The anomalous case is for acid-terminated Ag–SR SAMs. These have a rate constant greater than the same SAMs on gold, which will be rationalised in the Discussion.
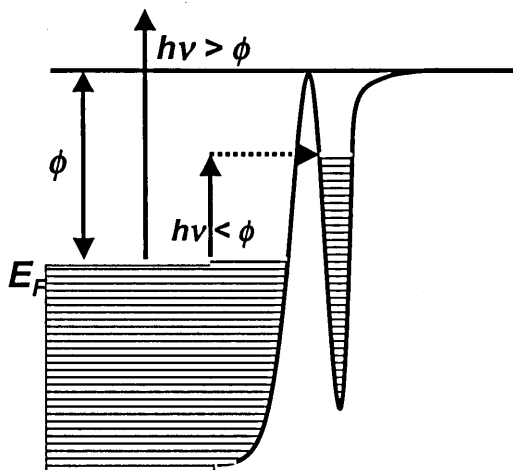
Figure 3.4.1   Tunnelling of hot electrons into Au–S σ^* orbital.

explanation for this result. It is proposed that bulky carboxylate groups in the acid-terminated SAMs on

Ag causes them to adopt a looser packing than the $(\sqrt{7} \times \sqrt{7})R10.9°$ observed for methyl-terminated

SAMs. This is commensurate with FFM data indicating that Ag–SC$_n$COOH SAMs have coefficients

of friction equal to or greater than the same systems on Au[32] (which suggests that the ω functionalities

are easily deformed more by the scanning AFM probe, which would require freedom of movement

not available in closer-packed films), and is supported by independent reports of looser packing or

adsorbate-induced substrate reconstruction on Ag[27,33]. A looser packing would allow easier penetration

of the oxidative species, and would imply fewer adsorbates per area on the substrate, which is supported

by the elevated photooxidation rate.

Treating the surface as a dipole sheet, it has been shown that the following relationship can be consid-

ered[13]:

$$\Delta V \propto \sigma l_s \qquad\qquad (3.4.1)$$

where l_s is the separation between the 'charged' sheets (*i.e.* the metal/headgroup and ω/air interfaces)

and σ is the 'charge' (or dipole) per unit area imposed by the adsorbate. From the above interpretation

of the anomaly of acid-terminated SAMs on silver, one might expect that decrease in adsorbates per

unit area would be accompanied by a decrease in the magnitude of the surface potential of, for example,

Ag–C$_{10}$COOH *cf.* Au–C$_{10}$COOH. This is -230.4 mV for the former, against -215.9 mV for the latter;

an increase in the magnitude of the surface potential, which is at odds with what might be expected.

However, it might be suggested that the difference in the nature of the Ag/S *vs.* Au/S interface would

no doubt also have an effect (the Ag–S bond is more polar; Au–S is more covalent due to having greater 'S' character from the Lanthanide contraction) thus making direct comparison difficult. Indeed, the difference ia also within the bounds of experimental error.

Previously, the data for SAM photooxidation kinetics were fitted as being first order. The validity of this in light of the proposal that the formation of hot electrons is the rate limiting step might also be considered. Zhou, Zhu and White reviewed photochemistry on a range of adsorbate-on-metal systems[6]. In their treatment, hot electrons are considered to be formed at a rate $\mathbf{R}_{if}$ dictated by Fermi's golden rule:

$$\mathbf{R}_{if} = \frac{\pi e}{i m_e h v} \, |< \phi_f \,|\, \bar{E} \cdot \mu \,|\, \phi_i >|^2 \delta(\Delta E_{if} - h v) \qquad (3.4.2)$$

where $\bar{E}$ is the electric field vector, μ is the transition dipole moment vector, ΔE_{if} is the energy difference between initial and final states, $h v$ is the photon energy, e is the fundamental charge, and m_e is the mass of an electron. The rate of formatation of hot electrons is proportional to the intensity of incident EMR when $\Delta E_{if} = h v$ and, following promotion to the conduction band, screening by electrons already present reduces the frequency of electron-hole recombination so that the mean free path remains independent of hot electron concentration. Thus, the rate of action of hot electrons is proportional to the incident EMR intensity, and photooxidation can be modelled as pseudo-first order overall due to the prevalence of ambient O_2; the fit is therefore valid.

While this work is suggestive of a single 'hot electron' mechanism of photooxidation when a largely monochromated source (*e.g.* the UV lamp, and of course the 244 nm laser) is used, it should be noted that for other sources, such as arc lamps that emit at a wavelength short enough to evolve ozone, other mechanisms may play an important rôle (*e.g.* ozonolysis).

3.4.1.2   Kinetics of Photooxidation of Pd–SR SAMs

Due to the growing interest in Pd–SR SAMs, the initial investigation described above was extended to include these novel systems. Photooxidation kinetics had not been previously studied for Pd–SR films, and so this presented an opportunity to gather data pertaining to photooxidation rates alongside a systematic investigation of Pd–SR SAM surface potentials.

As *per* the reasoning employed in Brewer *et al.*[26], photooxidation is assumed to proceed as a pseudo-first order change, and so natural log plots of $1 - f$ against time were shown in **figure 3.3.4** on page 116; this is almost certainly an oversimplification, as the diffusion of the oxidative species through a thicker SAM is impeded by the increased thickness and reduced chain mobility that arises from increased

packing density. It is possible that complex structures in the hydroxy– and acid-terminated SAMs, and the effect this imparts on the photo-oxidative mechanism, are a significant cause of deviations from linearity observed in the log plots. Nevertheless, the parameters yielded by this treatment of the contact angle data allow certain comparisons to be made.

Two methods of determination of the rates of photooxidation were presented. Previous work[34] on Au–SR SAMs has indicated that, when considering results from complimentary surface charcterisation techniques, XPS can yield a broader range of information (for example, chemical composition, and film thickness by the modulated attenuation of substrate photoelectrons) than ellipsometry (film thickness) or contact angles (surface free energy, defined by the functionality at the surface). As will be discussed, photooxidation kinetics data yielded by contact angle measurements and XPS of Pd–SR SAMs are generally similar, but there are differences. The advantage of XPS of Au–SR SAMs over other techniques arises from the well-defined orientation of component molecules, and the nature of photooxidised species in these SAMs is very well established. There has been the suggestion that there may be some small but important differences for the case of Pd–SR SAMs, notably physisorbed disulfides, ambiguous RAIRS spectra indicating complex unit cell organisation, and S–C bond scission[15]. Therefore, both contact angle data and XPS results will be considered together.

Pd–SR SAMs undergo photooxidation at a much slower rate than Au–SR SAMs. Penetration of the oxidative species from the atmosphere above the SAM to the S–Pd interface is necessary to form weakly-bound sulfonates, which are readily displaced. As has been described previously in subsection 1.2.2.2 on page 26, Pd–SR SAMs exhibit closer packing than Au–SR SAMs, so it could be the case that closer packing retards the migration of the oxidative species through the SAM film to the sulfur.

'Long' Pd–SR SAMs exhibit photooxidation trends in-line with Au–SR SAMs, having relative rates $COOH > OH > CH_3$. For the acid-terminated SAM, $\Phi_{C_{10}COOH} > h\nu$, and relatively rapid photooxidation is observed. This is supportive of the 'hot electron' hypothesis presented as a rationlisation of organosulfur SAMs on Au and Ag. The hydroxy-terminated SAM $C_{11}CH_2OH$ has a work function slightly <u>under</u> the photon energy and has a rate constant that is closer in magnitude to that of the methyl-terminated SAM. The Φ value in this case (4.86 eV) is within 2σ of the photon energy $h\nu$ and so is within the bounds of being 'roughly equal' to it, despite being ostensibly lower. It is assumed that, due to the nature of the process, 'hot' electrons will have a Boltzmann-type distribution of kinetic energies[*] and so at least some will be of compatible energy to tunnel into a state on the adsorbate sulfur where they can initiate photooxidation, hence the mean rate constant is double that for $C_{11}CH_3$. A very small

---

[*]also the lamp is not a monochromatic source, like the laser, and so the photons themselves will have a range of energies, dependent on the absorbance spectrum of its filter

rate constant was deduced for the SAM formed by adsorption of $C_{11}CH_3$ and it is significant that the smallest work function was determined for this surface. Its lower rate constant is also commensurate with Pd–SR SAMs adopting closer packing.

Shorter Pd–SR SAMs exhibit complex photo-oxidation trends, as observed by contact angle changes, having relative rates OH>CH3>COOH—this may be due to anomalous structural features of the SAM. Pd–SR SAMs do not always follow the wetting trends commonly observed for their Au–SR counterparts. Methyl-terminated Pd–SR SAMs are ostensibly more hydrophobic than are Au–SR SAMs, which is supportive of closer packing *or* increased roughness due to smaller Pd grain size[15] (which, according to Wenzel[35,36] increases θ_a by impart a more tumultuous and variable morphology within the SAM). However, Pd–SC$_n$COOH SAMs and, to a lesser extent, Pd–SC$_n$CH$_2$OH SAMs have an apparently semihydrophobic nature. Unlike gold, palladium is susceptible to aerial oxidation, so it could be that that a significant proportion of molecules are adsorbed through carboxylates (or hydroxides) to a metal oxide. However, despite extremely meticulous preparation (in order to reduce the likelihood of oxide formation prior to thiol adsorption and during storage), θ_a remained high. This was more marked in the case of the longer acid and hydroxy SAMs. It was initially thought that the carboxylic acid (or hydroxy) group is a competing stable ligand on Pd^0, as is the case in some industrial catalysts, for example in Stille coupling. For the longer thiol, which has greater lateral stabilising interactions within the film, this could be a kinetic trap, and indeed the contact angle actually initially falls for short exposures, possibly indicating the reordering of carboxylate-bound molecules in order to bind through a thermodynamically more favourable thiolate, which may be impeded at monolayer coverage. Assuming that a thiol surface is characterized by a $\theta_a(C_nSH)$ of 70–80°, and that $\theta_a(C_nCOOH)=10°$, a solution for f in the Cassie equation (equation (1.3.7) on page 36) yields 43 % H$^+$/$^-$OOC-bound, which is obviously a significant proportion. For the virgin Pd–C$_2$COOH SAM, $\theta_a=13.3°$, which is commensurate with wetting data for SAMs on Au and Ag, so it may be the case that a duality of binding modes (if that is indeed the cause of the anomalously high θ_a in the longer SAM) is less extensive in the shorter SAM, which from Au–SR studies is expected to be liquid-like and less stabilised by lateral interactions (*i.e.* less likely to be kinetically trapped). This pattern is also followed by the hydroxy-terminated SAMs, for which the longer thiol yields contact angle data that is more eccentric than that of the shorter hydroxy SAM, possibly for similar reasons.

An alternative explanation may be that there is some form of adlayer on the hydrophilic SAMs which is perturbed by immersion in the contrasting thiol, and removed by the vacuum of the XPS instrument. Love *et al.*[15] discussed the possibility of adlayer sulfide species, and perhaps the hydrophilic systems evolve these in greater number during the formation of the Pd–S interlayer. That the additional sulfide

species adlayer molecules might only be physisorbed would be supported by the lack of unbound sulfur seen in the S_{2p} spectra. Unbound sulfur would be an expected signal in the hypothesis presented previously (upside-down adsorbates), and it might be considered that this hypothesis has therefore been ruled out.

It might be considered that XPS spectra of S_{2p} regions of Pd–SR SAMs, previously published by Love *et al.*[15], indicated a number of environments that did not have a direct counterpart in Au–SR films. The evidence indicated that a Pd–S interlayer is formed, but the study did not extend to hydrophilic Pd–SR SAMs. Substantial S–C bond lengthening is predicted (*e.g.* in *Ref.*[37]) for a number of noble M–SR monolayers, due to backbonding from the metal. It could be the case that for the shorter SAMs, the formation of the Pd–S interlayer is promoted, and the resulting increase could frustrate the migration of hot electrons up from the metal film to the Pd–S σ^* orbital. This may cause the degeneration of the ordering of rate constants seen for other M–SR films, which are lacking in short Pd–SR SAMs. However, further work needs to be carried out to assess whether this is the case.

Comparison of the data yielded by contact angle measurements with that that taken from XPS curves indicates that a similar 'as-expected' hierarchy of rate constants for the longer SAMs are arrived at by both methods (with acid 'SAMs photooxidising faster than hydroxy-terminated SAMs, which in turn photooxidise faster than methyl-terminated SAMs) and also that the aberrative result for shorter SAMs, with the hydroxy-terminated SAM 'photooxidising' faster, is also reproduced. Rate constants arrived at by both methods are in close agreement ($\sim$1–10 % discrepancy) for the range of SAMs studied. It is suggested that a likely cause of the wetting anomaly is linked to the complex nature of the Pd–SR SAMs as compared with related films on Au, although further investigation is needed to understand why the trends are so different for the hydrophilic SAMs.

Analysis of the rate constants alongside work function data indicates that, as observed for gold and silver, there is a correlation between surface potentials and rates of photooxidation. Polar ω groups (such as hydroxy or carboxylic acid termini) tend to increase Φ, and these SAMs photooxidise more quickly. As is the case for gold and silver, it is suggested that 'hot' electrons are formed near the surface of the metal, and these are able to tunnel into the Pd–S* antibonding orbital and initiate the oxidative process. The longer methyl-terminated SAM ($C_{11}CH_3$) experiences the slowest rate, which is matched by it imposing the most positive surface potential on the substrate (thereby giving it the lowest work function). Shown in **table 3.3** on the next page, for comparison, are the photo-oxidation kinetics alongside surface potential data for the three substrates that have been studied. It cn be seen that palladium SAMs photooxidise much slower than either gold or silver, by a considerable degree. It

Adsorbate	Φ_{Au}/eV	k_{Au}/min^{-1}	Φ_{Ag}/eV	k_{Ag}/min^{-1}	Φ_{Pd}/eV	k_{Pd}/min^{-1}
C_3CH_3	4.98	0.0371	4.58	0.0198	4.83	0.00376
C_2CH_2OH	5.41	Untested	(4.86)	Untested	5.30	0.00518
C_2COOH	5.64	0.1339	5.09	0.1339	5.43	0.00344
$C_{11}CH_3$	4.78	0.0200	4.36	0.0015	4.74	0.00236
$C_{10}CH_2OH$	5.48	Untested	(4.89)	Untested	4.86	0.00443
$C_{10}COOH$	5.53	0.0325	5.22	0.0405	5.00	0.0184

Table 3.3   Table showing effective work functions Φ_{Eff} in electronvolts (eV) for a range of SAMs on Au, Ag and Pd and also the associated first order rate constants of photooxidation. Underlined values of Φ_{Eff} are below the photon energy of the 254 nm lamp used in the photooxidation experiment; values where the photon energy lies 2× the standard error (whether the average value is either below or above the photon energy) are given in brackets.

may be the case that the intermediate lattice spacing of the most favourable sites, as compared with the closer spacing on silver and further spacing on gold, causes the Pd–SR monolayers to pack extremely tightly, impeding the penetration of the oxidative species. It is known that the presence of bulky ω functionalities in Ag–SR SAMs causes them to adopt a looser mode of packing, characterised by $\sqrt{7} \times \sqrt{7}$, which increases k for the $C_{10}COOH$ SAM, while in general photooxidation proceeds much more slowly on Ag. If, however, the steric clashes are not sufficient enough on the marginally less tightly-packed Pd–SR SAM to force the thermodynamically less favourable adoption of a looser packing mode, $\sqrt{3} \times \sqrt{3}$ packing density might be maintained. It is suggested that, if this is the case, Pd–SR SAMs may require a much longer formation time, in order to heal defects in the SAM, as rate of healing is proportional to the chain mobility.

3.4.2   Photodegradation of OEO-SAMs

3.4.2.1   Investigation into Surface Composition as a Function of Exposure to 244 nm Light

A significant development in SAM photochemistry has been a shift away from the SAM-as-photoresist concept towards the design and building-in of photoactive groups or photocleavable linkers into the SAM molecule[38,39]. These are particularly well-suited to 'multicolour' photolithography or patterning *in situ e.g.* in a microfluidic cell, where it is not possible to have multiple separate 'wet' stages (which in any case increase the likelihood of sample contamination); it is much more desirable to be able to introduce structure by discreet exposure (or multiple exposures) to monochromated light. Of particular interest is the suggestion that photoactive groups might be transplantable into a variety of SAMs on substrates other than metals; silicon especially is cheaper and more readily compatible with present industrial microfabrication processes, and presents a flat, clean substrate for the formation of silane SAMs. These are thermodynamically more stable than M–SR SAMs. Mirroring the development of

polymeric photoresists used by the semiconductor industry, SAMs with photoactive or photocleavable groups have necessitated the inclusion of exotic chromophores, which present a synthetic challenge and are subsequently expensive. More readily available functional groups that exhibit useful photochemistry are therefore of great interest.

Following an initial structural investigation, a more extensive, time-resolved study was carried out. It was thought that, if the photodegradation process does in fact yield aldehydes, these should be conducive to the immobilisation of proteins. Glutaraldehyde coupling to aminated surfaces had been previously demonstrated as an efficient means to bind proteins that have exposed lysine groups, as these each contain a nitrogen with a free lone pair (nitrogens in bridging peptide functionalities, or even at the N-terminus of a polypeptide chain, are α to a carbonyl and so are sp^2 as apposed to lysine's side group nitrogen, which is sp^3 hybridised). The method of attachment is depicted in **figure 3.4.2** on the following page; the reaction scheme indicates that imine linkages are formed. However, aminated thiols have been shown to be bound by both moieties (*e.g.* as seen from the multiple binding modes of cysteine[40]) and under some biologically relevant conditions can etch gold[41], and so a method or irreversibly attaching proteins via aldehydes that does not require an aminated surface is desirable. The need to understand how the surface composition changes as a function of exposure arises because photochemical changes may be frustrated by competing reaction pathways. For instance, chloromethylphenylsiloxane SAMs produce aldehydes upon exposure to 244 nm light[39], which can natively bind free amines, but the reaction often progresses to carboxylic acids, which require an activation step. Moreover, OEO-SAMs have been shown to be effective films for resistance to biological adhesion, and so a one-step method to reverse resistance and produce a surface that is conducive to biomolecule immobilisation is extremely useful.
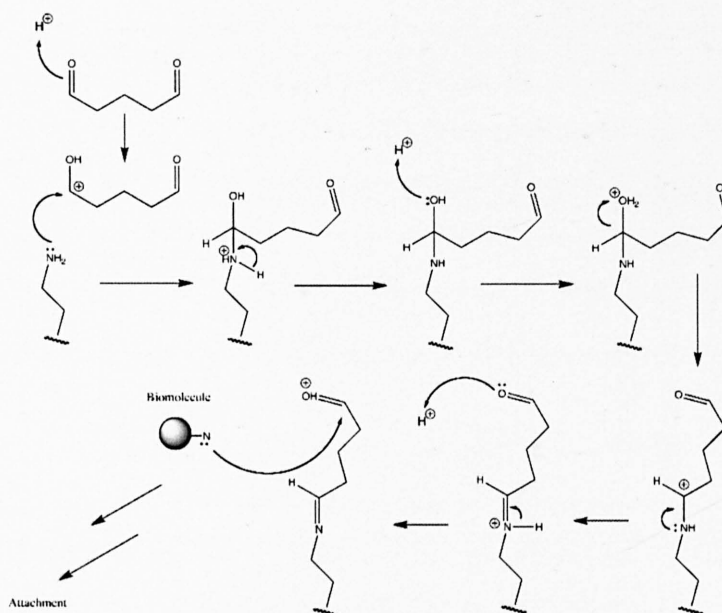
Figure 3.4.2   Glutaraldehyde Coupling Scheme

The composition of 'photodegraded' OEO SAMs for varying irradiative dosages was shown in figure 3.3.8 on page 123, which illustrates the formation of aldehyde groups on the surface. Clearly, the limiting yield is substantially less than one, though this is in-line with other surface bound reactions[28], which are often sterically constrained (so that an adduct may, by its bulk, eclipse some reactive groups surrounding that to which it has attached), and may disallow kinetically-optimal reaction geometries due to fixed orientations of reactive groups. In spite of this possible reduction in reactivity, biological attachment does not require the availability of a large number of activated groups—for instance, there may be only a small fraction of amino acids in an entire protein that are able to form covalent bonds in this manner (*i.e.* amines), and so covalent attachment at a few posistions on the biomolecule would be sufficient. As will be demonstrated in the next chapter, carboxylic acid groups are not necessarily a disadvantage (even if they are not activated by the use of a carbodiimide-activated ester chemistry), and may promote initial interactions between a biomolecule and functional surface, thus facilitating covalent attachment by aldehydes.

3.4.2.2   Biological Attachment to Photodegraded OEO-SAMs

The affinity of streptavidin for biotin has been the focus of much work in the field of materials biointerfaces, including force pulling work carried out by AFM[17]. In this instance, the affinity has been used to specifically capture a biotinylated plasma protein, IgG. The increased height observed following a short

immersion in a solution of the biotinylated protein increased the overall height of the regions previously covered by streptavidin, which had been attached by the selective irradiation of an OEO-SAM through a mask. This indicates in a qualitative fashion that the immobilisation has not perturbed, to the point of retarding its function, the geometry of pocket of streptavidin that has an affinity for biotin. This suggests that the immobilisation of functional biomolecules by this method is therefore potentially viable.

3.4.3   Glutaraldehyde Coupling of Thiols to Mercaptosiloxane SAMs

The promise of a simple route to thiol chemistry on silicon merited investigation. Because of the greater thermodynamic stability of silane SAMs, it has become desirable to find an efficient route to OEO systems on silicon, and some important work has been reported that sets out to do just this[42,43]. Although the attachment of the fluorinated amine to the photodegraded OEO film on the mercaptosilane SAM is modest, it might be considered that attachment to the photodegraded OEO-SAM on gold (figure 3.3.10 on page 124) was not entirely extensive, despite a greater density of photodegradable ether units. Again, it is suggested that only a few available sites are required to successfully immobilise a protein. Additionally, it has been shown that cysteine-containing proteins, as well as those which contain lysines, which are residues that have long being used to attach proteins, are likely to be immobilised by this method. Mechanistically, the transferability of the photodegradation chemistry onto a substrate other than gold implies that the elecronic rearrangements needed for photodegradation could be radical in nature. This hypothesis is supported by the appearance* of a peak at a shift of 2.02 eV, in the C_{1s} spectrum on gold, when exposed to a low dosage (*e.g.* 0.3 J cm^{-2}) of 244 nm laser. Such a shift may be indicative of epoxide formation in the initial stages; epoxides, with their strained geometries, are often formed by radical processes.

The work presented in this section is incomplete, but is generally suggestive of a novel means of attachment of biomolecules onto SAMs that merits further investigation, in order to optimise and fully characterise the processes that are taking place.

3.5   Conclusions

Photooxidation kinetics of a variety of SAMs on three substrates (Au, Ag & Pd) have been rationalised in the context of surface potentials imposed by their ω functionalites, and the variation of chain length

---

*not shown here—this is a possible alternative fit for the C_{1s} spectrum of an OEO SAM exposed to a dosage of 244 nm laser, as shown in figure 3.3.9 on page 124 (far left panel).

of the adsorbate molecules. The findings when a largely monochromated light source (*e.g.* the lamp) is used are consistent with the 'hot electron' model put forth by Huang and Hemminger, whereby sub-vacuum electrons made mobile by incident EMR of sufficient energy are able to tunnel into an orbital at the sulfur-metal interface and initiate the photooxidation process. For gold and silver, photooxidation chemistry of alkylthiolate SAMs is relatively simple. There is a strong correlation between the imposed surface potential of the SAM ω group and the rate of photooxidation. On silver, there is a precedent for competing processes occuring, whereby the S–C bond is cleaved by the action of UV light. There is the suggestion that Pd–SR SAMs may undergo at least partial S–C scission even as the films adsorb, potentially evolving an adlayer structure, which is easily removed by immersion in a contrasting thiol solution or when under vacuum. This explains why the ordering of rate constants follows very similar patterns for the long SAMs. For the short SAMs, there may be additional complexity due to the Pd–S interface. However, this is speculative and further work needs to be carried out to address whether this is the case.

Photodegradation of OEO-SAMs compares well with UV light-based activation of chloromethylphenyl-siloxane SAMs as a means to introduce biomolecules . In the case of the latter, halting the radical oxidation of the methylene group at the aldehyde stage requires accurate timing; it is difficult to stop the aldehyde becoming a carboxylic acid. In order to immobilise proteins on carboxylic acid surfaces, an 'EDC-NHS' activation is necessary. However, photodegradation of OEO-SAMs yields a higher proportion of aldehydes than carboxylic acids even at prolonged exposures, and aldehydes have been demonstrated as efficient means of immobilising SAMs with exposed lysine groups. Therefore, the 'one-step' nature of immobilisation of biomolecules via the photodegradation of the OEO functionality is assured. No further activation is required.

Attachment of thiols onto glutaraldehyde-activated mercaptosilane SAMs is a novel way to introduce thiol chemistry onto silicon, and it may be the case that many elusive functionalities for silicon systems can be introduced. The application of 'simple' organic chemistry to surface-bound modifications has a long precedent, and mechanisms investigated include esterifications, reductions, additions and substitutions. Simple coupling chemistries have facilitated the immobilisation of biomolecules on surfaces. Coupling of thiols to aldehydes presented the possibility of a new method of attachment. However, the nature of this work is preliminary and much further work needs to be done to assess whether the integrity and stability of these films is sufficient to enable biomolecular work in the laboratory.

Some of the work presented in this chapter has been published in Refs.[26,44]

List of Figures in Chapter 3

List of Tables in Chapter 3

Notes and References for Chapter 3

[1] G. E. Moore, "No exponential is forever: but "forever" can be delayed!," in *Solid-State Circuits Conference, 2003. Digest of Technical Papers. ISSCC. 2003 IEEE International*, pp. 20–23 vol.1, 2003.

[2] G. E. Moore, "Cramming more components onto integrated circuits," *Electronics*, vol. 38, pp. 114–117, April 1965.

[3] N. J. Brewer, *The structure, reactivity and bonding of self-assembled monolayers of gold and silver substrates*. PhD thesis, The University of Manchester, 2001.

[4] M. J. Tarlov, D. R. F. Burgess, and G. Gillen, "UV photopatterning of alkanethiolate monolayers self-assembled on gold and silver," *Journal of the American Chemical Society*, vol. 115, no. 12, pp. 5305–5306, 1993.

[5] J. Huang and J. C. Hemminger, "Photooxidation of thiols in self-assembled monolayers on gold," *Journal of the American Chemical Society*, vol. 115, no. 8, pp. 3342–3343, 1993.

[6] Zhou, Zhu, and J. M. White, "Photochemistry at adsorbate/metal interfaces," *Surface Science Reports*, vol. 13, no. 3-6, pp. 73–220, 1991.

[7] H. Rieley, N. J. Price, R. G. White, R. I. R. Blyth, and A. W. Robinson, "A nexafs and ups study of thiol monolayers self-assembled on gold," *Surface Science*, vol. 331-333, pp. 189–195, July 1995.

[8] M. H. Schoenfisch and J. E. Pemberton, "Air stability of alkanethiol self-assembled monolayers on silver and gold surfaces," *J. Am. Chem. Soc.*, vol. 120, pp. 4502–4513, May 1998.

[9] Y. Zhang, R. H. Terrill, T. A. Tanzer, and P. W. Bohn, "Ozonolysis is the primary cause of uv photooxidation of alkanethiolate monolayers at low irradiance," *Journal of the American Chemical Society*, vol. 120, no. 11, pp. 2654–2655, 1998.

[10] Y. Zhang, R. H. Terrill, and P. W. Bohn, "Ultraviolet photochemistry and ex situ ozonolysis of alkanethiol self-assembled monolayers on gold," *Chem. Mater.*, vol. 11, pp. 2191–2198, August 1999.

[11] N. J. Brewer, R. E. Rawsterne, S. Kothari, and G. J. Leggett, "Oxidation of self-assembled monolayers by uv light with a wavelength of 254 nm," *Journal of the American Chemical Society*, vol. 123, no. 17, pp. 4089–4090, 2001.

[12] D. R. Lide, *CRC Handbook of Chemistry and Physics, 88th Edition (Crc Handbook of Chemistry and Physics)*. CRC, June 2007.

[13] S. D. Evans and A. Ulman, "Surface potential studies of alkyl-thiol monolayers adsorbed on gold," *Chemical Physics Letters*, vol. 170, pp. 462–466, July 1990.

[14] D. M. Alloway, M. Hofmann, D. L. Smith, N. E. Gruhn, A. L. Graham, R. Colorado, V. H. Wysocki, T. R. Lee, P. A. Lee, and N. R. Armstrong, "Interface dipoles arising from self-assembled monolayers on gold: Uv-photoemission studies of alkanethiols and partially fluorinated alkanethiols," *J. Phys. Chem. B*, vol. 107, pp. 11690–11699, October 2003.

[15] J. C. Love, D. B. Wolfe, R. Haasch, M. L. Chabinyc, K. E. Paul, G. M. Whitesides, and R. G. Nuzzo, "Formation and structure of self-assembled monolayers of alkanethiolates on palladium," *Journal of the American Chemical Society*, vol. 125, pp. 2597–2609, March 2003.

[16] M. Montague, R. E. Ducker, K. S. L. Chong, R. J. Manning, F. J. M. Rutten, M. C. Davies, and G. J. Leggett, "Fabrication of biomolecular nanostructures by scanning near-field photolithography of oligo(ethylene glycol)-terminated self-assembled monolayers," *Langmuir*, vol. 23, pp. 7328–7337, June 2007.

[17] L. Häussling, B. Michel, H. Ringsdorf, and H. Rohrer, "Direct observation of streptavidin specifically adsorbed on biotin-functionalized self-assembled monolayers with the scanning tunneling microscope," *Angewandte Chemie International Edition in English*, vol. 30, no. 5, pp. 569–572, 1991.

[18] H. A. Biebuyck and G. M. Whitesides, "Interchange between monolayers on gold formed from unsymmetrical disulfides and solutions of thiols: evidence for sulfur-sulfur bond cleavage by gold metal," *Langmuir*, vol. 9, no. 7, pp. 1766–1770, 1993.

[19] Wolfram-Research, *Mathematica*. Wolfram Research, Inc., Champaign, IL, USA, 4.2 ed., 2002.

[20] The command has the format: N[Solve[Cos{C Degree}==f Cos{B Degree} + (1 − f){A Degree}, f]] where C is the measured contact angle (θ_a) of the photooxidised (binary) monolayer, B is the θ_a of the second replacing monolayer alone, and A is the θ_a of the SAM under study prior to photooxidation.

[21] D. A. Hutt and G. J. Leggett, "Desorption of butanethiol from au(111) during storage in ultrahigh vacuum: Effects on surface coverage and stability toward displacement by solution-phase thiols," *Langmuir*, vol. 13, no. 11, pp. 3055–3058, 1997.

[22] C. Pale-Grosdemange, E. S. Simon, K. L. Prime, and G. M. Whitesides, "Formation of self-assembled monolayers by chemisorption of derivatives of oligo(ethylene glycol) of structure $HS(CH_2)11(OCH_2CH_2)_mOH$ on gold," *Journal of the American Chemical Society*, vol. 113, no. 1, pp. 12–20, 1991.

[23] D. Briggs, *Surface Analysis of Polymers by XPS and Static SIMS (Cambridge Solid State Science Series)*. Cambridge University Press, May 1998.

[24] J. P. Rabe, J. D. Swalen, D. A. Outka, and J. Stohr, "Near-edge x-ray absorption fine structure studies of oriented molecular chains in polyethylene and langmuir-blodgett monolayers on si(111)," *Thin Solid Films*, vol. 159, pp. 275–283, May 1988.

[25] A. Ulman, "Formation and structure of self-assembled monolayers," *Chemical Reviews*, vol. 96, no. 4, pp. 1533–1554, 1996.

[26] N. J. Brewer, S. Janusz, K. Critchley, S. D. Evans, and G. J. Leggett, "Photooxidation of self-assembled monolayers by exposure to light of wavelength 254 nm: A static sims study," *Journal of Physical Chemistry B*, vol. 109, pp. 11247–11256, June 2005.

[27] P. Harder, M. Grunze, R. Dahint, G. M. Whitesides, and P. E. Laibinis, "Molecular conformation in oligo(ethylene glycol)-terminated self-assembled monolayers on gold and silver surfaces determines their ability to resist protein adsorption," *Journal of Physical Chemistry B*, vol. 102, pp. 426–436, January 1998.

[28] D. A. Hutt and G. J. Leggett, "Functionalization of hydroxyl and carboxylic acid terminated self-assembled monolayers," *Langmuir*, vol. 13, pp. 2740–2748, May 1997.

[29] D. A. Hutt and G. J. Leggett, "Influence of adsorbate ordering on rates of uv photooxidation of self-assembled monolayers," *J. Phys. Chem.*, vol. 100, pp. 6657–6662, April 1996.

[30] J. Clayden, N. Greeves, S. Warren, and P. Wothers, *Organic Chemistry*. Oxford University Press, USA, August 2000.

[31] K. L. Prime and G. M. Whitesides, "Adsorption of proteins onto surfaces containing end-attached oligo(ethylene oxide): a model system using self-assembled monolayers," *Journal of the American Chemical Society*, vol. 115, no. 23, pp. 10714–10721, 1993.

[32] N. J. Brewer, T. T. Foster, G. J. Leggett, M. R. Alexander, and E. McAlpine, "Comparative investigations of the packing and ambient stability of self-assembled monolayers of alkanethiols on gold and silver by friction force microscopy," *J. Phys. Chem. B*, vol. 108, pp. 4723–4728, April 2004.

[33] M. Yu, D. P. Woodruff, N. Bovet, C. J. Satterley, K. Lovelock, R. G. Jones, and V. Dhanak, "Structure investigation of ag(111) by x-ray standing waves: A case of thiol-induced substrate reconstruction," *Journal of Physical Chemistry B*, vol. 110, pp. 2164–2170, February 2006.

[34] J. P. Folkers, P. E. Laibinis, and G. M. Whitesides, "Self-assembled monolayers of alkanethiols on gold: comparisons of monolayers containing mixtures of short- and long-chain constituents with methyl and hydroxymethyl terminal groups," *Langmuir*, vol. 8, no. 5, pp. 1330–1341, 1992.

[35] R. N. Wenzel, "Resistance of solid surfaces to wetting by water," *Industrial & Engineering Chemistry*, vol. 28, no. 8, pp. 988–994, 1936.

[36] R. N. Wenzel, "Surface roughness and contact angle.," *Journal of Physical Chemistry*, vol. 53, no. 9, pp. 1466–1467, 1949.

[37] H. Sellers, A. Ulman, Y. Shnidman, and J. E. Eilers, "Structure and binding of alkanethiolates on gold and silver surfaces: implications for self-assembled monolayers," *Journal of the American Chemical Society*, vol. 115, no. 21, pp. 9389–9401, 1993.

[38] K. Critchley, L. Zhang, H. Fukushima, M. Ishida, T. Shimoda, R. J. Bushby, and S. D. Evans, "Soft-uv photolithography using self-assembled monolayers," *J. Phys. Chem. B*, vol. 110, pp. 17167–17174, August 2006.

[39] S. Sun, M. Montague, K. Critchley, M. S. Chen, W. J. Dressick, S. D. Evans, and G. J. Leggett, "Fabrication of biological nanostructures by scanning near-field photolithography of chloromethylphenylsiloxane monolayers," *Nano Lett.*, vol. 6, pp. 29–33, January 2006.

[40] R. Di Felice and A. Selloni, "Adsorption modes of cysteine on au(111): Thiolate, amino-thiolate, disulfide," *The Journal of Chemical Physics*, vol. 120, no. 10, pp. 4906–4914, 2004.

[41] R. E. Ducker and G. J. Leggett, "A mild etch for the fabrication of three-dimensional nanostructures in gold," *J. Am. Chem. Soc.*, vol. 128, pp. 392–393, January 2006.

[42] T. Bocking, K. A. Kilian, T. Hanley, S. Ilyas, K. Gaus, M. Gal, and J. J. Gooding, "Formation of tetra(ethylene oxide) terminated si-c linked monolayers and their derivatization with glycine: An example of a generic strategy for the immobilization of biomolecules on silicon," *Langmuir*, vol. 21, pp. 10522–10529, November 2005.

[43] T. L. Clare, B. H. Clare, B. M. Nichols, N. L. Abbott, and R. J. Hamers, "Functional monolayers for improved resistance to protein adsorption: Oligo(ethylene glycol)-modified silicon and diamond surfaces," *Langmuir*, vol. 21, pp. 6344–6355, July 2005.

[44] R. E. Ducker, S. Janusz, S. Sun, and G. J. Leggett, "One-step photochemical introduction of nanopatterned protein-binding functionalities to oligo(ethylene glycol)-terminated self-assembled monolayers," *J. Am. Chem. Soc.*, vol. 129, pp. 14842–14843, December 2007.

144

Chapter 4

Patterning of a Biological

Light-Harvesting Complex

Patterning of LH2 Contents

4.1 Introduction

4.1.1 Integrating Light-Harvesting Complexes into SAMs

The concept of integrating biological components into artificial molecular architectures—the 'bioklep-tic' approach—was presented in Chapter 1 as a viable means to solve some of the engineering problems facing nanotechnology. Like any machine (in the broadest sense of the term) that comprises all or part of a system, the placement of the biological component needs to be precise, and requires careful consideration of its fragility outside of the cellular environment from where it originates. Immobilisa-tion chemistries should be specific and thermodynamically favourable, but without compromising the structural integrity of the biological molecule or complex that is being integrated.

Precise structure, as has been discussed in Chapter 1, often affords an optimal efficiency in the working of the biological machine: Its abiliy to to transmute one form of energy into another. Retention of functionality is obviously desirable, and therefore the structure of the biomolecule should be protected during its integration. Self-assembled monolayers, with the broad range of surface ω groups available, are extraordinarily adaptable surfaces that have been demonstrated as viable biocompatible materials, both in terms of resistance to, and adhesiveness towards, biological structures (*e.g.* Refs[1–6]). Crucially, multiple procedures for directing immobilisation of biomolecules have been demonstrated that promote retention of biological functionality.

Mutagenesis of DNA from an organism to promote the expression of a protein featuring a 'mutant' amino acid with a functionality that better facilitates incorporation into a SAM has been explored by previous workers as a potential means of patterning. One particular approach is to introduce cys-teines (which feature mercaptomethyl *R* groups) into the protein structure to promote binding of the biomolecule to a gold or palladium surface in the same way as any other organothiol molecule. By this reasoning, it should be possible to photooxidise a region of SAM and introduce a cysteine-bearing biomolecule which will displace the weakly-bound sulfonates formed by photooxidation, and be immo-bilised in the patterned regions by the fomation of M–SR thiolate bonds. This is one potential method for incorporating biological systems into SAMs that will be explored.

Central to the implementation of structure at the supramolecular scale—the precise placement of the integrated biomolecule—is the formation of patterns, characterised by contrasting surface groups that aim to attract or repel biostructures. Several competing theories aim to account for the varied re-sponse of biomolecules in contact with SAM-modified surfaces presenting different ω chemistries,
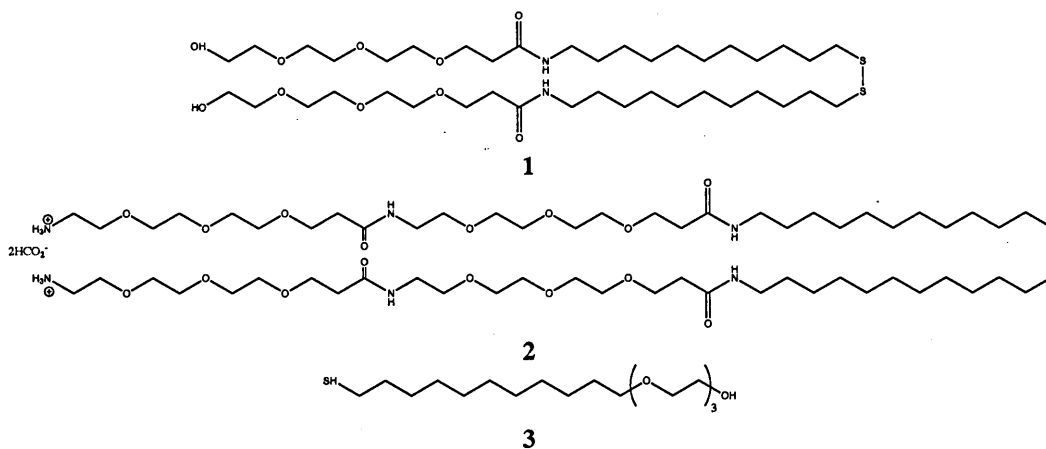
Figure 4.1.1   Structures of three oligo-ethylene oxide disulfide/thiol SAM molecules

including correlation with wetting behaviours (*i.e.* $\Delta G_{surface}$), and with the geometry of surface-bound oligo(ethylene oxide) moieties, among others.   While trends relating biocompatibility and chemical structures have become apparent, the lack of firm consensus on *e.g.* the mechanism of protein repulsion, necessitates a systematic exploration of a wide range of potentially viable surfaces. Indeed, much of the work already documented in the literature deals with the immobilisation of plasma proteins, whereas investigations into the immobilisation of membrane proteins, like the light-harvesting 2 complex (LH2) from *Rhodobacter sphaeroides*, which is the focus of this chapter, are not as widely reported. The first focus of this chapter will be a systematic exporation of of the affinity for LH2 of SAMs presenting different terminal group functionalities.

4.1.2   Stability of Biocompatible Surfaces

Long-term stability of SAMs in biological conditions, and also biocompatible SAMs in conditions like those used in patterning (*i.e.* in an organic solvent with 'contrasting' thiols or other SAM molecules, or an activating species or reactant) is of much interest for applications such as 'lab-on-a-chip' analysis, bioMEMs, and photolithography in liquid. Therefore, SAMs which demonstrate stability and retention of integrity over extended periods are desirable.

Liedberg and co-workers have demonstrated OEO-SAMs that have that amide links along their chain length[7,8]. These are depicted in **figure 4.1.1**, with short labels for reference to SPR spectrographs shown in the results.   It has been suggested that the amide links afford SAMs of these molecules a greater stability, by the formation of lateral interchain hydrogen bonds. An investigation of this hypothesis will form the second focus for this chapter.

4.1.3   Patterning LH2 and Demonstration of Retention of Biological Functionality

Photolithography has been shown to be an elegant means to introduce patterns on surfaces at very small scales, with a demonstrably high precision. While other techniques, such as μCP or DPN might produce structures with apparently comparable resolution under laboratory conditions, they perform rather less well than photopatterning does in an ultraclean environment. The obvious example would be the semiconductor industry, which is (at the time of writing) beginning to implement a 45 nm fabrication process. The precise, quantifiable action of light on photoactive molecular structures, plus the development of chemical activation processes with a minimal number of individual steps, ensures that photolithographic fabrication yields stable structures that are not as open to the risk of contamination inherent in direct-contact printing methods.

Knowledge of suitable surfaces for LH2 immobilisation can be considered alongside the photooxidation kinetics reviewed in Chapter 3 in order to optimise pattern fabrication. In addition to mask-based photolithography, scanning near-field photolithography (SNP) will be investigated as a potential tool, in order to determine whether LH2 is amenable to the formation of nanoscale patterns.

It has been stipulated that an essential criterion in assessing whether the patterning of functional biomolecular structures has been successful is the retention of functionality. Previously shown, in Chapter 3 on page 125, are results demonstrating retention of functionality of streptavidin, through its continued affinity for biotin following immobilisation; an affinity which derives largely from their respective shapes and proximal chemical groups when they are in contact. The most readily measurable function of LH2 is its fluorescence following irradiation, which occurs at a 50 nm shift to longer wavelength ($\lambda_{Abs_{Max}}$ = 800 nm; $\lambda_{Flu_{Max}}$ = 850 nm). Therefore, a system capable of measuring the fluorescence, as well as its intensity with spatial resolution, is required in order to assess successful immobilisation. This will form the third focus of this chapter.

4.2   Experimental Details

4.2.1   Integrating Light-Harvesting Complexes into SAMs

In order at assess whether the mutagenesis of *Rhodobacter sphaeroides* plasmid DNA to produce LH2 complexes containing cysteine was a viable method of immobilising LH2, viable bacterial cells with

this modification were generously provided by Dr. John Timney[*]. This particular modification featured a replacement of the *N*-terminal threonine of the β-subunit by a cysteine, as shown in figure 2.3.23 on page 90. The complexes were purified according the procedure outlined in subsection 2.3.3.1 on page 89. Additionally, LH2 'wildtype' complexes (which are those found in non-genertically modified strains) were obtained, already purified, and were a gift from Dr. John Olsen[†]. Following an unsatisfactory attempt to pattern LH2[‡] by the assumed photooxidation of OEO-SAMs on Au (which, as was shown in subsection 3.3.2 on page 122, is frustrated by competing processes), AFM topographs were collected of LH2 cysteine mutant and wildtype deposited from a HEPES/β-OG buffer solution onto flame annealed flat gold by immersion in the solution for 5 min. This was done to assess the state of the protein following immobilisation: Did the adsorption process cause denaturing, rendering the height less than that expected, and perhaps undetectable on polycrystalline films? Images were collected using a Nanoscope IIIa multimode AFM in tapping mode in air.

A range of SAMs were investigated to test for suitability for the directed immobilisation of LH2. Au–SR SAMs were made according to procedures outlined in section 2.5 on page 92, with the particular specifications that the Cr primer layer should be between 1.5–2 nm thick, and the gold layer 48 nm thick. It was found that these values match closely those of 'chips' available commercially, as measured by AFM height profile of a scratched slide, and films made to these specifications produced the most meaningful responses for SPR analysis. SAMs in any one repetition (of three) were made at the same time, with special consideration made to the placement of slides relative to the evaporation boats in the vacuum evaporator, as the quartz thickness sensor is calibrated for sample positions immediately above the evaporation boats, whereas places to the side of the vessel may have a substantially lower coverage. A reduced gold thickness can dramatically affect the sensitivity of the SPR experiment. Therefore, samples from directly above the boats were used.

In order to assess whether the cysteine mutants were afforded a greater affinity for the gold films, SPR experiments were performed using a Biacore 3000 SPR spectrometer. Ultra-low concentrations ($0.65\,\mu g\,mL^{-1}$) of LH2 cysteine mutant and wildtype in 400 mM HEPES/β-OG (1 %) buffer were introduced into a carrier stream of the same buffer at a flow rate of $10\,\mu L\,min^{-1}$. Typically, the concentrations used in work preceeding the author's to create good patterns have been an order of magnitude above this, *e.g.* $\sim$5 $\mu g\,mL^{-1}$, and the reason such a low concentration was chosen was to gauge the comparitive affinity of the mutant and wildtype when arriving at the surface more or less individually, rather than a large mass, which could obfuscate the clarity of the result if differences were small. The results, which

---

[*]Hunter Research Group, Department of Microbiology and Biotechnology, University of Sheffield, UK
[†]as above
[‡]not shown in this thesis

will be shown in figure 4.3.1 on page 154 then informed, along with the topographic AFM images, which

will be shown in figure 4.3.2 on page 155, the rest of the experiment. LH2 wildtype was then adopted

as the complex which would be investigated further. Therefore, subsequent SPR measurements and

immobilisation experiments use the wildtype. An improved purification protocol was also developed by

Dr. John Timney, which is based on a Tris buffer at pH 8 with 0.1 % LDAO surfactant, which was used

in subsequent experiments.

A range of C_{11} SAMs were chosen to represent a number of different surface types (the OEO-SAM

is slightly longer than this; the perfluorinated SAM, slightly shorter). Additionally, an activated ester

('$C_{11}COO$-∗'—the succinimide ester capable of binding proteins shown in figure 2.7.1 on page 95)

was tested; it had been previously demonstrated to covalently attach proteins that have exposed lysine

groups (which LH2 does—recall figure 2.3.23 on page 90; a XRD-solved structure, highlighting the

lysine residues, will be shown in the *discussion*).

Measurements were carried out on a Biacore 3000 spectrometer. All four flow cells were used for any

one run of a SAM, and these were averaged over three runs to produce a mean-response single trace for

each SAM. LH2 wildtype was produced in the same way as the cysteine mutant, and was a gift from

Dr. John Timney. 100 μL of LH2 in 10 mM Tris/LDAO buffer at a concentration of 6.5 μg mL^{-1} was

injected into a carrier stream∗ of the same buffer at a flow rate of 20 μL min^{-1} for 10 min, before elution

by Tris/LDAO buffer for 3 min and subsequent washing by the injection of an aqueous solution of 1 %

SDS for 10 s.

4.2.2   Stability of Biocompatible Surfaces

SAMs of the three OEO-terminated organosulfur molecules depicted in figure 4.1.1 on page 147 were

made according to standard SAM formation procedures outlined in section 2.5 on page 92, but at the

reduced concentrations of 0.25 mM. SAMs of molecule **2** were formed from aqueous solution using

nanopure water rather than HPLC grade ethanol, as the substance was received as a formate salt (as

shown in figure 4.1.1 on page 147), which is more soluble in water. In order to determine the response

of these SAMs to biological material, series of protein binding experiments were carried out using a

commercial Biacore 3000 SPR spectrometer. Again, 48 nm of gold was evaporated onto borosilicate

slides, primed with 2 nm of Cr. The response of the films to a variety of proteins, including LH2,

---

∗The carrier stream—buffer only—was allowed to run for 30 min prior to injection of LH2; penetration of water is thought
to be of importance in imparting biological resistance in OEO films, and short durations of exposure to aqueous and biological
media were shown to have little negative effect on SAM integrity.

was investigated. The proteins, each at a concentration of $5 \, \mu g \, mL^{-1}$, were injected into buffer-matched carrier streams running at a flow rate of $10 \, \mu L \, min^{-1}$ for 5 min, and the response was recorded.

In order to determine the relative stability of the amide-containing OEO films to the standard OEO-SAM, films were immersed in 10 mM of a C_{16} n-thiol for a range of durations. These samples were then analysed by XPS to determine the ratio $[C\text{-}\underline{C}\text{-}O]/[Au_{4f7/2}]$ in each case: A decrease in the value of this ratio might be interpreted as a loss of OEO-terminated molecules. 20 eV 'narrow' scans were collected corresponding to C_{1s} and Au_{4f} for each sample. Curves were fit using the CASAXPS software, which uses an iterative Marquadt sampling algorithm to converge Gauss-Lorentzian curves, representative of electron orbital environments, to the kinetic energy density profile of electrons ejected from the sample. The value at t=0 for each film was used to normalise the data, and this was set to 1 in each case, so that a value for χ, the mole fraction of the remaining OEO-SAM, could be calculated. For the amine/ammonium-terminated OEO-SAM **2**, a constraint was put on the curve fitting for the peak representing $C\text{-}C\text{-}NH_3^+$. The environment is close in binding energy to aliphatic $C\text{-}\underline{C}\text{-}C$ (at 285.65 eV vs. 285.0 eV), and thus may be masked. By considering equation (1.3.24) on page 44 and estimating the film thickness between the terminus and characteristic intrachain amide groups, it was calculated that the area should be $\approx 1.11 \times [N\text{-}C\text{=}O]$.

The experiment was repeated in triplicate and mean values are shown in the results.

4.2.3 Patterning LH2 and Demonstration of Retention of Biological Functionality

$C_2(CF_2)_5CF_3$ SAMs on gold were exposed to 244 nm UV using a frequency-doubled argon ion lase (model Coherent FreD 300C), using 1500 mesh or 2000 mesh Cu SEM grids as masks, for a period of 10 min, before being immersed in an ethanolic solution of a $C_{10}COOH$ thiol for a period of ~ 1 h to produce regions of carboxylic acid-terminated SAMs. For the lateral force images, which aim to demonstrate the nature of the template prior to protein immobilisation, samples were then removed from the second thiol and washed with HPLC grade ethanol, before being imaged. Samples were imaged using a Digital Instruments Nanoscope IIIa in contact mode, using a Si_3N_4 probe (nominal force constant $0.06 \, N \, m^{-1}$).

For the LH2 patterns, $C_{10}COOH$ regions on the pattern (which correspond to the unmasked areas) were activated by carbodiimide chemistry to introduce a thermodynamically metastable succinimide ester[*],

---

[*]A scheme is shown on on page 95

which is readily displaced by basic groups such as primary amines, which LH2 features in some number on its surface. This was achieved by immersing the patterned SAM in an ethanolic solution of 20 mM N-(3-Dimethylaminopropyl)-N-ethylcarbodiimide ('EDC') and 20 mM N-hydroxysuccinimide for 20 min. Following washing, the patterned and activated samples was immersed in a 6.5 µg mL^{-1} solution of LH2 wildtype in 20 mM Tris, 0.1 % (wt.) LDAO, 150 mM KCl buffer for 15 min. The sample was then washed with a 1 % (wt.) solution of aqueous ammonium acetate (using nanopure water), followed by 'clean' nanopure water. This washing cycle was repeated 3 times. The sample was then dried under a stream of nitrogen and its topography was imaged in intermittent contact mode (Digital Instruments Nanoscope IIIa, Tapping Mode) using a silicon probe (k=30 N m^{-1}, f_0=232–262 kHz).

Additionally, the amenability of LH2 to patterning on the nanoscale was explored. Scanning near-field photolithography (SNP) was carried out with the help of Rob Ducker*. For the work presented here, a commercially-sourced Jasco probe was used. The position of the stylus relative to the surface was controlled by the use of the Aurora III NSOM system. During SNP, the output of the laser was 2 mW, and the writing speed was 0.1 µm s^{-1}.

4.2.3.1 Optical Measurements of LH2

For the optical measurements, samples were quickly transferred from solution containing the LH2 complexes to a 'clean' Tris/LDAO buffer solution, to wash away non-specifically bound complexes. The sample was then dried under a stream of helium to allow the underside to be glued to a copper mount in the cryostat, and remove excess buffer from the sample. This was done without subsequent washing with ammonium acetate or water following the buffer wash†. The atmosphere in the cryostat was then evacuated to a pressure of 10^{-9} mbar prior to cooling by liquid helium, to avoid the condensation of liquified gases on the sample. The sample was then illuminated using a 800 nm laser photodiode, and fluorescence as a function of wavelength was measured using a CCD. In order to remove any signal caused by the excitation source leaking into longer wavelengths, a long-pass filter (>825 nm) was used. Measurements were made 'in the dark', with the utmost care taken to remove any light sources that could cause interference, *e.g.* from computer monitors *etc.*

Spatially-resolved fluorescence measurements were carried out using an avalanche photodiode (APD) in place of the CCD in the same optical arrangement as that described above, again using a long pass filter. A XYZ stage movable in the XY plane by computer-controlled piezotransducer was used to control the

---

*currently in the Zauscher laboratory, Duke University, NC, USA
†the reason for these omissions will be given in the discussion

position of the objective lens in relation to the patterned sample, achieving a maximum resolution of $\sim 2\,\mu m$. The software used to do this was developed by Pu Qian[*] and Luke Wilson[†] using the LabView development system. The piezo allows the stage supporting the lens to be moved by precise amounts prior to recording an integration of the photon count for a given period *e.g.* 400 ms, in order to produce and effective intensity map of the fluorescence.
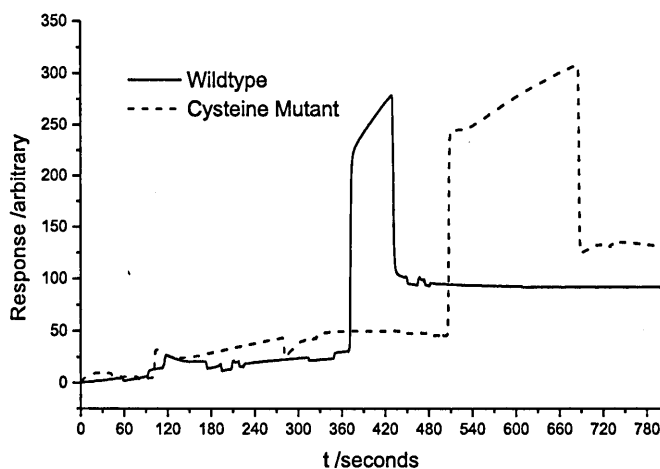
[*]now in the Department of Molecular Biology and Biotechnology, University of Sheffield; then in Department of Physics and Astronomy, University of Sheffield

[†]Department of Physics and Astronomy, University of Sheffield

4.3 Results

4.3.1 Integrating Light-Harvesting Complexes into SAMs

Figure 4.3.1 Surface plasmon resonance spectrograph indicating the degree of interaction between wildtype (solid line) and cysteine mutant (dashed line) LH2 complexes and a gold surface; greater affinity is indicated by a larger response.

Figure 4.3.1 shows typical SPR traces of LH2. The response units on the y-axis, though supposedly parametrized so that $1000\,RU \equiv 1\,ng\,cm^{-2}$, are here largely considered to be arbitrary. What is to be assessed is the comparitive difference following injection and elution between both strains of LH2. The traces in this instance reflect the fact that solutions were injected at arbitary times during each trace for arbitary periods. Traces for the the opposing strains were collected at different times and have been overlaid for comparison. The major injection for the wildtype (solid line) occurs just after 60 s and and the injection continues for approximately 1 min, before elution by buffer. The height difference after injection is ~57 RU. The major injection for the mutant occurs at 510 s and lasts 3 min; the height difference in this instance is ~82 RU. While the injection periods were not equal, it is clear that the introduction of cysteines into the complex affords LH2 only a minor increase in affinity for the gold, which will be discussed further on on page 171.

Shown in **figure 4.3.2** on the next page are AFM topographs of cysteine mutant (a) and wildtype (b) LH2 deposited on flame-annealed epitaxial flat gold. Shown in (c) and (d) are phase images of (a) and (b), respectively, to assist in seeing the shape of the complexes. It can be seen that the complexes tend to be aligned along the edges of atomic terraces in both instances. However, it appears that the cysteine

(a) LH2 cysteine mutant topography   (b) LH2 wildtype topography

(c) Phase image of above   (d) Phase Image of Above
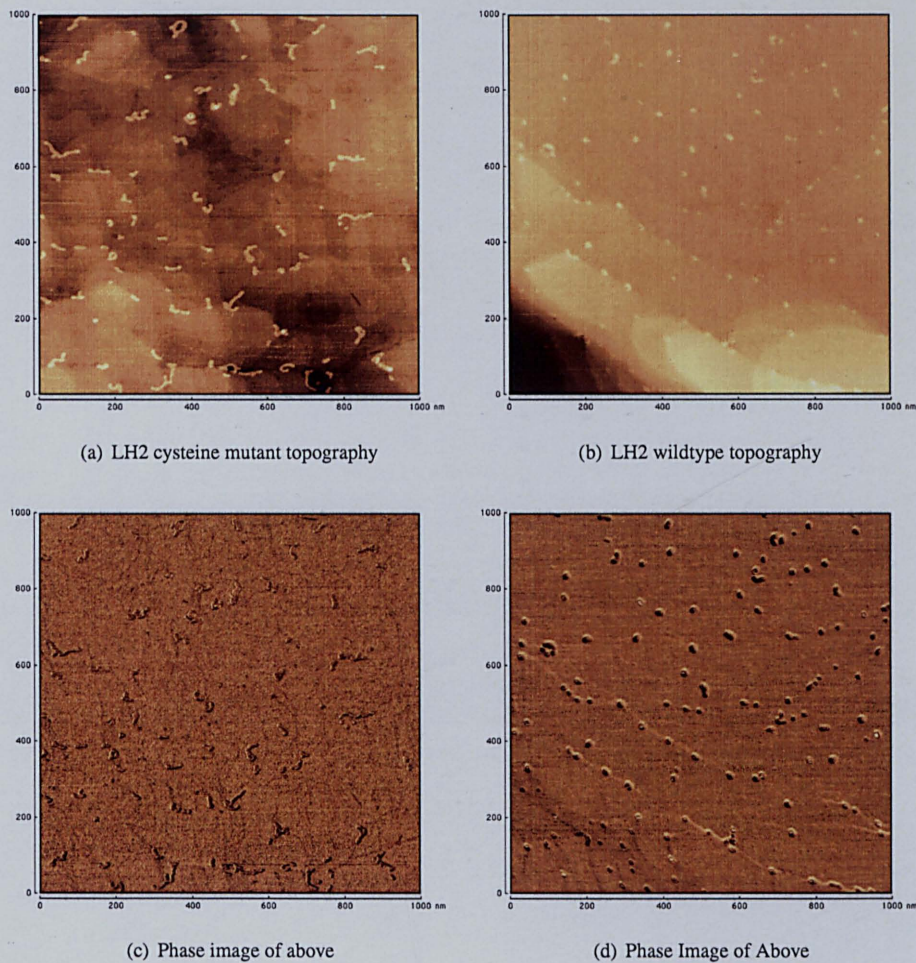
Figure 4.3.2   LH2 on flame-annealed flat gold

mutant (a, c), appears as strands, perhaps indicating denaturing of the complex, whereas wildtype (b, d) appears as intact rings. An explanation for this result will be put forth in the *discussion*.

In order to assess suitability of a wide range of SAMs for the incorporation of LH2 complexes, a wider study of adsorption of the wildtype on a variety of SAMs was carried out. The results are shown in **figure 4.3.3** on the following page. Upon injection, it can be seen that some degree of interaction occurs for each of the SAMs that were studied, due to the influx of such a large molecular weight species into the region proximal to the SAM. Following the 10 min injection period, a buffer-only flow for a duration of 3 min allows an assessment of physisorption to be made. It is clear that the OEO-SAM (trace 6) is indeed resistant to LH2 bioadhesion (as indicated by a rapid return to the signal baseline), as might be expected. However, two hydrophobic SAMs, $C_{11}CH_3$ (trace 5) and $C_2(CF_2)_5CF_3$ (trace 7), also exhibit resistance to LH2, which might not have been expected. A rationalisation of this will be put forth in the *discussion*.
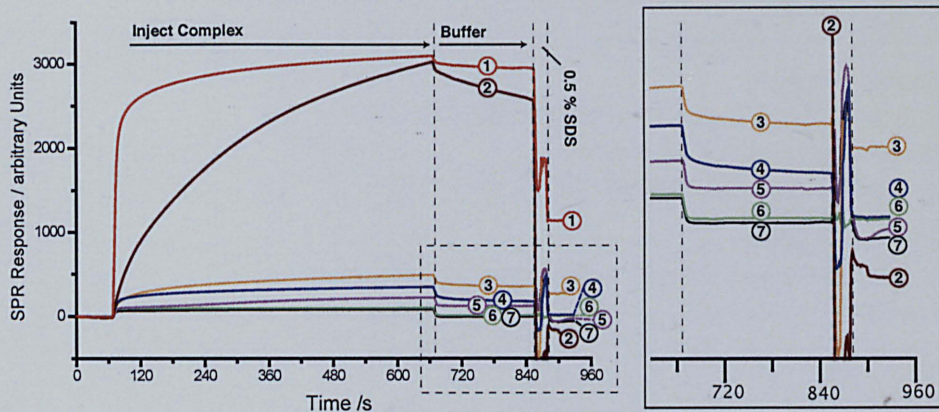
① 'C₁₀COO-*' ② C₁₀COOH ③ Bare gold ④ C₁₁OH ⑤ C₁₁CH₃ ⑥ C₁₁(OCH₂)₃OH ⑦ C₂(CF₂)CF₃

Figure 4.3.3   SPR Curves for a range of SAMs showing the level of interaction with $6.5\,\mu g\,mL^{-1}$ wildtype LH2 from *Rhodobacter sphaeroides*

4.3.2   Stability of Biocompatible Surfaces

In order to assess whether films composed of the molecular structures '**1**' and '**2**' from figure 4.1.1 on page 147 were in fact protein-resistant, a series of SPR experiments were carried out. Four biomolecules consisting of single proteins, complexes and enzymes were used. These were:

BSA   bovine serum albumin from *Bos taurus*

ACP   acyl carrier protein from *Bacillus circulans*

LH2   light harvesting complex 2 from *Rhodobacter sphaeroides*

PPTase   phosphoryl transferase from *Bacillus circulans*

Four sets of traces for each protein show averaged traces from three repeat measurements for each film in **figure 4.3.4** on the following page. In each trace, '**1**' is represented by a dashed line, '**2**' by a dotted line, and '**3**' by a solid line. For each of the four proteins tested, a similar response that is indicative of a degree of protein resistance is observed on '**1**' as it is for '**3**', which is already well-established as a protein-resistant SAM. '**2**' demonstrates an increased affinity for protein overall, but the degree to which this can be stated varies for each of the different proteins. In order to allow a comparison to be made between the amount of biomolecular material retained during elution by buffer on each film following injection of each protein, the difference between the RU value before and after injection is tabulated in table 4.1 on page 158.

(a) Bovine serum albumin

(b) Acyl carrier protein

(c) LH2 wildtype

(d) Phosphoryl transferase
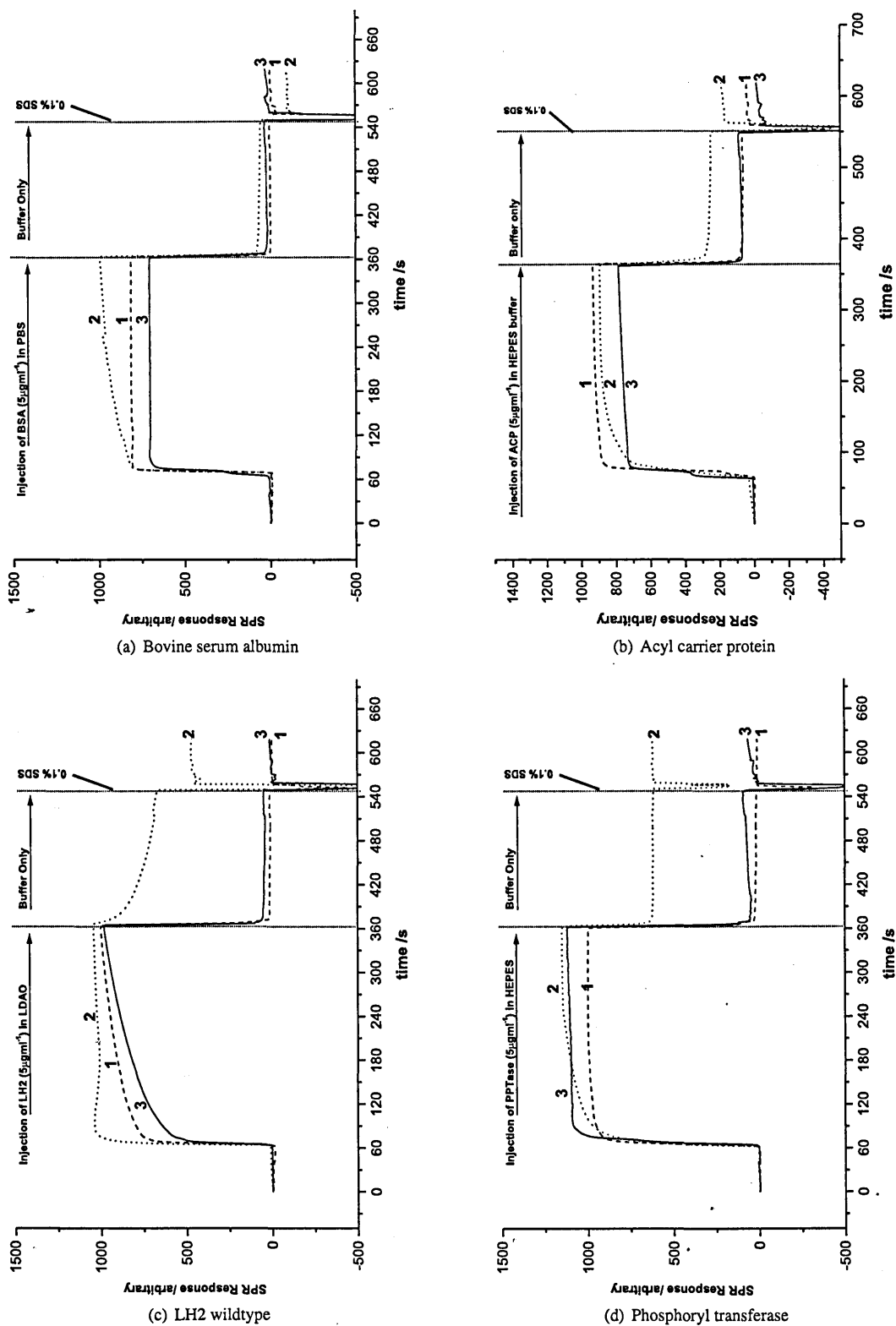
Figure 4.3.4   Surface plasmon resonance traces indicating the degree of interaction between 4 different polypeptides and three different OEO SAMs, the structures of which are shown in figure 4.1.1 on page 147.

157

	Biomolecule			
SAM	BSA	ACP	LH2	PPTase
1	4.5	67	25	~0
2	55.5	214	662.5	2.2
c	14	67	43.4	0.2

Table 4.1 Comparison of binding of the four proteins tested (in RU) on each of SAMs **1, 2** and **3**

It can be seen that the biggest increase in affinity for **2** over **1** or **3** is for the complex LH2, the structure of which was introduced in subsection 1.5.3 on page 70. Acyl carrier protein exhibits the second greatest affinity for **2** as compared with **1** or **3**, and bovine serum albumin the third, although the response when BSA was injected was lower for **1** or **3** than when ACP was injected (BSA on **1** was lowest overall), suggesting that BSA had less of an affinity for all three surfaces. PPTase demonstrated remarkably low affinity for any of the surfaces. Possible reasons for these differences will follow, in the *discussion*.

Shown in **figure 4.3.5** on the next page are typical C_{1s} spectra from three OEO-SAMs, at top as they were made; and at bottom after immersion in a 10 mM solution of $HSC_{15}CH_3$ for 180 h. It can be seen that the characteristic C-$\underline{C}$-O peak associated with all three OEO SAMs has decreased over the duration of the experiment, and this is matched in **1** and **3** by a decrease in N-$\underline{C}$=O, and in **2** by a decrease in C-$\underline{C}$-NH_3^+. Shown in **figure 4.3.6** on page 160 are three plots showing the change in the ratio C-$\underline{C}$-O/$Au_{4f7/2}$ over time, fitted as 0, 1st and 2nd order changes. While previous work[9] has considered the kinetics of replacement to be well-modelled as a first order change, it is not apparent from these results that this is the case here. It is possible that there is a degree of cooperativity afforded by the additional intrachain amide moieties that retards detachment even after the thiolate has oxidised and the weakly-bound species is immersed in a solution of contrasting thiol. A second order fit is most satisfying for 1 and 2, whereas for 3, none of the fits are particularly satisfying. It is possible that in all cases, desorption is characterised first by a period of fairly rapid detachment at grain boundaries *etc.* where the stabilising lateral interactions are diminished, followed by a much slower rate of detachment.
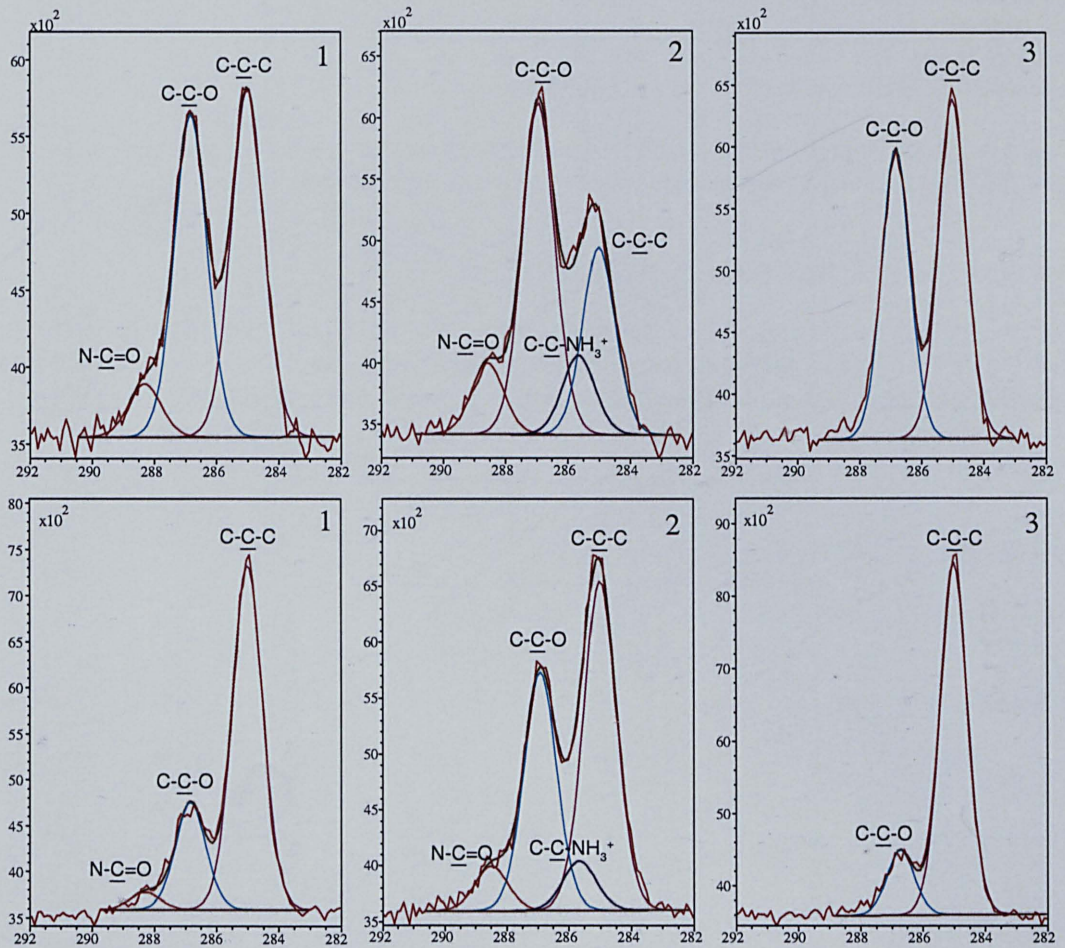
Figure 4.3.5 XPS C spectra of the three OEO-SAMs shown in as made (top row) and following immersion in 10 ethanolic solution of HSCCH for 180 (bottom row).
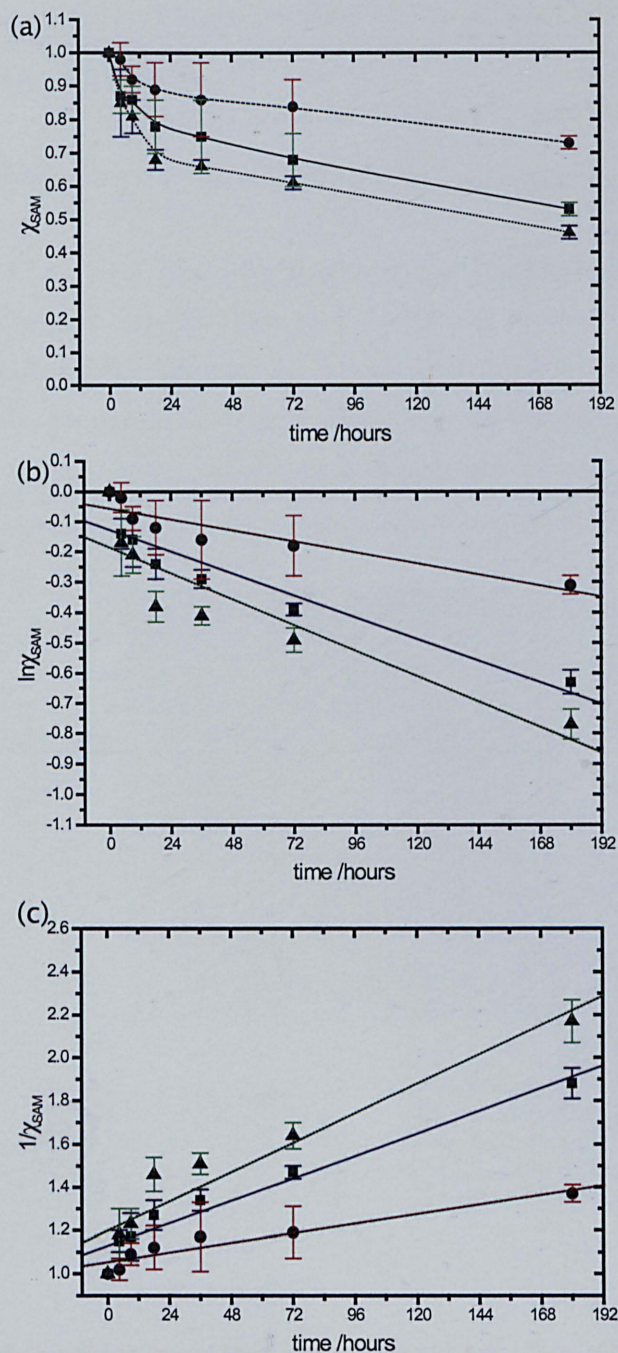
Adsorbate	Symbol	1st order k_d/h^{-1}	relative 1st order k_d	2nd order k_d/Θ^{-1}h^{-1}	relative 2nd order k_d
1	■	0.00299	0.85	0.00435	0.76
2	●	0.00151	0.43	0.00185	0.33
3	▲	0.00353	1	0.00569	1

Figure 4.3.6 (a) Plot showing remaining monolayer fractions () of OEO SAMs **1, 2 & 3** (from 4.1.1) remaining after immersion in 10 mM C$_{16}$ thiol solution for a range of durations. (b) shows the natural logarithm of the remaining fraction against immersion time to test the fit as a 1st order change, while (c) shows the reciprocal of the fraction remaining to test the fit of the data as a 2nd order change. In (b) and (c), the fit to a straight line indicates adherence to the model of rate order being tested.

4.3.3 Patterning LH2 and Demonstration of Retention of Biological Functionality

4.3.3.1 Lateral force images of patterned SAMs

Shown in **figure 4.3.7** is a lateral force image of a patterned $C_2(CF_2)_5CF_3$ SAM; the dark 'bar' regions are the perfluorinated SAM, while the lighter squares are the acid-terminated regions which have replaced the photooxidised perfluorinated regions. The polar Si_3N_4 tip adheres more strongly to the polar regions, giving rise to a higher rate of energy dissipation there and hence a higher friction force. The scan angle was set at 90°, as this maximises the effect of lateral deflection, producing an image with an optimal contrast range.
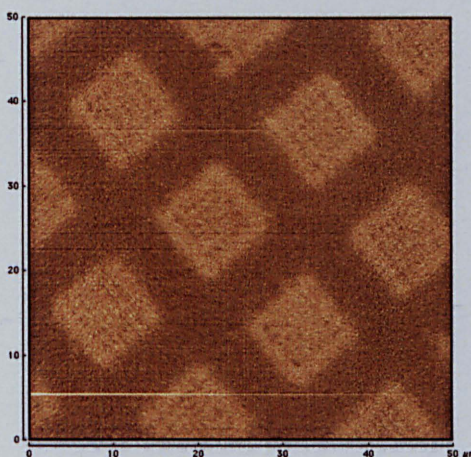
Figure 4.3.7   Lateral force image of a $C_2(CF_2)_5CF_3$ SAM that has been exposed to a 244 nm laser set at 100 mW for 10 min through a 1500 gauze Cu SEM grid, before being immersed in a 1 mM $C_{10}COOH$ solution for 10 min and then washed with ethanol. Scan angle was 90°, scan rate was 3 Hz. Lighter squares indicate where the polar Si_3N_4 tip adheres more strongly, corresponding to an acid-terminated surface, while darker regions correspond to the initial fluorinated surface that was not exposed to the laser.

4.3.3.2 Intermittent contact-mode mode images of LH2

Shown in **figure 4.3.8** on the following page is an AFM height image of a sample made in the same way as that shown in 4.3.7, following activation by carbodiimide solution, and then immersion in a solution of LH2 in aqueous biological buffer (6.5 µg mL^{-1} in 10 mM Tris/LDAO : 0.1 %) . The sample was in the biological solution for 10 min. The measured height, at ~4 nm, is actually below that expected for LH2 (ca. 7 nm), but it is not uncommon for measurements of soft samples by AFM to yield topgraphical heights that are anomalously low. Even in intermittent contact, the sample can be deformed by a

161

relatively hard silicon AFM probe as it comes into contact. The consistency of the image shows that

LH2 is successfully patternable by this method.
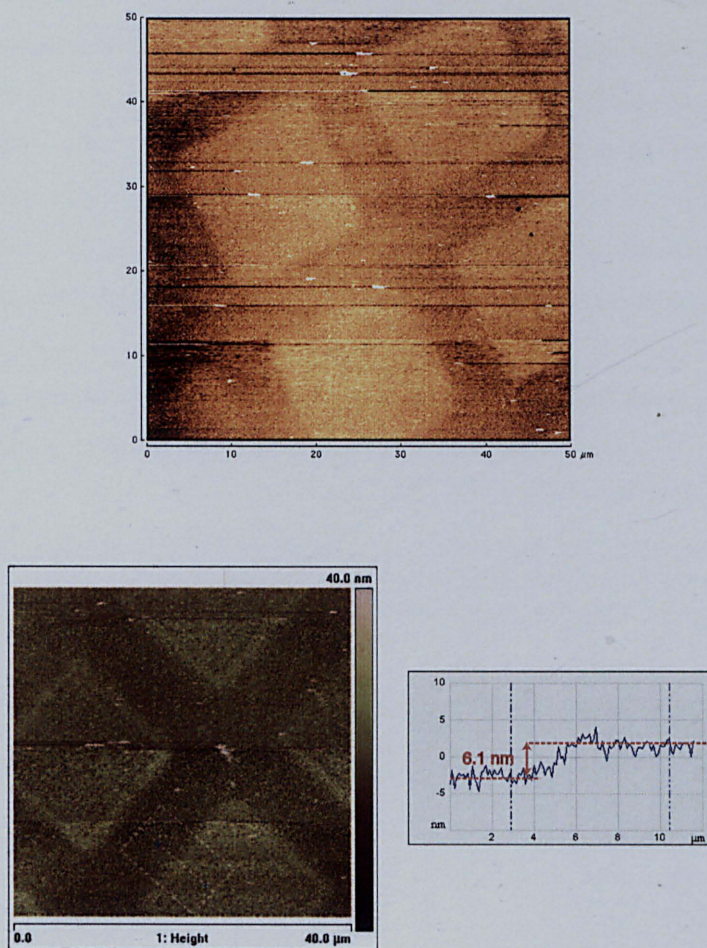
Figure 4.3.8 AFM tapping mode height image and line section of a patterned C(CF)CF/CCOOH
sample made in the same way as that shown in 4.3.7, that has been activated by immersion in
carbodiimide solution, and then immersed in a solution of LH2 in aqueous biological buffer. LH2
has been immobilised in the square regions, as indicated by the height difference as compared
with the surrounding regions, which are the initial C(CF)CF SAM, to which LH2 will not stick.
Scan rate was 1 Hz.

### 4.3.3.3   Lateral force mode images of nanopatterned SAMs

In order to explore the amenability of the perfluorinated SAM to patterning by scanning near-field

photolithography, an array of spots was formed by configuring the NSOM system to include a number

of equidistant dwell points along a line (in this instance, five, spaced 2.5 µm apart), and repeating this for

a a series of equidistant parallel lines (again, five) to create an array of photooxidation points. The probe was rastered quickly between each dwell point (velocity~$10\,\mu m\,s^{-1}$) and the dwell time was set to 4 s. The nominal power output of the 244 nm laser used was 2 mW. Following the lithography procedure, the SAM was immersed in a 1 mM solution of $C_{10}COOH$ thiol for 20 min, before removal, washing with HPLC grade ethanol and drying under a stream of nitrogen. A lateral force micrograph of the $C_{10}COOH$ dot array 'written' on a $C_2(CF_2)_5CF_3$ SAM was acquired in air at a scan rate of 2 Hz, at scan angle of 90°. This is shown in **figure 4.3.9**. Although there is a good contrast in the image, the spot size is actually quite large, with a full-width half maximum height (fwhm) dimension of 237 nm. This result was somewhat unexpected given the relatively slow rate of photooxidation of the $C_2(CF_2)_5CF_3$ SAM; it was thought that longer dwell times would be required, and that it might be difficult to form nanoscale lines by SNP on the perfluorintaed SAM. This informed the subsequent experiment, in which a series of lines were drawn by SNP using the same patterning system as for the array.
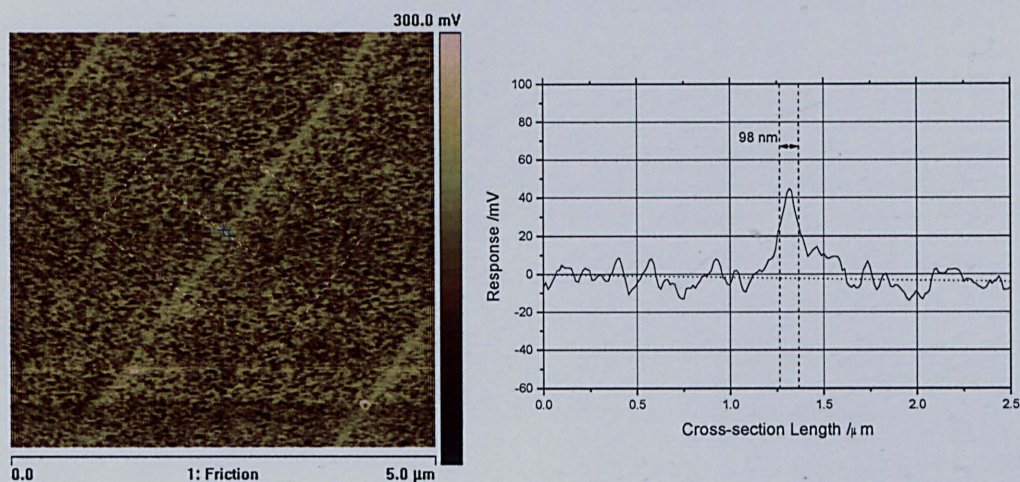

fwhm = 237 nm
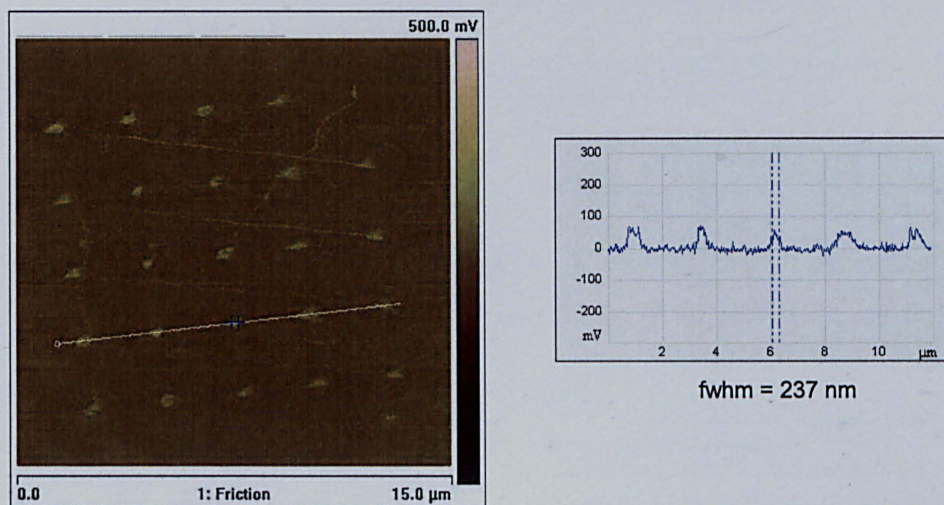
Figure 4.3.9   AFM contact mode image of $C_{10}COOH$ 'dots' written into a $C_2(CF_2)_5CF_3$ SAM by exposure of a SAM of the latter thiol to 244 nm laser through a NSOM probe maintained in the near field. The scan angle was 90° and the scan rate was 3 Hz. The polar Si_3N_4 tip adheres more strongly to the acid-terminated dots, resulting in greater contrast, than the surround perfluorinated region, which the tip adheres to less strongly. The full width half maximum height (fwhm) of the features—a good estimation of their true dimension accounting for distorion due to finite tip size—is 237 nm.

Figure 4.3.10 on the following page shows a series of 5 lines, 10 μm in length and spaced 2.5 μm apart, that were drawn using the SNP method into a $C_2(CF_2)_5CF_3$ SAM, as for the array shown previously, before immersion into a contrasting thiol of $C_{10}COOH$ for 20 min. In this instance, the nominal laser power was 2 mW, and the writing speed was $0.1\,\mu m\,s^{-1}$. The image shown was collected at a scan rate of 2 Hz at a scan angle of 90°. A section analysis indicates that the fwhm width of the line is 98 nm.
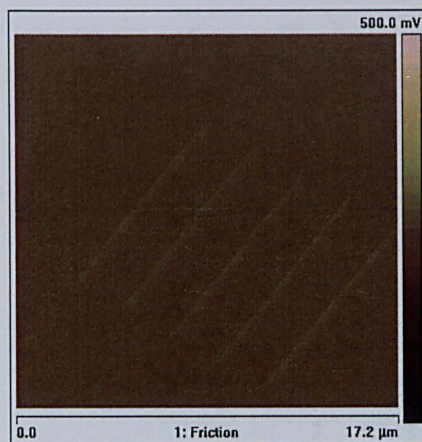
(a) LFM micrograph of nanolines of $C_{10}COOH$ in a SAM of $C_2(CF_2)_5CF_3$

(b) Expansion of above and averaged line section indicating line width

Figure 4.3.10   AFM contact mode image of $C_{10}COOH$ lines written into a $C_2(CF_2)_5CF_3$ SAM by exposure of a SAM of the latter thiol to 244 nm laser through a NSOM probe maintained in the near field. The scan angle was 90° and the scan rate was 3 Hz. The polar Si_3N_4 tip adheres more strongly to the acid-terminated lines, resulting in greater contrast, than the surround perfluorinated region, which the tip adheres to less strongly. The full width half maximum height (fwhm) of the lines is 98 nm. This is markedly smaller than the diameter of the 'dots' shown in 4.3.9.

### 4.3.3.4   Intermittent-contact mode images of nanopatterned LH2

Shown in **figure 4.3.11** on the next page are tapping mode mode images of the LH2 nanolines collected on a Nanoscope IIIa AFM at a 0° scan angle at a scan rate of 1 Hz. Lines shown in the image were measured to be approximately 98 nm wide (mean average), and as low as 93 nm over shorter averaged cross sections (shown). Lines were subjected to a statistical analysis of their profiles at regular intervals along their length, as depicted in **figure 4.3.12** on page 166. By a statistical analysis of 5 cross sections of

the lines, perpendicular to their direction in the surface plane, the mean line height was determined to be

6.2 nm with a standard deviation of ±1.8 nm, which is commensurate with there being a monomolecular

layer of LH2 on the surface.

fwhm = 93 nm
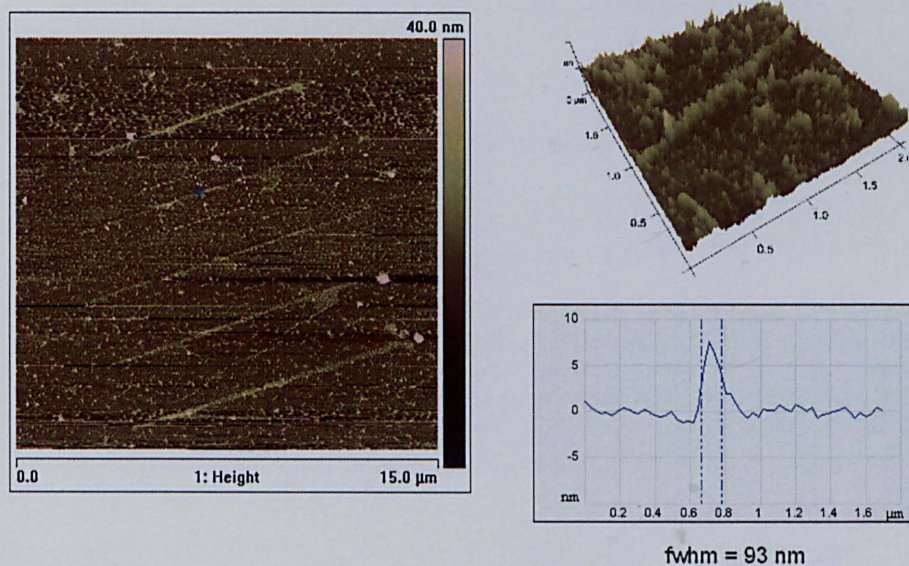
Figure 4.3.11   AFM tapping mode of a $C_2(CF_2)_5CF_3$ SAM patterned using a NSOM probe in the same manner as was used to create the C_{10} lines in figure 4.3.10 on the preceding page, which has then been activated by immersion in carbodiimide solution, and then immersed in a solution of LH2 in aqueous biological buffer. LH2 is deposited along the activated lines, as indicated by their greater height as compared with the surrounding perfluorinated region. The height difference correlates closely to the average cross sectional dimensions of LH2. The full width half maximum height of the features is 93 nm. The image was acquired at a scan rate of 1 Hz; scan angle was 0°.
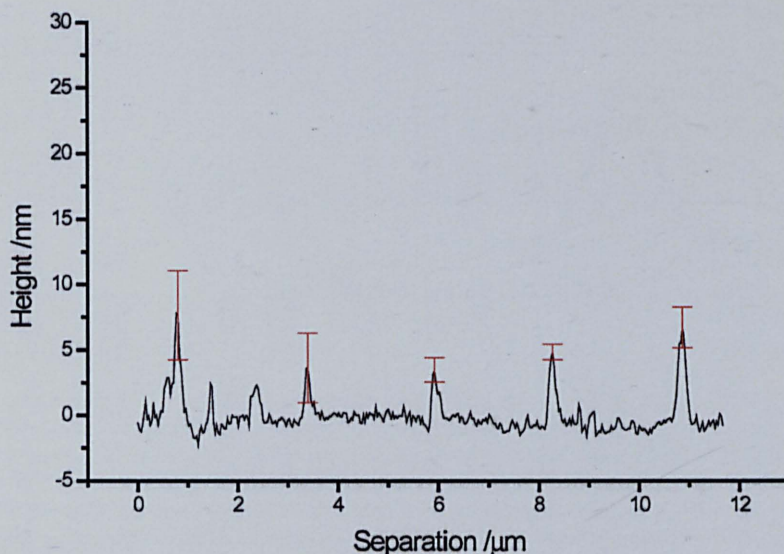
Figure 4.3.12   Typical cross-sectional profile of the LH2 'nanolines' shown in 4.3.11. Red bars show
the variance in line height of each of the five lines. These correlate with the dimensions of a
single LH2 complex in the four lines to the right of the plot, indicating monolayer coverage. It is
possible that there may be a second layer along some of the length of the line, the cross section
of which is shown at the far left of the plot, although the mean height still closely matches that
which would be expected from the deposition of a single layer of complexes.

4.3.3.5   Optical Measurements of LH2

In order to assess whether the biological function of LH2 was retained during immobilisation, a number
of optical measurements were made of LH2 in both the solution phase and following directed patterning
onto a SAM. The principal rôle of LH2 is to 'retune' incident EMR to a longer wavelength by a Stokes-
shifted fluorescence, which effectively shifts the fluorescence maximum to a longer wavelength (for
LH2, the absorbance maximum is at 850 nm, while the fluorescence maximum is at 800 nm).

Fluorescence spectra were collected at room temperature in a liquid cell in the dark, using a CCD. A
long-pass filter (>825 nm) was used to occlude the 800 nm photodiode excitation source. Two spectra
are shown, in **figure 4.3.13** on the next page, for LH2 immobilised via the EDC-NHS method onto an
acid-terminated region of a patterned SAM (right hand side). For comparison, the spectral response of
solution phase LH2 (in buffer) is also shown (left hand side). It can be seen that the signal is much
lower when the complex is bound to the surface (roughly 6 % of that in the bulk), which reflects the
fact that the fluorescence arised from a single layer of complexes, rather than from solution, in which a
large number of complexes are present in a three-dimensional volume within the focal length range of
the collection spot.

In order to test whether it was possible to collect spatially-resolved fluorescence images of patterned
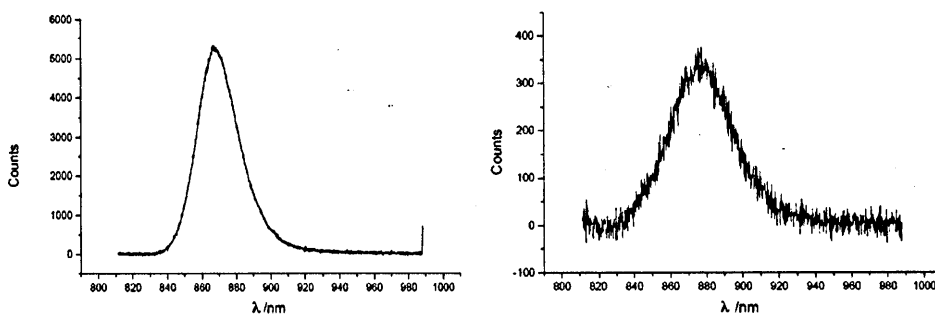
Figure 4.3.13   (a) CCD luminescence Spectrum of $260\,\mu g\,mL^{-1}$ LH2 in aqueous biological buffer following excitation using a 800 nm laser photodiode; (b) CCD luminescence spectrum of LH2 immobilised on a CCOOH SAM on gold following excitation using a 800 nm laser photodiode. Note that, though lower in intensity, the spectrum immobilised on the surface is essentially the same as free in solution, indicating retention of spectral properties. A band pass filter filtering out wavelengths 825 nm was placed in the collection optics during acquisition of both spectra.

LH2, micron-scale patterns were first formed in the same manner as in subsection 4.3.3.2 on page 161. Samples were not washed in water and ammonium acetate as was the case for the AFM experiments, but were immediately transferred to a buffer devoid of LH2, in order to remove complexes that are non-specifically bound, then removed and dried under helium to remove the fluid and glued to a support in a vacuum cryostat, before being put under vacuum and cooled to $<10\,K$ using liquid helium. The Labview software, APD and stepped-piezo-driven XY stage described in subsection 4.2.3.1 on page 152 was used to collect an image of size $60\,\mu m \times 60\,\mu m$. This is shown in **figure 4.3.14** on the following page. Light squares indicate the presence of light of wavlengths greater than 825 nm, indicating that the source is most likely fluorescence from LH2 rather than a tail-off to longer wavelength of light emitted by the photodiode. The light patches also correspond to the squares where the LH2 is expected to be immobilised by the carbodiimide, further supporting this conclsion. It is clear that LH2 directed to form patterns using this chemistry must have retained its biological function (fluorescence at $\sim 850\,nm$ following excitation at 800 nm), despite being at tested conditions that differ greatly from those within the organism (*i.e.* in a very good vacuum, at $<10\,K$) which is a testament to the resilience of these structures.
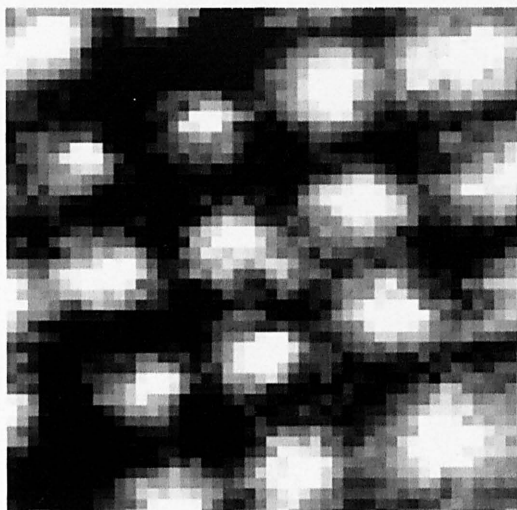
Figure 4.3.14 $60\,\mu m$ square scan of a $C_2(CF_2)_5CF_3$ SAM that has been exposed to $244\,nm$ laser at $100\,mW$ power for $10\,min$ before immersion into $1\,mM$ ethanolic $C_{10}COOH$ thiol solution, to make a patterned surface like that shown in figure 4.3.7 on page 161. LH2 complexes were then immobilised on the acid-terminated (square) regions using carbodiimide chemistry, in the same manner as were used to make the sample shown in figure 4.3.8 on page 162. The sample was then washed in buffer, dried under helium and affixed to the inside of a vacuum cryostat. Sample luminescence at a wavelength $>825\,nm$, following excitation using a $800\,nm$ laser photodiode, was then measured at discrete points to build up the image; wavelengths $<825\,nm$ were filtered with a band pass filter.

4.4   Discussion

4.4.1   Assessment of SAM Suitability by SPR

While some degree of correlation between surface free energy and growth of cells has been demonstrated[4,5,10], a large body of previous work has indicated that plasma proteins will adjust their secondary structures when proximal to an interface no matter how low $\Delta_{Surface}G$ is initially. Indeed, it is widely thought that, with the exception of repeated units of ethylene oxide, plasma proteins will stick to almost anything. The enthalpic reward yielded by interactions between domains in the folded protein are sacrificed as the protein denatures and becomes irreversibly bound by increasing its interfacial area with a surface. However, the selective binding of membrane complexes such as LH2 to surfaces has not been the subject of extensive studies previously. In this case, each LH2 complex is surrounded by a surfactant 'skirt' (*n*-dodecyl-β-maltoside—'DDM') that presents a wholly hydrophilic exterior to the biomolecule, and it is suggested that this causes it to be repelled by the hydrophobic surfaces.

The surfaces which demonstrated the greatest affinity for LH2 were the 'activated' carboxylate-N-succinimide ester (1), and carboxylic acid-terminated (2) SAMs. While this might, at first, seem

commensurate with the hypothesis that sticking in the case of LH2 can be correlated with surface free energy, the hydroxy-terminated SAM does not exhibit a particularly marked affinity for LH2, despite it having a 'hydrophilic' charcter. It might therefore be suggested that the superlative adhesion observed in the case of both carboxylate-functionalised SAMs is electrostatic in origin; the cytoplasmic face of LH2 is afforded a $\delta+$ve charge by a lysine group, which could produce such an interaction.

Following the cessation of the injection period, the carboxylate functionalities also exhibit a retention of LH2. This is not observed in the other cases, except to a much smaller degree in the case of bare gold, which will be discussed shortly. The end of the buffer elution period was marked by a single injection of 0.1 % (wt.) sodium dodecyl sulfate (SDS), which is a surfactant. While all the SAMs studied showed loss of some weakly-bound material, the $C_{10}COO-*$ surface, the 'activated ester', exhibited retention of $\sim$40 % of the material, indicating that a significant proportion was covalently bound. The $C_{10}COOH$ SAM appears to exhibit rapid loss of the physisorbed material at the interface, to a level *below* baseline. Such facile detachment is supportive of the hypothesis that the initial interaction is electrostatic; the $\delta+$ve attraction would be readily displaced by an full ionic interaction with a sulfate group. It is possible that that anomalous result (returning to a level *below* baseline) is due to the SDS surfactant disrupting interactions between buffer salts (*e.g.* LDAO). SDS aggregation into cyclindrical forms has also been observed at solid/liquid interfaces[11], which may cause the refractive index of the analyte to change near the surface, although it might be argued that the short injection time is insufficient for such aggregates to coalesce. Alternatively, the SDS may disrupt an interaction that occurs between the buffer an chip surface, which is experienced as a baseline.

That gold exhibits a significant retention of biological material even following SDS 'washing' is likely to be in part due to its unique surface properties. Most other metals are covered by thin oxide layers, and polar solvents (*e.g.* water, THF) tend to wet these materials ($\theta_a < 10°$), while apolar, organic solvents show the opposite wetting behaviour ($\theta_a > 90°$). The other major group of materials for which wetting behaviours have been extensively investigated are hydrocarbon polymers, which (unless they contain a large fraction of polar heteroatoms) tend to be wetted by apolar solvents, but not wetted by polar solvents, *i.e.* they show opposite wetting behaviour to polar surfaces. This diametric bifurcation of wetting behaviour over the two 'groups' (metals and polymers) is an oversimplification which is confounded by solvents other than water often being neglected in wetting experiments. Gold is variously described as 'hydrophilic', 'semihydrophobic', or 'slightly hydrophobic'; in reality gold is 'hydrophilic', but it is also 'oleophilic', thanks to its diffuse d electrons, which are able to stabilise adsorbates by van der Waals interactions (which are masked by directional dipoles on oxide-covered metal surfaces), as well as more polar interactions (it is '$\delta+$ve' when $\delta-$ve species are present at the surface). Biological molecules,

which contain a large number of hydrocarbons, but also a wide variety of polar groups, are therefore able to bind to gold through a wide variety of weak interactions. This rationale is supported the result in figure 4.3.1 on page 154 that shows that cysteine mutants of LH2 do not fare significantly better in terms of binding than wildtypes: Once a large protein such as LH2 has begun to adsorb onto a gold surface, it is likely to become kinetically trapped, because there are a large number of local energy minima on the interaction potential that prevent the proteins from reaching the thermodynamically most stable arrangement, *i.e.* cysteines down.

In order to have a better degree of control over orientation during the immobilisation process, there-fore, it is suggested that specific SAM-biomolecule interactions are more viable than using cysteine-functionalised proteins on gold. Of those investigated, OEO– and hydrophobic SAMs show the best resistance to LH2 adsorption, while the activated ester, $C_{11}COO-*$, demonstrates the best retention of LH2, due to covalent attachment.

4.4.2   Amide-Stabilised OEO films

As can be seen from the four SPR spectrographs in **figure 4.3.4** on page 157, the amide stabilised hydroxy-terminated OEO-SAM, '**1**', performs consistently as well as, if not better than conventional $C_{11}EO_3OH$ ('**c**') films at resisting protein. The ammonium-terminated molecule '**2**' was designed to immobilise proteins, and so demonstration of multiple proteins binding to this surface suggests that it is a good candidate for directed protein immmobilisation. Moreover, the data show that the inclusion of amide functionalities increase the stability of **1** and **2** in the presence of solution-phase thiol, as compared with films of **c**. However, the degree by which stability is increased is greater when there are two intrachain amides (*e.g.* in 2), and that little increased stability is afforded in the case of 1 as compared with c. Intermolecular interactions contain both repulsive as attractive terms, and the former is embodied by the concept of steric clashes: molecules have a finite size. Dipole-dipole and H-bonding are both dependent on direcion, and are characterised by having an optimum distance of interaction (for instance, the H-bonding in water ice, which causes its decreased density as compared with liquid water). It might be the case that, as well as providing a further stabilising effect, there is a repulsive ineraction which reduces the stability lower than might be expected. In the case of 2, the additional intrachain amide group may lead to a cooperative effect that renders it considerably more stable than 1. In order to assess whether this is the case, future experiments might consider additional units.

4.4.3 Patterning LH2

Clear patterns of LH2 sought by the (presumed) photooxidation of a $C_{11}EO_3OH$ SAM and the intro-
duction of a cysteine mutant strain initially proved elusive. At the time, the presence of a competing
photochemical process, the photodegradation of the EO moiety to yield aldehydes and carboxylic
acids demonstrated in Chapter 3, subsection 3.3.2 on page 122, was not known. Due to the fact that
photooxidation of the $C_{11}EO_3OH$ SAM has been shown to proceed much more slowly than previously
described, it is unlikely that the film would have fully photooxidised to yield sulfonates within the
timeframe of the experiment. Furthermore, the potential for aldehydes to drive the attachment of
thiols by the formation of (hemi)thioacetals, as described in subsection 3.3.3 on page 126, was also
not known. It is possible that either or both of these effects could have interfered with the patterning
process initially. When investigating the attachment of trifluoroethylamine (TFEA) to the photodegraded
$C_{11}EO_3OH$ SAM, as presented in subsection 3.3.2 on page 122, it was discovered that attachment is
very much dependent upon the exact protocol employed. Samples which were treated identically to
those shown to attach TFEA did not register a peak in the F_{1s} spectrum, in contrast to those spectra
shown in figure 3.3.10 on page 124, which showed a clear F_{1s} peak that has been interpreted at showing
successful attachment*. Therefore, if the OEO-SAM had been photodegraded, yielding aldehydes, it is
possible that either the protocol employed or the buffer conditions could have caused the adhesive effect
of the aldehyde to be nulled, possibly an unwarranted further oxidation to a carboxylic acid. Other
than $C_{10}COO$-*, most SAMs were shown to bind LH2 very weakly, and this attraction was quickly
reversed by the introduction of a detergent or high salt content. If the aldehydes were converted to
another functionality, *e.g.* a carboxylic acid or hydroxy group, then the binding of LH2 would not be
specific. A further complication arises if a (presumed) photooxidised $C_{11}EO_3OH$ SAM is immersed into
a contrasting thiol, *e.g.* $C_{10}COOH$ in order to activate it by the EDC-NHS method (forming $C_{10}COO$-*),
because hemithioacetals may be formed.

The SPR traces presented in 4.3.1 on page 154 suggest that, in the case of LH2 at least, thiolated
biomolecular complexes only exhibit a marginally increased binding compared to wildtypes that have
no native cysteines. There are good reasons why this may be generally true for other proteins. The
topographic AFM image shown in figure 4.3.2 on page 155, part (a), may indicate that the biomolecule
integrity can be compromise by the enhanced affinity of cysteines for defect sites of atomic steps on the
surface. It is possible that the cysteine mutant is more easily denatured, either due to its altered structure,
or the cysteines pulling the complex apart. Perhaps the same is true for the cysteine-mutant strain on an

---

*indeed, this was then supported by the attachment of streptavidin and biotinylated IgG

aldehyde-rich surface, and this merits further study. Nevertheless, the systematic SPR investigation did suggest a viable method of attachment that was in fact successful, and this is presented here.

The relatively long exposure times required to achieve a good-quality pattern with the perfluorintaed SAM on the micron-scale is at odds with the large negative surface potential observed when a fluorinated ester is formed at a SAM ω position, by the reaction of a perfluoroacid anhydride with a C_nOH SAM (see Chapter 3). However, it is difficult to make a direct comparison, because the former film contained an intrachain ester bond, and the extent of the reaction is limited to 50–60 %, whereas in this instance the entire SAM is perfluorinated. It has been suggested that perfluorinated SAMs are less polarisable than *n*-alkanes, although evidence of a strong dipole at the hydrcarbon/fluorocarbon boundary has been supported by NEXAFS studies[12]. Penetration of the molecular oxygen to the Au–S interface is also crucial. Fluorine can be considered as being isosteric with oxygen when connected to a carbon, but the chains in a perfluorinated SAM adopt a helical conformation which increases the effective van der Waals radius to 5.7 Å, *cf.* 4.2 Å for an all-*trans n*-alkane SAM; consequently, it is thought that a looser packing structure is adopted $(\sqrt{7} \times \sqrt{7})$[12]. It is possible that the helical geometry adopted by perfluorintaed SAMs retards the penetration of oxygen, leading to a slow photooxidation rate.

Originally, the stability of the perfluorinated thiol against aerial oxidation, and relatively slow micron-scale patterning process were thought to translate to a requirement for a much slower scanning rate for the SNP process. Therefore, experiments were carried out to create 'dots', using the lithography software to specify an appropriate dwell time (*e.g.* 4 s at 2 mW). These are shown in figure 4.3.9 on page 163. However, it was found that a lithography power and writing speed of lines at settings suitable for the NSOM lithography of acid-terminated SAMs was sufficient, as can be seen in 4.3.10 on page 164. The optimal settings for SNP of this system was determined to be a scan rate of 0.5 μm s^{-1}, and a laser power output of 2 mW. This is at odds with the required time for micron-scale patterning. In almost all SAMs explored for both micron— and nanoscale work, the rates of photooxidation are of the same order at both scales. It is possible that the helical geometry allowd facile penetration of oxygen on small scales, but that the structural disorder created by lifting a region of SAM that has been partially oxidised to a sulfonate retards further penetration *en masse*. Regardless of the physical basis of this result, it suggests that perfluorinated SAMs are good nanoscale photoresists, because they photooxidise quickly, like acid-terminated SAMs, but have very different surface properties, and are generally much more stable *e.g.* to aerial oxidation.

(a) From the side   (b) From the top
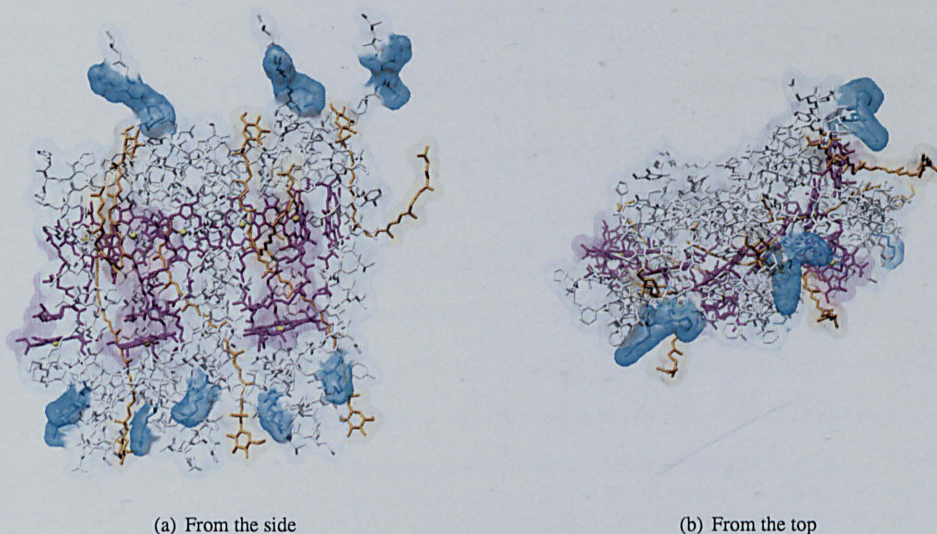
Figure 4.4.15   Cartoons showing the position of available lysine residues from the XRD structure of *Rhodopseudomonas acidophila* LH2—rendered using CHIMERA.

The 'height' of the nanoscale lines of LH2 might be considered in the context of a solved XRD crystal structure of the complex as found in *Rhodobacter sphaeroides*. Shown in **figure 4.4.15** is the XRD structure of a trimeric part (*i.e.* a third of the nonomer) of the complex from the similar bacterium, *Rhodopseudomonas acidophila*, as solved by Papiz *et al.*[13]. Bacteriochlorophylls are labelled purple, and carotenoids are orange. Also highlighted are the positions of lysine residues, in light blue. The amino acid sequence of *Rhodobacter sphaeroides*' LH2 is slightly different (see figure 2.3.23 on page 90), but it can be seen that there is a lysine group on the cytoplasmic face. Coordinate data from the pdb file used to render this image indicates that the extent of the polypeptide is $\sim$6.2 nm, which is the value arrived at by a statistical analysis along each of the lines, depicted in figure 4.3.12 on page 166. *Rhodobacter sphaeroides* LH2 has very similar dimensions. This shows very clearly that the lines are made of monolayers of LH2 complexes.

Through a series of trials it was discovered that biological functionality—namely, fluorescence in the spectral region expected—was compromised if the LH2 complex patterns were washed with water. This is part the standard cleaning protocol for AFM images of SAMs containing biomolecules, when it is desirable to remove salts deposited on the surface by the buffer, to improve the quality of the image. However, it is likely that the LH2 patterns presented above contained complexes whose functionality had been removed—although this was undetectable by AFM—as it is suggested that the likely cause of failure to produce a normal optical response was the unwarranted solvation of BChl Mg^{2+}, which would alter the electronic structure of the chromophore and, therefore, its optical properties. Spectro-

graphs acquired in appropriate buffer indicate that functionality is retained, and a parallel study* has shown that patterned samples imaged in biological buffer using a hybrid AFM-confocal system retain their functionality at room temperature. For this particular study, conditions were optimised for low temperatures (<10 K) in a vacuum cryostat.

The image shown in figure 4.3.11 on page 165 shows that the amount of biological material on the surrounding perfluorinated region is not zero. If the resistance to adhesion of light harvesting complexes does indeed arise due to hydrophobic/hydrophilic repulsion afforded by the surrounding surfactant skirt, as is supposed, then adsorption may occur by loss of surfactant molecules from the complexes. The height of these non-specifically-bound molecules is the same as the lines, and so they are probably not made up of lipids or other residual impurities from the extraction process. Indeed, fluorescence in the perfluorinated regions is not zero, suggesting the non-specifically bound molecules are still optically active.

It should be noted that the non-specific adsorption is more widespread along grain boundaries. The curvature of the substrate in these regions is likely to lower the integrity of the SAM. Indeed, as has been suggested, desorption of constituent molecules is likely to be increased at the grain boundaries. It is also possible, therefore, that these regions are less hydrophobic, and the complexes are better able to maximise interactions with the gold substrate.

4.5   Conclusions

The light harvesting 2 complex (LH2) from *Rhodobacter sphaeroides* has been successfully patterned using photolithographic methods. The successful patterning of functional membrane proteins, with retention of biological functionality, has far-reaching implications. In this particular instance, patterning of complexes involved in photosynthesis is of interest as a route to novel, 'biokleptic' photovoltaic devices, the first step towards which would be the selective immobilisation of biomolecules with preservation of structure and functionality.

Because initial attempts to pattern mutant complexes with substituent cysteine residues against biomolecule-repulsive OEO-SAMs did not yield promising results, a wider survey of potential films for the inclusion and immobilisation of LH2 was made. It was found that, contrary to an increasingly well-understood rationalisation for the patterning of plasma proteins, which has largely ruled out a surface free energy

---

*carried out by Nick Reynolds at The University of Twente, Enschede, Netherlands

basis for biomolecule repulsion, low energy surfaces (such as are provided by perfluorinated SAMs) do in fact retard the irreversible adsorption of LH2. An electrostatic basis was suggested for those surfaces that are suitable for the inclusion of LH2, but it was found that immobilisation required the use of an activated ester, which would covalent bind the complex at the position of its available lysine residues.

A previous biomolecule patterning protocol which relied on the (purported) photooxidation of an OEO-SAM did not yield easily obtainable patterns in the case of LH2. It was found that LH2 could be patterned by using a very hydrophobic SAM as a resistant surface, and an activated hydrophilic SAM to specifically immobilise the polypeptide component of the complex. It may be the case that what is now understood to be the photodegradation of the OEO moiety, yielding carbonyl surfaces, is not a suitable method for patterning this type of protein, or that the method requires modification to facilitate LH2 immobilisation.

The stability of amide-containing OEO-SAMs was explored alongside their protein resistance. It was found that such films could easily match the protein resistance of OEO-SAMs that do not contain amide groups. It was also shown that there is a relationship between the stability of the film and the number of intrachain amide groups it contains, and that the increased stability was more marked for two intrachain amides than one, which only slightly increased stability over none. It is suggested that films of this type might be used to pattern biomolecules, by photodegradation.

While seeking to demonstrate retention of biological functionality in LH2, it was found that the complex was sensitive to the washing protocol that was employed. Specifically, it has been postulated that water, or any other aqueous media not containing the requisite buffer and surfactant, might wash out Mg^{2+}. Assemblies that consist of discrete ionic, atomic and macromolecular components require very careful control during integration into other systems. Another perspective might suggest that potential biomimetic systems make modifications that would impart greater resilience during patterning procedures. For example, chlorin units, whether in natural or artificial light harvesting antennae, might adopt Zn^{2+} as a more stable ion that would resist such wasking procedures.

The patterning of LH2 presented in this chapter has been modest. Nevertheless, a succesful patterning protocol has been developed, and will be useful in informing the direction of future work.

Some of the work presented in this chapter has been previously published, see *Ref.*[14], while some is in preparation for publication, *Ref.*[15]

List of Figures in Chapter 4

List of Tables in Chapter 4

Notes and References for Chapter 4

[1] R. G. Chapman, E. Ostuni, L. Yan, and G. M. Whitesides, "Preparation of mixed self-assembled monolayers (sams) that resist adsorption of proteins using the reaction of amines with a sam that presents interchain carboxylic anhydride groups," *Langmuir*, vol. 16, pp. 6927–6936, August 2000.

[2] X. Jiang, D. A. Bruzewicz, M. M. Thant, and G. M. Whitesides, "Palladium as a substrate for self-assembled monolayers used in biotechnology," *Anal. Chem.*, vol. 76, pp. 6116–6121, October 2004.

[3] C. Pale-Grosdemange, E. S. Simon, K. L. Prime, and G. M. Whitesides, "Formation of self-assembled monolayers by chemisorption of derivatives of oligo(ethylene glycol) of structure hs(ch2)11(och2ch2)moh on gold," *Journal of the American Chemical Society*, vol. 113, no. 1, pp. 12–20, 1991.

[4] C. A. Scotchford, E. Cooper, G. J. Leggett, and S. Downes, "Growth of human osteoblast-like cells on alkanethiol on gold self-assembled monolayers: The effect of surface chemistry," *Journal of Biomedical Materials Research*, vol. 41, no. 3, pp. 431–442, 1998.

[5] C. A. Scotchford, C. P. Gilmore, E. Cooper, G. J. Leggett, and S. Downes, "Protein adsorption and human osteoblast-like cell attachment and growth on alkylthiol on gold self-assembled monolayers," *Journal of Biomedical Materials Research*, vol. 59, no. 1, pp. 84–99, 2002.

[6] R. L. C. Wang, H. J. Kreuzer, and M. Grunze, "Molecular conformation and solvation of oligo(ethylene glycol)-terminated self-assembled monolayers and their resistance to protein adsorption," *Journal of Physical Chemistry B*, vol. 101, pp. 9767–9773, November 1997.

[7] R. Valiokas, S. Svedhem, M. Östblom, S. C. T. Svensson, and B. Liedberg, "Influence of specific intermolecular interactions on the self-assembly and phase behavior of oligo(ethylene glycol)-terminated alkanethiolates on gold," *J. Phys. Chem. B*, vol. 105, pp. 5459–5469, June 2001.

[8] R. Valiokas, M. Östblom, S. Svedhem, S. C. T. Svensson, and B. Liedberg, "Thermal stability of self-assembled monolayers: Influence of lateral hydrogen bonding," *J. Phys. Chem. B*, vol. 106, pp. 10401–10409, October 2002.

[9] J. B. Schlenoff, M. Li, and H. Ly, "Stability and self-exchange in alkanethiol monolayers," *Journal of the American Chemical Society*, vol. 117, no. 50, pp. 12528–12536, 1995.

[10] E. Cooper, L. Parker, C. A. Scotchford, S. Downes, G. J. Leggett, and T. L. Parker, "The effect of alkyl chain length and terminal group chemistry on the attachment and growth of murine 3t3 fibroblasts and primary human osteoblasts on self-assembled monolayers of alkanethiols on gold," *The Journal of Materials Chemistry*, vol. 10, no. 1, pp. 133–139, 2000.

[11] H. Dominguez, "Self-aggregation of the sds surfactant at a solid-liquid interface," *J. Phys. Chem. B*, vol. 111, pp. 4054–4059, April 2007.

[12] D. Barriet and R. T. Lee, "Fluorinated self-assembled monolayers: composition, structure and interfacial properties," *Current Opinion in Colloid & Interface Science*, vol. 8, pp. 236–242, August 2003.

[13] M. Z. Papiz, S. M. Prince, T. Howard, R. J. Cogdell, and N. W. Isaacs, "The structure and thermal motion of the b800-850 lh2 complex from rps.acidophila at 2.0a resolution and 100k: new structural features and functionally relevant motions.," *Journal of molecular biology*, vol. 326, pp. 1523–1538, March 2003.

[14] N. P. Reynolds, S. Janusz, M. Escalante-Marun, J. Timney, R. E. Ducker, J. D. Olsen, C. Otto, V. Subramaniam, G. J. Leggett, and C. N. Hunter, "Directed formation of micro- and nanoscale patterns of functional light-harvesting lh2 complexes," *J. Am. Chem. Soc.*, vol. 129, pp. 14625–14631, November 2007.

[15] L. S. Wong, S. J. Janusz, G. J. Leggett, and J. Micklefield, *Solid Phase Organic Synthesis of Pegylated Disulfides for the generation of Biocompatible Self-assembled Monolayers*. In preparation.

Chapter 5

Conclusions and Future Work

This work set out to explore the integration of a functional biological structure—a biological light harvesting membrane complex—into an artificial self-assembling system, and to do so with directed patterning and demonstrable retention of biological functionality. From the outset, it was thought that the best approach to this challenge was to develop a clear, fundamental understanding of the nature of the artificial systems which could be applied to the integration of biological structures. SAMs had been used for patterning proteins, but the exact mechanisms by which they undergo photooxidation remained unclear.

In Chapter 3, a number of significant results were presented from a series of investigations into the action of short wavelength light on SAMs. A large body of previous work had shown that SAMs were effective photoresists for the fabrication of micro– and nanostructures. Studies of the photooxidation kinetics of organothiolate SAMs on gold and silver, by wetting, XPS and SIMS, had indicated that the nature of the terminal (ω) functionality played an important rôle in determining the rate of photooxidation. Initial work present aimed to rationalise trends in M–SR photooxidation kinetics on Au and Ag that had previously been investigated, by the systematic measurement of surface potentials on the SAMs primarily used to make patterns. From the findings, it was suggested that the data are supportive of a 'hot electron' model of photooxidation, whereby the average kinetic energy (from a Maxwell-Boltzmann type distribution) of electrons excited by incident light is dependent on the surface potential imposed by the SAM. In SAMs with ω functionalities which impose a negative surface potential (such as carboxylic acids), the effective work function is increased. The average kinetic energy of electrons is not sufficient to allow ejection to the vacuum level, and so the large number of sub-vacuum electrons so-formed expedite the photooxidative desorption of the SAM molecules by tunnelling into the M–S

178

σ^* antibonding orbital. However, for SAMs which impose a positive surface potential, the effective work function is decreased, and so the average kinetic energy of electrons is sufficient for them to be ejected to the vacuum level (as photoelectrons). The same pattern can be seen for silver organothiolate SAMs that is observable in gold thiolate SAMs. The study was then extended to include palladium organothiolate SAMs. While some trends follow those of SAMs made on gold and silver, wetting characteristics were observably different for the 'long' hydrophilic ω-terminated SAMs. A number of physicochemical rationalisations were put forth for the aberrant results, but it is clear that further work needs to be carried out to elucidate the fundamental structures of Pd–SR SAMs with different ω groups, and the mechanism(s) by which they are photooxidised.

The photodegradation of oligo(ethylene oxide)-terminated SAMs presents a novel, 'one-step' procedure for the directed immobilisation of at least some biomolecules. This is extremely promising and suggests a very simple solution for the formation of bionomics arrays, or arrays of functional biological struc-tures. There is also the suggestion that this chemistry can be transported onto other substrates. Initial exploratory work was presented that demonstrated the possibility of using glutaraldehyde coupling to attach thiols to mercaptosilane monolayers on silicon. It was shown that OEO-terminated thiols could be attached by this method, and photodegraded to facilitate the immobilisation of fluorinated amines (and, it is suggested, biomolecules). A control OEO-terminated thiol attached via this coupling chemistry did not show attachment of the amine. This indicates that the chemistry may work, but much further work needs to be done to assess its viability as a means to pattern protein on silicon substrates (which, it is thought, could be expanded to glass for biofluorescence work). In particular, it should be demonstrated that the OEO film density per unit area lies between 0.4–0.6, when protein resistance is greatest.

While the advances made in patterning LH2 were only very modest, a patterning protocol was eventually developed. It was shown that reasonably well-defined patterns, one complex thick, could be formed by introducing areas of high or low surface free energy, and introducing capturing groups with particular specificity on the areas of high surface free energy. It was demonstrated that the same chemistry could be used to form nanoscale patterns. In demonstrating retention of biological functionality, it was found that the complexes were extremely sensitive to any washing conditions. From the perspective of future applications, using either a similar 'biokleptic' approach, or with artificial antennae designs perhaps based on synthetic chlorins (*i.e.* 'biomimetic' structures and devices), modifications might be made. For example, Zn^{2+} might be adopted as a more stable ion than Mg^{2+} in chlorin units. Additionally, porphyrin-based artificial antennae do not have to rely on weak associations between polypeptide domains, and structures similar to those in nature can be synthesised to perform a similar task for photovoltaic systems.

An interesting development regarding the integration of biological light-harvesting systems would be the immobilisation of all the discrete components of, for instance, *Rhodobacter sphaeroides'* photosystem. Gradient SAM systems, or 'multicolour' lithography, might be used to specifically place arrays of both LH2 and LH1, with or without RC, in arrangements close to, or even deviating wildly from, those found in the native membrane architecture. This would provide useful information regarding the efficiency of energy migration in biological systems, which would in turn inform the design of artificial systems.